

A Search for New Particles Decaying into $t\bar{t}$ Pairs

by

Josh A. Cassada

Submitted in Partial Fulfillment

of the

Requirements for the Degree

Doctor of Philosophy

Supervised by

Professor Paul Tipton

Department of Physics and Astronomy

The College

Arts and Sciences

University of Rochester

Rochester, New York

1999

UMI Number: 9960729

UMI[®]

UMI Microform 9960729

Copyright 2000 by Bell & Howell Information and Learning Company.

All rights reserved. This microform edition is protected against
unauthorized copying under Title 17, United States Code.

Bell & Howell Information and Learning Company
300 North Zeeb Road
P.O. Box 1346
Ann Arbor, MI 48106-1346

Curriculum Vitae

The author [REDACTED] received his Bachelor of Arts degree in Physics from Albion College in 1995. In June 1995, he began his tenure as a research assistant under the direction of Professor Paul L. Tipton. In May 1997, he received his Masters of Arts degree from the Department of Physics and Astronomy at the University of Rochester.

Acknowledgements

The research presented here would not have been possible without the efforts and support of a vast number of people. And while I owe a tremendous amount of gratitude to so many, it is unfortunately not possible to thank everyone individually in the next few paragraphs.

First, I offer my thanks to all of my CDF collaborators and to the Fermilab staff because much of my work relied heavily upon the accomplishments of those before me — many of whom I have never even had the pleasure of meeting, much less having the opportunity to thank personally. I can only hope that my contributions will also prove beneficial to future physics conducted at the lab. I am indebted to Robert Harris, David Stuart, and Michele Gallinaro — this analysis benefited greatly from their careful review and many suggestions. And to my fellow students back at Rochester, studying along side such a genuine group of people made the long days as enjoyable as they were educational. A special thanks to Carl Welch — neither of us were about to take the prelim lying down, but it was great not to have to go it alone. And I am indebted to Connie, Sue, Judy, and Barbara who always took good care of me and made sure that any required paperwork was as painless as possible.

Thanks to Roser who, since the day I met him, has been as selfless with his time and his truck as he has recently been with his new home. When I needed it, he was always quick to assist with any struggles in my work and in paying for the tab at the sports bar, both of which I'll miss dearly. Also, I owe much appreciation to Mark Kruse with whom I have worked closely on this particular analysis as well as several other topics. He has hitherto been very tolerant of my endless barrage of questions, often spending much time uncovering the answers with me; but soon I'll no longer be across the hall and then maybe his own scientific efforts can

go undisturbed. And thanks to Phil Koehn who was always available for honest discussion of any topic, be it related to analysis or life.

I am also indebted to JJ Schmidt, Luc Demortier, Steve Blusk, George Velez, and Kirsten Tollefson who routinely bailed me out of the many technical difficulties that arose during this analysis. Thanks to my officemate, Ben Kilminster, who has graciously tolerated the intensity surrounding various deadlines and, in light of yet another one, even volunteered to create the figure on page 52. And thanks to my good friend Sondra Rosenberg — hers is a refreshing outlook on life and was always very welcome when she magically reappeared every summer. And while he was always willing to lend his insight on coursework back in Rochester, I owe special appreciation to Bob Henderson for his continued great friendship and, as always, his unwavering encouragement.

Thanks to my wonderful family, who were so supportive when I needed them the most and who only rarely refused to accept the long-distance charges. And to Meg, my best friend, who has given me so much and upon whom I have leaned so heavily — her understanding and comfort have been never-ending. And, plus, she and I laugh really hard together.

Yet, of all those to whom I owe appreciation for their role in my graduate career, none has been more influential than my advisor, Paul Tipton. In addition to guiding me as a developing scientist, he has taught me how to always keep things in perspective, in physics as well as in life. His support during these many years can only be rivaled by his incredible friendship. And for that, I can never thank him enough. But I'll probably end up trying anyway.

And, of course, to my most formidable adversary during my tenure as a graduate student, Fermilab's legion of Canadian geese: you may have won the battle, but you certainly haven't won the war.

Abstract

We use 106 pb^{-1} of data collected with the Collider Detector at Fermilab to search for narrow-width particles decaying to a top and an anti-top quark. We measure the $t\bar{t}$ invariant mass distribution by requiring that either t or \bar{t} decays semileptonically to an electron or muon and the other decays hadronically. Model independent upper limits on the cross section for narrow resonances decaying to $t\bar{t}$ are presented. At the 95% confidence level, we exclude the existence of a leptophobic Z' boson in a model of topcolor-assisted technicolor with mass $M_{Z'} < 480 \text{ GeV}/c^2$ for natural width $\Gamma = 0.012 M_{Z'}$, and $M_{Z'} < 780 \text{ GeV}/c^2$ for $\Gamma = 0.04 M_{Z'}$.

Contents

1	Introduction	1
1.1	The Standard Model	2
1.2	The Top Quark	9
1.2.1	Top Quark Production at Fermilab	10
1.2.2	Top Quark Decay	13
1.2.3	Beyond the Standard Model and $t\bar{t}$ Resonances	15
2	Experimental Apparatus	19
2.1	The Tevatron	19
2.2	The CDF Detector	23
2.2.1	The Tracking System	23
2.2.2	The Calorimetry	28
2.2.3	The Muon Chambers	31
2.2.4	Event Triggers	32
3	$M_{t\bar{t}}$ Event Samples	35
3.1	Primary Event Selection	36
3.1.1	Electron Selection	36
3.1.2	Muon Selection	40
3.1.3	W Selection	45

3.1.4	Jet Selection	48
3.1.5	Summary of Primary Event Selection	54
3.2	Monte Carlo Simulation and Background	54
3.2.1	Backgrounds	56
3.3	Jet Corrections	61
3.3.1	Generic Jet Energy Corrections	61
3.3.2	$t\bar{t}$ Jet Energy Corrections	64
3.4	Measuring $M_{t\bar{t}}$	66
3.4.1	Mass Fitter	69
3.4.2	6-Body Mass Method	71
3.4.3	Unconstrained Method	74
3.4.4	Constrained Method	74
3.5	$t\bar{t}$ Resonance Selection Criteria	76
3.5.1	Effect of Wrong Combinations on $M_{t\bar{t}}$	76
3.5.2	M_{3-body} Cut	84
3.5.3	χ^2 Cut	86
3.6	Signal Acceptances	100
4	Measurement of the $M_{t\bar{t}}$ Spectrum	102
4.1	$M_{t\bar{t}}$ Spectrum	103
4.2	$X \rightarrow t\bar{t}$ Cross-section Limits	106
4.2.1	Establishing Upper Limits	106
4.2.2	Verifying the 95% Level of Confidence	108
5	Systematic Uncertainties	114
5.1	Determining the Likelihood Uncertainty	115
5.1.1	Shape Effects	115

5.1.2	Acceptance Effects	116
5.2	Sources of Systematic Uncertainty	117
5.2.1	Jet E_T Systematic	117
5.2.2	M_{top} Systematic	120
5.2.3	Initial State Radiation Systematic	122
5.2.4	Final State Radiation Systematic	123
5.2.5	b -tagging Systematic	131
5.2.6	Structure Function Systematic	134
5.2.7	QCD Background Shape Systematic	136
5.2.8	Additional Acceptance Systematics	137
5.2.9	Luminosity Systematic	137
5.2.10	Summary of Acceptance Systematics	138
5.2.11	Correlation Between Jet E_T and M_{top} Systematics	138
5.2.12	Combining Systematics	139
5.2.13	Systematics for $\Gamma = 0.04M_X$	140
5.3	Results Including Systematic Uncertainty	148
6	Conclusions	153
	Bibliography	156

List of Figures

1.1	The fundamental particles of the standard model. Fermions interact via different forces mediated by the exchange of massless or massive gauge bosons.	6
1.2	Various single top quark production processes.	12
1.3	$t\bar{t}$ pair production processes. At Fermilab, the $q\bar{q}$ annihilation mechanism dominates.	12
1.4	Tree level $q\bar{q} \rightarrow t\bar{t}$ production followed by standard model top quark decay.	16
1.5	The 15 left and right-handed fermions of the first generation of the standard model. Each quark exists in three different colors.	17
2.1	Schematic diagram of the Fermilab accelerator. While the Tevatron and Main Ring have the same radius, for the sake of clarity the two have not been superimposed.	20
2.2	One quarter cross-section of the CDF detector which is forward-backward symmetric about the nominal interaction point located in the lower right of the figure.	24
2.3	A schematic diagram of the CTC cross-section which illustrates how the 84 drift layers are arranged in the superlayer geometry.	26

2.4	A schematic diagram of one SVX barrel. The four layers of the barrel are divided into 12 wedges in ϕ . The SVX detector is comprised of two barrels placed end-to-end.	28
2.5	A schematic diagram of the central electromagnetic and hadronic calorimeters. The projective tower geometry points back to the nominal interaction point. The central muon chambers are also depicted.	30
3.1	Distributions of several electron variables (described in the text) for electrons in CDF $Z \rightarrow e^+e^-$ events. The primary electron identification requirements used in the $t\bar{t}$ resonance search are shown as dashed lines and are listed in Table 3.1.	39
3.2	Distributions of several muon variables (described in the text) for CMU and/or CMP muons in CDF $Z \rightarrow \mu^+\mu^-$ events. The primary muon identification requirements used in the $t\bar{t}$ resonance search are shown as dashed lines and are listed in Table 3.2.	43
3.3	Distributions of several muon variables (described in the text) for CMX muons in CDF $Z \rightarrow \mu^+\mu^-$ events. The primary muon identification requirements used in the $t\bar{t}$ resonance search are shown as dashed lines and are listed in Table 3.2.	44
3.4	The lepton-neutrino invariant transverse mass for events in the W sample. The left (right) plot shows the M_T spectrum for events containing a primary electron (muon).	49
3.5	Schematic diagram of a typical secondary vertex which is associated with a jet resulting from the heavy-flavor quark decay.	52
3.6	Semileptonic b quark decays.	53

3.7	$Wb\bar{b}$, $Wc\bar{c}$, and Wc production processes which contribute to the non- $t\bar{t}$ backgrounds for the search for $X \rightarrow t\bar{t}$ search.	57
3.8	The fractional jet correction as a function of uncorrected jet E_T for each of the flavor-independent corrections: (a) relative energy scale, (b) absolute energy scale, (c) underlying event, and (d) out-of-cone. In addition to the constant offset shown in (a), the relative energy correction has an additional η -dependent component. The functional form of the underlying event correction shown in (b) is applicable to singular vertex Run 1b events. Underlying event corrections for events from Run 1a and multiple vertex Run 1b events are described in the text.	65
3.9	The parton-specific jet correction factor for (A) jets from hadronic W boson decay, (B) b -quark jets that are tagged only by the SVX, (C) b -quark jets that are tagged only by the presence of an SLT electron, and (D) b -quark jets that are tagged only by the presence of an SLT muon.	67
3.10	The uncertainty in corrected jet P_T for (A) jets from hadronic W boson decay, (B) b -quark jets that are tagged only by the SVX, (C) b -quark jets that are tagged only by the presence of an SLT electron, (D) b -quark jets that are tagged only by the presence of an SLT muon, and (E) any extra jets in the event.	68
3.11	$M_{t\bar{t}}$ determined by the 6-body mass method for $M_{Z'} = 600 \text{ GeV}/c^2$ PYTHIA Monte Carlo. Top: 6-body $M_{t\bar{t}}$ for all events passing the selection selection criteria ("tagged" and "untagged" events). Bottom: The subset of events in which the "best" configuration has the four jets correctly identified.	73

3.12	$M_{t\bar{t}}$ determined by the unconstrained method for $M_{Z'} = 600 \text{ GeV}/c^2$ PYTHIA Monte Carlo. Top: Unconstrained $M_{t\bar{t}}$ for all events passing the selection criteria (“tagged” and “untagged” events). Bottom: The subset of events in which the “best” configuration has the four jets correctly identified.	75
3.13	$M_{t\bar{t}}$ determined by the constrained method for $M_{Z'} = 600 \text{ GeV}/c^2$ PYTHIA Monte Carlo. Top: Constrained $M_{t\bar{t}}$ for all events passing the selection criteria (“tagged” and “untagged” events). Bottom: The subset of events in which the “best” configuration has the four jets correctly identified.	77
3.14	Constrained $M_{t\bar{t}}$ for those $M_{Z'} = 600 \text{ GeV}/c^2$ PYTHIA Monte Carlo events (“tagged” and “untagged”) in which the constrained method selects a jet configuration which is incorrect.	79
3.15	Constrained $M_{t\bar{t}}$ for those $M_{Z'} = 600 \text{ GeV}/c^2$ PYTHIA Monte Carlo events (“tagged” and “untagged”) in which the constrained method selects a jet configuration which has at least one b -jet incorrectly exchanged with a hadronic W -jet.	80
3.16	PYTHIA $M_{Z'} = 600 \text{ GeV}/c^2$ Monte Carlo events (“tagged” and “untagged”) in which one of the four leading jets is not the direct result of $t\bar{t}$ decay. Top: Generator level transverse momentum (P_T) of the jet resulting from $t\bar{t}$ decay which was not included the leading four jets. Bottom: Reconstructed P_T of the extra jet which replaced the lost $t\bar{t}$ jet.	83

3.17	PYTHIA $M_{Z'} = 600 \text{ GeV}/c^2$ Monte Carlo events (“tagged” and “untagged”) in which the constrained $M_{l\bar{l}}$ method selects an incorrect jet configuration. The abscissa represents the constrained $M_{l\bar{l}}$ for a given event. M_{jjj}^u and $M_{l\nu j}^u$ are the three-body invariant masses returned by the unconstrained method using the configuration selected by the constrained method.	85
3.18	Distribution of M_{jjj}^u and $M_{l\nu j}^u$ for PYTHIA $M_{Z'} = 600 \text{ GeV}/c^2$ Monte Carlo events (“tagged” and “untagged”).	87
3.19	Distribution of M_{jjj}^u and $M_{l\nu j}^u$ for PYTHIA $M_{Z'} = 400 \text{ GeV}/c^2$ Monte Carlo events (“tagged” and “untagged”).	88
3.20	$M_{l\bar{l}}$ determined by the constrained method for $M_{Z'} = 400 \text{ GeV}/c^2$ PYTHIA Monte Carlo (“tagged” and “untagged” events). Top: Effects of $150 \text{ GeV}/c^2 < M_{3\text{-body}} < 200 \text{ GeV}/c^2$ on all events passing the selection criteria. Also, $M_{l\bar{l}}$ for events with correct and incorrect jet configuration which pass the $M_{3\text{-body}}$ cut. Bottom: Events eliminated by the $M_{3\text{-body}}$ cut.	89
3.21	$M_{l\bar{l}}$ determined by the constrained method for $M_{Z'} = 500 \text{ GeV}/c^2$ PYTHIA Monte Carlo (“tagged” and “untagged” events). Top: Effects of $150 \text{ GeV}/c^2 < M_{3\text{-body}} < 200 \text{ GeV}/c^2$ on all events passing the selection criteria. Also, $M_{l\bar{l}}$ for events with correct and incorrect jet configuration which pass the $M_{3\text{-body}}$ cut. Bottom: Events eliminated by the $M_{3\text{-body}}$ cut.	90

- 3.22 $M_{t\bar{t}}$ determined by the constrained method for $M_{Z'} = 600 \text{ GeV}/c^2$ PYTHIA Monte Carlo (“tagged” and “untagged” events). Top: Effects of $150 \text{ GeV}/c^2 < M_{3\text{-body}} < 200 \text{ GeV}/c^2$ on all events passing the selection criteria. Also, $M_{t\bar{t}}$ for events with correct and incorrect jet configuration which pass the $M_{3\text{-body}}$ cut. Bottom: Events eliminated by the $M_{3\text{-body}}$ cut. 91
- 3.23 $M_{t\bar{t}}$ determined by the constrained method for $M_{Z'} = 700 \text{ GeV}/c^2$ PYTHIA Monte Carlo (“tagged” and “untagged” events). Top: Effects of $150 \text{ GeV}/c^2 < M_{3\text{-body}} < 200 \text{ GeV}/c^2$ on all events passing the selection criteria. Also, $M_{t\bar{t}}$ for events with correct and incorrect jet configuration which pass the $M_{3\text{-body}}$ cut. Bottom: Events eliminated by the $M_{3\text{-body}}$ cut. 92
- 3.24 Significance as a function of applied χ_c^2 cut for PYTHIA 5.7 Z' Monte Carlo ($M_{Z'} = 400 \text{ GeV}/c^2$). Three different $M_{t\bar{t}}$ windows are employed as the “signal region.” For χ_c^2 cuts which yield over-lapping error bars for different $M_{t\bar{t}}$ windows, the points have been shifted slightly along the abscissa to avoid ambiguity. 96
- 3.25 Significance as a function of applied χ_c^2 cut for PYTHIA 5.7 Z' Monte Carlo ($M_{Z'} = 500 \text{ GeV}/c^2$). Three different $M_{t\bar{t}}$ windows are employed as the “signal region.” For χ_c^2 cuts which yield over-lapping error bars for different $M_{t\bar{t}}$ windows, the points have been shifted slightly along the abscissa to avoid ambiguity. 97
- 3.26 Significance as a function of applied χ_c^2 cut for PYTHIA 5.7 Z' Monte Carlo ($M_{Z'} = 600 \text{ GeV}/c^2$). Three different $M_{t\bar{t}}$ windows are employed as the “signal region.” For χ_c^2 cuts which yield over-lapping error bars for different $M_{t\bar{t}}$ windows, the points have been shifted slightly along the abscissa to avoid ambiguity. 98

3.27	Significance as a function of applied χ_c^2 cut for PYTHIA 5.7 Z' Monte Carlo ($M_{Z'} = 700 \text{ GeV}/c^2$). Three different $M_{t\bar{t}}$ windows are employed as the “signal region.” For χ_c^2 cuts which yield over-lapping error bars for different $M_{t\bar{t}}$ windows, the points have been shifted slightly along the abscissa to avoid ambiguity.	99
4.1	Background and signal ($\Gamma = 0.012M_{Z'}$) $M_{t\bar{t}}$ templates from Monte Carlo events that survive $M_{t\bar{t}}$ event selection.	104
4.2	The observed $M_{t\bar{t}}$ spectrum (points) compared to the QCD W +jets background (fine dashed) and the total standard model prediction including both QCD W +jets and $t\bar{t}$ production (thick dashed). The $t\bar{t}$ prediction has been normalized such that the number of events in the total standard model prediction is equal to the number of events in the data. The inset shows the expected $M_{t\bar{t}}$ shape resulting from the simulation of a narrow resonance ($M_{Z'} = 500 \text{ GeV}/c^2$, $\Gamma = 0.012M_{Z'}$) in the CDF detector.	107
4.3	Likelihood as a function of $X \rightarrow t\bar{t}$ production cross-section times branching ratio for $M_X = 400, 500, 600$, and $700 \text{ GeV}/c^2$ and natural width $\Gamma = 0.012M_X$. The effects of systematic uncertainties are not included.	109
4.4	The 95% C.L. upper limits on $\sigma_X \cdot \text{BR}\{X \rightarrow t\bar{t}\}$ as a function of M_X . The effects of systematic uncertainties are not included.	110
5.1	The shape and acceptance contributions to the likelihood systematic uncertainty, Δ , resulting from $\pm 1\sigma$ shifts in jet E_T	119
5.2	The shape and acceptance contributions to the likelihood systematic uncertainty, Δ , resulting from $\pm 1\sigma$ shifts in M_{top}	121

5.3	The shape and acceptance contributions to the likelihood systematic uncertainty, Δ , resulting from $\pm 1\sigma$ shifts in ISR.	124
5.4	The shape and acceptance contributions to the likelihood systematic uncertainty, Δ , resulting from $\pm 1\sigma$ shifts in FSR.	127
5.5	The shape and acceptance contributions to the likelihood systematic uncertainty, Δ , resulting from $\pm 1\sigma$ shifts in the b -tagging efficiency. The $+1\sigma$ curve is obtained by using a template comprised of only Monte Carlo events which contain a b -tag, while the -1σ curve results from using the distribution of untagged simulated events. . .	132
5.6	The shape and acceptance contributions to the likelihood systematic uncertainty, Δ , resulting from $\pm 1\sigma$ shifts in structure function. . . .	135
5.7	The total and individual contributions to the likelihood uncertainty, Δ , for $M_X = 400 \text{ GeV}/c^2$ resulting from $\pm 1\sigma$ shifts in each source of systematic uncertainty.	141
5.8	The total and individual contributions to the likelihood uncertainty, Δ , for $M_X = 500 \text{ GeV}/c^2$ resulting from $\pm 1\sigma$ shifts in each source of systematic uncertainty.	142
5.9	The total and individual contributions to the likelihood uncertainty, Δ , for $M_X = 600 \text{ GeV}/c^2$ resulting from $\pm 1\sigma$ shifts in each source of systematic uncertainty.	143
5.10	The total and individual contributions to the likelihood uncertainty, Δ , for $M_X = 700 \text{ GeV}/c^2$ resulting from $\pm 1\sigma$ shifts in each source of systematic uncertainty.	144
5.11	The total and individual contributions to the likelihood uncertainty, Δ , for $M_X = 800 \text{ GeV}/c^2$ resulting from $\pm 1\sigma$ shifts in each source of systematic uncertainty.	145

5.12	Likelihood as a function of $X \rightarrow t\bar{t}$ production cross-section times branching ratio for $M_X = 400, 500, 600$, and $700 \text{ GeV}/c^2$ and natural width $\Gamma = 0.012M_X$. Both the likelihood shape for statistical uncertainties only (dashed) and the likelihood with systematic uncertainties (solid) are shown.	149
5.13	The CDF Run 1 95% confidence level $\sigma_X \cdot \text{BR}\{X \rightarrow t\bar{t}\}$ limits as a function of M_X . The effects of systematic uncertainties are included.	150
6.1	The CDF Run 1 95% confidence level $\sigma_X \cdot \text{BR}\{X \rightarrow t\bar{t}\}$ upper limits as a function of resonance mass M_X . The effects of systematic uncertainties are included. Included for reference are the predicted topcolor Z' cross-sections for a width = 1.2% and 4.0% of $M_{Z'}$. . .	155

List of Tables

1.1	The $t\bar{t}$ decay channels and their corresponding lowest order branching ratios.	14
1.2	The 18 independent parameters of the standard model.	16
2.1	Specifications of the CDF calorimetry systems.	31
3.1	Selection cuts for primary electrons.	40
3.2	Selection cuts for primary muons.	42
3.3	The secondary electron cuts used for Z boson removal.	46
3.4	The secondary muon cuts used for Z boson removal.	47
3.5	The non- $t\bar{t}$ background contributions as calculated in the top quark mass analysis before the updated Run 1 measurement of the ratio of b -tagging rates for Monte Carlo and data.	60
3.6	The non- $t\bar{t}$ background contributions as calculated in the top quark mass analysis after the updated Run 1 measurement of the ratio of b -tagging rates for Monte Carlo and data.	60
3.7	Signal acceptance, A , as determined from Monte Carlo. The statistical uncertainties on these values result from finite Monte Carlo statistics and vary from 1.8 to 1.9%.	101

4.1	The estimated non- $t\bar{t}$ background contributions to the Run 1 data events satisfying the $M_{t\bar{t}}$ selection criteria.	105
4.2	The most probable values of cross-section times branching ratio for narrow resonances (with natural width $\Gamma = 0.012M_X$ and $\Gamma = 0.04M_X$) decaying to $t\bar{t}$. These values do not include the effects of systematic uncertainties.	111
4.3	The 95% C.L. upper limits cross-section times branching ratio for narrow resonances (with natural width $\Gamma = 0.012M_X$ and $\Gamma = 0.04M_X$) decaying to $t\bar{t}$. These values do not include the effects of systematic uncertainties.	112
5.1	The change in Monte Carlo signal acceptance rate, ΔA , due to shifting jet E_T by $\pm 1\sigma$	118
5.2	The change in Monte Carlo signal acceptance rate, ΔA , due to shifting M_{top} by $\pm 1\sigma$	120
5.3	The change in Monte Carlo signal acceptance rate due to eliminating ISR. One-half of this change is taken to be the -1σ uncertainty in signal acceptance due to ISR. The -1σ and $+1\sigma$ uncertainties are assumed to be symmetric.	123
5.4	Number of events and acceptance ratio for N_{jet} subsamples described in the text. Note: $\frac{A_{no\ ISR}^{4'}}{A_{no\ ISR}^4} = \frac{N_{no\ ISR}^{4'}}{N_{no\ ISR}^4}$ only holds <i>approximately</i> due tagging, lepton identification, and "Level 3" efficiencies.	130
5.5	Monte Carlo signal acceptance rates as described in the text. The upper limit on the change in acceptance due to no FSR is given by $\frac{\Delta A^4}{A_{no\ ISR}^4} \cdot A$	131

5.6	The change in Monte Carlo signal acceptance rate, ΔA , due to using the MRSD0' structure function instead of CTEQ2L (assumed to be a -1σ shift in structure function uncertainty).	136
5.7	The 1σ uncertainty in Monte Carlo signal acceptance rate, ΔA , due to several additional acceptance sources such as trigger efficiency, lepton identification efficiency, tracking efficiency, z-vertex efficiency, and Monte Carlo statistics.	137
5.8	The 1σ systematic uncertainty (ΔA) in the Monte Carlo signal acceptance, A . The top and bottom values for each entry represent changes due to shifting the given systematic by $+1\sigma$ and -1σ , respectively.	138
5.9	The systematic uncertainty in likelihood value as a percentage of $\sigma_X \cdot \text{BR}\{X \rightarrow t\bar{t}\}$. These values are determined directly using methods described in Section 5 with results depicted in Figures 5.7 through 5.11. We take these values to be valid only for $\sigma_X \cdot \text{BR}\{X \rightarrow t\bar{t}\}$ greater than the 95% C.L. limits which do <i>not</i> include systematic uncertainties (Table 4.3). Below the unsmeared 95% C.L. limit, the total systematic uncertainty is assumed to be constant.	146
5.10	For $M_X = 400 \text{ GeV}/c^2$ to $1 \text{ TeV}/c^2$, the total systematic likelihood uncertainty, Δ , listed as percentage of $\sigma_X \cdot \text{BR}\{X \rightarrow t\bar{t}\}$. We take these values to be valid only for $\sigma_X \cdot \text{BR}\{X \rightarrow t\bar{t}\}$ greater than the 95% C.L. limits which do <i>not</i> include systematic uncertainties (Table 4.3). Below the unsmeared 95% C.L. limit, the total systematic uncertainty is assumed to be constant.	147

- 5.11 The most probable values of cross-section times branching ratio for narrow resonances (with natural width $\Gamma = 0.012M_X$ and $\Gamma = 0.04M_X$) decaying to $t\bar{t}$. These values include the effects of systematic uncertainties. 151
- 5.12 The 95% C.L. upper limits cross-section times branching ratio for narrow resonances (with natural width $\Gamma = 0.012M_X$ and $\Gamma = 0.04M_X$) decaying to $t\bar{t}$. These values include the effects of systematic uncertainties. 152

Chapter 1

Introduction

It has been said that, “The eternal mystery of the world is its comprehensibility... The fact that it is comprehensible is a miracle”[1]. It has become the role of elementary particle physics to uncover the mysteries of nature by gaining an ever deepening understanding of the fundamental constituents of matter and how they interact. While such insight is tremendously exciting in its own right, we realize that these particles and their interactions form the basic ingredients for every physical process on earth – from photosynthesis to the launching of the space shuttle. Accordingly, the particle physics community, armed with ingenious and often enormous experimental facilities, as well as with previously developed knowledge and the constant motivation of recent suggestive results, has been in constant pursuit of more complete answers to the question, “What is the world made of?”

In the early days of particle physics, the answer to this fundamental scientific question was: “Apparently, not much.” It was discovered in Rutherford’s famous gold-foil experiment of 1911 that matter consists primarily of empty space, peppered with the occasional subatomic-particle. After the discoveries of the proton and neutron (which, along with the electron, were thought to be the most fun-

damental components of the atom), our basic understanding of nature was really quite simplistic. Then further studies in the 1940's and 1950's lead to exciting, yet bewildering discoveries of a rich garden of particles which provided evidence that our naive model of matter was incomplete. In the early 1960's, the world of particle physics was in a somewhat chaotic state and was in dire need of a theory that could make sense of the apparent disorder caused by the proliferation of new particles. By 1978, the highly pragmatic "standard model" was developed and it continues to prove remarkably successful in predicting and explaining the body of experimental results in particle physics.

1.1 The Standard Model

Our current understanding indicates that there exist four fundamental forces of nature:

- the familiar **electromagnetic force** which acts between charged particles,
- the aptly named **strong force** which, within the nucleus, dwarfs the repulsive effects of the electromagnetic force and binds together the constituent nucleons (*viz.*, protons and neutrons),
- the **weak force** which accounts for nuclear beta decay and other processes,
- and **gravity**, the weakest and, yet, most familiar of the four forces.

The effects of each of these forces are "mediated," or transmitted by, the exchange of a particle: the electromagnetic force is mediated by the *photon*; the weak force results from the exchange of *intermediate W^\pm and Z vector bosons*; *gluon* exchange accounts for the strong force; and the gravitational force is mediated by the *graviton*. The effects of a force are realized not by simple kinematical recoil (which

might serve to explain repulsion, but not particle *attraction*), but are the result of the transmission of the force itself, carried by the mediator.

The standard model is a synthesis of several quantum field theories which describe the fundamental particles and their interactions by combining the probabilistic nature of quantum mechanics with both the theory of special relativity and adherence to various symmetry laws. These interactions are described by two gauge theories: (1) the Glashow-Weinberg-Salam (GWS) theory which unifies the seemingly distinct electromagnetic interactions (described by *Quantum Electrodynamics* or QED) and the weak interactions by considering them to simply be different manifestations of the same *electroweak* force; and (2) *Quantum Chromodynamics* (QCD) which encompasses the theory of strong interactions.* In the standard model, the most fundamental building blocks of nature are called “quarks,” which interact via the strong and electroweak forces, and “leptons,” which interact through the electroweak force.

The leptons’ most famous member is the electron, commonly denoted just by e . Its more massive twins, the muon (μ) and tau (τ), along with each of the corresponding massless neutrinos (ν_e , ν_μ , and ν_τ), round out the leptons which are grouped into the three isospin “generations” shown in Figure 1.1. Because the electrically neutral neutrinos interact so weakly with matter, they easily pass through modern particle detectors without leaving any direct evidence of their existence. The concept of a neutrino was first introduced to explain a curiosity that occurs in nuclear beta decay. In this process, now understood to be the disintegration of the neutron, the only observed decay products are a proton and an electron. Supposing that nuclear beta decay proceeds via a two-body decay (as it appeared to), the

*In the realm of elementary particle physics, the gravitational force is far too weak to have any noticable effects and is, therefore, not considered. However, today much work continues in various efforts to include all four forces in a single unified theory.

predicted energy of the electron, E , is a fixed value and can be determined from simple relativistic kinematics. However, it was found that although they never exceed the value of E , electron energies from beta decay are not fixed, but vary between 0 and E . The neutrino was proposed as an “invisible” particle that was able to carry away the missing energy while eluding detection and preserving the sacred physical law of energy conservation. On theoretical grounds, the neutrino proved to be enormously successful and, eventually, its skeptical reception as a physical particle was repudiated by experimental evidence which overwhelmingly verified its existence.

QED, the theory of electromagnetic phenomena, describes interactions between charged particles. Like all fundamental interactions, QED derives from a principle known as “local gauge invariance.” By starting with the quantum mechanical wave equation for spin- $\frac{1}{2}$ particles and merely modifying it such that it is unchanged by time- and space-dependent phase transformations (local gauge invariance), we can derive Maxwell’s equations which thoroughly describe classical electromagnetism. Furthermore, enforcing this local gauge symmetry dictates that charged particles interact via the exchange of massless, electrically neutral “gauge bosons” known as photons. Feynman calculus simplifies the relativistic quantum mechanical calculation of probability amplitudes for a given process by employing perturbation theory to take advantage of the small size of the electromagnetic coupling constant ($\alpha = \frac{1}{137}$), which is a measure of the probability that a Dirac particle emits or absorbs a photon. In addition, QED is a “renormalizable” quantum field theory which ensures that calculated observable quantities remain finite. Because of its many desirable theoretical features and because it has proven to be a highly successful dynamical theory by predicting experimental results with astounding accuracy, QED is used as the model upon which the gauge theory framework for the other fundamental interactions is based.

The quark model was originally introduced after it was found that, based upon their characteristics, classes of observed particles called “mesons” and “baryons” (collectively known as “hadrons”) could be grouped into curious patterns[2]. It was suggested that mesons and baryons are actually composites of two and three smaller constituent quarks of fractional charge. Originally thought to be more of a convenient mathematical construct than actual physical objects, the true existence of quarks began to receive credibility as results from experiments that probed the nucleus suggested a substructure to the nucleon. When the 1974 J/ψ discovery [3] was explained as a new quark/anti-quark pair ($c\bar{c}$) and the new particles predicted by the existence of the “charm” quark were soon discovered, the quark model was quickly on a very stable footing. After the 1995 discovery of the sixth (and final?) quark, experiment had verified the existence of each of the different types, or flavors, of quark in the standard model: “up” (u), “down” (d), “charm” (c), “strange” (s), “top” (t), and “bottom” (b). Like the leptons, these quark flavors, with electrical charge as given in Figure 1.1, are also grouped into three “generations” whose sole distinguishing feature is particle mass.[†]

In addition to the fractional electric charges already mentioned, quarks possess an additional quantum number which is unique to fundamental particles participating in strong interactions. Quarks, like leptons, are fermions with $\text{spin} = 1/2$ and therefore must obey the Pauli exclusion principle which forbids particles of half-integer spin from occupying the same state. Thus, the introduction of a new quantity called “color,” which is the QCD analog to electrical charge in QED, was initially an attempt to avoid the apparent violation of the exclusion principle in baryons such as the Δ^{++} which is comprised of uuu . By assigning to each u -quark

[†]Not depicted in Figure 1.1 are the corresponding anti-particles, one of which exists for each fundamental particle. A particle’s anti-matter partner has the same mass as the given particle, but has the opposite sign for every other identifying “quantum number.” Complicating matters somewhat is the fact that some particles are their own anti-particles.

Fermions			Bosons	
Quarks	Q/e	Weak Isospin	$\begin{pmatrix} W^+ \\ Z^0 \\ W^- \end{pmatrix}$	
$\begin{pmatrix} u \\ d \end{pmatrix} \begin{pmatrix} c \\ s \end{pmatrix} \begin{pmatrix} t \\ b \end{pmatrix}$	$\begin{pmatrix} +\frac{2}{3} \\ -\frac{1}{3} \end{pmatrix}$	$\begin{pmatrix} +\frac{1}{2} \\ -\frac{1}{2} \end{pmatrix}$	8 Gluons (g)	Higgs (h)
Leptons			Photon (γ)	
$\begin{pmatrix} e \\ \nu_e \end{pmatrix} \begin{pmatrix} \mu \\ \nu_\mu \end{pmatrix} \begin{pmatrix} \tau \\ \nu_\tau \end{pmatrix}$	$\begin{pmatrix} -1 \\ 0 \end{pmatrix}$	$\begin{pmatrix} -\frac{1}{2} \\ +\frac{1}{2} \end{pmatrix}$		

Figure 1.1: The fundamental particles of the standard model. Fermions interact via different forces mediated by the exchange of massless or massive gauge bosons.

a different color, “red” (R), “green” (G), or “blue” (B)[†], the quarks in the Δ^{++} are considered to be in different states. The notion of color, which initially might appear somewhat *ad hoc*, has proven to be quite necessary and has lead to rich phenomenological physics – most notably the contention that all observable particles are colorless (*i.e.*, net color must sum to zero). This requirement, while far from obvious, offers an explanation as to why quarks don’t appear as free particles or in qq states, both of which are necessarily colored (the latter would have to be colored in order to again satisfy the Pauli exclusion principle).

The existence of three distinct quark colors was illustrated beautifully by several experiments which investigated the “cross-section” for various inelastic e^+e^- collisions. In particle physics, a cross-section is akin to the traditional cross-sectional area presented by a target but further depends on both the incoming and outgoing particles, making it also related to the probability of observing a certain process. Through particle annihilation in collisions with center-of-mass energy, E , in excess

[†]Anti-quarks are assigned colors of “anti-red” (\bar{R}), “anti-green” (\bar{G}), and “anti-blue” (\bar{B}).

of twice the muon mass, e^+e^- interactions can create a “virtual”[‡] photon which can then decay to either $\mu^+\mu^-$ or a quark-antiquark pair. Using only QED, it can be shown that as a function of center-of-mass energy, the ratio of cross-sections for $e^+e^- \rightarrow q\bar{q}$ and $e^+e^- \rightarrow \mu^+\mu^-$ is approximately given by

$$R(E) \equiv \frac{\sigma(e^+e^- \rightarrow q\bar{q})}{\sigma(e^+e^- \rightarrow \mu^+\mu^-)} = 3 \sum_i e_q^2$$

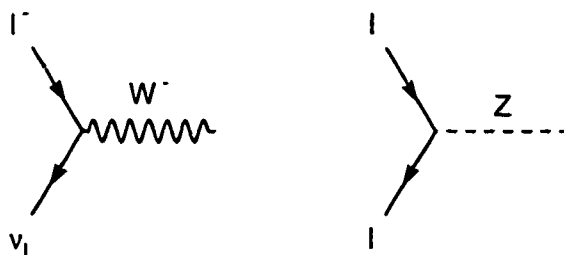
where e_q is the electrical charge of the i^{th} quark and the summation is over the number of quark flavors with mass less than $\frac{E}{2}$. Here the factor of “3” arises entirely from assuming the existence of three different possible colors for each quark. Accordingly, R is predicted to be 2 for the u, d , and s quarks and $\frac{10}{3}$ ($\frac{11}{3}$) as the collision energy surpasses the c (b) quark mass threshold. The conclusive experimental agreement with these predictions and the necessary factor of “3” validated the existence of the different quark flavors, as well as their three different colors.

Not unlike the exchange of photons which mediates electromagnetic interactions, quarks interact strongly via the exchange of one of eight massless gluons. In QED, an effect known as “charge screening” results in an increase of a particle’s effective charge as the distance decreases between the point of measurement and the particle itself. However, while the photon carries no electrical charge, gluons themselves carry color (strong “charge”) and, as a result, can interact strongly with other gluons. Because the colored gluons diffuse the quark’s effective color charge, the same process that leads to “charge screening” in QED, has the opposite effect in QCD, causing the effective color of a quark to increase with distance.

[‡]Virtual particles can exist only *within* the mechanism of a process; they are not observed particles. Therefore, virtual particles are not required to have the same mass as their “real” counterparts and can be “off-shell” to ensure that energy and momentum are conserved.

This result, known formally as “asymptotic freedom,” yields a strong force coupling “constant” which is anything but. For quarks in close proximity, the coupling strength asymptotically vanishes, resulting in quarks behaving essentially as free particles. This feature permits the use of Feynman calculus at small distances (which can result from very high energy interactions). However, as their separation increases, the strong interaction between the quarks increases dramatically, resulting in the quarks’ “confinement” within hadrons and, therefore, offering more explanation for why free quarks are not observed.

Leptons, however, do not carry color and, therefore, do not interact via the strong force; they interact via the weak force through the exchange of the intermediate gauge bosons, viz., the charged W^\pm and the electrically neutral Z . Both of these bosons are quite massive which consequently limits the range of the force. While emission or absorption of a W^\pm or Z connects two leptons *within* the same generation,



cross-generational coupling between the leptons is forbidden. Quarks also interact via the weak force, but the CKM matrix allows for conversion, albeit somewhat suppressed, between the quark generations. Unlike the other fundamental interactions, flavor is generally not conserved at a weak vertex, and so the theory is occasionally referred to as “flavordynamics.”

In spite of the fact that photons are massless while the W^\pm and Z bosons are incredibly massive, QED and the weak interactions have been shown to be manifestations of the same “electroweak” force. The apparent disparity resulting from

the undeniable W^\pm and Z boson masses is explained by a phenomena known as “electroweak symmetry breaking.” As mentioned previously, quantum field theory calculations are necessarily based upon perturbation theory in the form of Feynman calculus. In addition, assuming that the potential energy is symmetric about its minimum, the perturbative series solution is expanded about this point and predicts the existence of a massless gauge boson, such as the photon in the ever-successful theory of QED. However, when QED and weak interactions are combined into a single quantum field theory, the potential energy apparently has an infinite number of minima, about none of which is the function symmetric. This “spontaneous” symmetry breaking along with the requirement of local gauge invariance yields a process known as the “Higgs mechanism” which predicts the existence of the massless photon, the massive W^\pm and Z bosons, and the yet undetected Higgs particle (or particles) which is (are) theoretically responsible for imparting mass to all of the massive fundamental particles in the standard model. In the coming millenium, one of the primary goals of experimental particle physics is the discovery of the Higgs particle(s) which would only add to the predictive achievements of the already remarkably successful standard model.

1.2 The Top Quark

After the 1977 discovery of the b quark in the $\Upsilon = b\bar{b}$ resonance state, attention quickly turned to the search for its partner in the third generation isospin doublet, the top quark. While it was plausible that the t did not actually exist and that the b was simply a member of a weak isospin singlet state, theoretical considerations and experimental studies indicated otherwise. For example, in the inelastic process $e^+e^- \rightarrow Z \rightarrow b\bar{b}$, several measurements of the forward-backward asymmetry of $b\bar{b}$ pairs, $A_{FB}^{b\bar{b}}$, were consistent with standard model predictions which

assume that the b is a member of an isospin doublet [4],[5],[6]. More importantly, these measurements were decidedly not consistent with $A_{FB}^{b\bar{b}} = 0$ which would be indicative of a third generation isospin singlet and, thus, the non-existence of the t . In addition to the theoretical motivation of ensuring that the gauge theory of electroweak interactions be renormalizable, the existence of the top quark was further supported by the absence of experimental evidence for flavor changing neutral currents in B meson decays.

Yet, as the race to find the t quickly gained much fervor, an appropriate t quark mass range could not be determined *a priori* because only once the Higgs is discovered will the fermion masses be theoretically calculable. For years, further studies of $R(E)$, mentioned previously, searched for a transition at the t quark mass threshold and continued to establish increasing experimental lower limits on the top quark mass. Experiments at proton-antiproton ($p\bar{p}$) colliders, first at CERN and later Fermilab, steadily increased this lower limit until 1995 when the CDF and DØ collaborations announced the discovery of the top quark at a mass of $\approx 175 \text{ GeV}/c^2$ – a mass that is staggering in relation to the other quarks. Even its isospin partner, the massive b quark, has a mass of only $\approx 5 \text{ GeV}/c^2$.

1.2.1 Top Quark Production at Fermilab

At high energy $p\bar{p}$ colliders, such as the Fermilab Tevatron, top quark production occurs via interactions between the constituent p and \bar{p} partons[¶]. While it is well-known that the proton (antiproton) is a baryon with quark content of uud ($\bar{u}\bar{u}\bar{d}$), it is an oversimplification to assume that these “valence” quarks are its only constituents. “Deep,” or high energy inelastic scattering experiments have shown

[¶]Partons are fundamental particles that participate in strong interactions, *viz.*, quarks and gluons.

that, on average, nearly half of the proton momentum is carried by the uncharged gluons which mediate the interactions between the valence quarks. Furthermore, these gluons produce many transient $q\bar{q}$ pairs known as “sea” quarks^{||} which is especially true for gluons exchanged between valence quarks that carry a relatively smaller fraction of the proton momentum. Accordingly, in $p\bar{p}$ collisions top quark production can proceed through quark-quark, gluon-gluon, or quark-gluon interactions.

At the Tevatron center-of-mass energy ($\sqrt{s} = 1.8$ TeV), top quarks can be produced in $t\bar{t}$ pairs or as single t ’s in association with a generic quark flavor or specifically with a b or both. As shown in Fig. 1.2, “single top” production proceeds through an electroweak vertex via “W-gluon fusion” or qq' annihilation to an off-shell W . However, due to increased experimental sensitivity and because its expected production cross-section exceeds that of single top by nearly a factor of three, QCD pair-production is the dominant contributor to the observation of top quarks at Fermilab. $t\bar{t}$ production proceeds via the strong interactions in $q\bar{q}$ annihilation and gluon fusion, depicted in Fig. 1.3. At $\sqrt{s} = 1.8$ TeV, however, the $t\bar{t}$ cross-section for production via $q\bar{q}$ annihilation is dominant by a factor of ≈ 5 . This disparity exists not because the $q\bar{q}$ luminosity^{**} exceeds that of gg , but rather because gg interactions at the Tevatron rarely contain enough energy to produce a $t\bar{t}$ pair since an individual gluon tends to account for only a very small fraction of the proton momentum.

^{||}These are often $u\bar{u}$ and $d\bar{d}$ pairs since the probability producing a specific sea quark pair is inversely proportional to the quark mass.

^{**}The number of interactions per unit area per unit time is often referred to as the “instantaneous luminosity.” The “total integrated luminosity” results from an integration over time and has the units of number per unit area.

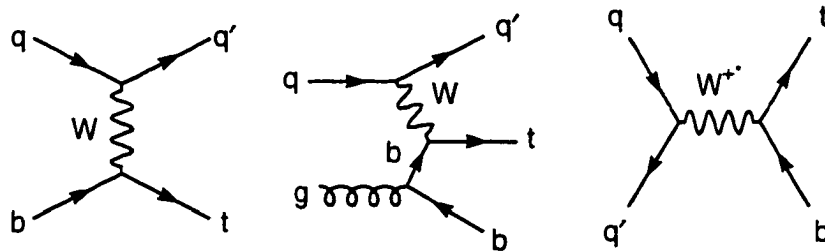


Figure 1.2: Various single top quark production processes.

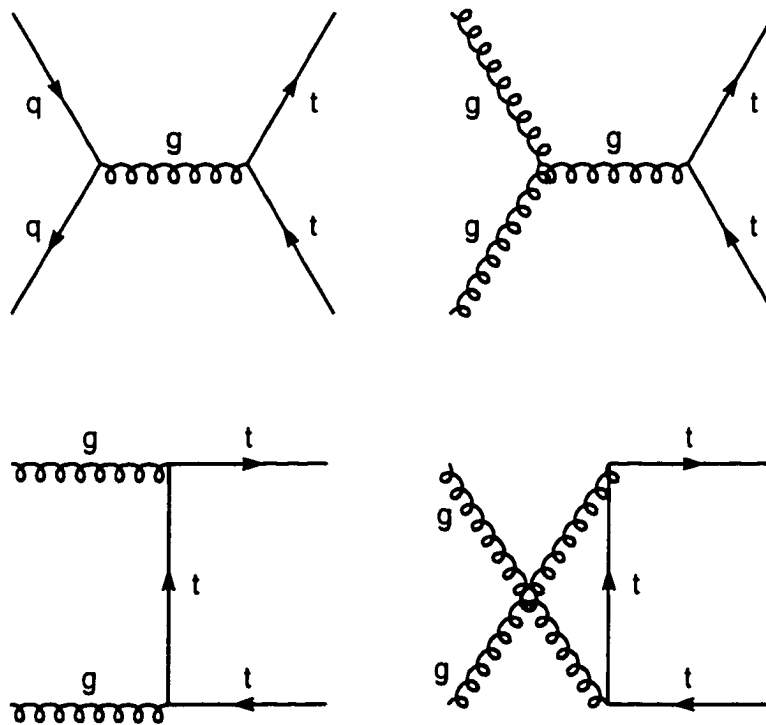


Figure 1.3: $t\bar{t}$ pair production processes. At Fermilab, the $q\bar{q}$ annihilation mechanism dominates.

1.2.2 Top Quark Decay

Without the incorporation of the previously mentioned CKM matrix, the standard model event rate predictions for several processes are disturbingly inconsistent with experimental results. But by including this unitary matrix which couples the weak eigenstates and the mass eigenstates for the d , s , and b quarks, new cancelling diagrams are permitted (known as the “GIM mechanism”[7]), thereby reducing the theoretical amplitudes and bringing the predicted rates into superb agreement with experiment. However, requiring that the CKM matrix be unitary effectively eliminates the possibility of any top quark cross-generational coupling, *i.e.*, $V_{tb} \approx 1$. Within the standard model then, the $\sim 175 \text{ GeV}/c^2$ top quark is expected to decay almost exclusively to a real W^+ and a b since the decays to W^+d and W^+s are dramatically suppressed.

Typically, when a $q\bar{q}$ pair is created through head-on annihilation, the two quarks momentarily rush apart from one another as free particles. Yet, because the strong force increases with distance, the potential energy quickly becomes sufficient (at a separation of approximately 10^{-15} m) to produce a new quark-antiquark pair. As the original quark and antiquark continue to separate, more $q\bar{q}$ pairs are produced and eventually collect into a variety hadronic combinations. The experimentally detectable result, called “hadronization,” is fragmentation into two sprays or “jets” of colorless particles travelling in the directions of the original quark and antiquark. Yet, for the top quark, the expected partial width and lifetime τ are:

$$\Gamma(t \rightarrow Wb) = 1.55 \text{ GeV}/c^2 \Rightarrow \tau \approx 4 \times 10^{-25} \text{ sec},$$

assuming $V_{tb} = 1$, a top quark mass of $M_{top} = 175 \text{ GeV}/c^2$, and a W boson mass of $M_W = 80.4 \text{ GeV}/c^2$. With such a short lifetime, the top quark can be treated

essentially as a free quark because it is expected to decay well before the time scale for QCD hadronization, $\sim \mathcal{O}(10^{-23} \text{ sec})$. Only if the top quark mass were less than $120 \text{ GeV}/c^2$ could the effects of fragmentation no longer be ignored[8].

Decay channels for $t\bar{t}$ events (see Fig. 1.4) are then distinguished simply by the decay modes of the daughter W 's which can decay either leptonically or hadronically:

$$W^+ \rightarrow (e^+ \nu_e), (\mu^+ \nu_\mu), (\tau^+ \nu_\tau), (u\bar{d}), \text{ or } (c\bar{s})$$

$$W^- \rightarrow (e^- \bar{\nu}_e), (\mu^- \bar{\nu}_\mu), (\tau^- \bar{\nu}_\tau), (\bar{u}d), \text{ or } (\bar{c}s)$$

Noting that each of the hadronic pairs may occur in any one of three different colorless combinations, lowest order calculations estimate that the nine decay modes for each W are equally probable. As shown in Table 1.1, the "all-hadronic" decay mode, which possesses the highest branching ratio, occurs when both W 's decay hadronically. Unfortunately, the 6-jet signature for events in this channel is fre-

CDF Decay Channel	Decay Mode	Branching Ratio
All-Hadronic	$t\bar{t} \rightarrow q\bar{q}'b\,q\bar{q}'\bar{b}$	$36/81 \} \quad 44\%$
Dilepton	$t\bar{t} \rightarrow e\nu b\,e\nu\bar{b}$	$1/81 \}$
	$t\bar{t} \rightarrow \mu\nu b\,\mu\nu\bar{b}$	$1/81 \}$
	$t\bar{t} \rightarrow \mu\nu b\,e\nu\bar{b}$	$2/81 \} \quad 5\%$
Lepton + jets	$t\bar{t} \rightarrow e\nu b\,q\bar{q}'\bar{b}$	$12/81 \}$
	$t\bar{t} \rightarrow \mu\nu b\,q\bar{q}'\bar{b}$	$12/81 \} \quad 30\%$

Table 1.1: The $t\bar{t}$ decay channels and their corresponding lowest order branching ratios.

quently mimicked by other non- $t\bar{t}$ QCD processes which make it difficult to extract a $t\bar{t}$ signal. Because τ decays are quite difficult to identify experimentally at CDF, the “dilepton” channel represents only events in which each W decays either to a muon or an electron. While the dilepton channel suffers from a small branching ratio, it represents the cleanest $t\bar{t}$ signal with approximately 2.5 times more signal events expected over background[9]. Finally, the “lepton plus jets” channel, which is the focus of this thesis, represents $t\bar{t}$ events in which one W decays hadronically and the other decays leptonically to an electron or muon. Requiring a leptonically decaying W significantly reduces the amount of background which is present in the all-hadronic channel, but does not prohibitively reduce the expected branching ratio.

1.2.3 Beyond the Standard Model and $t\bar{t}$ Resonances

Motivated by the striking successes of the standard model, the aim of particle physics has focused on efforts to understand at a more basic level the laws which govern fundamental interactions. As shown in Table 1.2, the standard model requires the input of 18 independent free parameters which cannot be calculated theoretically, but must be determined through experiment. Because it is understood that the standard model is not the complete theory of fundamental physics, we are now in search of a larger (unbroken) symmetry of nature. It is thought that the standard model, as it stands, is likely just the low-energy limit of a more global symmetry which might serve to explain electroweak symmetry breaking and the actual values of the parameters in Table 1.2, as well as account for the observation of three fermion generations.

One such potential new symmetry is called “supersymmetry,” which extends the symmetry of space-time with the introduction of several additional quantum me-

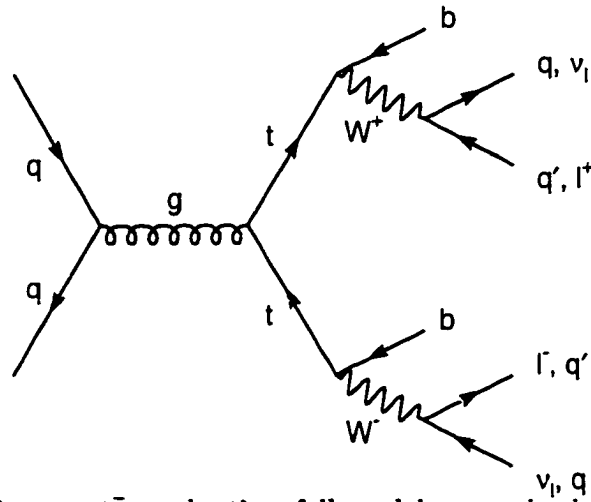


Figure 1.4: Tree level $q\bar{q} \rightarrow t\bar{t}$ production followed by standard model top quark decay.

Quantity	Number of parameters
Quark masses	6
e , μ , and τ masses	3
Coupling constants	3
Independent parameters of CKM matrix	3
Magnitude of CP violation	1
Fundamental electroweak mass scale	1
Higgs mass	1

Table 1.2: The 18 independent parameters of the standard model.

$$\begin{pmatrix} u \\ d \end{pmatrix}_{L,R} \quad \begin{pmatrix} e \\ \nu \end{pmatrix}_L \quad (e)_R$$

Figure 1.5: The 15 left and right-handed fermions of the first generation of the standard model. Each quark exists in three different colors.

chanical dimensions. In addition to providing a method for electroweak symmetry breaking, supersymmetry predicts the existence of a supersymmetric partner for each observed fermion as well as the existence of several Higgs particles. Another proposed theory, “technicolor,” also provides a mechanism for imparting mass to the W and Z bosons, but instead introduces a new strong force which is analogous to the strong color force. Furthermore, the large value of the top quark mass suggests the introduction of new strong dynamics which couple preferentially to the third generation. And so, a related theory known as “topcolor-assisted technicolor” accounts for the large top quark mass and electroweak symmetry breaking, while predicting the existence of a residual global symmetry at energies below ~ 1 TeV. This residual symmetry would result in the generation of “topgluons” and a topcolor Z' with both decaying to $t\bar{t}$ and $b\bar{b}$.

Because the coupling strengths within the standard model are energy-dependent, it is thought that at an energy many orders of magnitude greater than the weak scale, a grand unified theory (GUT) governs the fundamental laws of nature. Within a GUT, the interaction strengths of the electromagnetic, weak and strong forces merge, unifying the different types of interactions into one fundamental force. In addition, the 15 ostensibly distinct members which comprise each fermion generation (see Figure 1.5) are regarded as components of one single particle. GUTs suggest that at energies below the unification scale, this fundamental symmetry is broken and the local symmetries of the standard model distinguish the individual

members of each generation, just as we observe in nature.

Not unlike the revolutionary discoveries of special relativity and quantum mechanics in the early part of this century, today's particle physics community eagerly anticipates radical new developments in the understanding of fundamental interactions — a dramatic transformation of paradigm which would supercede the standard model. And, today, while the details of this imminent theoretical revolution are merely speculation, important efforts to discover evidence of physics beyond the standard model focus the scope of new physical theories and serve as the motivation for the research presented here.

And within the framework of the standard model, no particle decays to a $t\bar{t}$ pair^{††}. While the Z boson, with a mass of approximately $90 \text{ GeV}/c^2$, can and does decay to $b\bar{b}$, energy conservation precludes its decay to $t\bar{t}$ which would require a mass in excess of $\sim 350 \text{ GeV}/c^2$. Consequently, the $t\bar{t}$ mass spectrum is a readily available experimental test for direct evidence of physics beyond the standard model. Verification of a $t\bar{t}$ resonance might point to the existence of a supersymmetric Higgs, a variety of technicolor particles, a topcolor boson, or some other manifestation of new physics. A thorough search for a $t\bar{t}$ resonance is the subject of this thesis and the following chapters discuss the experimental methods and analysis of data collected from proton/anti-proton collisions at Fermilab's CDF detector between 1992 and 1995.

^{††}It is true that the standard model Higgs must couple to the t quark, but the expected production cross-section for $H \rightarrow t\bar{t}$ at the Tevatron is immeasurably small.

Chapter 2

Experimental Apparatus

Fermilab's superconducting Tevatron accelerates proton (p) and anti-proton (\bar{p}) bunches along a path four miles in circumference and within a beampipe housed 20 feet beneath the plains of northeastern Illinois. During "Run 1," which occurred from August 1992 to May 1993 (Run 1a) and January 1994 to July 1995 (Run 1b), these p and \bar{p} bunches were accelerated to 900 GeV. The resulting 1.8 TeV center-of-mass energy for nucleon collisions is currently unmatched by any other particle accelerator in the world. Such high energy collisions are highly desirable because they probe the standard model at increasingly shorter distances and provide the additional energy necessary for producing heavy particles such as the top quark.

2.1 The Tevatron

At Fermilab, these high energy interactions occur only after the completion of several stages, depicted in Fig. 2.1. Common hydrogen gas (H_2) is first ionized, forming negative hydrogen ions (H^-) which are accelerated to 750 keV via a Cockcroft-Walton accelerator. The H^- ions are then passed to a linear accelerator,

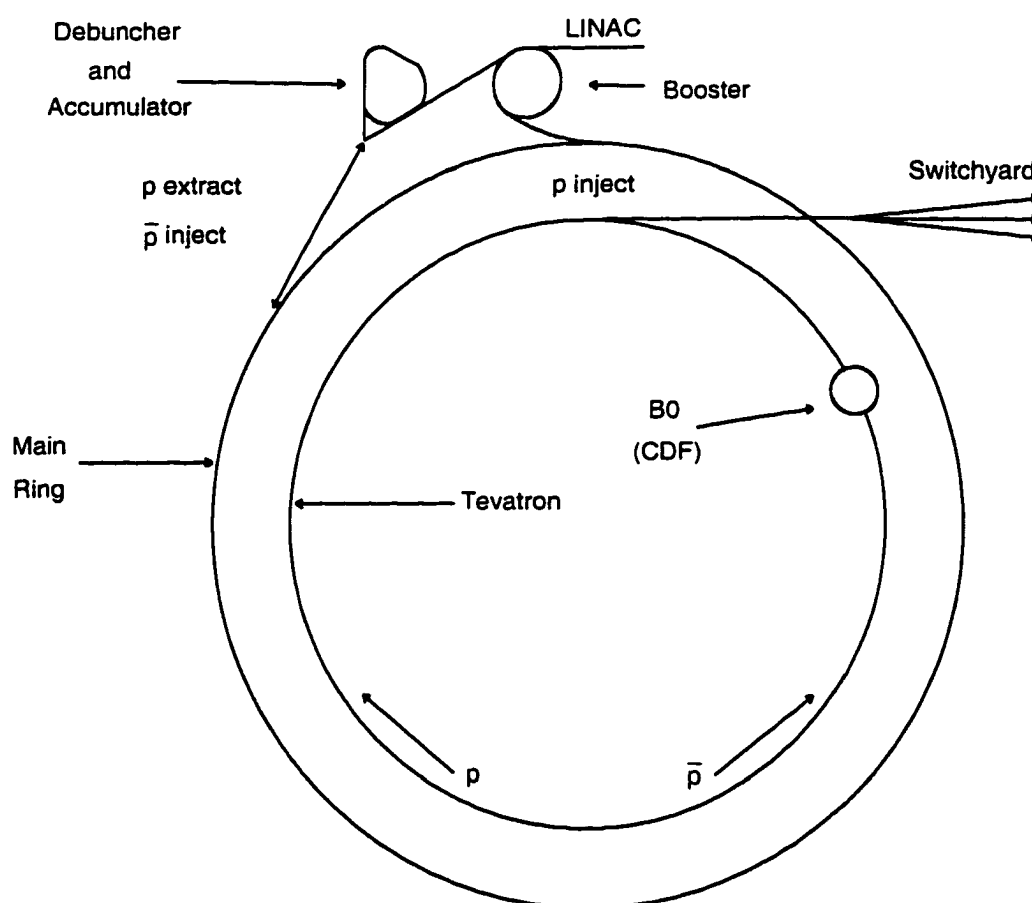


Figure 2.1: Schematic diagram of the Fermilab accelerator. While the Tevatron and Main Ring have the same radius, for the sake of clarity the two have not been superimposed.

the Linac, in which an oscillating electric field is applied with increasing separation, bringing the ions to an energy of 400 MeV. By passing the H^- ions through a carbon foil, the electrons are removed, leaving only the proton nuclei. These protons are then accelerated to an energy of 8 GeV in the Booster, a synchrotron 500 feet in diameter. In a synchrotron, like a linear accelerator, charged particles are accelerated by the application of an electric field. However, synchrotron magnets bend the particles' path into a circle so that they can be repeatedly subjected to an electrical "push" upon each revolution. The Booster operates in 12 cycles, transferring a dozen distinct proton bunches into another synchrotron, called the Main Ring, which is four miles in circumference and accelerates the bunches to 150 GeV. After being coalesced into one bunch, the approximately 2×10^{11} protons are injected into the Tevatron which resides directly below the Main Ring, sharing the same tunnel. The Tevatron has the same basic structure as the Main Ring, with the major exception being the Tevatron's superconducting magnets. Superconducting technology allows this synchrotron to attain much greater energies than are available to the Main Ring which employs conventional magnets to bend the beam's path. A total of six proton bunches are ultimately transferred to the Tevatron in the manner briefly described above.

Obtaining sufficient numbers of anti-protons is a more complex process and is significantly more time-consuming, serving as the primary limitation on $p\bar{p}$ luminosity at Fermilab. In the first stage of \bar{p} production, protons in the Booster are diverted to the Main Ring and accelerated to 120 GeV. These protons are then extracted and focused on a fixed tungsten target, creating interactions through which anti-protons (among many other secondary particles) are produced. A lithium lens is then used to select 8 GeV anti-protons which are then transferred to the Debuncher, a rounded triangular-shaped synchrotron whose primary purpose is to reduce the \bar{p} momentum spread by rotating (and thereby cooling) the \bar{p} bunches[10].

(In addition, the Debuncher also aids in reducing oscillations in the transverse plane.) The beam is then sent to the Accumulator, a second triangular-shaped synchrotron which stores and continues to stochastically cool the 8 GeV anti-protons. Once approximately 1×10^{12} anti-protons have been “stacked,” six \bar{p} bunches are injected one-by-one into the Main Ring where they are accelerated to 150 GeV before entering the Tevatron.

In the final stage of acceleration, the Tevatron brings the counter-rotating p and \bar{p} bunches each to an energy of 900 GeV. The beams travel in a double helical path and therefore cross only at two interaction regions, known as BØ and DØ, where quadrupole magnets focus the beams to a transverse diameter of approximately $35 \mu\text{m}$. The Collider Detector at Fermilab (CDF) is located at BØ and is used to investigate the 1.8 TeV $p\bar{p}$ collisions.

At beam-colliding machines, event rates are measured in terms of instantaneous luminosity, \mathcal{L} , which is given by

$$\mathcal{L} = \frac{N_p N_{\bar{p}} B f_0}{4\pi\sigma^2}$$

where N_p is the total number protons per bunch, $N_{\bar{p}}$ is the total number antiprotons per bunch, B is number of bunches of each type, f_0 is the frequency of bunch revolution (47.7 kHz), and σ^2 is the cross-sectional area of the bunches ($\sim 5 \times 10^{-5} \text{ cm}^2$). The peak instantaneous luminosity for Run 1 was $2.8 \times 10^{31} \text{ cm}^2 \text{ s}^{-1}$, while more typical values were $0.54 \times 10^{31} \text{ cm}^2 \text{ s}^{-1}$ for Run 1a and $1.6 \times 10^{31} \text{ cm}^2 \text{ s}^{-1}$ for Run 1b. The total Run 1 integrated luminosity, $\int \mathcal{L} dt$, was measured to be $106 \times 10^{12} \text{ cm}^{-2}$ or equivalently, 106 pb^{-1} [11].

2.2 The CDF Detector

The CDF detector is designed to identify and measure the energy and momentum of the electrons, muons, photons, and jets which result from $p\bar{p}$ interactions at the Tevatron. The right-handed coordinate system of the cylindrical CDF detector, which is approximately symmetric about its nominal interaction point, defines the z -axis along the p direction, the azimuthal angle ϕ with respect to the x -axis, and θ as the polar angle (see Fig. 2.2). Typically in hadron colliding experiments, pseudorapidity, $\eta = -\log(\tan \frac{\theta}{2})$, is preferred over θ because, in the limit of massless particles, η is a Lorentz invariant quantity; therefore, particle multiplicity is expected to be constant per unit of η . Accordingly, the CDF geometry is divided into three η ranges: the central, plug, and forward regions. While the CDF detector is actually a complex synthesis of numerous separate detectors, commonly labeled with TLAs*, it is further divided into three primary detection systems: charged particle tracking, electromagnetic and hadronic calorimetry, and muon tracking chambers.

2.2.1 The Tracking System

CDF's innermost system, charged particle tracking, is comprised of three tracking detectors which are surrounded by a superconducting toroidal magnet 1.5 m in radius and 4.8 m in length whose 1.4 T field is directed along the p direction. This tracking system, coupled with presence of a magnetic field, serves as a crucial part of the CDF experiment because the resulting curvature of an identified particle's trajectory provides a direct measurement of its momentum.

*Three Letter Acronyms.

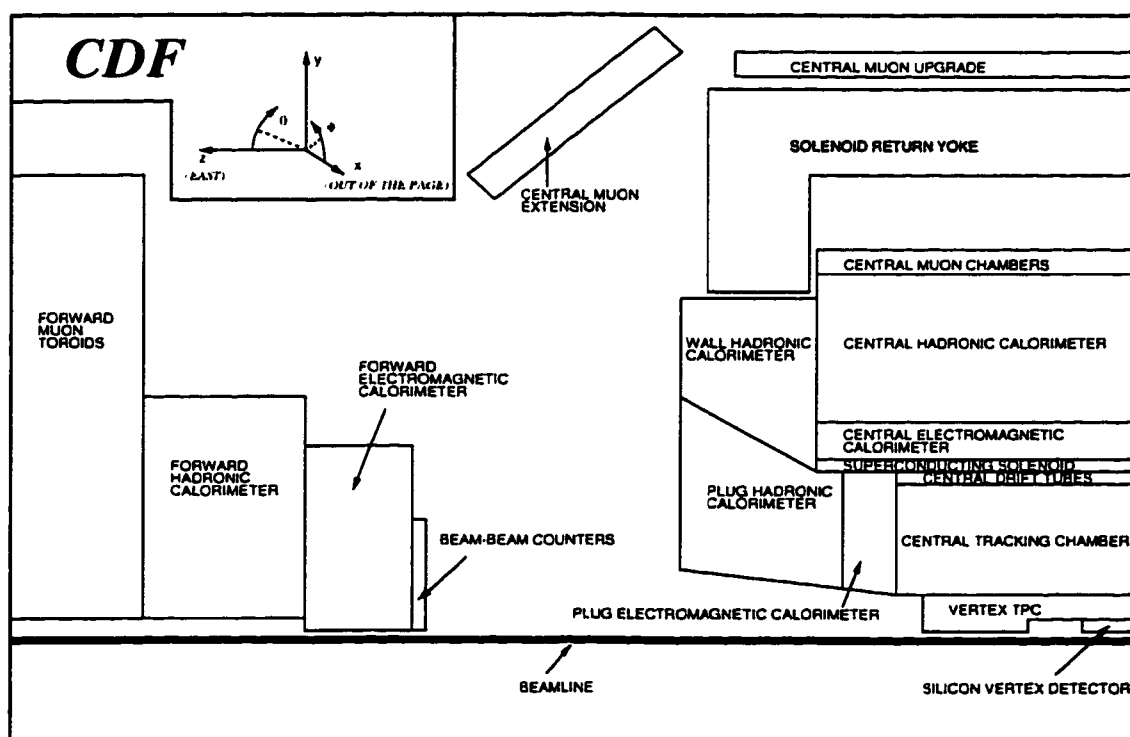


Figure 2.2: One quarter cross-section of the CDF detector which is forward-backward symmetric about the nominal interaction point located in the lower right of the figure.

The CTC

Just inside the superconducting magnet, a large wire drift chamber called the Central Tracking Chamber, or CTC, provides excellent three-dimensional tracking in the central region for $\eta < 1.0$. Fig. 2.3 shows how the CTC cells are arranged into nine “superlayers,” five of which are axial running parallel to the beam line, while the remaining four stereo layers are at an angle of $\pm 3^\circ$ relative to the z -axis. Twelve sense wires run the length of each axial cell, whereas each stereo cell consists of six, yielding a total of 84 drift layers in the CTC. Due to the presence of crossed electric and magnetic fields, the CTC cells, filled with argon-ethane-ethanol gas, are tilted at 45° relative to the radial direction causing the drift electron trajectories to be approximately azimuthal[12]. Using hits in the CTC fit to an arc of a helix, the resolution of momentum in the transverse plane (P_T) is given by $\delta P_T/P_T < 0.002 P_T$.

The VTX

Mounted inside the CTC, the Vertex Time Projection Chamber (VTX) is used primarily for z -vertex information used to separate the multiple interactions which frequently occur within a single bunch crossing. The VTX is comprised of eight octagonal modules filled with 50/50 argon-ethane gas, each divided into two 15.25 cm long drift regions by a central high voltage grid. Drift electrons, resulting from ionization by a charged particle, pass through a cathode grid at the end of a module’s drift chambers and enter the endcap region which houses 192 sense wires divided equally into octants. It is the arrival times of drift electrons at the sense wires which provide detailed charged particle tracking in the $r - z$ direction. Covering $\eta < 3.25$, the VTX determines the z position of event vertices with an uncertainty of less than approximately 1 mm.

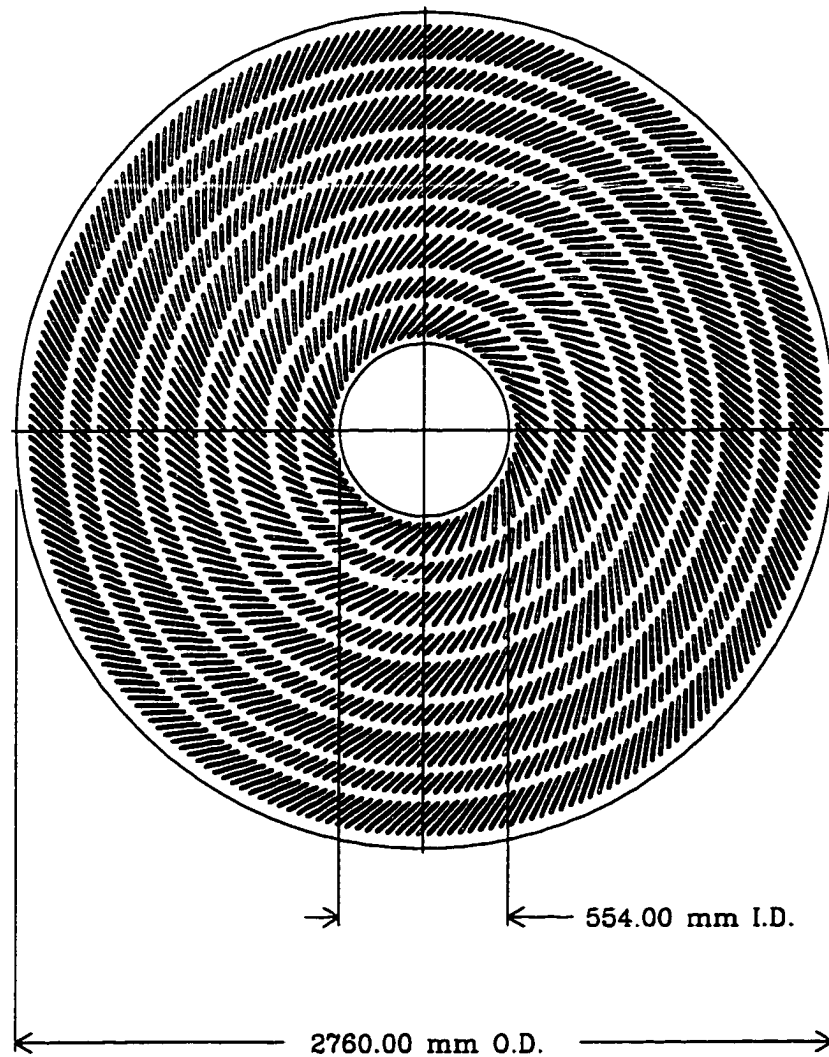


Figure 2.3: A schematic diagram of the CTC cross-section which illustrates how the 84 drift layers are arranged in the superlayer geometry.

The SVX

The Silicon Vertex Detector (SVX) is supported by the VTX and immediately surrounds the beryllium beampipe itself. Due a significant amount of radiation damage suffered during Run 1a, the SVX was replaced with the SVX' between Run 1a and Run 1b. The SVX and SVX' detectors are identical with the exception of a few improvements that were included in the latter design, most notably the incorporation of radiation hard readout chips in anticipation of increased luminosity in Run 1b. Centered about the nominal CDF interaction point, the 54 cm long SVX is able to provide precise $r - \phi$ tracking for most events since the primary z -vertex position of all $p\bar{p}$ interactions at B \bar{O} is gaussian distributed about $z = 0$ with $\sigma \approx 30\text{cm}$. The SVX is comprised of two identical 25.5 cm cylindrical barrels which are separated by an uninstrumented 2.15 cm gap at $z = 0$. As shown in Fig. 2.4, bulkheads at the ends of each barrel support four layers of concentric silicon strip detectors, with each layer equally divided into 12 ϕ -wedges. Within a wedge, each layer (at radii of 2.861 cm, 4.256 cm, 5.687 cm, and 7.866 cm) amounts to the rohacell carbon fiber rails of a "ladder" which supports three 8.5 cm silicon detector wafers laid end-to-end with aluminum read-out strips running parallel to the beamline. For charged particle hits, the intrinsic resolution of approximately $13\mu\text{m}$ in $r - \phi$ results from the $60\mu\text{m}$ pitch, or separation between read-out strips, in the inner three layers and the $55\mu\text{m}$ pitch in the outer layer.

One of the most significant accomplishments of the SVX is its ability to discern secondary vertices in the plane transverse to the beamline. Combined with CTC tracking information, for high momentum tracks, the SVX provides impact parameter[†] resolution of approximately $15\mu\text{m}$. In high energy $p\bar{p}$ collisions, such

[†]Impact parameter is defined as the distance of closest approach to the primary vertex of an event.

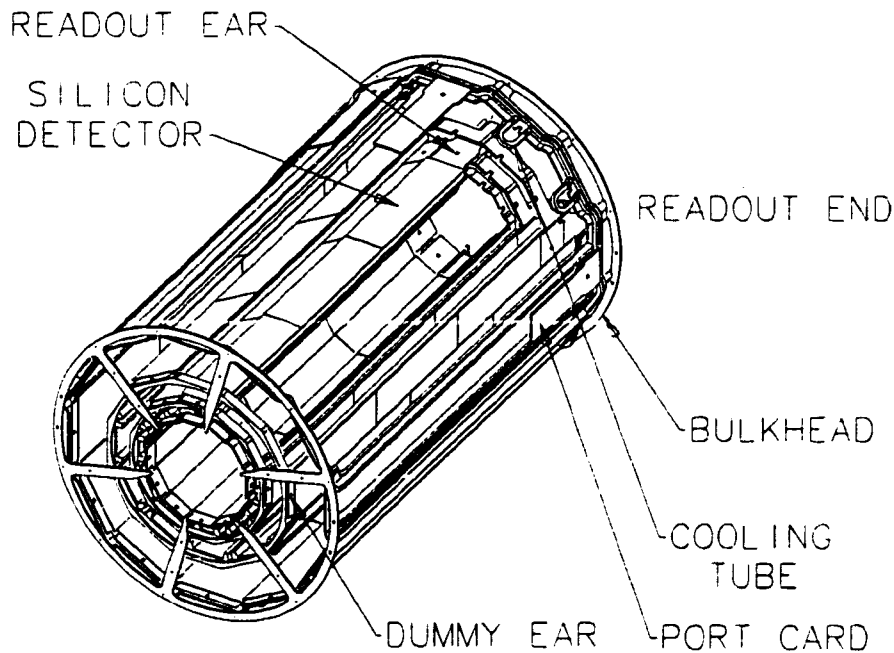


Figure 2.4: A schematic diagram of one SVX barrel. The four layers of the barrel are divided into 12 wedges in ϕ . The SVX detector is comprised of two barrels placed end-to-end.

capability aids tremendously in identifying b and c quarks which form long-lived mesons and typically travel for a measurable distance in the $r - \phi$ plane before decaying.

2.2.2 The Calorimetry

Electromagnetic and hadronic calorimeters, located immediately beyond the superconducting solenoid, measure the energy of electrons, photons, and jets within the fiducial volume of $\eta < 4.2$ and 2π in azimuth. The calorimetry is segmented into η and ϕ “towers” which are directed radially outward from the nominal CDF interaction point. Both types of calorimeters use alternating layers of scintillator as the active medium. However, lead serves as the absorber for the electromagnetic calorimetry while the hadronic calorimeters employs layers of iron. As an electron or photon passes through the active medium, an electromagnetic cascade resulting

from Bremsstrahlung occurs with a probability that depends on the number of radiation lengths through which the particle has traversed. Likewise, as a jet or hadron penetrates the scintillator of the hadronic calorimetry, daughter hadrons are produced in inelastic interactions and elastic scattering within the material, causing a similar shower of particles. The original energy of the incident particle can then be determined by the amount of showering radiation collected in the active medium. Because electromagnetic showers develop faster than hadronic showers, the hadronic calorimetry is placed outside of the electromagnetic calorimeters in each of the central, plug, and forward regions. However, the forward calorimetry, which covers $2.4 < |\eta| < 4.2$, has limited use in this analysis.

The central electromagnetic calorimeters (CEM) cover approximately $|\eta| < 1.0$, as does the combination of the central hadronic (CHA) and wall hadronic (WHA) calorimeters. The two cylindrical barrels which constitute the central calorimetry meet at $z = 0$ and are both divided into 24 ϕ -wedges of 15° each. Each of the ten projective towers within a wedge (see Fig. 2.5) covers $\Delta\eta = 0.11$, such that towers 0 through 8 combine for full η coverage out to 1.0. Because tower 9 does not contain the full thickness of the electromagnetic calorimetry, electron candidates in this analysis are required to be produced at $|\eta| < 1.0$, i.e., in CEM towers 0 through 8 (see Section 3.1.1).[†]

Within the CEM, wire proportional strip chambers, collectively called the CES, are placed at a depth of 5.9 radiation lengths which is the location that corresponds to maximum average electromagnetic shower development. The CES provides shower position information both in $r - \phi$ (using sense wires running parallel to the beamline) and in z (using strips perpendicular to the sense wires).

[†]Acrylic is appropriately substituted for lead absorber in certain layers, so that for any given axis parallel to the beamline, the effective radiation length thickness within towers 0 through 8 remains constant as a function of polar angle.

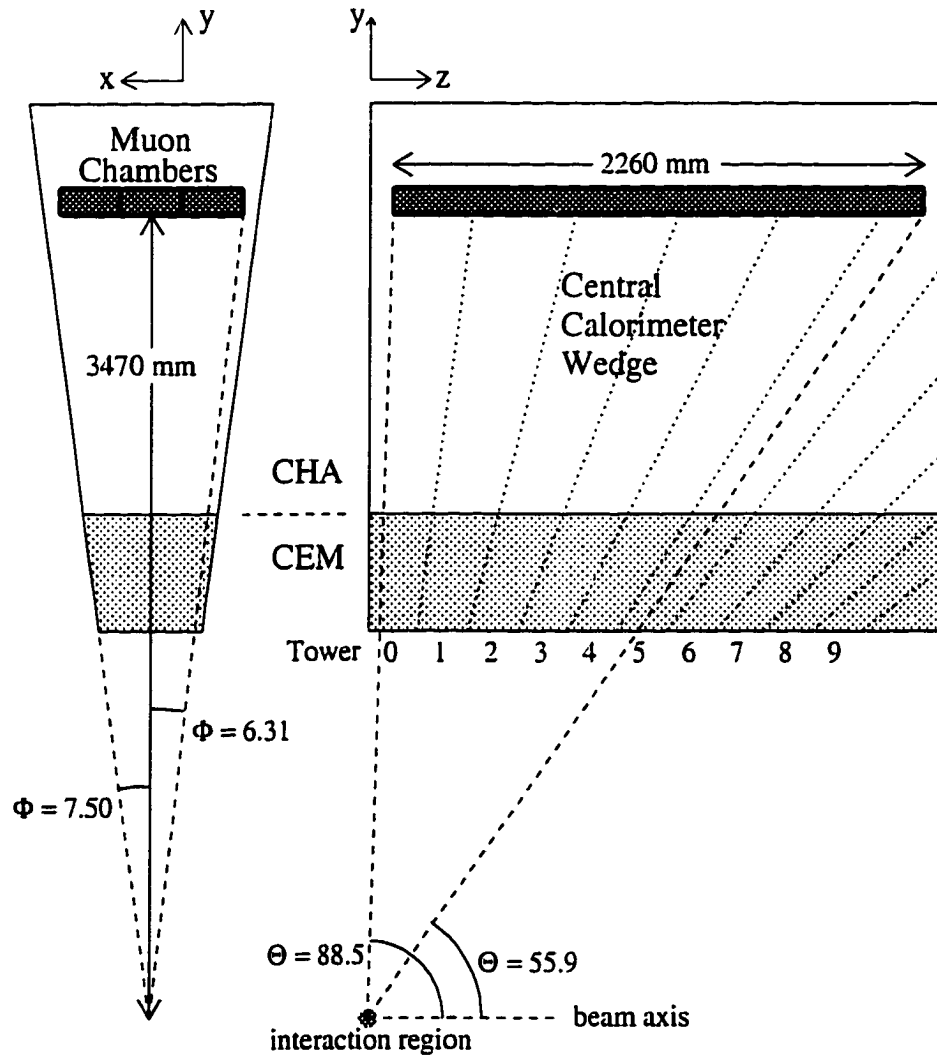


Figure 2.5: A schematic diagram of the central electromagnetic and hadronic calorimeters. The projective tower geometry points back to the nominal interaction point. The central muon chambers are also depicted.

System	Coverage ($ \eta $)	Segmentation ($\Delta\eta \times \Delta\phi$)	Energy resolution (GeV)	Thickness
CEM	< 1.1	$0.11 \times 15^\circ$	$13.7\%/\sqrt{E_T} \oplus 2\%$	$18 X_0$
CHA	< 0.9	$0.11 \times 15^\circ$	$50\%/\sqrt{E_T} \oplus 3\%$	$4.5 \lambda_0$
WHA	$0.7 - 1.3$	$0.11 \times 15^\circ$	$75\%/\sqrt{E_T} \oplus 4\%$	$4.5 \lambda_0$
PEM	$1.1 - 2.4$	$0.11 \times 5^\circ$	$22\%/\sqrt{E_T} \oplus 2\%$	$18 - 21 X_0$
PHA	$1.3 - 2.4$	$0.11 \times 5^\circ$	$106\%/\sqrt{E_T} \oplus 6\%$	$5.7 \lambda_0$
FEM	$2.2 - 4.2$	$0.11 \times 5^\circ$	$26\%/\sqrt{E_T} \oplus 2\%$	$25 X_0$
FHA	$2.4 - 4.2$	$0.11 \times 5^\circ$	$137\%/\sqrt{E_T} \oplus 3\%$	$7.7 \lambda_0$

Table 2.1: Specifications of the CDF calorimetry systems.

The end plug electromagnetic and hadronic calorimetry (PEM and PHA, respectively) covers the region out to $\eta = 2.4$. Due to difficulties resulting from using scintillator in the plug region, the disc-shaped PEM instead consists of 34 alternating layers of lead and proportional tube arrays. Likewise, alternating iron sheets and proportional chambers with cathode read-out make up the PHA. The calorimetry energy resolution and additional specifications for the central, plug, and forward regions are given in Table 2.2.2.

2.2.3 The Muon Chambers

High P_T muons are identified in muon chambers comprised of arrays of drift tubes located outside of the calorimetry. The central muon detection system is divided into three subsystems: the central muon chambers (CMU), the central muon upgrade (CMP), and the central muon extension (CMX), all shown in Fig. 2.2.

A CMU chamber, consisting of three modules filled with argon/ethane/ethanol gas, covers 12.6° in ϕ and is located behind each of the 48 central calorimeter wedges as shown in Fig 2.5. Each of the three modules contains four layers of four single-wire, rectangular drift cells. Because the ϕ location of each sense wire

is offset by $\pm 2\text{mm}$ in alternating layers, each module provides two independent measurements of the particle trajectory relative to the radial line passing through the wires. By tracking their path, muon candidates are matched to CTC tracks, resulting in momentum resolution of better than $\delta P_T/P_T = 0.002P_T$, as previously mentioned.

After nearly 5 interaction lengths of material presented by the calorimeters' absorbing media, high P_T muons are essentially the only surviving particles which are detected in the CMU. Occasionally, however, hadrons are not absorbed in the calorimetry and "punch through" to the CMU. To reduce the rate of "fake muons," 60 cm of absorbing steel was placed between the central calorimeters and the CMU in 1993, between Run 1a and Run 1b. The CMP, consisting of four additional layers of staggered drift chambers, was also added at this time. For $|\eta| < 0.6$, 85% of the solid angle is covered by the CMU, 63% by the CMP, and 53% by both.

Muon detection is extended to $|\eta| < 1.0$ with the CMX consisting of four free-standing conical arches each made up of eight staggered layers of rectangular drift tubes. The central muon extension scintillators (CSX), which reside on either side of the CMX layers, serve as accurate timing counters used for muon triggering (see Section 2.2.4). The CMX system covers 71% of the solid angle for $0.6 < |\eta| < 1.0$. Additionally, the toroidal muon spectrometer of the forward muon system (FMU) covers $2.0 < |\eta| < 3.6$ but is not used in this analysis due to large non-muon background rates and trigger inefficiencies.

2.2.4 Event Triggers

At $B\bar{O}$, bunch crossings occurred at a rate of 280,000 per second during Run 1, with approximately 1 interaction per crossing in Run 1a and over 3 interactions per

crossing in Run 1b. Because events at CDF can be written to 8 mm magnetic only at a rate of 5-10 Hz, a sophisticated trigger system was introduced to maximize the number of interesting events which are stored, while minimizing the amount of “dead-time,” *i.e.* the time during which additional $p\bar{p}$ interactions cannot be recorded.

Because not all event information is immediately available, the basic structure of the CDF trigger system consists of successive layers processing increasingly less events, but at a greater level of sophistication. This three-level system selects events with electrons, muons, or jets which are then recorded for subsequent offline analysis.

Level 1

The first level of selection, Level 1, uses only hardware triggers to perform a cursory search for either large energy clusters or muon tracks. Level 1 requires that: (1) the summed calorimeter trigger towers (of size $\Delta\eta \times \Delta\phi = 0.2 \times 15^\circ$) exceed a certain region-specific threshold, (2) a large transverse energy imbalance exists within the calorimetry (known as \cancel{E}_T , or “missing E_T ,” which can be indicative of the presence of a neutrino), or (3) that hits are registered in the muon chambers. While no tracking information is available to Level 1, fast outputs from the central muon detectors and the calorimetry result in a decision time of less than $3.5 \mu s$. The output from Level 1 at a typical Run 1a luminosity of $5 \times 10^{30} cm^{-2}s^{-1}$ is approximately 1 kHz.

Level 2

It is in Level 2, with more detailed use of calorimeter information, that the majority of events are eliminated. Within Level 2, a hardware “cluster finder” identifies a

“seed” tower above a certain energy threshold and subsequently includes the energy of neighboring towers. Furthermore, the central fast tracker (CFT), uses CTC hits to reconstruct high momentum tracks in $r - \phi$ with momentum resolution of $\delta P_T / P_T \approx 0.035 P_T$. As tracks are matched to either CEM clusters forming electron candidates or to track segments in the CMU, CMP, or CMX for muon candidates, the decision time for Level 2 increases to approximately $20ms$, reducing the output rate to nearly 12 Hz.

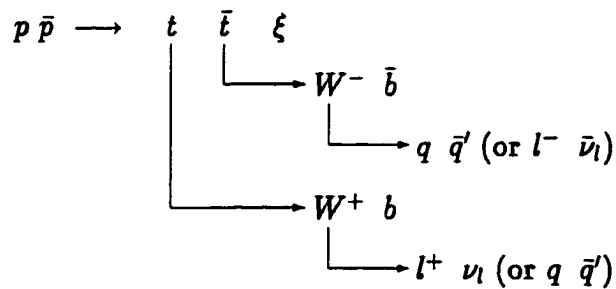
Level 3

The final level of the trigger system is exclusively software based. Events surviving Level 2 are processed by common processors which constitute Level 3. At this level, events are nearly fully reconstructed differing only in that offline reconstruction performs three-dimension tracking, while Level 3 track reconstruction is limited to the $r - \phi$ plane. Events surviving Level 3 were written to tape at a rate of 3-5 Hz for Run 1a and nearly 8 Hz for Run 1b.

Chapter 3

$M_{t\bar{t}}$ Event Samples

From the millions of events which survive the triggering system outlined in Section 2.2.4, we must select the subset which are relevant to our search for a $t\bar{t}$ resonance. At the Tevatron, standard model $t\bar{t}$ production in $p\bar{p}$ collisions at a center of mass energy of $\sqrt{s} = 1.8$ TeV is dominated by $q\bar{q}$ annihilation, while approximately 10% is attributable to gluon-gluon fusion (see Figure 1.3). To establish selection criteria (or “cuts”) for such events, we assume that $t\bar{t}$ pairs follow the expected standard model top quark decay of $t \rightarrow Wb$ (see Section 1.2.2) and, in this analysis, we search explicitly in the “lepton + jets” channel depicted below:



With ξ representing the recoiling system, the event signature of such a $t\bar{t}$ event includes a highly energetic “primary lepton” (either an electron or muon) as the result of a leptonic W decay, large missing energy due to the presence of an un-

detected neutrino, and four hadronic jets. This chapter outlines (a) the primary event selection criteria for $t\bar{t}$ events, (b) the data and monte carlo samples used in this analysis, and (c) additional cuts pertinent to our search for a resonance in the $t\bar{t}$ invariant mass spectrum.

3.1 Primary Event Selection

Identifying the presence of either an electron or muon resulting from the decay of a W boson is of paramount importance to distinguishing $t\bar{t}$ events from the vast majority of events produced at CDF. These final state leptons typically differ from those produced via the semileptonic decay of b or c quarks because leptons from W boson decay are usually isolated from jet activity. Furthermore, leptons from W boson decay are often more energetic than those from b and c decays. $t\bar{t}$ candidate events must satisfy several electron or muon criteria before being considered to contain a “primary lepton.”

3.1.1 Electron Selection

This analysis considers electron candidates only in the central region, requiring that $|\eta| < 1.0$. Candidates in the plug region are not included because such events are not expected to contribute significantly to the $t\bar{t}$ lepton + jets acceptance [9]. Also, the limited tracking at high $|\eta|$ dramatically increases the probability of misidentifying charged hadrons as electrons (generically called “fake” electrons). Additionally, several specific “fiducial cuts” [9] require that the electron shower position (as measured by the CES) is sufficiently far from CEM wedge boundaries and any other known inactive regions. These requirements ensure that the electron energy is well measured in the active volume of the CEM calorimetry. As part

of these fiducial electron cuts, a three-dimensional reconstructed CTC track is required to point to this electromagnetic shower.

Because we are ultimately searching for highly energetic electrons from W boson decay, additional selection criteria are imposed to reduce acceptance for background sources such as photon conversion, charged hadrons, and b and c quark decays. As previously mentioned, electrons from W boson decay are typically more energetic than those from background sources and, thus, this analysis requires that a primary electron have $E_T > 20$ GeV. Also, because electrons from Z boson decays tend to have characteristics similar to those from W boson decays, a large data sample of $Z \rightarrow e^+e^-$ events was utilized to establish additional criteria which improve primary electron identification. It was the investigation of the following set of electron variables which was used to identify $Z \rightarrow e^+e^-$ events as well as to establish the final criteria for primary electron selection:

- E/P is the ratio of electromagnetic energy in the CEM cluster to the track momentum as determined in the CTC.
- $E_{\text{HAD}}/E_{\text{EM}}$ is the ratio of the amount of energy the electron candidate deposited in the central hadronic calorimeter to the amount of energy deposited in the CEM.
- L_{shr} , the “lateral shower profile,” investigates the energy distribution in the calorimeter towers adjacent to the seed tower. The expression for L_{shr} , which quantifies a comparison between the candidate electron’s energy profile and that which was observed in studies using test beam electrons, is given by:

$$L_{\text{shr}} = 0.14 \sum_i \frac{E_i^{\text{obs}} - E_i^{\text{pred}}}{\sqrt{(0.14\sqrt{E})^2 + \sigma_{\text{pred}}^2}}$$

where the sum is over the adjacent towers, E_i^{obs} is the observed energy in tower i , E_i^{pred} is the predicted energy in tower i , σ_{pred} is the uncertainty on the predicted value, and $0.14\sqrt{E}$ is the uncertainty on the measured energy. Cutting on the L_{shr} variable increases the rejection of fake electrons, such as multiple particle backgrounds which tend to present a wider electromagnetic cluster in the CEM.

- χ_{strip}^2 , not unlike L_{shr} , compares the profile of the CES electron shower shape to that predicted by test beam studies.
- Δx and Δz represent the difference between the electron candidate's extrapolated CTC track and the location of the CES shower in $r - \phi$ and z , respectively.
- **z-vertex match** is defined to be the longitudinal distance between the primary vertex of the event and the $r = 0$ z -vertex obtained from an extrapolation of the electron track.

Using $Z \rightarrow e^+e^-$ data events, Figure 3.1 shows distributions of these variables for electrons at CDF. To identify $Z \rightarrow e^+e^-$ events, each was required to contain a primary electron which satisfied the tight cuts listed in Table 3.1. An event was classified as $Z \rightarrow e^+e^-$ if a second electron candidate passed both the fiducial and $E_T > 20$ GeV cuts and reconstructed an invariant mass with the primary electron which fell between 75 and 105 GeV/c². These secondary electrons in $Z \rightarrow e^+e^-$ events comprise an unbiased sample of electrons in the CDF data and make up the distributions shown in Figure 3.1. The electron identification cuts used in our search for a $t\bar{t}$ resonance, which are identical to the previously mentioned tight electron criteria listed in Table 3.1, are also shown in Figure 3.1.

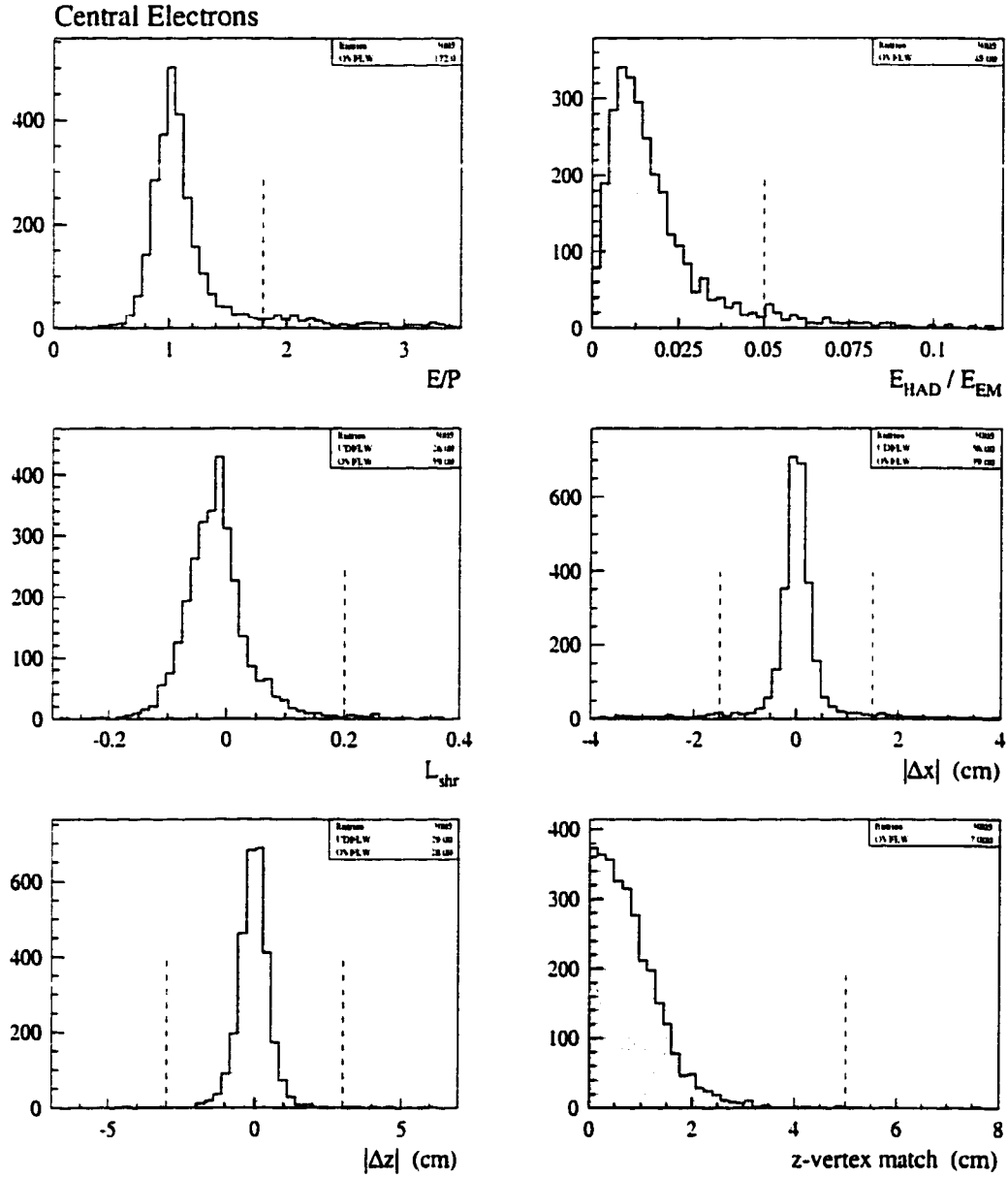


Figure 3.1: Distributions of several electron variables (described in the text) for electrons in CDF $Z \rightarrow e^+e^-$ events. The primary electron identification requirements used in the $t\bar{t}$ resonance search are shown as dashed lines and are listed in Table 3.1.

Variable	Cut
E_T	$> 20 \text{ GeV}$
E/P	< 1.8
$E_{\text{HAD}}/E_{\text{EM}}$	< 0.05
L_{shr}	< 0.2
$ \Delta x $	$< 1.5 \text{ cm}$
$ \Delta z $	$< 3.0 \text{ cm}$
$z\text{-vertex match}$	$< 5.0 \text{ cm}$
χ^2_{strip}	< 10.0

Table 3.1: Selection cuts for primary electrons.

Finally, when a photon interacts with detector material, it can convert to an e^+e^- pair, which can result in a fake primary electron. The presence of an additional oppositely signed track which extrapolates to a common vertex is indicative of a conversion. Accordingly, electron candidates which yield a small e^+e^- invariant mass and are within 0.2 cm in $r - \phi$ and $\cot \theta < 0.06$ relative to such an opposite-sign track are rejected, allowing us to largely remove conversions from our data sample. Also, to be considered a conversion, the common vertex is required to be no more than 50 cm in the radial direction from the beamline. This ensures that the conversion is not located within the CTC volume where there is a dramatic increase in the probability that the conversion candidate is not actually the result of an $\gamma \rightarrow e^+e^-$ conversion.

3.1.2 Muon Selection

As with electrons, this analysis only considers muon candidates in the central region with $|\eta| < 1.0$. We search for primary muons by first requiring that at least one muon track segment (or “stub”) in the central muon chambers match to a CTC track. Primary muon candidates are classified according to the muon

chamber(s) in which the stub is observed; i.e., they are labeled as CMX, CMU, CMP, or CMU/CMP muons. Because these muons, by definition, are detected in the central region, no additional fiducial cuts are necessary. In addition to cosmic rays, the principal muon background is charged hadron showers in which a secondary particle “punches through” the CDF calorimetry and fakes a muon track in the muon chambers.

Like the electron identification cuts described in Section 3.1.1, the remaining selection criteria for primary muons were established using actual $Z \rightarrow \mu^+\mu^-$ events collected at CDF. Various cuts on the following muon variables were applied in order to select $Z \rightarrow \mu^+\mu^-$ data events and also to identify primary muons in this analysis:

- P_T is the particle’s momentum in the transverse plane as determined from its trajectory measured in the CTC. The P_T is said to be “beam constrained” because the reconstructed track is constrained to pass through the beamline. Because we search for high P_T leptons in this analysis, primary muon candidates are required to have $P_T > 20$ GeV/c.
- E_{HAD} (E_{EM}) is the amount of energy the muon candidate deposits in the central hadronic (electromagnetic) calorimetry. Because a muon is a minimum ionizing particle and results in characteristically small calorimeter energy deposition, muon backgrounds are reduced by requiring that the values of these variables fall within a certain range.
- d_0 , the “impact parameter,” is given by the distance of closest approach between the extrapolation of the reconstructed CTC track and the beamline. Requiring d_0 to be less than a certain value aids in reducing cosmic ray backgrounds which, in general, are not consistent with muons that originate near the nominal beamline.

- $|\Delta x|_{\text{CMU}}$, $|\Delta x|_{\text{CMP}}$, and $|\Delta x|_{\text{CMX}}$ represent the difference, in $r - \phi$, between the extrapolated CTC track and the location of the corresponding muon stub.
- **z-vertex match** is defined to be the longitudinal distance between the primary vertex of the event and the $r = 0$ z-vertex obtained from an extrapolation of the muon track.

Using $Z \rightarrow \mu^+\mu^-$ data events, Figures 3.2 and 3.3 show distributions of these variables for muons at CDF. Identifying $Z \rightarrow \mu^+\mu^-$ events first required that each contained a primary muon which satisfied the tight cuts listed in Table 3.2. An event was classified as $Z \rightarrow \mu^+\mu^-$ if a secondary muon candidate passed the $P_T > 20$ GeV/c cut, and if its invariant mass with the primary muon fell between 75 and 105 GeV/c². As with the electron selection studies, it is these secondary muons in $Z \rightarrow \mu^+\mu^-$ events which comprise an unbiased sample of muons in the CDF data and make up the distributions shown in Figures 3.2 and 3.3. The muon identification cuts used in our search for a $t\bar{t}$ resonance, which are also listed in Table 3.2, are shown in these distributions.

Variable	Cut
P_T	$> 20 \text{ GeV/c}$
E_{EM}	$< 2 \text{ GeV}$
E_{HAD}	$< 6 \text{ GeV}$
$E_{\text{HAD}} + E_{\text{EM}}$	$> 0.1 \text{ GeV}$
d_0	$< 3 \text{ mm}$
$ \Delta x _{\text{CMU}}$	$< 2.0 \text{ cm}$
$ \Delta x _{\text{CMP}}$	$< 5.0 \text{ cm}$
$ \Delta x _{\text{CMX}}$	$< 5.0 \text{ cm}$
z-vertex match	$< 5.0 \text{ cm}$

Table 3.2: Selection cuts for primary muons.

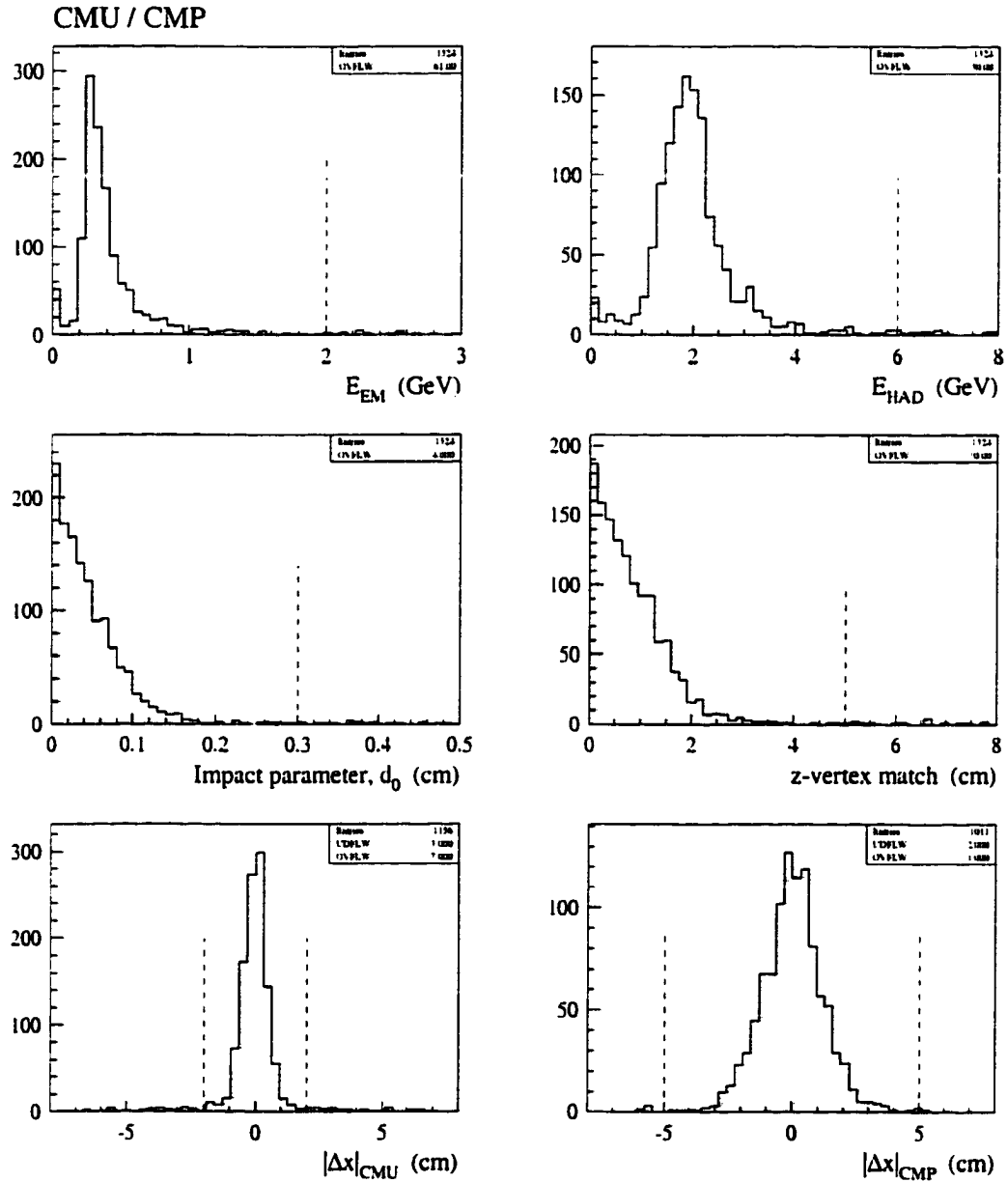


Figure 3.2: Distributions of several muon variables (described in the text) for CMU and/or CMP muons in CDF $Z \rightarrow \mu^+ \mu^-$ events. The primary muon identification requirements used in the $t\bar{t}$ resonance search are shown as dashed lines and are listed in Table 3.2.

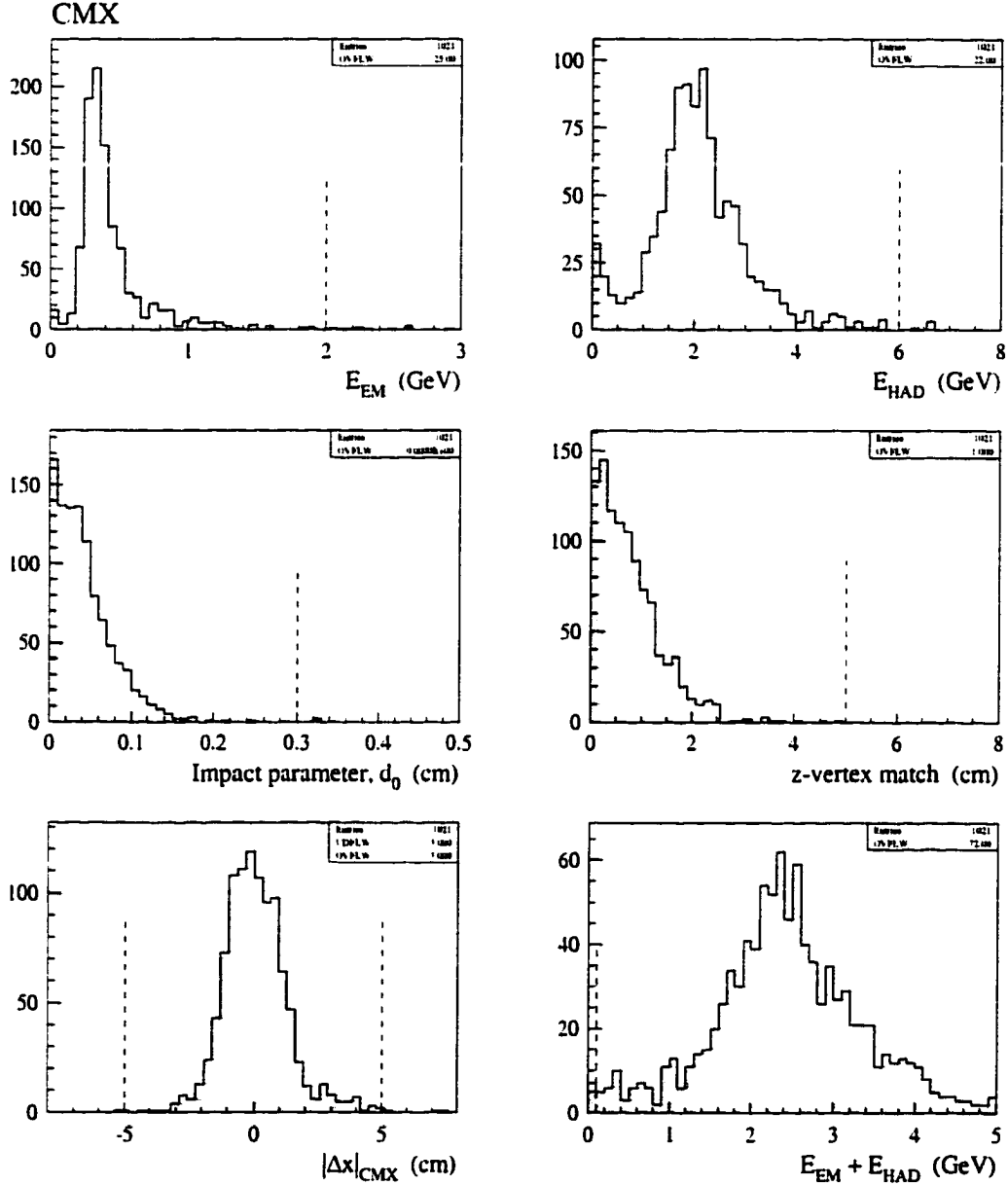


Figure 3.3: Distributions of several muon variables (described in the text) for CMX muons in CDF $Z \rightarrow \mu^+\mu^-$ events. The primary muon identification requirements used in the $t\bar{t}$ resonance search are shown as dashed lines and are listed in Table 3.2.

3.1.3 W Selection

After using the selection criteria outlined in Sections 3.1.1 and 3.1.2 to identify the set of events which contain either a primary electron or muon, an additional set of cuts is imposed to select a subset of events called the “ W sample.” As a fundamental requirement for lepton + jets $t\bar{t}$ events, these cuts select events which contain a single $W \rightarrow l\nu$ candidate decay.

To eliminate primary lepton contributions from background sources (such as semileptonic decays in $b\bar{b}$ events), we apply “isolation” cuts to electron and muon candidates to ensure that they are well isolated, far from jet activity. The isolation variable, I , measures the non-lepton contribution to the energy surrounding the primary lepton and is given by:

$$I = \begin{cases} \frac{E_T^{CAL} - E_T}{E_T} & \text{for electrons} \\ \frac{E_T^{CAL} - E_T}{P_T} & \text{for muons} \end{cases}$$

where

- E_T^{CAL} is the sum of the calorimeter transverse energy in a cone of radius $\Delta R \equiv \sqrt{(\Delta\eta)^2 + (\Delta\phi)^2} = 0.4$,
- E_T is given by the CEM tower cluster for electrons, and
- E_T for a muon is given by its beam constrained P_T , assuming that the muon mass (105 MeV/c²) is negligible.

W sample primary leptons are required to have $I < 0.1$.

The W sample also reflects selection criteria aimed at eliminating contributions due to Z boson decays. Clearly, establishing such cuts relies heavily upon the

$Z \rightarrow e^+e^-$ and $Z \rightarrow \mu^+\mu^-$ studies presented in Sections 3.1.1 and 3.1.2. After identifying a primary lepton (with $I < 0.1$), a somewhat looser set of selection criteria is employed to search for a second, opposite-signed lepton of the same generation. These secondary lepton cuts for Z boson removal are listed in Tables 3.3 and 3.4 for electrons and muons, respectively. In agreement with the earlier studies, an event is labeled as a Z boson decay and removed from the W sample if the invariant mass of the primary and secondary leptons is greater than 75 GeV/ c^2 , but less than 105 GeV/ c^2 . Z boson removal is expected to eliminate very few standard model $t\bar{t}$ events [13].

Variable	Cut
E_t	$> 10 \text{ GeV}$
$E_{\text{HAD}}/E_{\text{EM}}$	< 0.12
I	< 0.2
If secondary e is in CEM:	
E/P	< 2.0

Table 3.3: The secondary electron cuts used for Z boson removal.

Additionally, our selection criteria must also identify the presence of a neutrino candidate since we search for a leptonic W decay. Because neutrinos interact so weakly with matter and are undetected at CDF, their transverse energy can be measured indirectly by determining an event's E_T imbalance, known as the “missing E_T ” or \cancel{E}_T . Assuming that the net momentum of a collision's original $p\bar{p}$ pair is zero, a large imbalance in the total energy of the resulting debris is then attributable to the presence of a neutrino (detector errors notwithstanding). The “raw” \cancel{E}_T in an event is given by the negative of a vector sum of transverse energies which result from clustering signals in the calorimeter towers. However, because the muon is a minimum ionizing particle, its (relatively meager) calorime-

Variable	Cut
P_t	$> 10 \text{ GeV}/c$
If the secondary μ is associated with a stub:	
E_{EM}	$< 5.0 \text{ GeV}$
E_{HAD}	$< 10.0 \text{ GeV}$
$ \Delta x _{\text{CMU}}, \Delta x _{\text{CMP}}, \text{ or } \Delta x _{\text{CMX}}$	$< 5.0 \text{ cm}$
I	< 0.1
If the secondary μ is not associated with a stub:	
E_{EM}	$< 2.0 \text{ GeV}$
E_{HAD}	$< 6.0 \text{ GeV}$
$ \eta $	< 1.1
I	< 0.2

Table 3.4: The secondary muon cuts used for Z boson removal.

ter deposits are not included in the raw \cancel{E}_T calculation for events with a primary muon. In such events, the muon E_T is instead determined from its mass of $105 \text{ MeV}/c^2$ and its P_T measured in the CTC. Likewise, a similar correction procedure is performed for all minimum ionizing tracks with $P_T > 10 \text{ GeV}/c$. Raw \cancel{E}_T in excess of 20 GeV is required for events in the W sample.

The final W sample cut eliminates all events that satisfy the selection criteria used in the CDF dilepton top quark analysis [9]. While these top dilepton candidates must include at least one primary lepton as described in Sections 3.1.1 and 3.1.2, the second lepton is required to satisfy somewhat looser cuts, allowing for potential overlap between the lepton+jets and dilepton analysis. Explicitly eliminating dilepton candidates from the W sample ensures that exclusive sets of data events are used in the two analyses.

By measuring only the \cancel{E}_T in an event, the longitudinal component of the neutrino momentum is left undetermined and, therefore, prevents us from calculating the W invariant mass, M_W , for events in the W sample. However, a related quan-

tity known as the “transverse mass,” M_T , which is the two-dimensional analog to invariant mass, is our best alternative measure of M_W . Neglecting the charged lepton mass, the expression for M_T is given by:

$$M_T = \sqrt{(P_T^l + \cancel{E}_T)^2 - (\vec{P}_T^l + \vec{\cancel{E}}_T)^2}$$

or, equivalently,

$$M_T = \sqrt{2P_T^l \cancel{E}_T (1 - \cos\phi)}$$

where \vec{P}_T^l is the charged lepton transverse momentum vector, $\vec{\cancel{E}}_T$ is the vector representing the negative of the energy imbalance, $P_T^l = |\vec{P}_T^l|$, and ϕ is the angular separation between \vec{P}_T^l and $\vec{\cancel{E}}_T$. As expected, the M_T shape from events in the W sample, shown in Figure 3.4, peaks at $M_W \approx 80 \text{ GeV}/c^2$ and has the smeared Jacobian shape which results from performing the measurement in only two dimensions. A detailed study of the W sample M_T spectrum yields a measured M_W value of $80.433 \pm 0.079 \text{ GeV}/c^2$ [6], in agreement with the world average $M_W = 80.394 \pm 0.042 \text{ GeV}/c^2$ [6].

3.1.4 Jet Selection

Using only calorimeter tower information, a cone of $\Delta R = 0.4$ is used to reconstruct jet clusters as outlined in Section 2.2.4. From the total calorimeter energy, E , deposited within the clustering cone, the jet E_T is given by $E \sin \theta$, where θ is the azimuthal angle of the E_T weighted centroid of the clustered towers.

Like the CDF top quark mass analysis [14], our search for a $t\bar{t}$ resonant state in the lepton + jets channel requires that candidate events satisfy the W sample selection criteria and contain at least four jets. Of course, this latter cut is based upon the expected standard model $t\bar{t}$ decay to a b , \bar{b} , and two hadronic W daugh-

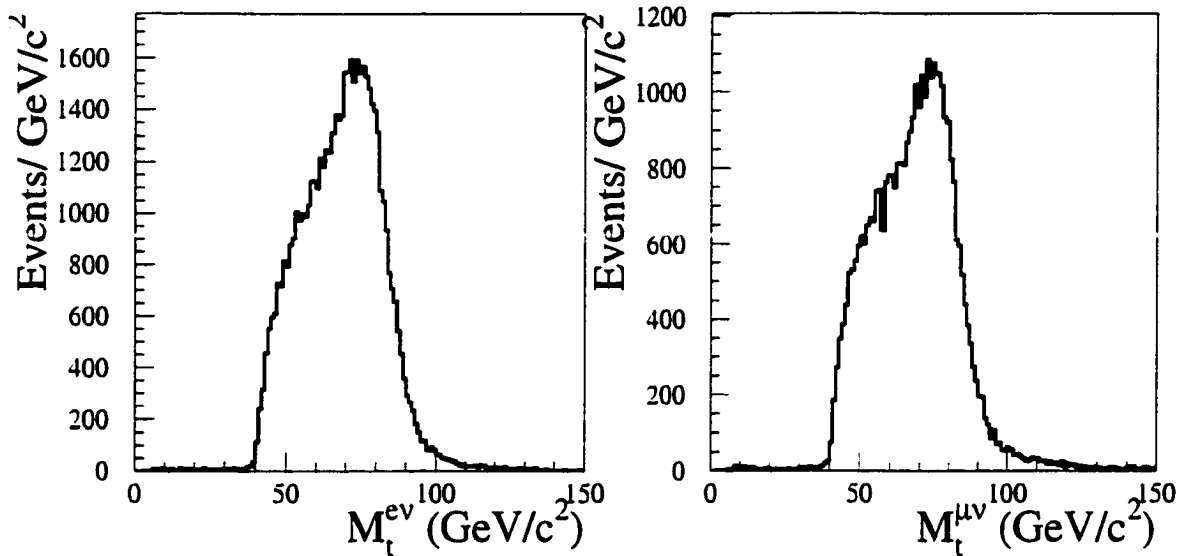


Figure 3.4: The lepton-neutrino invariant transverse mass for events in the W sample. The left (right) plot shows the M_T spectrum for events containing a primary electron (muon).

ters, all of which will fragment, forming jets in the CDF detector. Therefore, in this analysis, we select events from the W sample provided that they contain three jets with $E_T > 15$ GeV and $|\eta| < 2.0$ and a fourth with $E_T > 8$ GeV and $|\eta| < 2.4$. Event simulations indicate that the beneficial increase in $t\bar{t}$ acceptance which we gain by relaxing the requirements on the fourth jet outweighs the less dramatic increase in non- $t\bar{t}$ background. In 106 pb^{-1} of data collected at CDF in Run 1, 163 events from the W sample also satisfy these jet requirements.

Identifying b Jets

Of the various background sources in this analysis (see Section 3.2.1), the primary contribution comes from W boson production in association with jets, which rarely (approximately 1%) include an actual b jet. Therefore, distinguishing between signal events and these $W + \text{multijet}$ backgrounds can be greatly enhanced by

identifying one or both of the b jets which result from standard model $t\bar{t}$ decay.

Because the long b lifetime is only magnified in the lab frame due to a large boost from the massive $t\bar{t}$ system, the b quark will form a B hadron which can travel a measurable distance before decaying. Accordingly, the secondary-vertex algorithm (JETVTX) uses the Silicon Vertex Detector (SVX) to search within a $t\bar{t}$ candidate event for additional vertices that are displaced from the primary vertex. These secondary vertices aid in identifying (or “tagging”) jets that result from b (or c) quark decay. A second, complementary tagging algorithm, the soft lepton tagger (SLT), identifies b jets by searching for extra leptons in the event which are consistent with having come from semileptonic B hadron decay. These b tagging algorithms are discussed in more detail below.

SVX Tags

As previously mentioned, it is the long lifetime of the b quark which leads to a large B hadron proper decay length ($c\tau \approx 480 \mu m$ and depends on the specific hadron[6]) and, therefore, a measurable displaced secondary decay vertex. The primary vertex of an event is defined using a weighted fit of both the z -vertex position (as determined by the VTX) and the SVX tracks in the event which are not consistent with having come from a secondary vertex. While the actual primary vertex position is gaussian distributed in r and z about the center of the CDF detector (with approximate σ 's of $35\mu m$ and $30cm$, respectively), we correct for the varying relative slope between the beamline and the CDF detector axis and find that the measured primary vertex has $6\text{--}36 \mu m$ uncertainty in the transverse $r - \phi$ plane. The decay length separation between the primary and secondary vertices is projected into the transverse plane and is labeled as L_{xy} as is shown in Figure 3.5. The sign of L_{xy} is positive (negative) if the secondary vertex and its

associated jet are in the same (opposite) hemisphere. Also depicted in Figure 3.5 is the impact parameter, d_0 , which is defined as the distance of closest approach between the primary vertex and the extrapolation of the tracks which define the secondary vertex. The estimated uncertainty on d_0 is called σ_{d_0} .

After requiring that tracks satisfy certain quality criteria [15] and $|d_0|/\sigma_{d_0} > 3$ to ensure that they are displaced, the JETVTX algorithm is applied to all such tracks that match to a jet within $\cos \delta = 0.8$, where δ is the angular separation in the transverse plane between the track and the axis of any jet with $E_T > 15$ GeV and $|\eta| < 2.0$. If at least two such tracks exist for a given jet, the vertex is defined to be displaced. In order to increase the b (or c) purity of tagged jets, we suppress the background contributions from non-heavy flavor events with mismeasured tracks by further requiring that L_{xy} be both positive and greater than three times its uncertainty. Surviving jets are finally tagged as a heavy flavor quark jets provided that they are not consistent with coming from $K_s^0 \rightarrow \pi^+\pi^-$ and $\Lambda^0 \rightarrow p^+\pi^-$ decays.

SLT Tags

Using a complementary method for tagging jets, the SLT tagger exploits the semileptonic decays of the b and c quarks as shown in Figure 3.6. Both processes shown in this figure have an expected branching fraction of approximately 20%, making this a viable means for identifying b jets in $t\bar{t}$ decays. The leptons from B meson decay tend to have characteristically low P_T (on order of a few GeV/c) and are often found in the midst of jet activity resulting from the fragmentation of the b quark. To identify soft leptons from b decay, the energy (momentum) threshold for lepton selection as described in Section 3.1.1 (Section 3.1.2) is reduced to 2 GeV (2 GeV/c). Electrons produced by semileptonic b decays are required to contain a high-quality CTC track that matches to a CES cluster whose profile is consistent

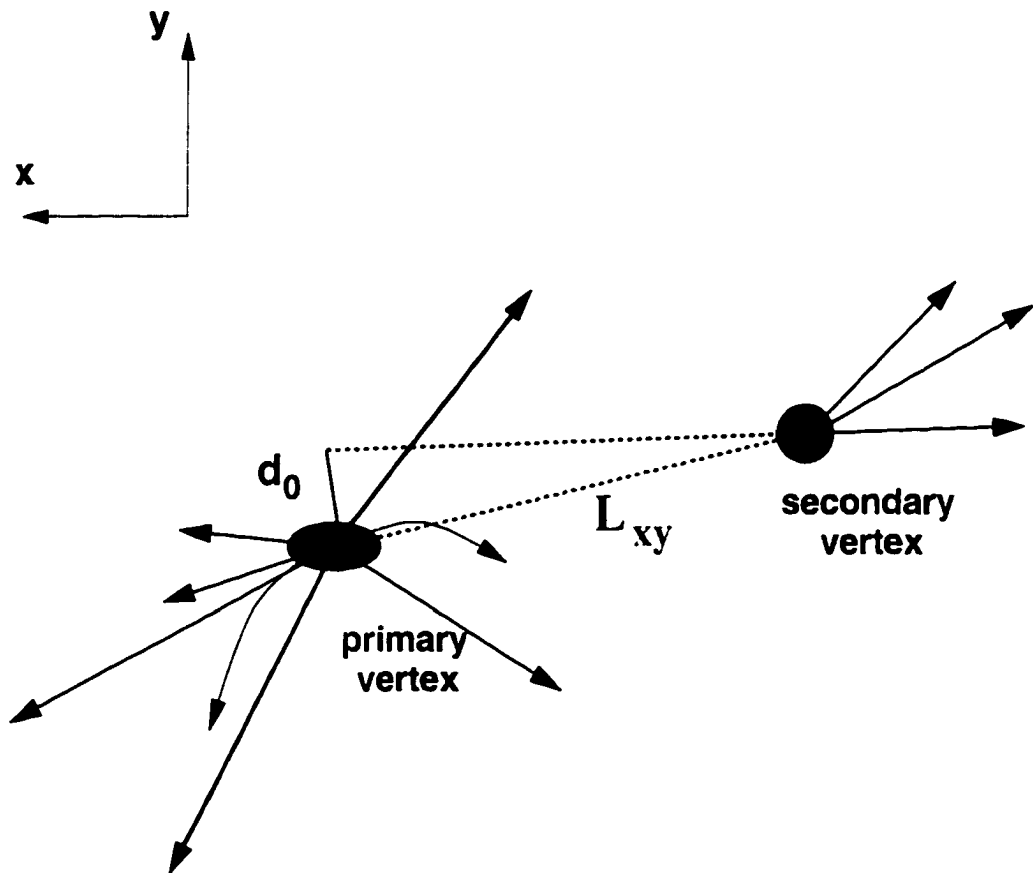


Figure 3.5: Schematic diagram of a typical secondary vertex which is associated with a jet resulting from the heavy-flavor quark decay.

with that of an electron shower. Likewise, the CTC track for SLT muons must match to a track in the central muon chambers. However, unlike primary leptons in the W sample, no isolation requirements are placed on SLT leptons as we expect them to be produced in association with significant amounts of jet activity. For this reason, SLT muons are not required to yield energy deposition that is consistent with a minimum ionizing particle as we demand for primary muons. The specific SLT cuts are optimized for selection of non-isolated leptons from semileptonic b decays and are described in more detail in Reference [16].

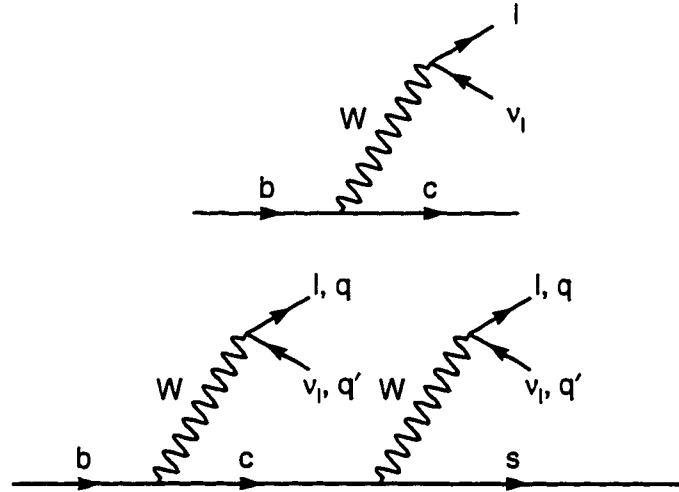


Figure 3.6: Semileptonic b quark decays.

Although the actual b purity of jets that are SVX tagged is significantly greater than that of SLT tags, both methods of b jet identification are critical to our search for a $t\bar{t}$ resonance. By utilizing information that is nearly uncorrelated, the combination of both algorithms allows us to enjoy a greater $t\bar{t}$ acceptance than using either tagger alone.

3.1.5 Summary of Primary Event Selection

In our search for a $t\bar{t}$ resonance we select only W boson candidate events which have:

- an isolated, high- P_T lepton (as required by the W sample selection criteria)
- $E_T > 20$ GeV (as required by the W sample selection criteria)
- 3 jets with $E_T > 15$ GeV, $|\eta| < 2.0$
- a 4th jet with $E_T > 8$ GeV, $|\eta| < 2.4$

Furthermore, we consider only events in the so-called “tagged” and “untagged” samples. “Tagged” events meet the additional requirement that they contain at least one SVX or SLT b -tag, while events which fall in the “untagged” sample are those which contain no b -tags but whose fourth jet satisfies the tighter jet requirements of $E_T > 15$ GeV, $|\eta| < 2.0$.

3.2 Monte Carlo Simulation and Background

Computer-generated event simulations, known as “Monte Carlo,” are used throughout this analysis to both aid in establishing selection criteria and to determine the expected signal and background event distributions once the final cuts have been set. These generators, which simulate multi-process $p\bar{p}$ event showers based on QCD and Electroweak theory, allow us to more thoroughly understand the signal and background contributions to our data sample. Understandably, however, Monte Carlo simulations are rarely accurate to more than leading order in α_s and often rely on QCD cascade approximations to simulate higher order processes. In this analysis, all event simulations have their b decays based upon the detailed

knowledge of B hadron decays which has been developed by the CLEO experiment and is reflected in our use of the QQ Monte Carlo package [17]. All other short-lived particles, however, decay according to the branching ratios reported by the Particle Data Group [6]. For each Monte Carlo sample used in this analysis, we employed the parton distribution function that was favored at the time of generation. The output of any Monte Carlo event generator is an extensive list of final state particle four-vectors, which in turn, serves as the input to a CDF detector simulation package called QFL [18]. This simulation models the detector response to final state particles using a parameterization that is based upon observed data distributions as well as test-beam studies.

We employ three different Monte Carlo generators to simulate signal and background sources which contribute to our search for a $t\bar{t}$ resonance:

- Because our search focuses on any narrow resonance particle, X , that decays to $t\bar{t}$, we use PYTHIA 5.7 [19] to model the signal process with $Z' \rightarrow t\bar{t}$ event for natural width Γ equal to 1.2% and 4% of $M_{Z'}$, the Z' mass. We generate $Z' \rightarrow t\bar{t}$ Monte Carlo samples at both widths for 13 values of $M_{Z'}$ between 400 GeV/c² and 1 TeV/c². These samples do not model the gamma or interference processes. The PYTHIA Monte Carlo package simulates $p\bar{p}$ collisions with parton fragmentation given by the Lund string model for u , d , and s quarks, while the Peterson fragmentation model is used for the c , b , and t quarks. Unless otherwise noted, the CTEQ2L parton distribution functions are used for all PYTHIA samples.
- Standard model $t\bar{t}$ production is modelled using the HERWIG [20] Monte Carlo package which is based on leading order QCD matrix elements for the hard processes, followed by coherent parton shower evolution, cluster hadronization, and an underlying event model based on data. Unless otherwise noted,

all subsequent references to the HERWIG $t\bar{t}$ sample explicitly imply that the MRSD0' structure functions were employed and that the events were generated with a top mass of 175 GeV/c².

- The non- $t\bar{t}$ background sources are modelled using VECBOS which is a parton-level program based on tree-level matrix element calculations for W +jets production. Partons resulting from VECBOS simulation of hard scattering processes are subsequently evolved and hadronized using a separate program derived from HERPRT, the parton shower model contained in HERWIG. Unless otherwise noted, the VECBOS samples used in this analysis use the MRSD0' structure functions and simulate W +jets events with the Q^2 scale of the hard scatter set equal to the average P_T^2 of the outgoing partons.

While there are other contributing sources to the non- $t\bar{t}$ background in this analysis, we have found the VECBOS W +jets sample alone sufficiently models the expected non- $t\bar{t}$ background distributions for all relevant event variables [14]. In the following section, we discuss the expected backgrounds in this analysis.

3.2.1 Backgrounds

In addition to standard model $t\bar{t}$ production itself, there are several non- $t\bar{t}$ sources which constitute background for our search of a narrow $t\bar{t}$ resonance. The sources considered here are W/Z +jets events which contain heavy flavor quarks, non- W/Z events, diboson (WW , ZZ , WZ) production, $Z \rightarrow \tau\tau$ processes, and single top quark decays.

W production in association with b and/or c quarks is modelled by VECBOS as described above and serves as the single largest non- $t\bar{t}$ background source in this analysis. Specifically, we consider $Wb\bar{b}$ and $Wc\bar{c}$ production resulting from gluon

splitting as well as Wc production (both processes are shown in Figure 3.7). From Monte Carlo simulation, we estimate the fraction of events surviving our selection criteria that result from these sources. By investigating only the $Z/W+1$ jet and $Z/W+2$ jets events, Monte Carlo studies show that the expected number of events in our data sample that are due to $Zb\bar{b}$, $Zc\bar{c}$, and Zc events can be determined by an appropriate scaling of the $Wb\bar{b}$, $Wc\bar{c}$, and Wc predictions.

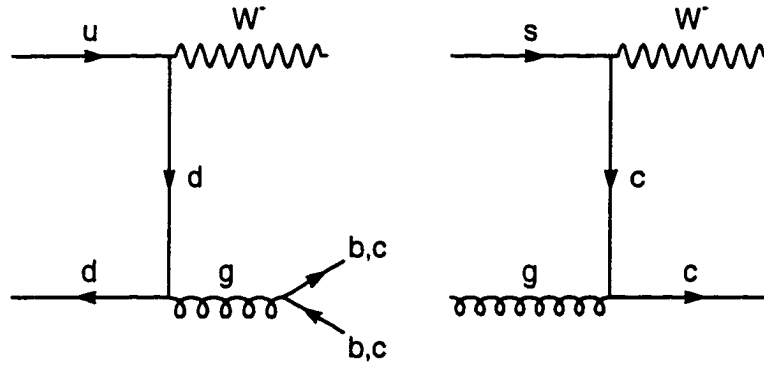


Figure 3.7: $Wb\bar{b}$, $Wc\bar{c}$, and Wc production processes which contribute to the non- $t\bar{t}$ backgrounds for the search for $X \rightarrow t\bar{t}$ search.

The expected contributions due to non- W/Z tagged events, such as direct $b\bar{b}$ and $c\bar{c}$ production, are estimated by determining the number of tags as a function of lepton isolation and \cancel{E}_T . Because it is unlikely that events include W boson production if they have both low \cancel{E}_T and a well-isolated lepton, investigation of this region of phase-space provides an estimate for the non- W/Z rates that contribute to non- $t\bar{t}$ background. Furthermore, the small backgrounds from diboson and single top production are estimated from their expected acceptances (determined from Monte Carlo) along with their measured and predicted production cross-sections, respectively. The signal contamination due to $Z \rightarrow \tau\tau$ is also estimated through Monte Carlo simulation with the normalization set such that the number

of expected $Z \rightarrow ll + \geq 1\text{-jet}$ events agrees with the number observed in the CDF data.

Also, the impurity of b -tagging (i.e., “fake” tags), which can come from any of the above sources, contributes to the expected background for $t\bar{t}$ production. In the JETVTX tagging algorithm, such fakes come from primary vertex tracks which, due to mismeasurement, erroneously reconstruct to a secondary vertex. Recall (Section 3.1.4) that in an attempt to eliminate such mistags, we require that $L_{xy} > 0$. It is, therefore, reasonable to assume that the L_{xy} distribution for fake displaced vertices which satisfy all the JETVTX selection criteria, save $L_{xy} > 0$, will be symmetric about $L_{xy} = 0$. Accordingly, events with negative L_{xy} allow us to parameterize the probability of obtaining a fake SVX tag for a given jet E_T , η , and number of SVX tracks in the jet. By applying this probability distribution function to events in our data sample, we determine an estimate for the number of fake SVX tags. Likewise, fake SLT tags are parameterized as a function of P_T through investigation of data samples of generic jet events [16].

Background Calculation

While the kinematics of these non- $t\bar{t}$ background sources are well-modelled by VECBOS, we utilize the expertise developed in CDF’s measurement of the top quark mass [14] to precisely calculate the overall normalization of the expected non- $t\bar{t}$ background contribution to our data sample. The data sample selection criteria discussed thus far are identical to those applied in the top mass analysis. Yet, to further increase signal purity, that particular analysis applies an additional χ^2 cut on the kinematic top mass fit and uses the expected background rates described above to determine the non- $t\bar{t}$ contribution to their data sample. For our purposes, the non- $t\bar{t}$ background contribution is calculated as in the CDF top

quark mass measurement, but with the appropriate scaling which results from additional acceptance calculations accounting for differences in selection criteria.

Using a maximal likelihood technique, the non- $t\bar{t}$ background contribution to the top mass analysis is calculated for four, exclusive event subsamples: events with (i) only SVX tags, (ii) only SLT tags, (iii) both SVX and SLT tags, but not necessarily on the same jet, and (iv) no tags. For each subsample, the expected number of events (N_{exp}) is determined as a function of both the number of $t\bar{t}$ events ($N_{t\bar{t}}$) and the number of non- $t\bar{t}$ events (N_W) which comprise the events in that particular subsample, *i.e.*,

$$N_{exp} = a \times N_{t\bar{t}} + \sum_k c_k \times N_k^{abs} + \sum_i d_i b_i \times (N_W) \quad (3.1)$$

where a is the tagging probability for standard model $t\bar{t}$ events in this particular subsample; the k (i) index sums over background sources for which an expected absolute number of events, N_k^{abs} (fraction of W candidate events, d_i) has been determined; and c_k and b_i are the corresponding tagging probabilities for background events. Then through a conventional likelihood technique, the most probable values of $N_{t\bar{t}}$ and N_W are determined by fitting to the number of events actually observed in each subsample. This likelihood procedure includes the constraint that $N_{t\bar{t}}$ and N_W for all four subsamples sum to 151, the total number of events surviving the selection criteria outlined thus far with the additional top mass analysis kinematic fit χ^2 cut.

During the period of time that we worked towards optimizing additional selection criteria for a $t\bar{t}$ resonance search, the fitted non- $t\bar{t}$ background contributions to the CDF top quark mass analysis were as listed in Table 3.5 [21]. Accordingly, for the top mass analysis, the uncertainty in the estimated total amount of non- $t\bar{t}$ background was given as approximately 27% [22]. We also use this value as a

reasonable estimate for the uncertainty in the amount of non- $t\bar{t}$ background since it only plays a very limited role in our search for a $t\bar{t}$ resonance. However, since that time, the CDF collaboration has improved its measurement of the ratio of b -tagging rates for Monte Carlo and data. Clearly, this change affects many of the quantities in Equation 3.1. The resulting non- $t\bar{t}$ background contributions to the CDF top quark mass analysis are listed in Table 3.6 [14].

Subsample	N_W
only SVX tags	1.5 ± 0.5
only SLT tags	5.9 ± 1.3
SVX and SLT tags	0.5 ± 0.3
No tags	23.9 ± 6.6

Table 3.5: The non- $t\bar{t}$ background contributions as calculated in the top quark mass analysis before the updated Run 1 measurement of the ratio of b -tagging rates for Monte Carlo and data.

Subsample	N_W
only SVX tags	2.1 ± 0.6
only SLT tags	7.7 ± 1.3
SVX and SLT tags	0.8 ± 0.3
No tags	30.7 ± 4.6

Table 3.6: The non- $t\bar{t}$ background contributions as calculated in the top quark mass analysis after the updated Run 1 measurement of the ratio of b -tagging rates for Monte Carlo and data.

While, in principle, a large change in the expected non- $t\bar{t}$ background contribution would affect where we set our χ^2 selection cut (described in Section 3.5.3), we expect that the difference between Tables 3.5 and 3.6 would have no noticeable effect on this analysis. Fortunately, as Section 3.5.3 details, not only is the χ^2 cut used in our search quite loose, but the fact that it was obtained from a compromise

of studies performed for several resonance masses makes it is even less dependent on the non- $t\bar{t}$ background normalization of Tables 3.5 and 3.6. Furthermore, the philosophy of this analysis has been to attempt to set selection criteria which increase our discovery potential for a narrow $t\bar{t}$ resonance, but to realize that the cuts may never be entirely “optimized.” The frequent aphorism has always been: “Cuts are neither ‘right’ nor ‘wrong’ – but they may only be ‘more optimal’ or ‘less optimal.’”

3.3 Jet Corrections

Before determining an event’s $t\bar{t}$ invariant mass ($M_{t\bar{t}}$) in an effort discover to evidence of a resonance in the $M_{t\bar{t}}$ spectrum, we first apply a detailed set of corrections to the jet energies in the event. These jet corrections account for the non-linear response of the calorimeter, non-instrumented regions of the detector, contributions from extra event activity, and a variety of other sources which affect jet energy measurements. In this analysis, jet corrections fall under two broad categories: flavor-independent corrections which are applied to all jets (with $E_T > 8$ GeV) and parton-specific corrections that are applicable to the four leading, or highest E_T , jets in an event which are assumed to result from $t\bar{t}$ decay in the lepton+jets channel.

3.3.1 Generic Jet Energy Corrections

The “generic,” or flavor-independent, jet energy corrections that are applied to all jets in $t\bar{t}$ candidate event account for both detector and reconstruction effects. These include corrections for:

- The relative energy scale

- The absolute energy scale
- Underlying event
- Out-of-cone effects

These corrections discussed in more detail below.

Relative Energy Scale Correction

To reduce any effects of η -dependent calorimeter response, we use a relative energy correction. This is derived from requiring the energy balancing in di-jet events collected in the data. This correction ensures that the different calorimeter regions are corrected relative to the central region, $0.2 < |\eta| < 0.7$. Due to degraded energy resolution and lower statistics, the uncertainty in the relative correction, which is parameterized as a function of η , is largest near cracks between detector modules.

Absolute Energy Scale Correction

The absolute energy scale is based on actual calorimeter response to incident pions and electrons from both data events and testbeam studies. An extensive detector simulation package was tuned to duplicate the observed calorimeter response to these particles. As a result of determining the Monte Carlo fragmentation parameters for simulated di-jet events which reproduce distributions of numerous event variables observed in the data, a direct mapping was established from which an incident particle's energy is deduced from the calorimeter response. In addition to the typical uncertainties from Monte Carlo studies, the uncertainty in the absolute energy scale correction is due to sources in the calorimeter response studies such as finite statistics and assumptions about the momentum spectrum at low-momentum.

Underlying Event Correction

This correction accounts for the effects of multiple $p\bar{p}$ interactions within the same event as well as the effects of any additional underlying events resulting from the primary interaction. Because the number of interactions per bunch crossing changed dramatically between Run 1a and Run 1b (see Section 2.2.4), this correction is different for the two cases. For events collected in Run 1a, subtraction of 0.72 GeV/c from jet P_T after applying the absolute correction is intended to account for the total effect. For Run 1b events, however, 0.297 GeV/c per interaction is subtracted from each raw jet P_T . After applying the absolute correction, we then subtract 0.65 GeV/c from the P_T of each jet to account for underlying events in Run 1b. An uncertainty of $\pm 30\%$ is assigned to the underlying event correction, which translates to less than approximately 0.5% for jets resulting from standard model $t\bar{t}$ decay.

Out-of-Cone Correction

As mentioned, jets in this analysis are defined by clustering calorimeter towers within a cone of $\Delta R = 0.4$. Derived from Monte Carlo simulations, the out-of-cone correction accounts for any jet energy falling outside $\Delta R = 0.4$ which is often due to the emission of low P_T final state gluons known as “soft gluon radiation.” The out-of-cone correction factor itself is a function of the jet P_T after the generic jet corrections have been applied. The uncertainty on the out-of-cone correction comes from investigating the amount of energy contained in $0.4 < \Delta R < 1.0$ for data and Monte Carlo $W+1$ jet events. This study indicates that our Monte Carlo simulation overestimates the amount of soft gluon radiation present in our data sample.

Figure 3.8 displays the fractional jet correction as a function of uncorrected jet

E_T for each of the flavor-independent corrections outlined above. However, the fractional jet correction factors shown in this figure do not represent the entire effect for all four corrections: in addition to a constant offset, the relative energy correction has an additional η -dependent component; the functional form of the underlying event correction in Figure 3.8 assumes singular vertex Run 1b events. Furthermore, the total uncertainty in the flavor-independent corrections described here also contains a small contribution due to the uncertainty in calorimeter stability over the course of Run 1.

3.3.2 $t\bar{t}$ Jet Energy Corrections

In addition to the generic jet corrections described above, the leading four jets in a $t\bar{t}$ candidate event are subject to parton-specific corrections which assume that they are the four decay products of a $t\bar{t}$ pair. These $t\bar{t}$ -specific corrections account for both:

- the difference between the flat P_T spectrum used to derive the absolute scale correction and the relatively hard P_T spectrum expected for jets from $t\bar{t}$ decay, and
- the energy losses attributable to neutrinos resulting from semileptonic b and c decays.

Using HERWIG Monte Carlo simulation for a top quark mass of $170 \text{ GeV}/c^2$, $t\bar{t}$ decays are simulated in the CDF detector and their reconstructed jets are subjected to only the flavor-independent jet corrections. Parton-specific corrections are determined from the fractional difference, Δ_{P_T} , between the P_T of the generated parton and that of the reconstructed jet to which it matches in $\eta - \phi$ within a cone of $\Delta R = 0.4$. The correction factor, as a function of the jet P_T , corrected

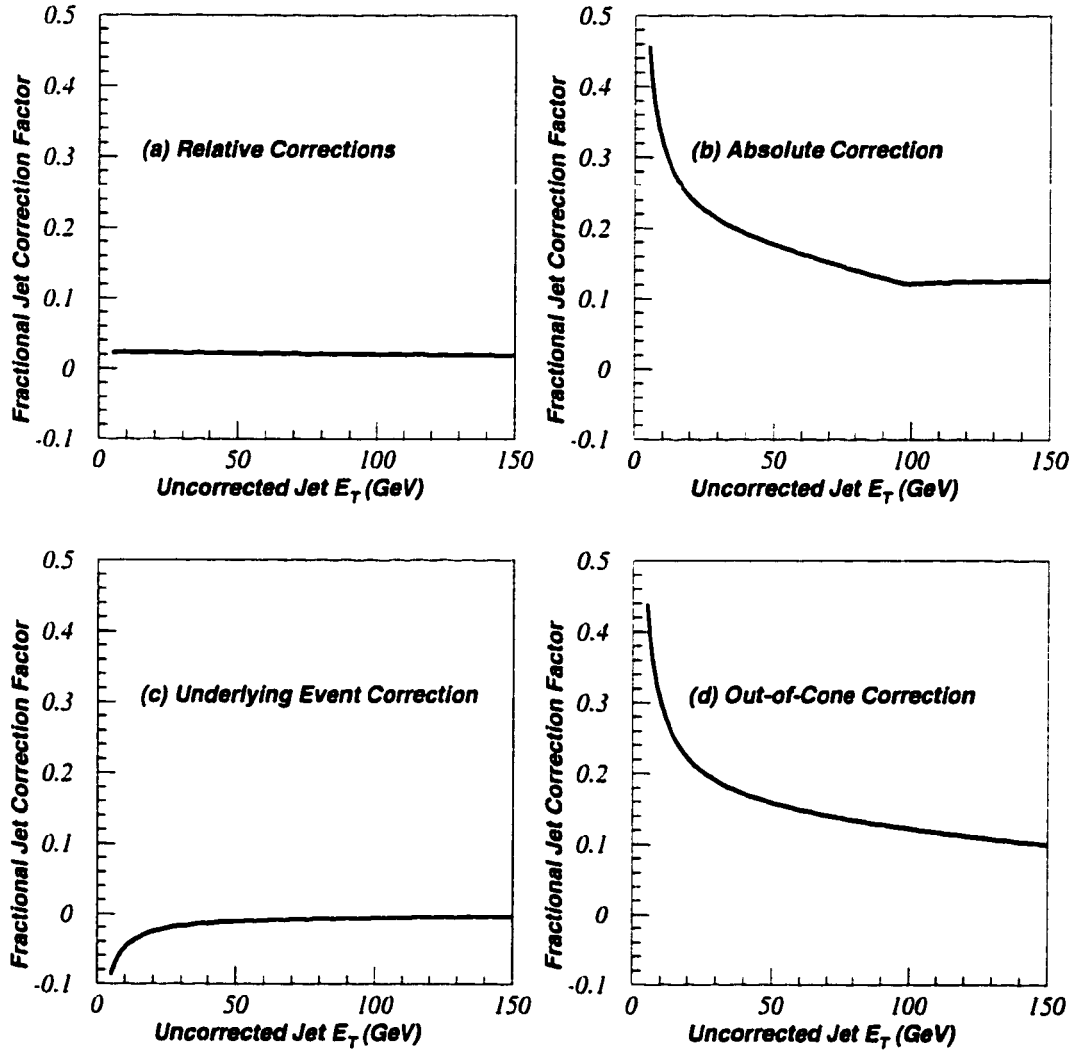


Figure 3.8: The fractional jet correction as a function of uncorrected jet E_T for each of the flavor-independent corrections: (a) relative energy scale, (b) absolute energy scale, (c) underlying event, and (d) out-of-cone. In addition to the constant offset shown in (a), the relative energy correction has an additional η -dependent component. The functional form of the underlying event correction shown in (b) is applicable to singular vertex Run 1b events. Underlying event corrections for events from Run 1a and multiple vertex Run 1b events are described in the text.

with the generic correction only, is given by the mean of Δ_{P_T} . Figure 3.9 shows the functional form of this correction factor for four types of $t\bar{t}$ event jets: (A) jets from hadronic W boson decay, (B) b -quark jets that are tagged only by the SVX, (C) b -quark jets that are tagged only by the presence of an SLT electron, and (D) b -quark jets that are tagged only by the presence of an SLT muon. As expected, SLT muon b -tagged jets are subject to the largest correction as a result of the fact that the muon deposits only minimum ionizing energy in the calorimetry in addition to the energy lost as a result of the undetected neutrino.

Both generic and parton-specific corrections are applied to the leading four jets in a $t\bar{t}$ candidate event. Like the correction factor itself, the jet E_T uncertainty, as a function of generically corrected jet P_T , is given by the RMS (root-mean-square) of Δ_{P_T} . Figure 3.10 shows the functional form of these uncertainties for the same four types of $t\bar{t}$ event jets shown in Figure 3.9. Additionally, the uncertainty in the corrected jet P_T for any extra jets in the event is included in Figure 3.10.

3.4 Measuring $M_{t\bar{t}}$

Here, we investigate three possible methods for measuring $M_{t\bar{t}}$ in $t\bar{t}$ candidate events. These techniques are known as the “6-body mass,” the “unconstrained,” and the “constrained” methods. Each method relies on the MINUIT mass fitting package (described below), although the 6-body mass method does so to a lesser degree. Unless otherwise noted, we establish the final selection criteria for a narrow $t\bar{t}$ resonance using Monte Carlo which models $Z' \rightarrow t\bar{t}$ decays with Z' mass $M_{Z'}$ and natural width $\Gamma = 0.012M_{Z'}$.

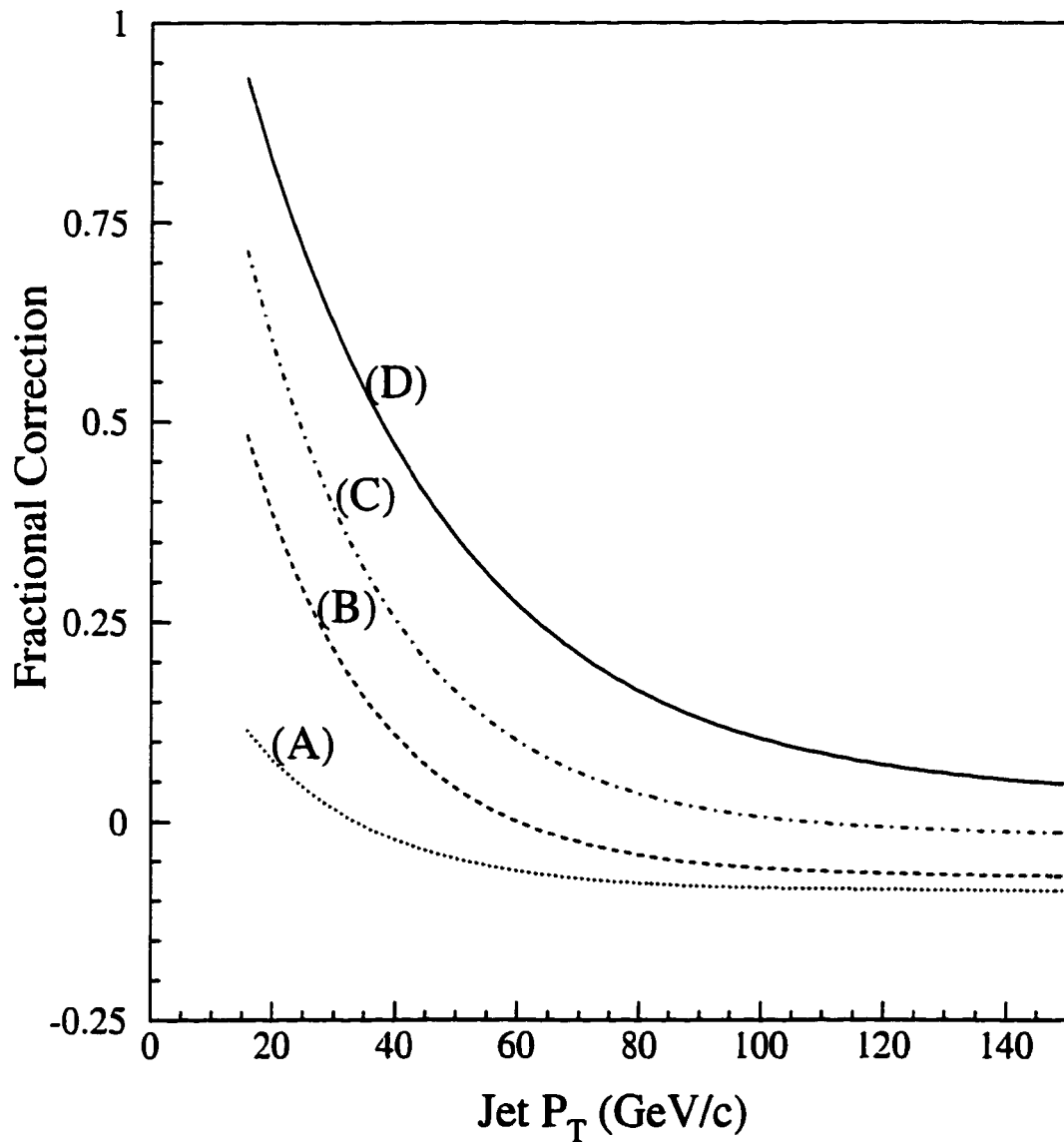


Figure 3.9: The parton-specific jet correction factor for (A) jets from hadronic W boson decay, (B) b -quark jets that are tagged only by the SVX, (C) b -quark jets that are tagged only by the presence of an SLT electron, and (D) b -quark jets that are tagged only by the presence of an SLT muon.

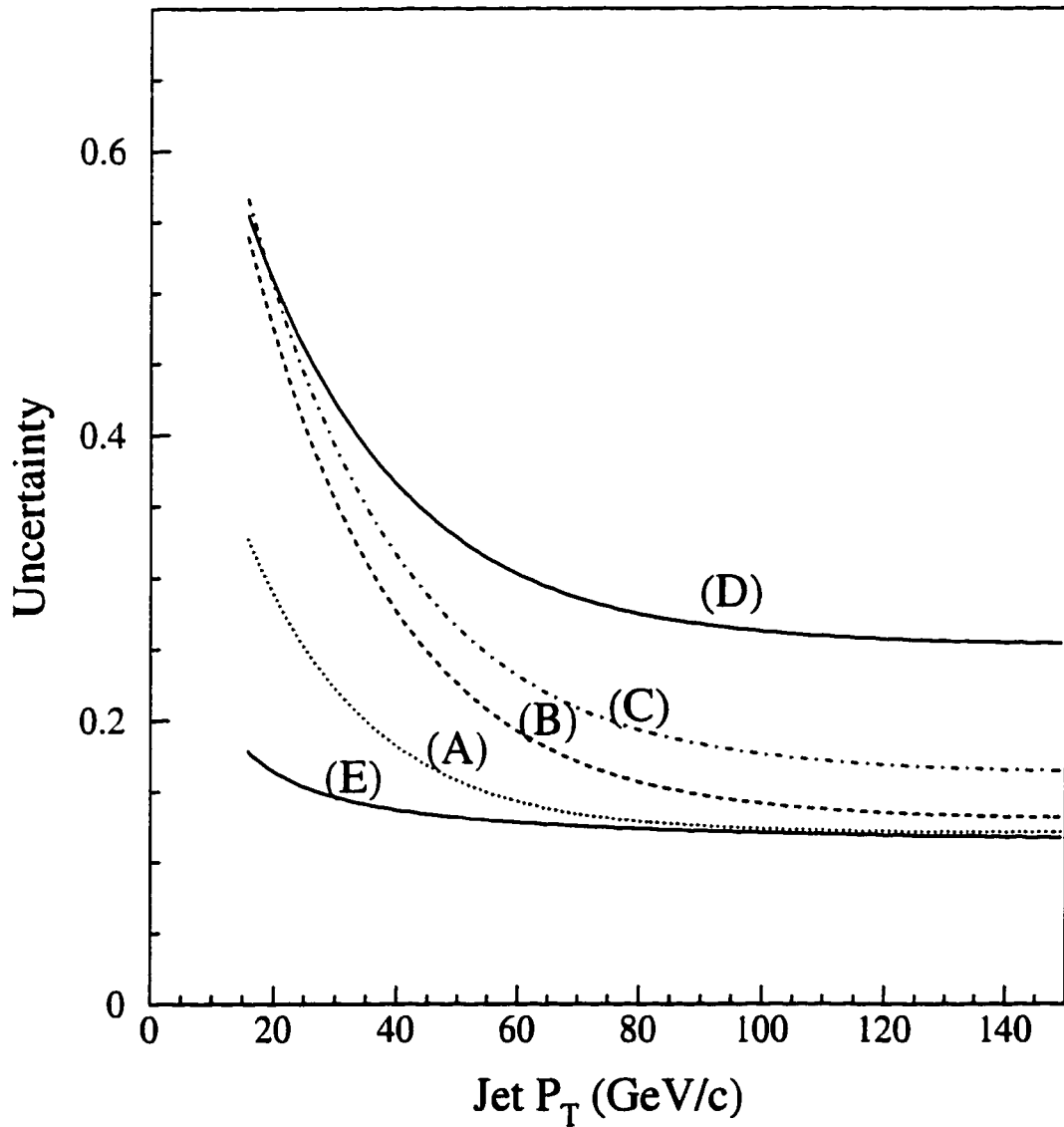
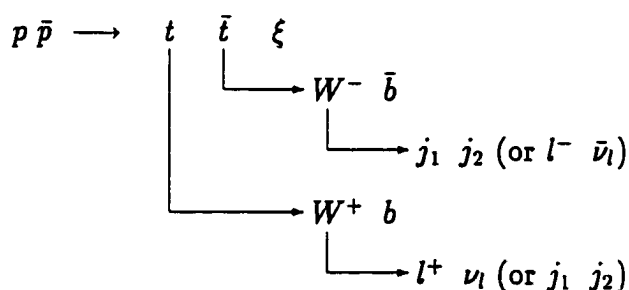


Figure 3.10: The uncertainty in corrected jet P_T for (A) jets from hadronic W boson decay, (B) b -quark jets that are tagged only by the SVX, (C) b -quark jets that are tagged only by the presence of an SLT electron, (D) b -quark jets that are tagged only by the presence of an SLT muon, and (E) any extra jets in the event.

3.4.1 Mass Fitter

The MINUIT mass fitting package was previously employed to measure the top quark mass in the “lepton + jets” channel as $175.9 \pm 4.8(\text{stat.}) \pm 5.3(\text{syst.})$ GeV/c² for Run 1[14]. We build upon this mass fitting expertise in order to measure $M_{t\bar{t}}$. In this fitting package, we assume the standard model $t\bar{t}$ lepton+jets decay chain for each event passing our primary event selection criteria (Section 3.1.5):



Imposing conservation of energy and momentum at each of the five vertices yields 20 equations of constraint. The 13 four-momenta (52 components) depicted above fully describe a $t\bar{t}$ event. Several assumptions result in reducing the number of unknown or unmeasured variables to 18:

- The $\bar{p}p$ system has a net momentum of zero and $\sqrt{s} = 1.8$ TeV. Assuming the mass of the p and \bar{p} to be $938 \text{ MeV}/c^2$ and that their three-momenta are entirely in the longitudinal direction yields 8 known variables.
- The top and anti-top quarks are required to have the same mass. This results in reducing the number of unknown components of the t and \bar{t} four-momenta by one.
- By measuring the total transverse energy in the event, we determine the E_T of ξ , the quantity representing the underlying event which recoils against the $t\bar{t}$ pair. This further reduces the number of unknown variables by two.

- The W 's are both required to have a mass of $80.4 \text{ GeV}/c^2$, yielding two more known variables.
- The three-momenta of the b , \bar{b} , j_1 , j_2 , and lepton are determined by direct measurement. Their masses are assumed as follows: the b -parton mass is set to $5 \text{ GeV}/c^2$, the hadronic W daughter mass is set to $0.5 \text{ GeV}/c^2$, and the lepton mass is assigned according to its identification as either an electron or muon. This further reduces the number of unknown variables by 20.
- Finally, the neutrino is presumed to be massless, adding one more known quantity.

The remaining 18 unknown variables are over-constrained by the 20 equations of constraint, allowing for complete event characterization determined through the minimization of a χ^2 which depends on measurement uncertainties. First, in order to reduce combinatorics, we use only the four highest E_T jets, leading to 12 possible ways to assign the labels “ b ”, “ \bar{b} ”, and “ j ” to these jets in a particular event. However, because we measure only the transverse component of the total energy (thereby determining \cancel{E}_T), there are two possible solutions for the longitudinal component of the neutrino momentum for each event. This ambiguity leads to 24 combinatoric possibilities per event. Tagging information, if available, will require that certain jets be used as b -jets, reducing the number of possible combinations. For each possible configuration, we use the MINUIT package to minimize the following χ^2 :

$$\chi^2 = \sum_{l,j} \frac{(\hat{E}_T - E_T)^2}{\sigma_{E_T}^2} + \sum_{i=x,y} \frac{(\hat{E}_i^U - E_i^U)^2}{\sigma_{E_i^U}^2}$$

$$\begin{aligned}
& + \frac{(M_{l\nu} - M_W)^2}{\sigma_{M_W}^2} + \frac{(M_{jj} - M_W)^2}{\sigma_{M_W}^2} \\
& + \frac{(M_{l\nu j} - M_{top})^2}{\sigma_{M_{top}}^2} + \frac{(M_{jjj} - M_{top})^2}{\sigma_{M_{top}}^2}
\end{aligned}$$

The first two sums in the χ^2 represent the uncertainty in pertinent detector measurements, while the remaining terms result from the application of kinematic constraints (within the uncertainty of the particular constraint). In each term, the “hatted” variables ($\hat{}$) represent the quantities which are varied during the minimization procedure. The “unhatted” quantities are fixed for each particular configuration and represent the values determined from detector measurements after the application of appropriate detector corrections. The first term is a sum over the transverse energies of the lepton and four jets; the second term is a sum over the transverse components of the unclustered energy in the event. The uncertainty in M_W is set by its natural width, 2.1 GeV/c² [6], and is labeled as σ_{M_W} , while the predicted natural width of the top quark sets $\sigma_{M_{top}}$ at 2.5 GeV/c².

We select the “best” of the 24 combinatoric possibilities as the one with the lowest χ^2 value and which satisfied all available b -tagging information.

3.4.2 6-Body Mass Method

The 6-body mass method, a relatively unsophisticated algorithm for evaluating $M_{t\bar{t}}$ for a given event, does not use the fitted four-momenta returned by the mass fitter. Instead, this method is simply a calculation of the invariant mass of the lepton, neutrino, and four jets ($M_{l\nu jjjj}$) using the unfitted four-momenta measured in the detector (the same four-momenta that are typically used as inputs to the mass fitting package). Initially, one might believe that the mass fitter described above is entirely unnecessary for determining the the 6-body $M_{t\bar{t}}$. However, in order to

determine $M_{l\nu jjj}$ from the input four-momenta, one of the 24 possible configurations must be selected because: 1) the longitudinal component of the neutrino momentum is not directly measured in the detector; 2) the input four-momenta for the four leading jets are dependent on jet corrections which are specific to their labelling as a b -, hadronic W -, or generic quark jet. We arbitrarily chose the configuration to be used in evaluating the 6-body $M_{t\bar{t}}$ by minimizing the above χ^2 expression with M_{top} fixed at 175 GeV/c² for each of the possible configurations. This procedure, known as constraining the top mass, improves the frequency of selecting the correct jet configuration from all of the combinatoric possibilities. Incidentally, the 6-body $M_{t\bar{t}}$ does not vary significantly for the different possible combinations within the same event. Regardless, our primary focus for establishing the 6-body $M_{t\bar{t}}$ method is solely pedagogical, as we hope to illustrate the improvement in resolving power which is possible with other techniques.

Displayed in Figure 3.11 is the 6-body $M_{t\bar{t}}$ spectrum for PYTHIA Z' events ($M_{Z'} = 600$ GeV/c², $\Gamma = 0.012M_{Z'}$). The “c” subscript on “ χ_c^2 ” denotes that this method uses the standard χ^2 expression with M_{top} constrained to 175 GeV/c². For this mass, the 6-body method tends to yield a wide distribution and a mean which is 3-4% low for all events passing our selection criteria and 1-2% low for events in which we have selected the correct jet configuration.

In this analysis, we determined the “correct” configuration by matching reconstructed jets to GENP generator-level b -quarks and hadronic W -daughters. A reconstructed jet is said to be matched to a generator-level quark if they differ by ΔR less than 0.4. We determined the correct combination as the one that matches all four reconstructed jets, if available, and results in the smallest possible ΔR for each.

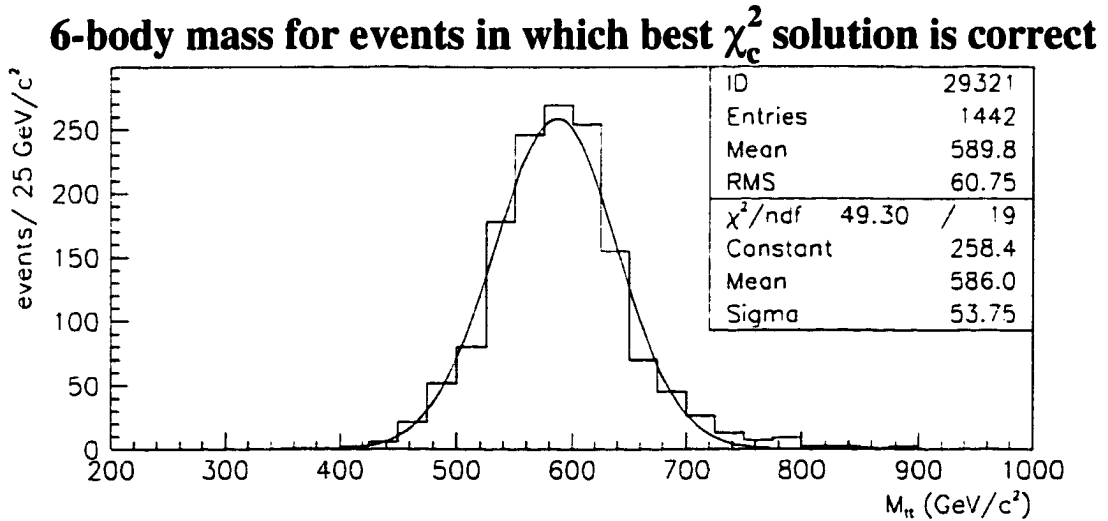
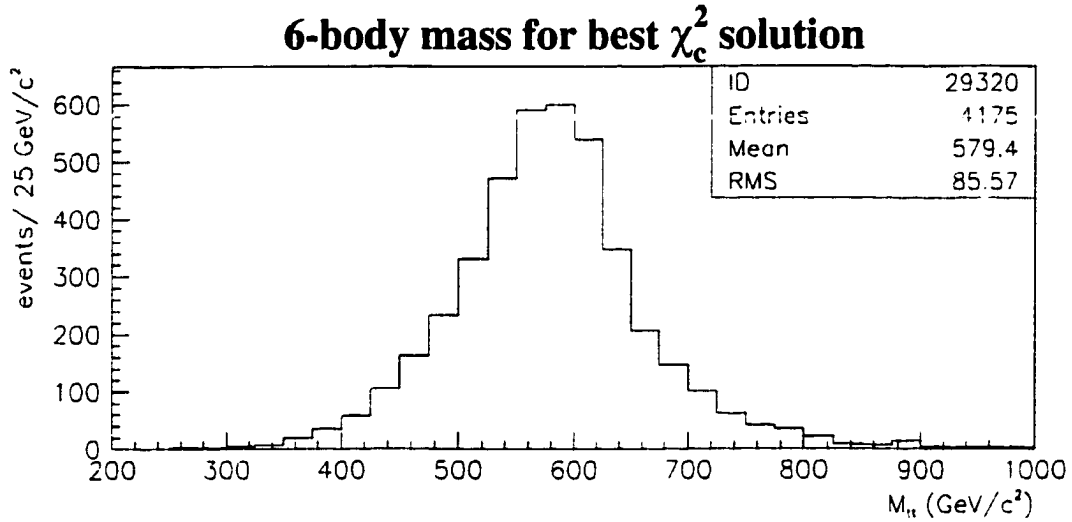


Figure 3.11: $M_{t\bar{t}}$ determined by the 6-body mass method for $M_{Z'} = 600 \text{ GeV}/c^2$ PYTHIA Monte Carlo. Top: 6-body $M_{t\bar{t}}$ for all events passing the selection criteria (“tagged” and “untagged” events). Bottom: The subset of events in which the “best” configuration has the four jets correctly identified.

3.4.3 Unconstrained Method

The unconstrained method for determining $M_{t\bar{t}}$ employs the mass fitting package with the value of M_{top} unrestricted. Using this method, we select the configuration which has the lowest χ^2 value (and, as always, satisfied all available tagging information). Then the unconstrained $M_{t\bar{t}}$ is determined by calculating $M_{l\nu jjjj}$ for this particular configuration using the fitted four-momenta returned by the mass fitter.

Figure 3.12 is the unconstrained $M_{t\bar{t}}$ spectrum for PYTHIA Z' events again for $M_{Z'} = 600 \text{ GeV}/c^2$ with $\Gamma = 0.012M_{Z'}$. The “u” subscript on “ χ_u^2 ” denotes that this method uses the standard χ^2 expression with M_{top} left unconstrained. Here, we observe that the unconstrained method also tends to yield a distribution whose mean is low. For events in which the unconstrained method selects the correct jet configuration, the width of the distribution is only marginally improved over the 6-body method.

3.4.4 Constrained Method

Determining $M_{t\bar{t}}$ with the constrained method also employs the mass fitting package but additionally has the value of M_{top} in the χ^2 expression constrained to $175 \text{ GeV}/c^2$, enforcing our knowledge of the top quark mass. As mentioned, this modification increases the likelihood that the configuration with the lowest χ^2 value has the correct identification for all four jets. The constrained $M_{t\bar{t}}$ is determined by calculating $M_{l\nu jjjj}$ for this particular configuration using the fitted four-momenta returned by the mass fitter.

Figure 3.13 is the constrained $M_{t\bar{t}}$ spectrum for PYTHIA Z' events with $M_{Z'} = 600 \text{ GeV}/c^2$, $\Gamma = 0.012M_{Z'}$. Although this spectrum for all events exhibits an unphysical excess at low values of $M_{t\bar{t}}$, we realize by comparison to the 6-body and

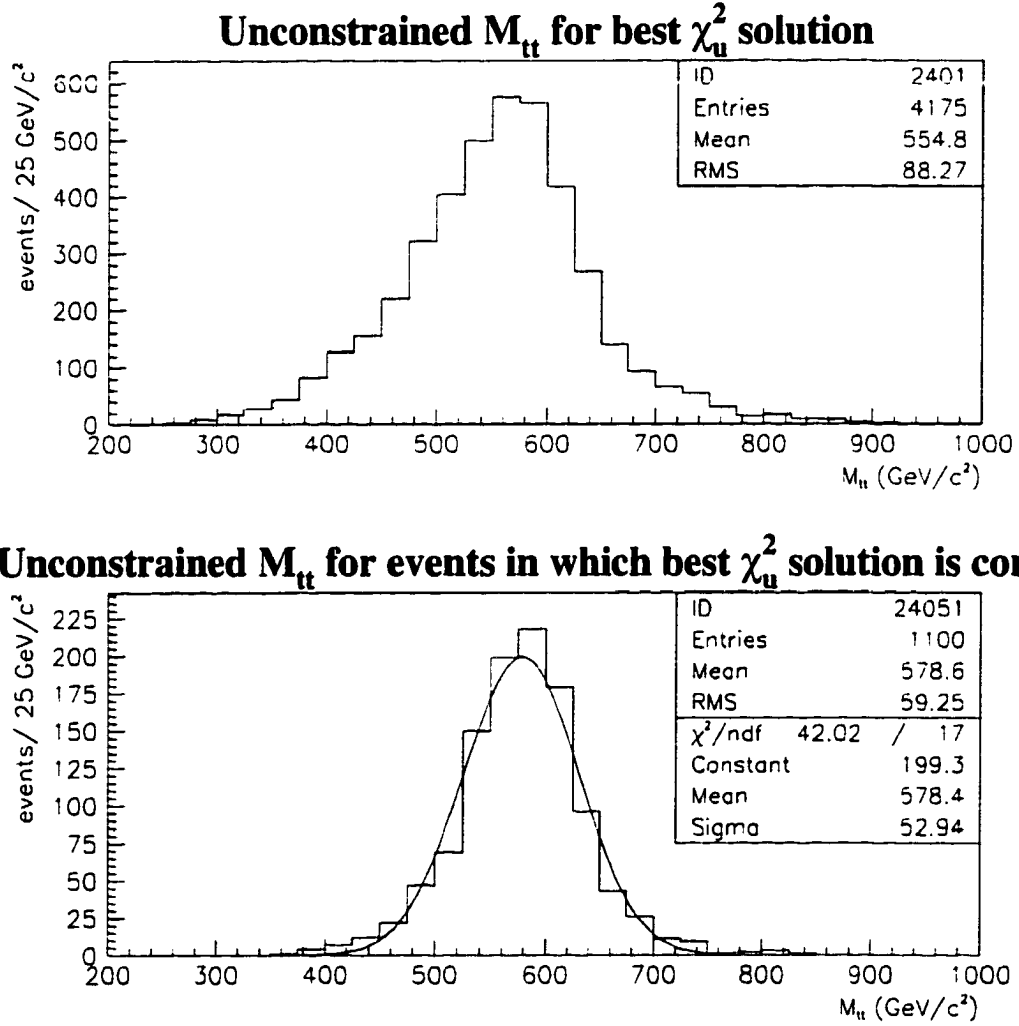


Figure 3.12: $M_{t\bar{t}}$ determined by the unconstrained method for $M_{Z'} = 600 \text{ GeV}/c^2$ PYTHIA Monte Carlo. Top: Unconstrained $M_{t\bar{t}}$ for all events passing the selection selection criteria (“tagged” and “untagged” events). Bottom: The subset of events in which the “best” configuration has the four jets correctly identified.

unconstrained $M_{t\bar{t}}$ distributions that this is simply an artifact of constraining M_{top} . Most importantly, it is clear that for events in which the constrained method selects a configuration with the correct jet identification, the mean of the distribution is as we expect and the resolution is superior to the previously mentioned techniques.

Because of its resolving power at all pertinent Z' masses, we choose the constrained method for determining $M_{t\bar{t}}$. However, in anticipation of performing a shape-fitting analysis, we hope to eliminate the unphysical excess at the low end of the constrained $M_{t\bar{t}}$ spectrum because this region is expected to also include a heavy concentration of events from standard model $t\bar{t}$ and QCD W +jets background.

3.5 $t\bar{t}$ Resonance Selection Criteria

3.5.1 Effect of Wrong Combinations on $M_{t\bar{t}}$

As evidenced by Figure 3.13, eliminating the unphysical excess of signal events at low values of constrained $M_{t\bar{t}}$ requires that we increase the purity of correct jet configurations in the signal sample. To this end, we look specifically at those events in which we have selected an incorrect jet configuration.

Focusing our attention on signal Monte Carlo with $M_{Z'} = 600 \text{ GeV}/c^2$, Figure 3.14 is the $M_{t\bar{t}}$ spectrum for the difference between the two distributions in Figure 3.13. Figure 3.14 further divides the incorrect combinations into three categories:

- Events with the wrong four jets. For these events, none of the 24 combinations represent the correct jet configuration because at least one of the leading four jets is not a b , \bar{b} , or hadronic W -jet resulting from $t\bar{t}$ decay.
- The “best” combination has at least one b -jet swapped for a hadronic W -jet relative to the correct jet configuration.

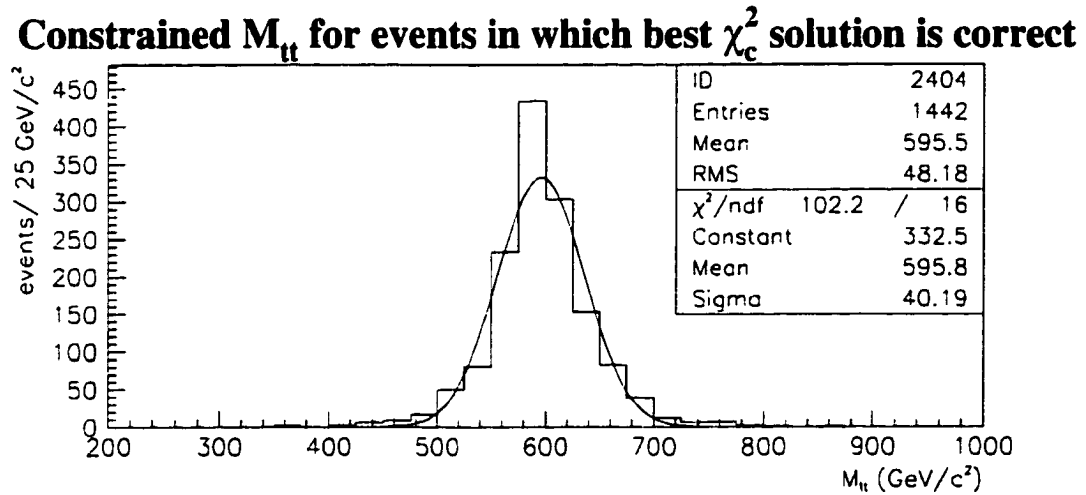
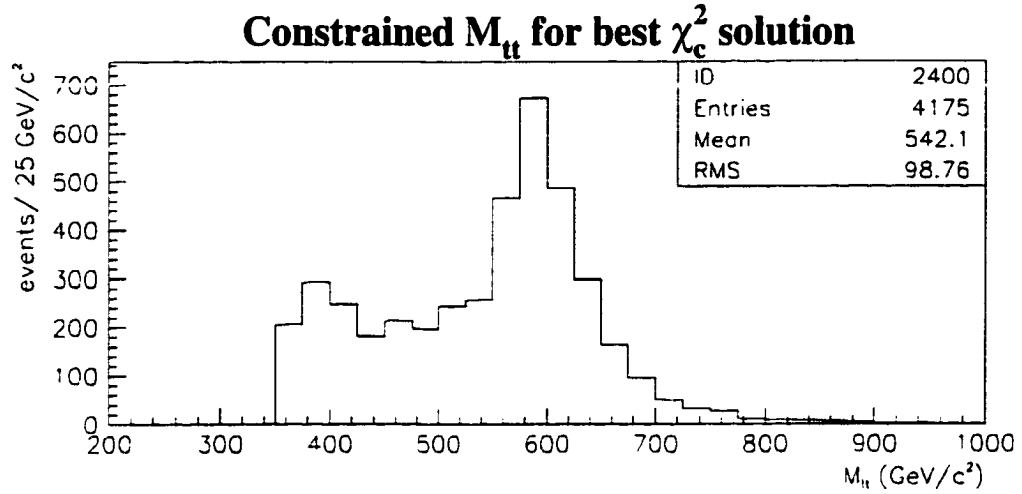


Figure 3.13: $M_{t\bar{t}}$ determined by the constrained method for $M_{Z'} = 600 \text{ GeV}/c^2$ PYTHIA Monte Carlo. Top: Constrained $M_{t\bar{t}}$ for all events passing the selection selection criteria (“tagged” and “untagged” events). Bottom: The subset of events in which the “best” configuration has the four jets correctly identified.

- The “best” combination has the b - and \bar{b} -jets swapped for one another relative to the correct jet configuration.

In hopes of understanding the anomalous structure at low $M_{t\bar{t}}$, we first focus on the curious bimodal distribution for events with at least one b -jet incorrectly exchanged with a hadronic W -jet. Figure 3.15 investigates only this distribution and further divides the shape into three subcategories:

- The “best” combination has the hadronic b -jet exchanged for a hadronic W -jet relative to the correct jet configuration; *i.e.*, the jet swapping occurs *within* the hadronic top quark.
- The “best” combination has the leptonic b -jet exchanged for a hadronic W -jet relative to the correct jet configuration; *i.e.*, the jet swapping occurs *between* the hadronic and the leptonic top quarks.
- Both the b - and \bar{b} -jets are misidentified and at least one of the b -jets is exchanged with a hadronic W -jet relative to the correct jet configuration.

Apparently, when an incorrect combination is selected for a particular event, but the correct jet configuration can be obtained by exchanging a W -jet for the hadronic b -jet, the value for $M_{t\bar{t}}$ tends to be consistent with the nominal Z' mass. However, if the correct jet configuration differs from that of the selected configuration by the exchange of a W -jet with the leptonic b -jet, then we will likely calculate an $M_{t\bar{t}}$ which is considerably lower than the expected $M_{Z'}$. This effect is undoubtedly an artifact of constraining M_{top} . As a possible explanation for this effect, suppose that a $t\bar{t}$ decay is represented by the following schematic drawing in the transverse plane:

Constrained $M_{t\bar{t}}$ for events in which best χ_c^2 solution is incorrect

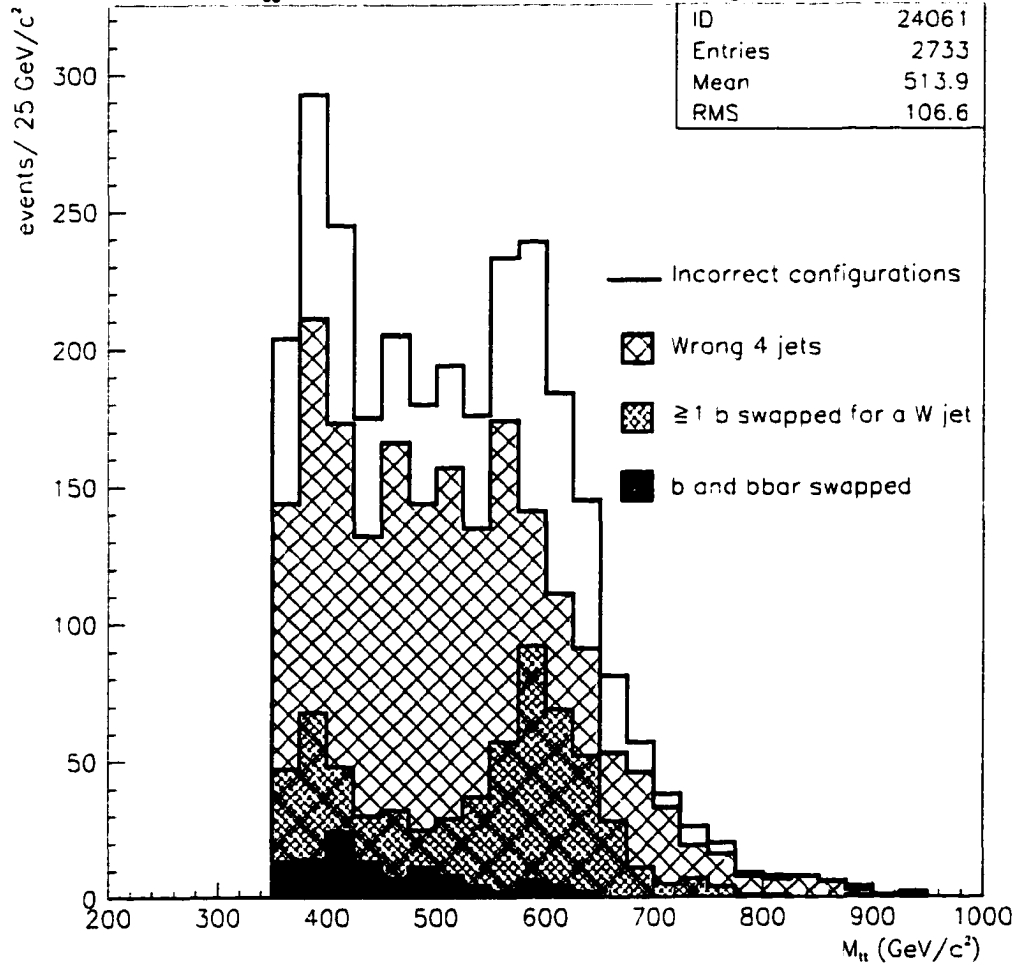


Figure 3.14: Constrained $M_{t\bar{t}}$ for those $M_{Z'} = 600$ GeV/c² PYTHIA Monte Carlo events (“tagged” and “untagged”) in which the constrained method selects a jet configuration which is incorrect.

Constrained M_{tt} for events in which ≥ 1 b is swapped for a W jet

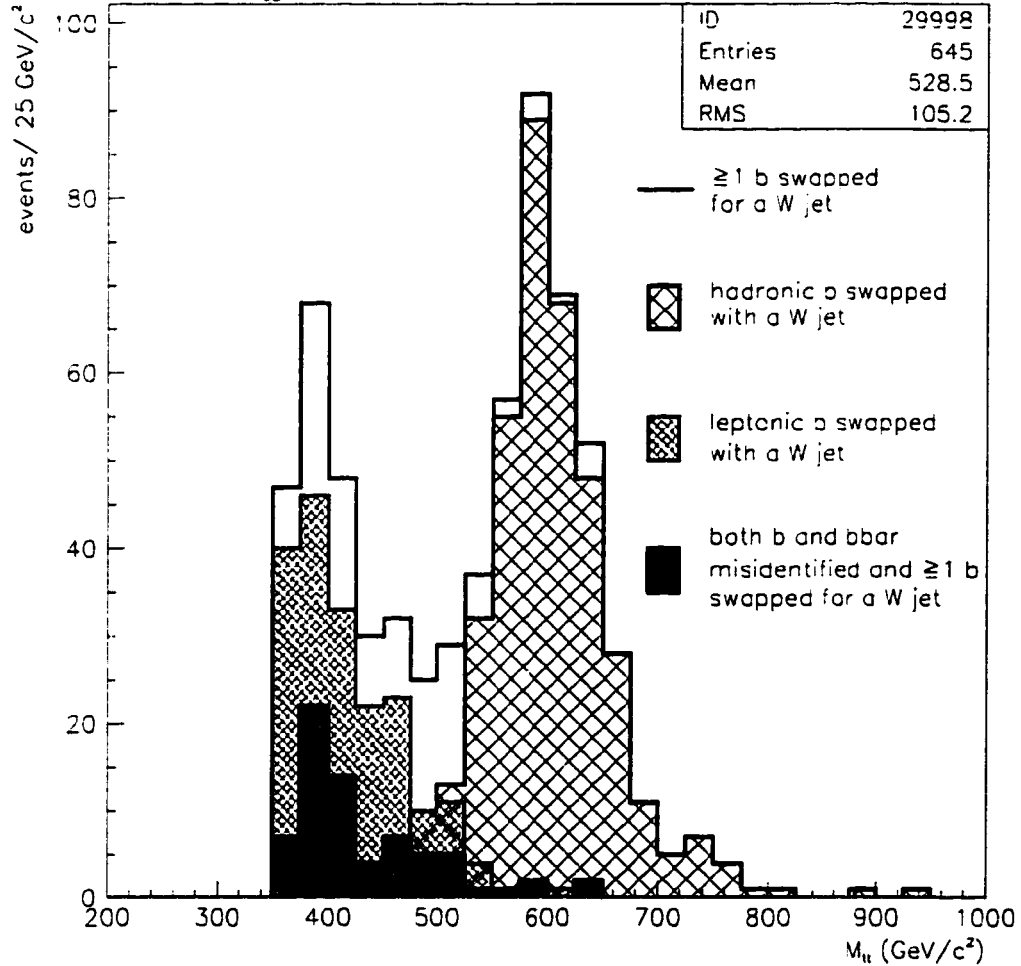
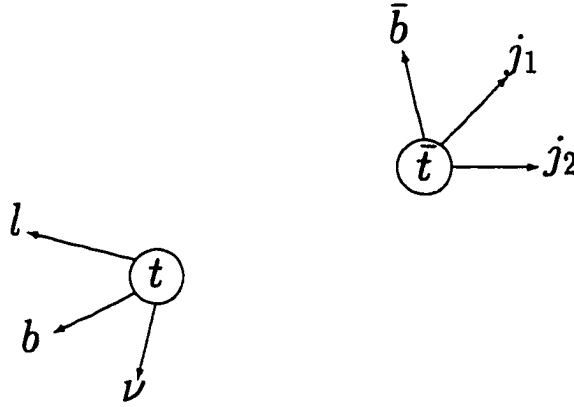


Figure 3.15: Constrained $M_{t\bar{t}}$ for those $M_{Z'} = 600$ GeV/c^2 PYTHIA Monte Carlo events (“tagged” and “untagged”) in which the constrained method selects a jet configuration which has at least one b -jet incorrectly exchanged with a hadronic W -jet.



Further suppose that the constrained $M_{t\bar{t}}$ method determines the “best” configuration to be one in which the b - and j_1 -jets are exchanged relative to the correct jet configuration. In this case, the \bar{t} would be erroneously thought to decay to the b -, \bar{b} -, and j_2 -jets. Likewise, the t would be thought to decay to the lepton, neutrino and j_1 -jet. Considering first the input four-momenta for these six particles and referring to the above diagram, the invariant masses of what are thought to be the leptonic top ($M_{l\nu j}$) and the hadronic anti-top (M_{jjj}) would tend to be higher than $M_{l\nu j}$ and M_{jjj} for the correct jet configuration. Additionally, the transverse momentum of what are thought to be the two top quarks ($P_T^{l\nu j}$ and P_T^{jjj}) would be determined to be lower, on average, than if the correct jet configuration had been selected. However, given that M_{top} is constrained in the χ^2 minimization process, the six daughters’ fitted four-momenta will tend to be pulled such that $M_{l\nu j}$ and M_{jjj} agree with M_{top} for this incorrect “best” configuration. The result is that the constrained $M_{t\bar{t}}$ method, for this particular event and configuration, returns fitted four-momenta which yield $M_{l\nu j}$ and M_{jjj} values very close to $175 \text{ GeV}/c^2$, while $P_T^{l\nu j}$ and P_T^{jjj} are lower on average than the correct jet configuration would yield. It is then apparent that, in this scenario, the calculated value of $M_{l\nu jjjj}$ would tend to be considerably lower than $M_{Z'}$.

On the other hand, suppose that for the diagram above, the constrained $M_{t\bar{t}}$ method determined the “best” configuration to be one in which the \bar{b} - and j_1 -jets are exchanged. In this case, we expect that M_{jjj} and P_T^{jjj} calculated with input four-momenta for the incorrect configuration will be unchanged (aside from b -specific jet corrections) if we instead used the correct jet configuration. Thus, when the selected configuration differs from the correct configuration by the exchange of the hadronic b -jet with a W -jet, the effect on $M_{t\bar{t}}$ is anticipated to be minimal.

Having developed an understanding of the $M_{t\bar{t}}$ spectrum shown in Figure 3.15, we hope to use a similar rationale to establish a plausibility argument for the structure of the $M_{t\bar{t}}$ distribution in Figure 3.14 for events in which the leading four jets are not the correct set of jets. For a particular event, suppose that three of the four jets resulting from $t\bar{t}$ decay pass our jet requirements. Furthermore, suppose that the fourth jet in the decay either goes undetected or has an E_T less than that of an extra jet in the event which happens to pass our jet requirements. Then for this event, it is not possible to calculate $M_{t\bar{t}}$ with the correct jet configuration because one of the four jets comes from an additional source such as radiative processes or an underlying event. Again referring to the schematic diagram above for a generic $t\bar{t}$ decay, suppose that one of the true $t\bar{t}$ decay jets is replaced by an extra jet in the event. Because the extra jet comes from a source other than $t\bar{t}$ decay, its direction will be more isotropically distributed (relative to the top quark direction) than will the lost $t\bar{t}$ jet which has been replaced. Moreover, in events such as this, it is interesting to note that, as shown in Figure 3.16, the transverse momentum of the extra jet tends to be comparable to that of the lost jet. In Figure 3.16, we note that the disparity between the upper and lower distributions in the first several bins is simply due to the jet E_T requirement listed in the primary event selection.

It now seems plausible to explain the “wrong 4 jets” distribution in Figure 3.14

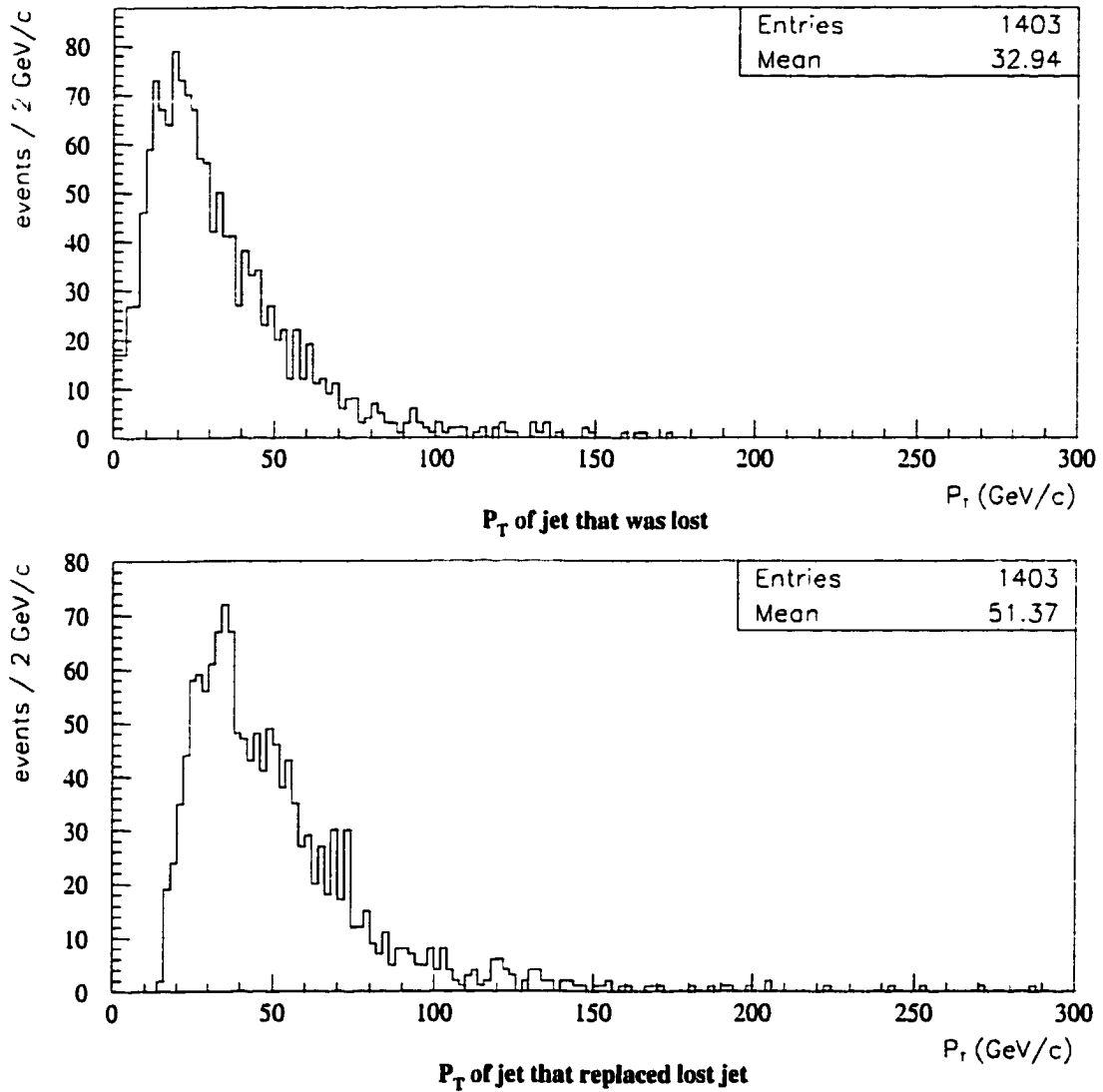


Figure 3.16: PYTHIA $M_{Z'} = 600 \text{ GeV}/c^2$ Monte Carlo events (“tagged” and “un-tagged”) in which one of the four leading jets is not the direct result of $t\bar{t}$ decay. Top: Generator level transverse momentum (P_T) of the jet resulting from $t\bar{t}$ decay which was not included the leading four jets. Bottom: Reconstructed P_T of the extra jet which replaced the lost $t\bar{t}$ jet.

with an argument similar to that used for Figure 3.15. Considering only input four-momenta, we expect that for those events in which the extra jet is comparable in P_T and tends to be in a direction different than that of the lost $t\bar{t}$ jet, the invariant mass of the incorrect three-body system will tend to exceed the true invariant mass of that top. Likewise, the P_T for what is erroneously believed to be a top quark will be calculated too low relative to the same determination using the correct configuration. Again, constraining M_{top} forces this three-body system to have a mass very close to $175 \text{ GeV}/c^2$ but has little effect on correcting its low P_T . The result is an event in which both three-body systems have a mass near $175 \text{ GeV}/c^2$, but the $M_{l\nu jjj}$ of the event is lower than the given $M_{Z'}$ due to underestimating the momentum of one of the top quarks.

3.5.2 $M_{3\text{-body}}$ Cut

If the previous hypotheses are correct, events located in the anomalous low $M_{t\bar{t}}$ excess in Figure 3.13's upper distribution will tend to favor higher values for M_{jjj} and $M_{l\nu j}$ when they are determined using the input four-momenta. By this argument, if the constrained $M_{t\bar{t}}$ method selects an incorrect configuration which results in a low $M_{t\bar{t}}$ value, then the unconstrained method *for that same incorrect configuration* will then favor higher returned values for the invariant mass of the two three-body systems. For the configuration selected by the constrained method, we call the returned unconstrained invariant mass of these two three-body systems " M_{jjj}^u " and " $M_{l\nu j}^u$ " to avoid ambiguity. Figure 3.17 shows the dependence of M_{jjj}^u and $M_{l\nu j}^u$ on $M_{t\bar{t}}$ determined by the constrained method for $M_{Z'} = 600 \text{ GeV}/c^2$ events in which an incorrect jet configuration is erroneously chosen.

As we expect, we observe that events with a low $M_{t\bar{t}}$ tended to favor higher M_{jjj}^u and $M_{l\nu j}^u$ values. Additionally, events with a higher $M_{t\bar{t}}$ seem to frequently

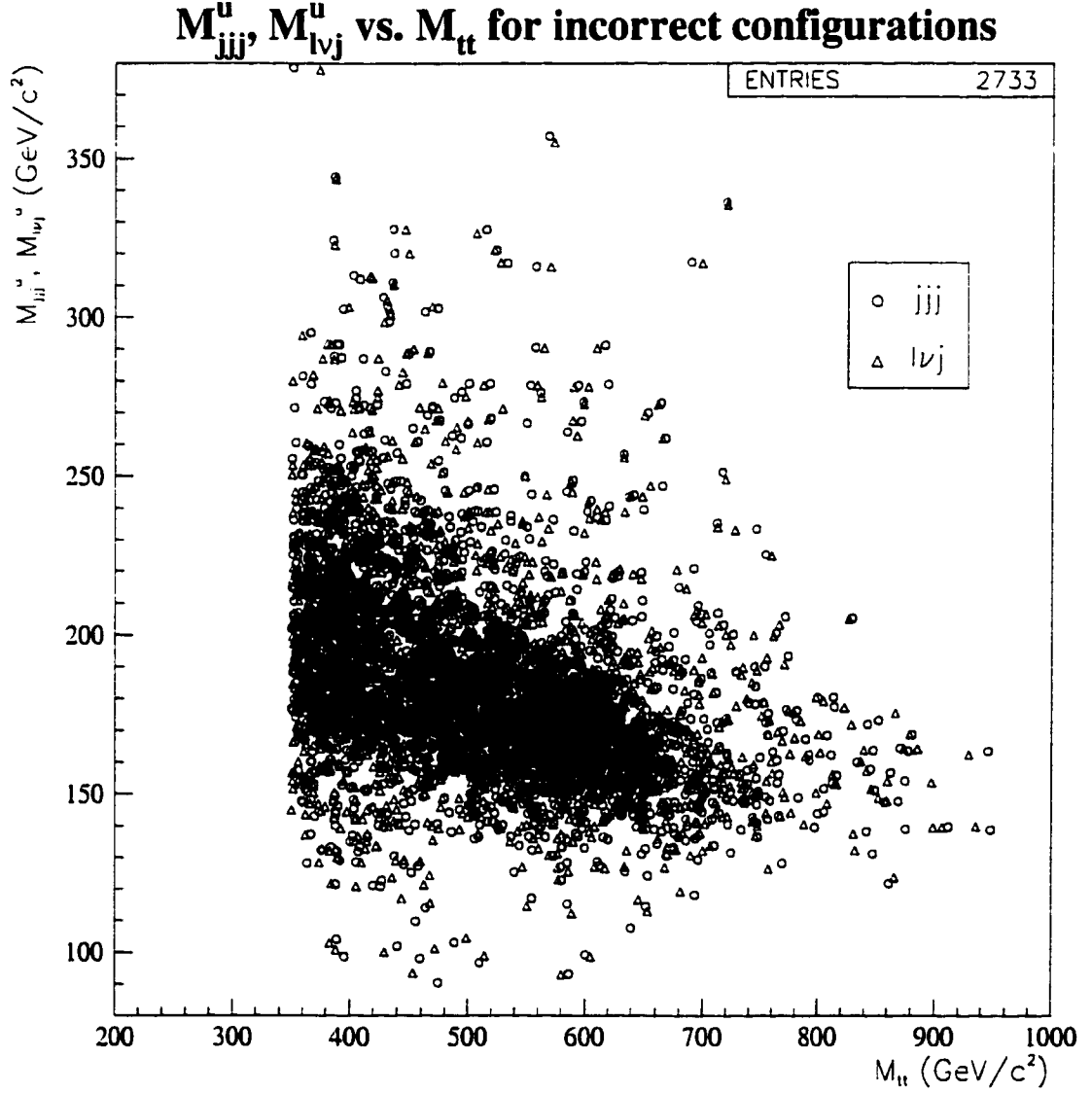


Figure 3.17: PYTHIA $M_{Z'} = 600 \text{ GeV/c}^2$ Monte Carlo events (“tagged” and “un-tagged”) in which the constrained $M_{t\bar{t}}$ method selects an incorrect jet configuration. The abscissa represents the constrained $M_{t\bar{t}}$ for a given event. M_{jjj}^u and $M_{l\nu j}^u$ are the three-body invariant masses returned by the unconstrained method using the configuration selected by the constrained method.

result in lower values of M_{jjj}^u and $M_{l\nu j}^u$. Therefore, in order to reduce excesses of signal events in the $M_{t\bar{t}}$ spectrum which fall outside of the expected signal region, we propose the additional requirement that all events have both M_{jjj}^u and $M_{l\nu j}^u$ within a certain mass range. To determine an appropriate mass window, Figure 3.18 shows the M_{jjj}^u and $M_{l\nu j}^u$ distribution for both incorrect and correct configurations, while we note that the latter results in an appropriate $M_{t\bar{t}}$ shape (see Figure 3.13).

It appears that a reasonable restriction on M_{jjj}^u and $M_{l\nu j}^u$ (collectively named “ M_{3-body} ”) is that they fall in the range of 150 GeV/c² to 200 GeV/c². Figure 3.19 displays the same M_{jjj}^u and $M_{l\nu j}^u$ distribution for $M_{Z'} = 400$ GeV/c², indicating that this M_{3-body} cut is sensible for a variety of Z' masses. Figures 3.20 through 3.23 detail the effect of the M_{3-body} cut on the constrained $M_{t\bar{t}}$ spectrum for $M_{Z'} = 400, 500, 600,$ and 700 GeV/c², respectively.

3.5.3 χ^2 Cut

We now consider imposing a maximum allowable value of the fitted χ_c^2 value. Such a χ^2 cut would reduce statistics in our data sample and, therefore, it was decided that it would be imposed only if it could be shown to increase our potential for discovering a $t\bar{t}$ resonance. To this end, we performed detailed counting experiments for PYTHIA Z' , HERWIG standard model $t\bar{t}$, and VECBOS W +jets Monte Carlo.

Monte Carlo Scale Factors

For each of the background and signal sources, we calculate $M_{t\bar{t}}$ for each event as described previously, requiring M_{3-body} to fall in the range of 150 to 200 GeV/c². For each sample, the number of events falling within a particular $M_{t\bar{t}}$ window for a certain χ^2 cut is determined. However, because these Monte Carlo samples

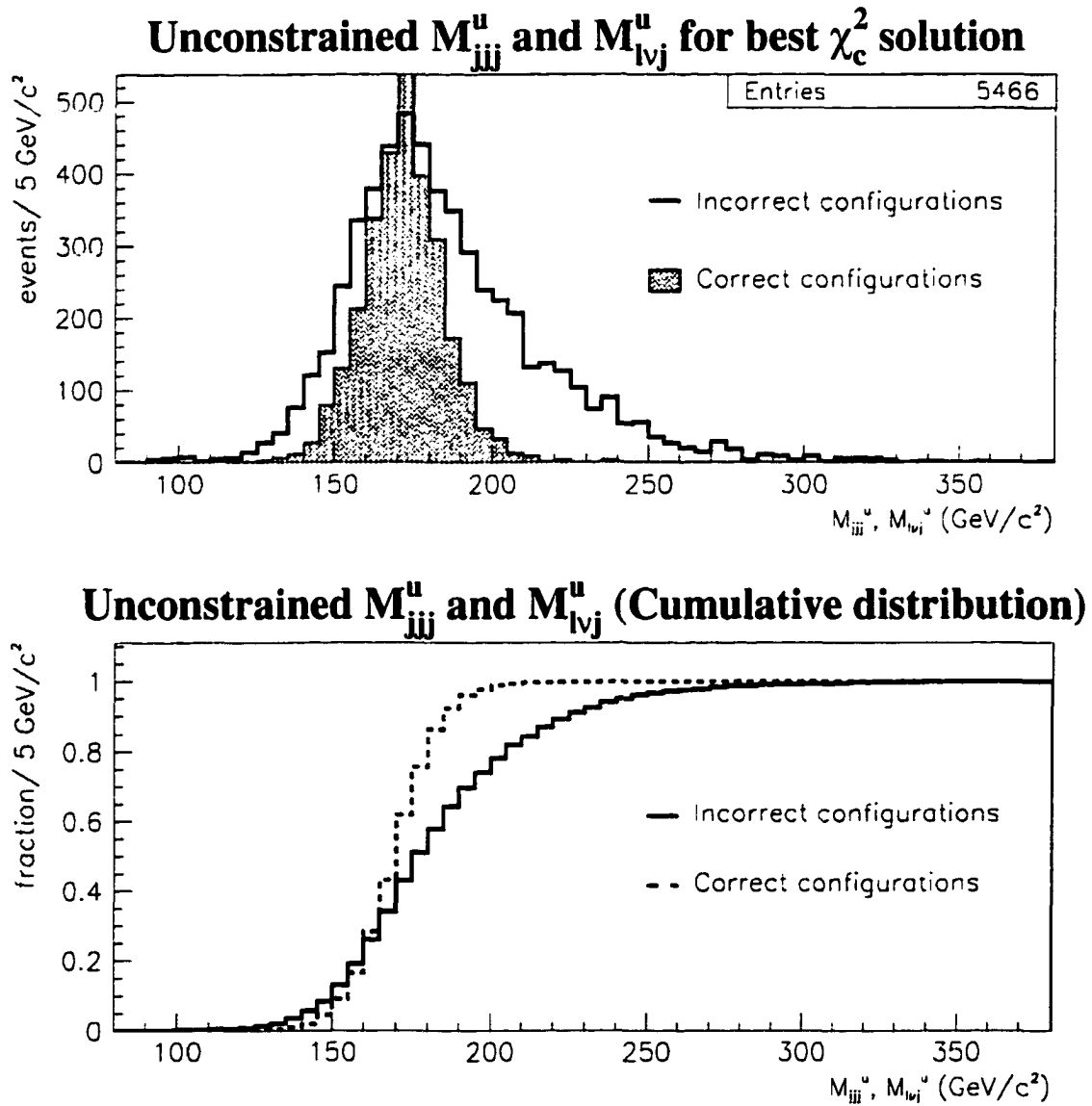


Figure 3.18: Distribution of M_{jjj}^u and M_{lvj}^u for PYTHIA $M_{Z'} = 600 \text{ GeV}/c^2$ Monte Carlo events (“tagged” and “untagged”).

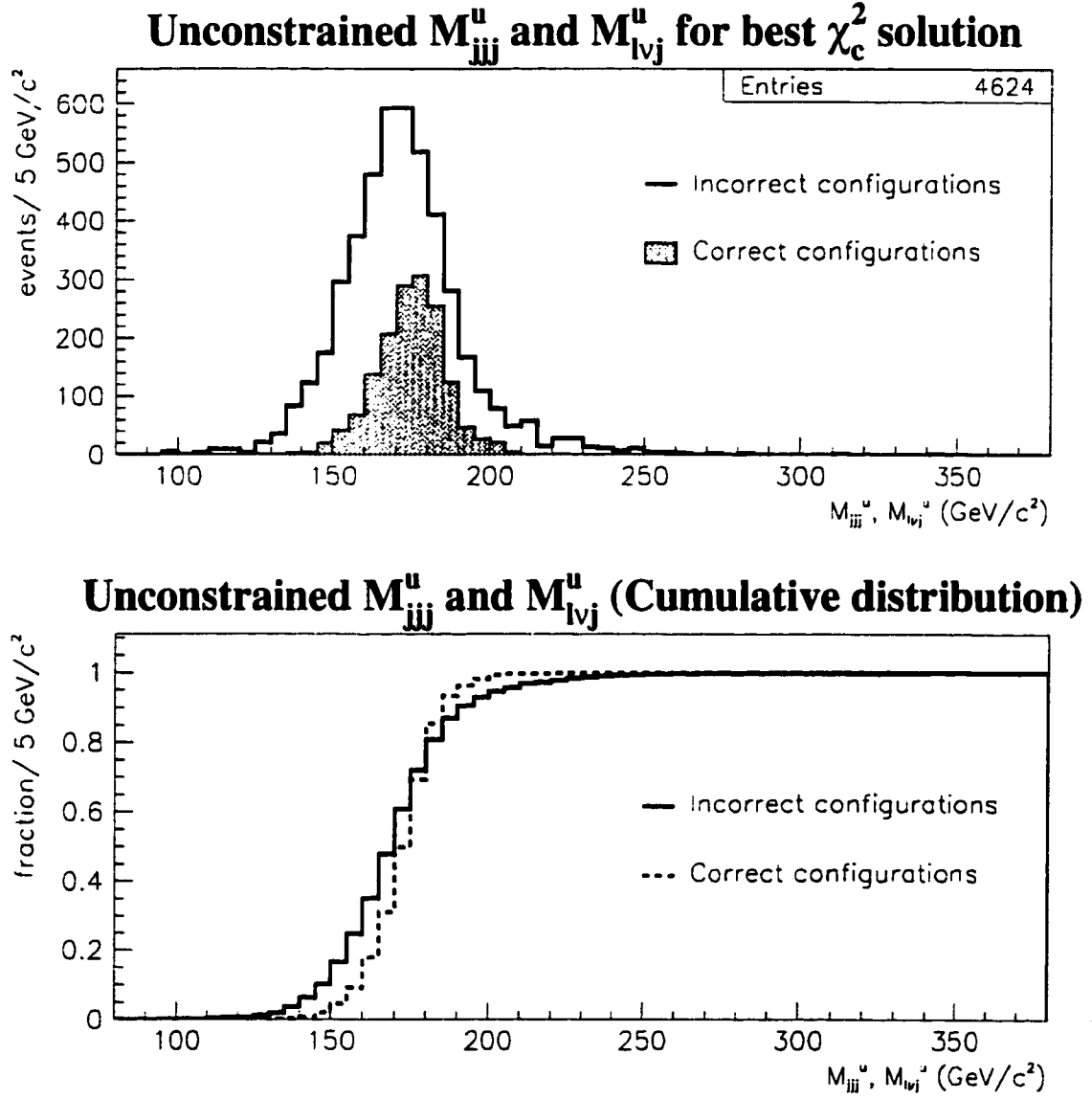


Figure 3.19: Distribution of M_{jjj}^u and M_{lvj}^u for PYTHIA $M_{Z'} = 400$ GeV/c² Monte Carlo events (“tagged” and “untagged”).

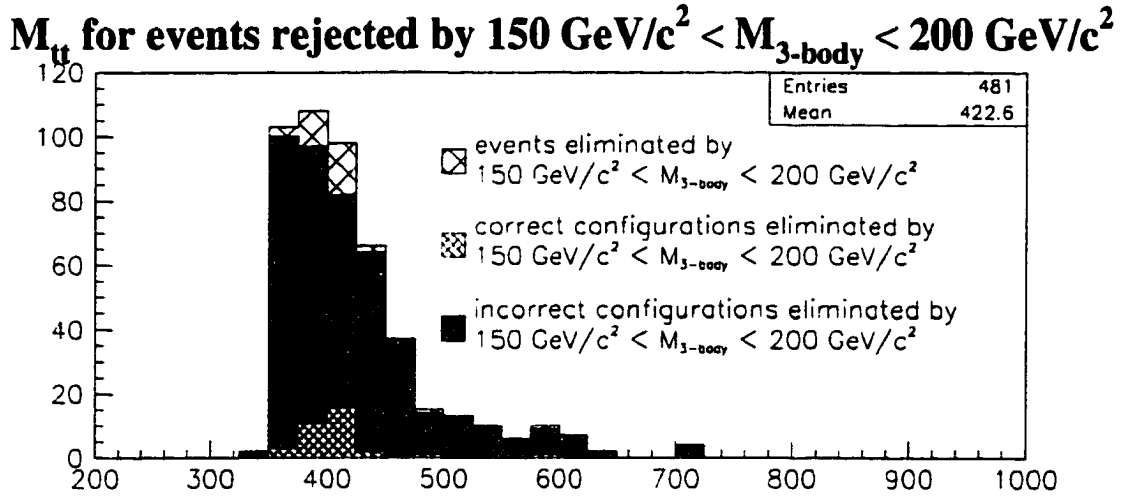
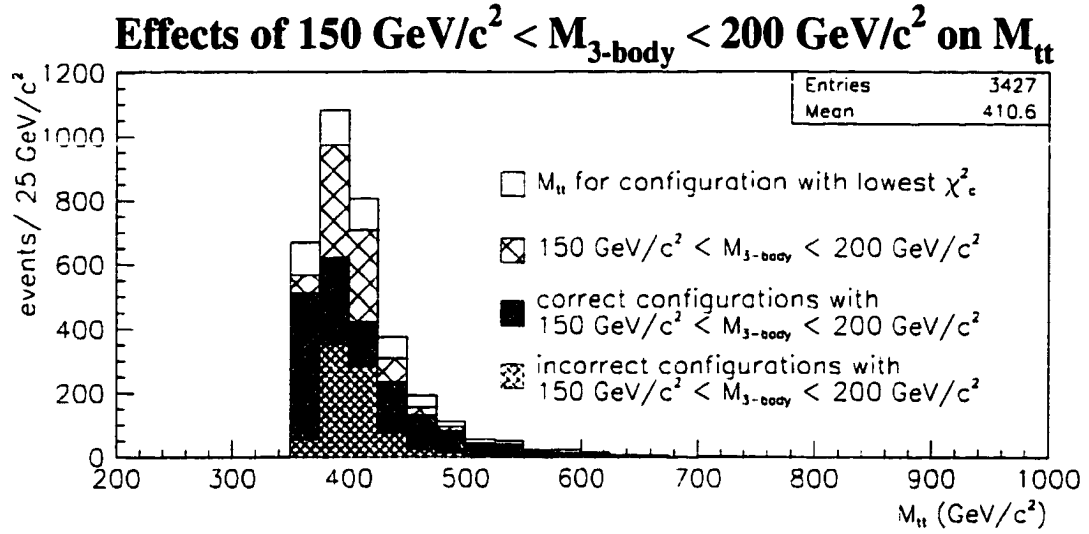


Figure 3.20: $M_{t\bar{t}}$ determined by the constrained method for $M_{Z'} = 400 \text{ GeV}/c^2$ PYTHIA Monte Carlo (“tagged” and “untagged” events). Top: Effects of $150 \text{ GeV}/c^2 < M_{3\text{-body}} < 200 \text{ GeV}/c^2$ on all events passing the selection criteria. Also, $M_{t\bar{t}}$ for events with correct and incorrect jet configuration which pass the $M_{3\text{-body}}$ cut. Bottom: Events eliminated by the $M_{3\text{-body}}$ cut.

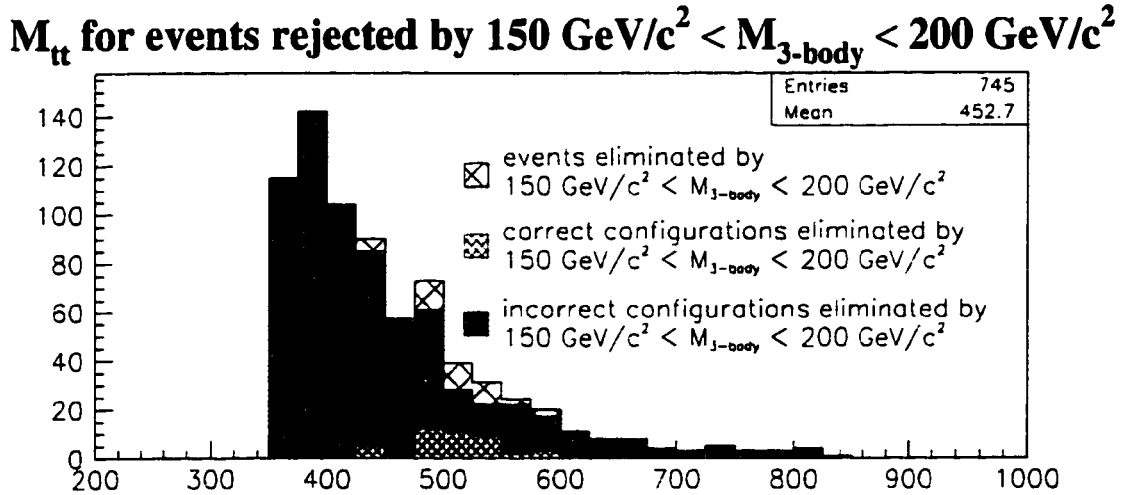
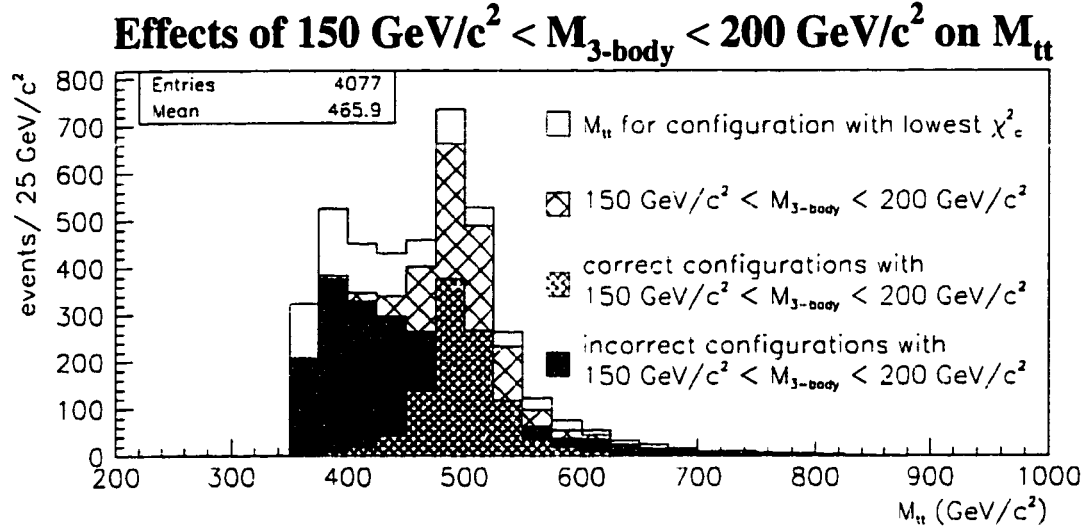


Figure 3.21: $M_{t\bar{t}}$ determined by the constrained method for $M_{Z'} = 500 \text{ GeV}/c^2$ PYTHIA Monte Carlo (“tagged” and “untagged” events). Top: Effects of $150 \text{ GeV}/c^2 < M_{3\text{-body}} < 200 \text{ GeV}/c^2$ on all events passing the selection criteria. Also, $M_{t\bar{t}}$ for events with correct and incorrect jet configuration which pass the $M_{3\text{-body}}$ cut. Bottom: Events eliminated by the $M_{3\text{-body}}$ cut.

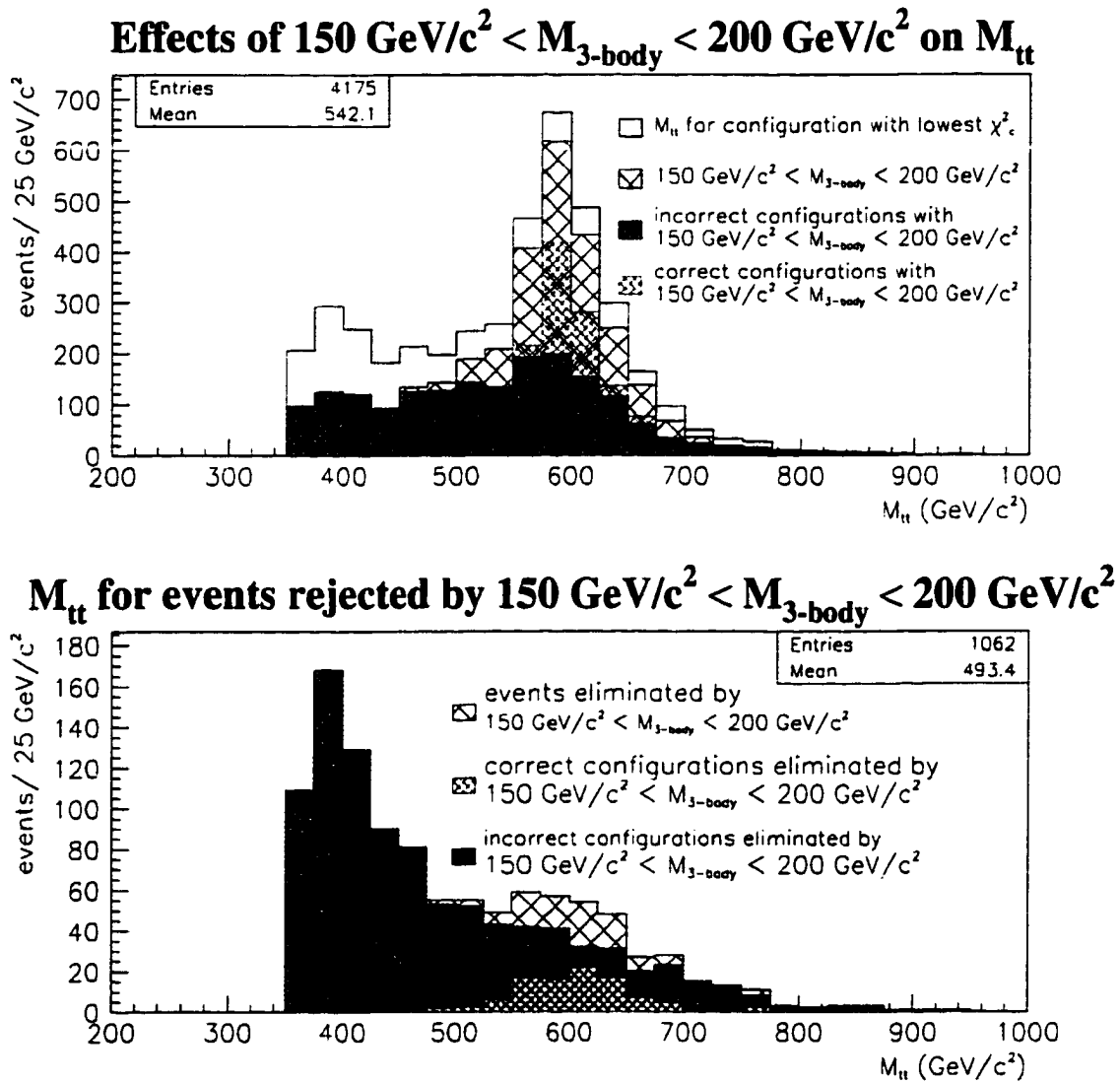


Figure 3.22: $M_{t\bar{t}}$ determined by the constrained method for $M_{Z'} = 600 \text{ GeV}/c^2$ PYTHIA Monte Carlo (“tagged” and “untagged” events). Top: Effects of $150 \text{ GeV}/c^2 < M_{3\text{-body}} < 200 \text{ GeV}/c^2$ on all events passing the selection criteria. Also, $M_{t\bar{t}}$ for events with correct and incorrect jet configuration which pass the $M_{3\text{-body}}$ cut. Bottom: Events eliminated by the $M_{3\text{-body}}$ cut.

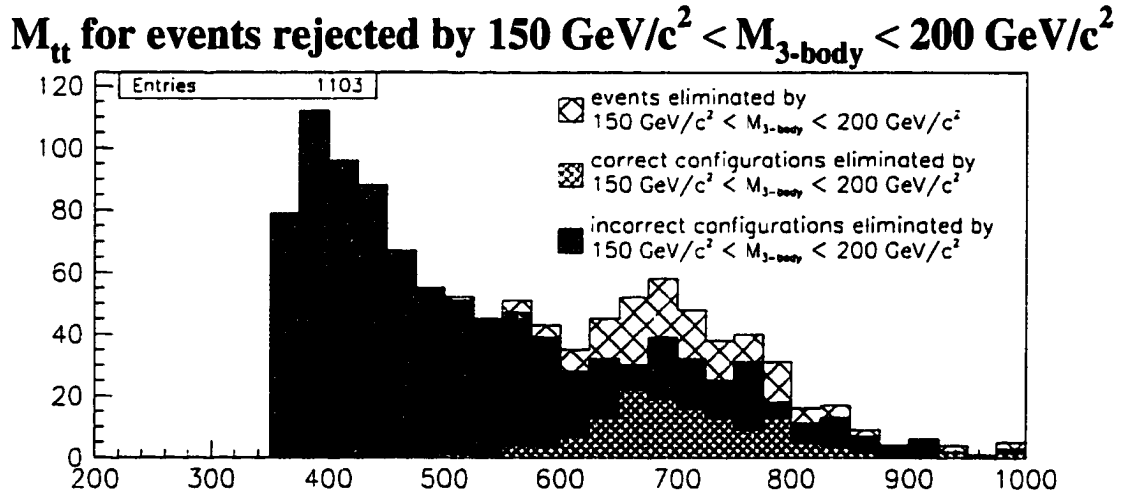
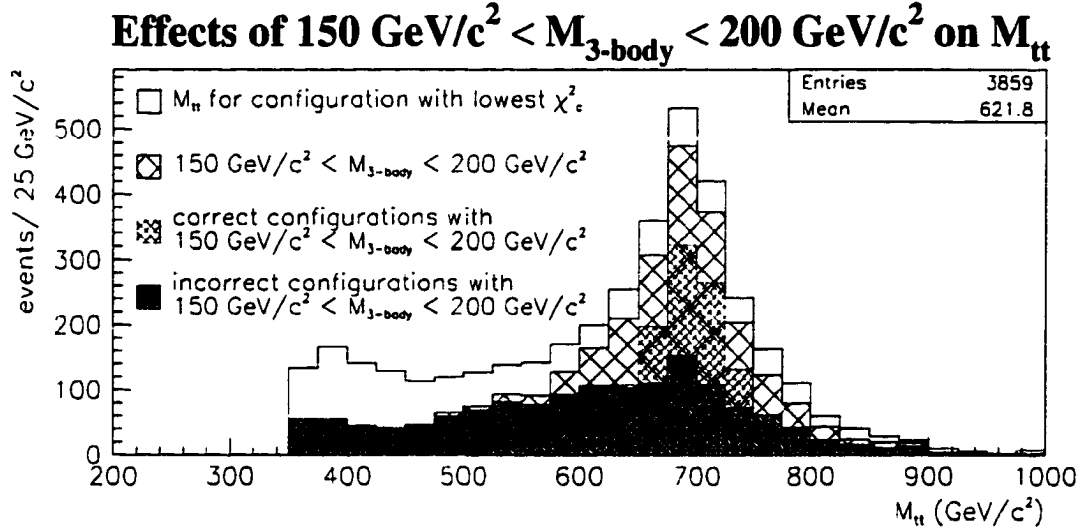


Figure 3.23: $M_{t\bar{t}}$ determined by the constrained method for $M_{Z'} = 700 \text{ GeV}/c^2$ PYTHIA Monte Carlo (“tagged” and “untagged” events). Top: Effects of $150 \text{ GeV}/c^2 < M_{3\text{-body}} < 200 \text{ GeV}/c^2$ on all events passing the selection criteria. Also, $M_{t\bar{t}}$ for events with correct and incorrect jet configuration which pass the $M_{3\text{-body}}$ cut. Bottom: Events eliminated by the $M_{3\text{-body}}$ cut.

were generated for different luminosities, we scaled the number of signal and background events appropriately so as to quantify the effects of the χ^2 cut on discovery potential. (At the time of this study, the Run 1 integrated luminosity had been measured to be 109 pb^{-1} [23]. Since then, this measurement has been improved [11] and, aside from Section 3.5.3, a Run 1 integrated luminosity of 106 pb^{-1} is assumed throughout this thesis.)

As mentioned in Section 3.2.1, we utilize the top mass analysis background calculation to determine the number of non- $t\bar{t}$ background events expected for our analysis of data collected during Run 1. According to these calculations which do not use the same method and cuts of this $X \rightarrow t\bar{t}$ search, the following numbers are predicted for non- $t\bar{t}$ background events which pass the standard primary event selection, are processed with the unconstrained mass fitter, and survive a $\chi_u^2 < 10$ requirement:

- 1.5 events with at least one SVX b -tag and no SLT tags,
- 5.9 events with at least one SLT b -tag and no SVX tags,
- 0.5 events with at least one SVX b -tag and at least one SLT b -tag, and
- 23.9 “untagged” events.

In our analysis, we determine the four QCD W +jets scale factors (one for each tagging category listed above) by calculating the ratio of the number of expected events to the number of Monte Carlo events in our VECBOS sample which meet the standard top quark mass analysis requirements. In our $X \rightarrow t\bar{t}$ search, we determine the amount of QCD W +jets background falling within a given $M_{t\bar{t}}$ window and surviving a particular χ_c^2 cut by simply scaling the absolute number of surviving VECBOS events by the appropriate scale factor.

We calculate the scale factor for standard model $t\bar{t}$ background in a similar fashion. In our HERWIG $t\bar{t}$ sample, the efficiency of passing the CDF top mass analysis cuts is determined to be 0.0363 ± 0.005 for “tagged” events and 0.0208 ± 0.003 for “untagged.” We then determine the number of expected standard model $t\bar{t}$ events for a luminosity of 109 pb^{-1} by assuming the theoretically favored $t\bar{t}$ cross-section of 5.0 pb [24]. Again, the scale factor for standard model $t\bar{t}$ is found by the ratio of the number expected $t\bar{t}$ events to the absolute number of HERWIG events in our Monte Carlo sample which survive the standard top quark mass analysis cuts.

Finally, the signal scale factor is found by assuming that any excess over the expected amount of background is due to a $t\bar{t}$ narrow resonance. In our Run 1 data set, 76 events survive the application of a $\chi_u^2 < 10$ cut after being processed through the unconstrained mass fitter. The expected amount of $X \rightarrow t\bar{t}$ is given by the excess in the data relative to the previously listed background sources which constitute 62.9 events. The signal scale factor is simply the ratio of this excess to the absolute number of PYTHIA Z' events which pass the standard top quark mass cuts. We determine a different scale factor for each Z' mass investigated in this analysis.

To be clear, for a given $M_{t\bar{t}}$ window and a particular χ_c^2 cut, we use the previously described scale factors to determine the relative amounts of background and signal. By scaling by the appropriate factor, the expected amount of each source (for 109 pb^{-1}) is determined using the absolute number of events in six categories: PYTHIA Z' , HERWIG $t\bar{t}$, and the four previously mentioned tagging classifications for VECBOS QCD W +jets.

Significance

To quantify and possibly improve the discovery potential of various χ^2 cuts, we introduce a quantity known as “significance.” We define significance as the poisson probability that the number of background events fluctuates to the total amount of signal and background or more. For a variety of $M_{t\bar{t}}$ windows, we calculate significance as a function of χ_c^2 cut, looking for values of low significance which imply a region of high discovery potential.

In general, our scale factor technique yields non-integral amounts of background and signal. So, for a given amount of signal, the significance is determined by interpolating between the significance-values of its two neighboring integers since this quantity is determined from a poisson probability.

Figures 3.24 through 3.27 display significance as function of χ^2 cut for several resonance masses, where we additionally include “differential errors” for each value of significance. That is, the number of non-inclusive signal and background events (relative to the immediately previous χ^2 cut) were poisson fluctuated 1000 times. Each time, a new significance was determined and the error bars represent the RMS of these 1000 significance values. In cases in which there were no non-inclusive events, the amount of signal or background was not fluctuated.

It is quite apparent that adding the “untagged” sample aids in the search for $X \rightarrow t\bar{t}$. Furthermore, for $M_{Z'} = 400, 500, \text{ and } 600 \text{ GeV}/c^2$, our discovery potential tends to be unaffected by the χ_c^2 cut provided that it is set looser than $\chi_c^2 \approx 30$ or 40. In addition, for $M_{Z'} = 700 \text{ GeV}/c^2$, it seems that a χ_c^2 cut of 50 is optimal. We, therefore, chose a χ_c^2 cut = 50 for all Z' masses in order to increase our discovery potential for a narrow $t\bar{t}$ resonance.

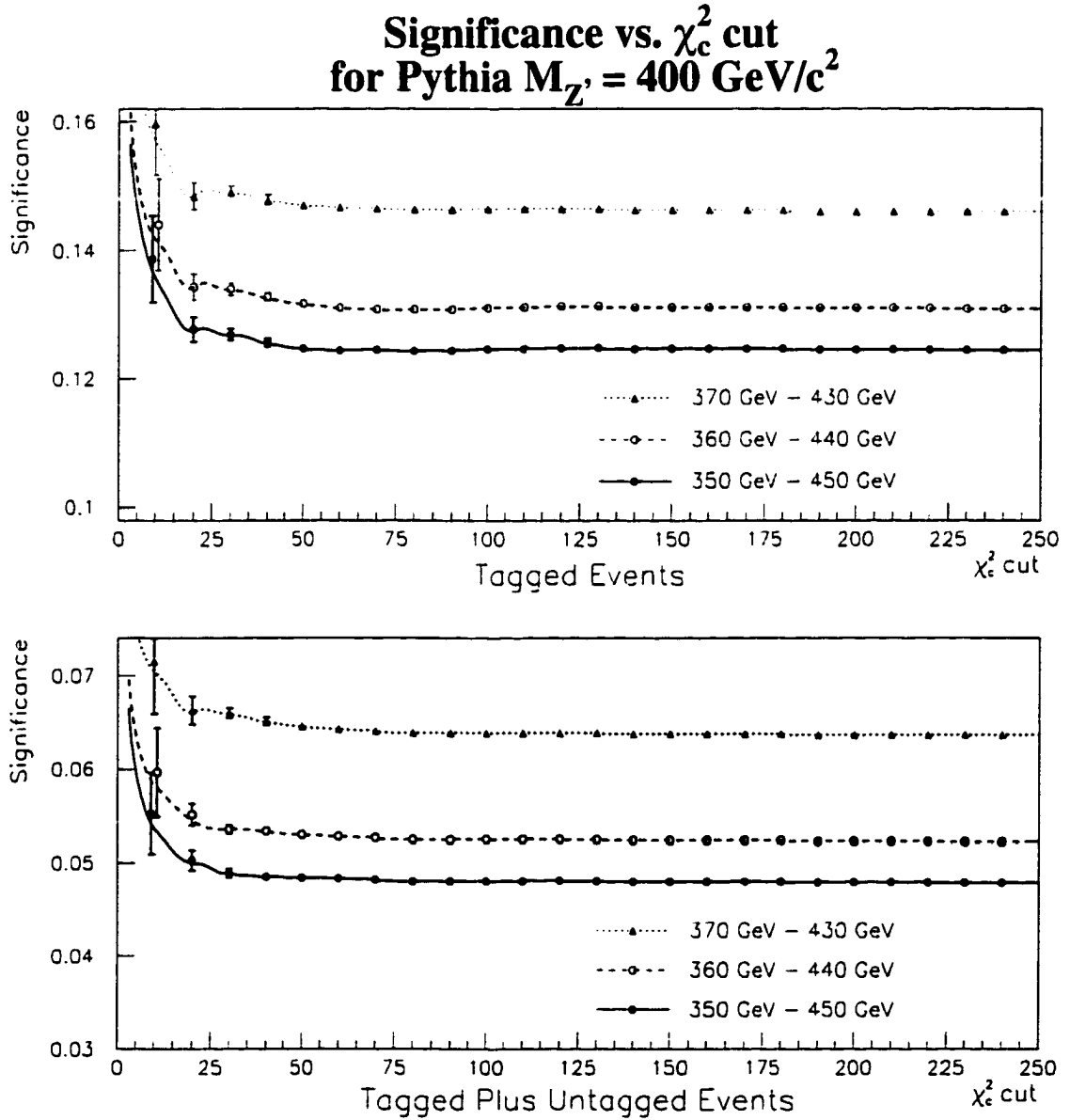


Figure 3.24: Significance as a function of applied χ_c^2 cut for PYTHIA 5.7 Z' Monte Carlo ($M_{Z'} = 400 \text{ GeV}/c^2$). Three different $M_{t\bar{t}}$ windows are employed as the “signal region.” For χ_c^2 cuts which yield over-lapping error bars for different $M_{t\bar{t}}$ windows, the points have been shifted slightly along the abscissa to avoid ambiguity.

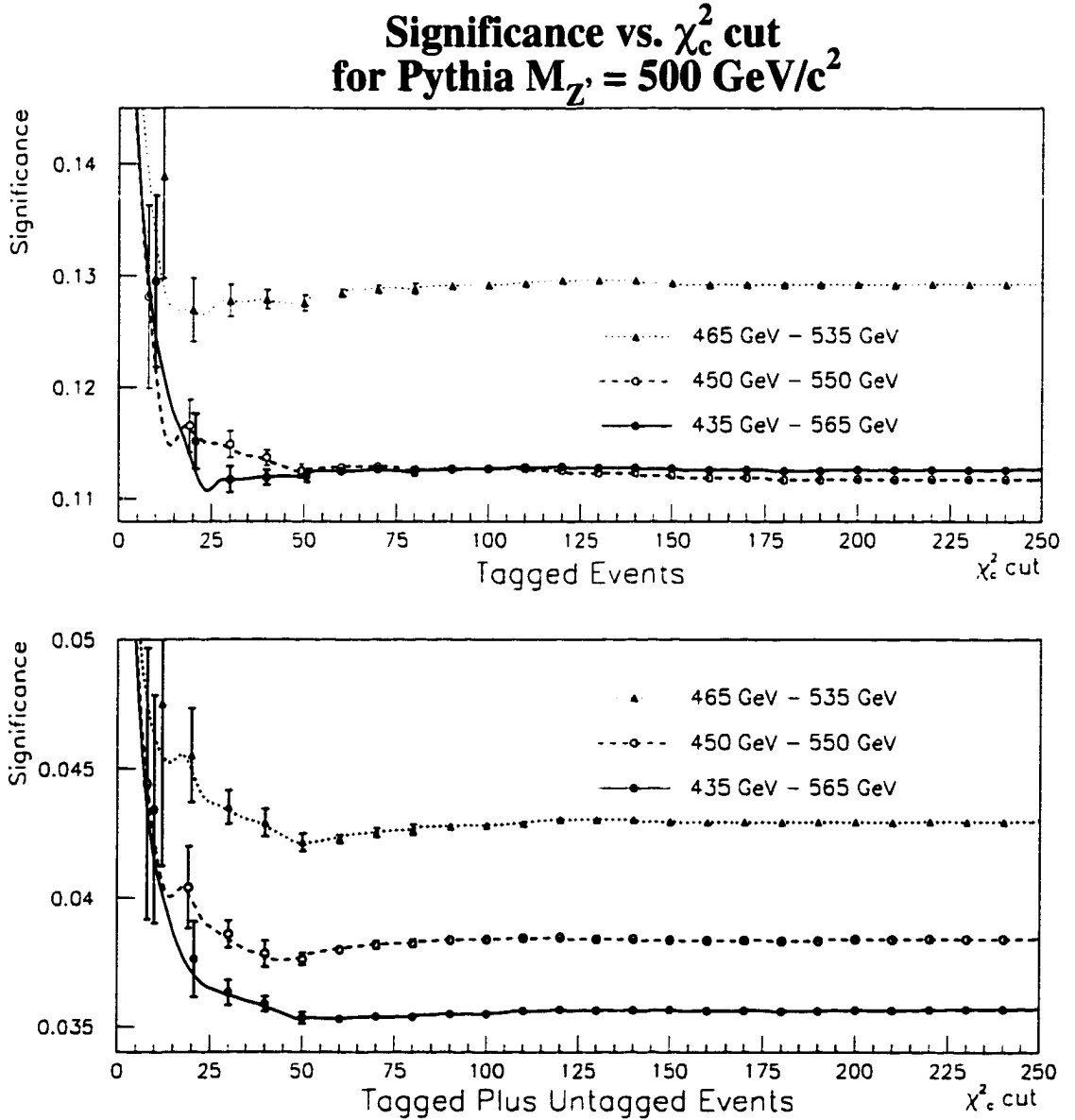


Figure 3.25: Significance as a function of applied χ_c^2 cut for PYTHIA 5.7 Z' Monte Carlo ($M_{Z'} = 500 \text{ GeV}/c^2$). Three different M_{ii} windows are employed as the “signal region.” For χ_c^2 cuts which yield over-lapping error bars for different M_{ii} windows, the points have been shifted slightly along the abscissa to avoid ambiguity.

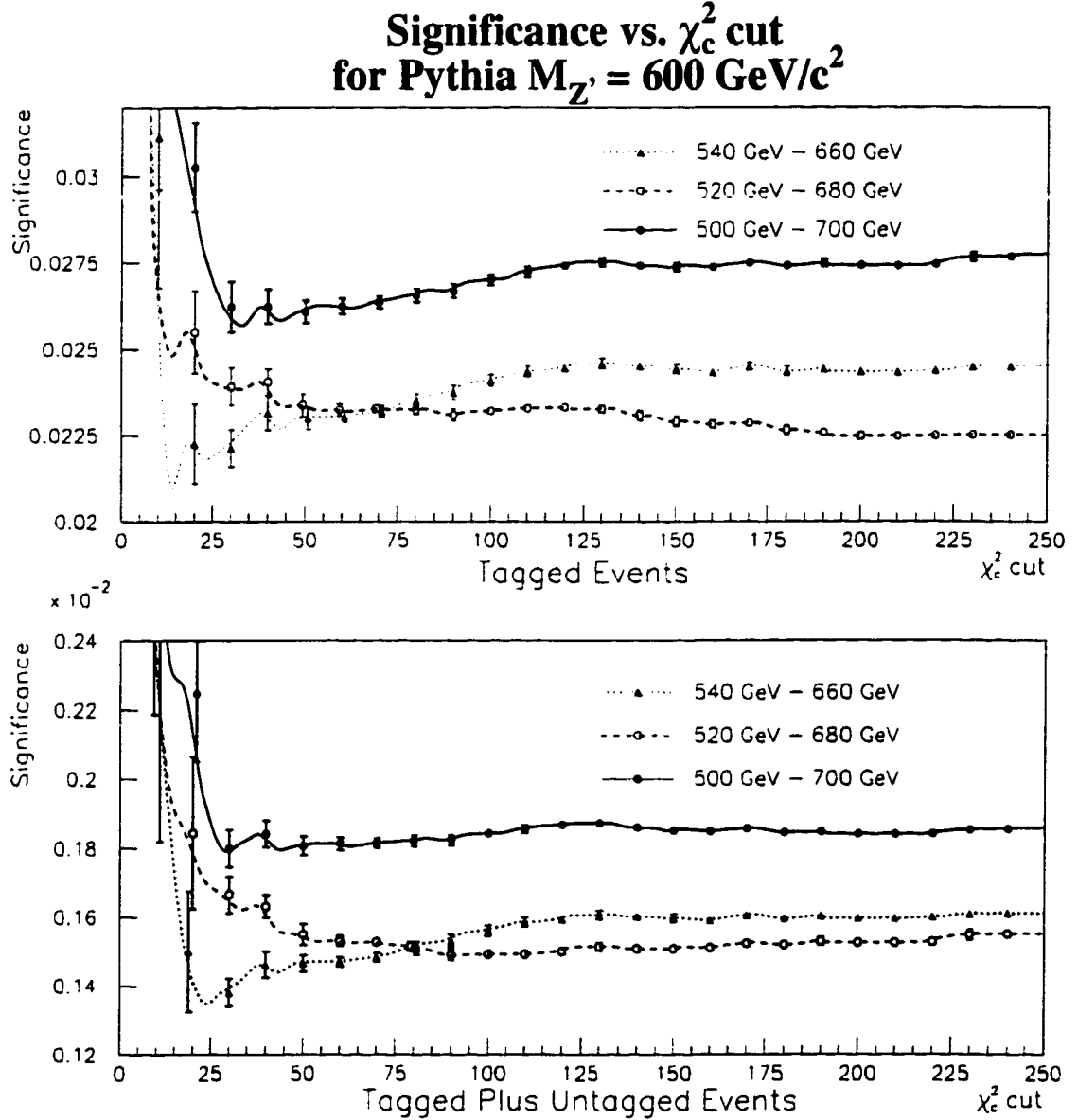


Figure 3.26: Significance as a function of applied χ_c^2 cut for PYTHIA 5.7 Z' Monte Carlo ($M_{Z'} = 600 \text{ GeV}/c^2$). Three different $M_{l\bar{l}}$ windows are employed as the “signal region.” For χ_c^2 cuts which yield over-lapping error bars for different $M_{l\bar{l}}$ windows, the points have been shifted slightly along the abscissa to avoid ambiguity.

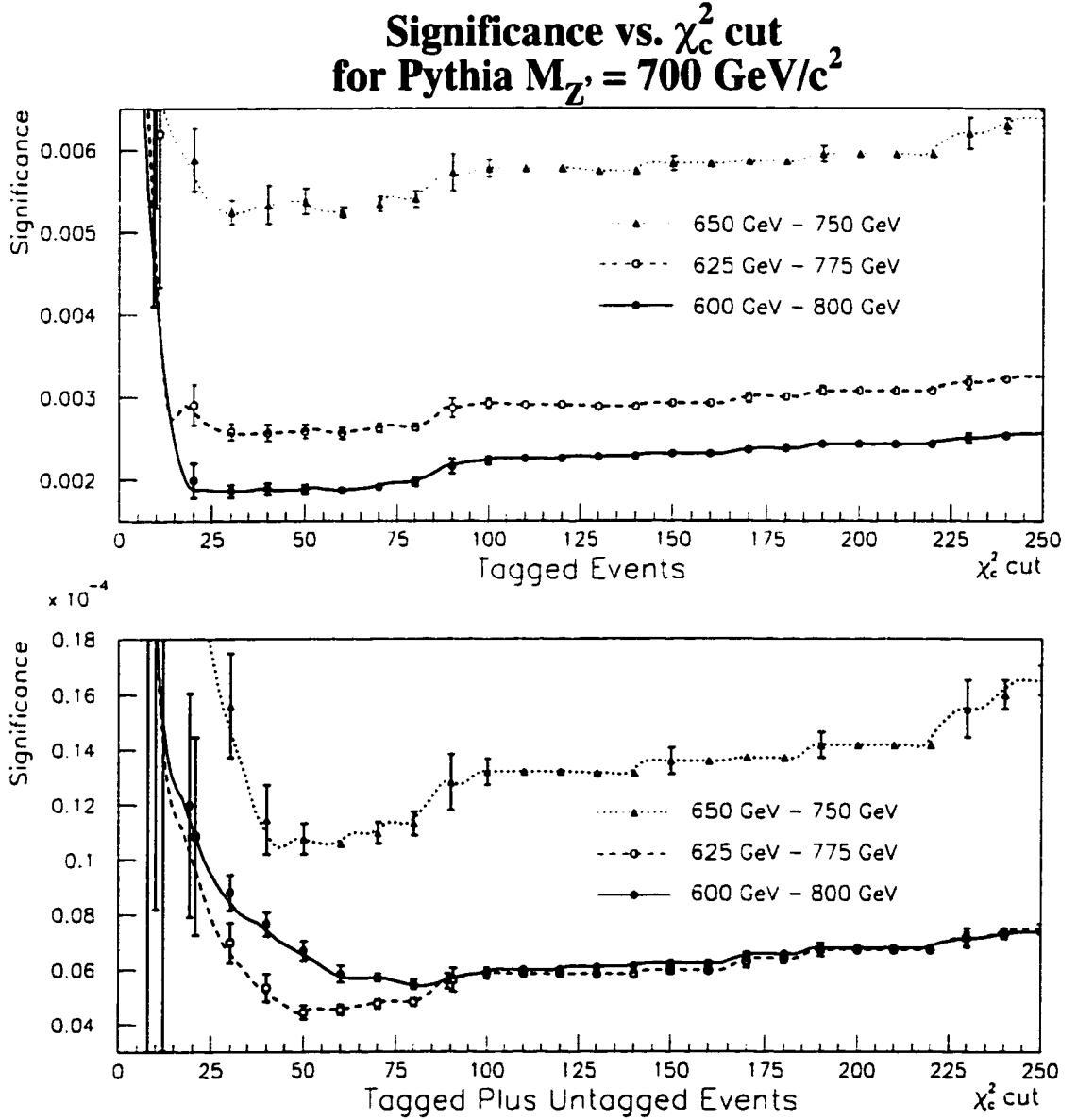


Figure 3.27: Significance as a function of applied χ_c^2 cut for PYTHIA 5.7 Z' Monte Carlo ($M_{Z'} = 700 \text{ GeV}/c^2$). Three different M_{ii} windows are employed as the "signal region." For χ_c^2 cuts which yield over-lapping error bars for different M_{ii} windows, the points have been shifted slightly along the abscissa to avoid ambiguity.

3.6 Signal Acceptances

Having established a method for determining an event's $t\bar{t}$ invariant mass, we now apply these selection criteria to Monte Carlo simulations of signal events in order to determine the expected acceptance rates. Using 50,000 event Monte Carlo samples of $Z' \rightarrow t\bar{t}$ decays which are generated for various values of $M_{Z'}$, we determine the expected $X \rightarrow t\bar{t}$ acceptance accounting for differences between Monte Carlo and data including:

- b -tagging rates
- lepton identification efficiencies
- VTX efficiency for locating primary vertices, and
- Level 3 triggering.

The estimated $X \rightarrow t\bar{t}$ acceptances are listed in Table 3.7 for $400 \text{ GeV}/c^2 \leq M_X \leq 1 \text{ TeV}/c^2$ and $\Gamma = 0.012M_X, 0.04M_X$. Furthermore, the acceptance for HERWIG $t\bar{t}$ is determined to be 0.0543.

M_X (GeV/c ²)	Signal Acceptance, A $\Gamma = 0.012M_X$	Signal Acceptance, A $\Gamma = 0.04M_X$
400	0.0512	0.0520
450	0.0567	0.0577
500	0.0586	0.0565
550	0.0576	0.0576
600	0.0573	0.0566
650	0.0574	0.0567
700	0.0537	0.0550
750	0.0540	0.0556
800	0.0538	0.0545
850	0.0516	0.0532
900	0.0470	0.0486
950	0.0448	0.0492
1000	0.0436	0.0472

Table 3.7: Signal acceptance, A , as determined from Monte Carlo. The statistical uncertainties on these values result from finite Monte Carlo statistics and vary from 1.8 to 1.9%.

Chapter 4

Measurement of the $M_{t\bar{t}}$ Spectrum

The previous chapter lists in detail the various selection criteria which are intended to accentuate the appearance of a narrow $t\bar{t}$ resonance in the $M_{t\bar{t}}$ spectrum if it exists. In brief summary, we demand that $t\bar{t}$ candidate events included in the $M_{t\bar{t}}$ spectrum satisfy the following requirements:

- Each event must contain one isolated, high- P_T lepton
- Each event must contain 3 jets with $E_T > 15$ GeV, $|\eta| < 2.0$ and a 4th with $E_T > 8$ GeV, $|\eta| < 2.4$
- Each event must contain $\cancel{E}_T > 20$ GeV
- The event must not be consistent with a Z boson decay
- Each event must contain at least one jet identified as a b -jet by the SVX or SLT taggers; otherwise, the event must contain four jets with $E_T > 15$ GeV, $|\eta| < 2.0$
- $150 \text{ GeV}/c^2 < M_{l\nu_j}^u, M_{jjj}^u < 200 \text{ GeV}/c^2$
- $\chi_c^2 < 50$

We obtain the expected signal and background $M_{t\bar{t}}$ spectra from the constrained mass fitter (Section 3.4.4) after applying these cuts to the corresponding Monte Carlo samples. Shown in Figure 4.1 are the HERWIG $t\bar{t}$ and VECBOS W +jets $M_{t\bar{t}}$ distributions as well as those for several Z' masses generated with natural width $\Gamma = 0.012M_{Z'}$. In anticipation of fitting the data to the sum of these spectra, we commonly refer to these distributions as “templates.”

4.1 $M_{t\bar{t}}$ Spectrum

Before applying the $M_{t\bar{t}}$ selection criteria to the CDF Run 1 data sample collected in 106 pb^{-1} , we first determine the expected contribution from the non- $t\bar{t}$ background sources listed in Section 3.2.1. In the top quark mass analysis [14], it has been determined that the non- $t\bar{t}$ components of Run 1 events surviving the primary event selection of Section 3.1.5 and $\chi_u^2 < 10$ (*cf.*, Table 3.6) are:

- 2.1 events with at least one SVX b -tag and no SLT tags,
- 7.7 events with at least one SLT b -tag and no SVX tags,
- 0.8 events with at least one SVX b -tag and at least one SLT b -tag, and
- 30.7 “untagged” events.

After scaling each of these predicted values by the acceptance rate relative to the $M_{t\bar{t}}$ cuts, we find that a total of 31.1 non- $t\bar{t}$ background events are expected in our $X \rightarrow t\bar{t}$ search. (As noted in Section 3.2.1, the uncertainty on this value is approximately 27%, *i.e.*, ± 8.5 events.) The contributions to each of the individual tagging categories are given in Table 4.1. Note that the VECBOS $M_{t\bar{t}}$ template in Figure 4.1 is the result of individual templates representing these four tagging categories summed with weights given in Table 4.1.

CDF Preliminary

Background and Signal Templates for $X \rightarrow t\bar{t}$ Search

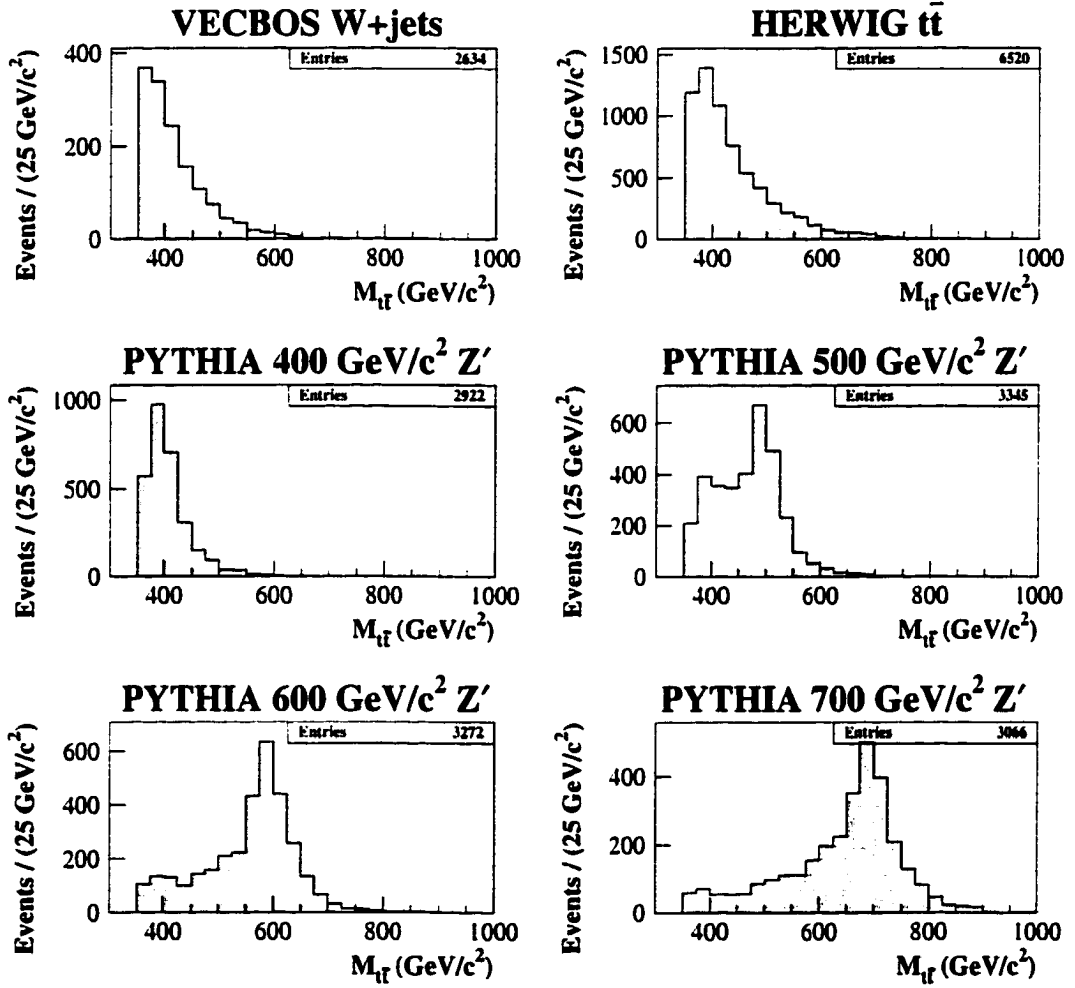


Figure 4.1: Background and signal ($\Gamma = 0.012M_{Z'}$) $M_{t\bar{t}}$ templates from Monte Carlo events that survive $M_{t\bar{t}}$ event selection.

Subsample	N_W
only SVX tags	1.4
only SLT tags	5.9
SVX and SLT tags	0.7
No tags	23.1

Table 4.1: The estimated non- $t\bar{t}$ background contributions to the Run 1 data events satisfying the $M_{t\bar{t}}$ selection criteria.

We find that 63 Run 1 data events pass the $M_{t\bar{t}}$ selection cuts, yielding the invariant $t\bar{t}$ mass spectrum shown in Figure 4.2. Also shown in Figure 4.2 are the expected background shapes from standard model $t\bar{t}$ and the predicted rate of non- $t\bar{t}$ events, the sum of which is normalized to 63 events. In addition to a slight excess in the region near 500 GeV/c², we observe an apparent discrepancy between data and Monte Carlo in the region of 350 GeV/c² and 375 GeV/c². Yet, we find that the $M_{t\bar{t}}$ distribution of 63 data events yields a χ^2 probability of 80% when compared to the hypothesis that the spectrum is comprised of standard model $t\bar{t}$ production and the predicted rate of non- $t\bar{t}$ background events, as shown in Fig. 4.2. This χ^2 comparison covers 17 bins — 16 bins (of width 25 GeV/c²) from 350 to 725 GeV/c² and one bin from 725 GeV/c² to ∞ — and takes the form:

$$\chi^2 = \sum_{i=1}^{17} \chi_i^2$$

where

$$\chi_i^2 = \begin{cases} \frac{(n_{data} - n_{mc})^2}{\sigma_{data}} & \text{if } n_{data} < n_{mc} \\ \frac{(n_{data} - n_{mc})^2}{\sigma_{data}} & \text{if } n_{data} > n_{mc} \end{cases}$$

and σ_{data}^- and σ_{data}^+ are the lower and upper (asymmetric) poisson statistical errors.

4.2 $X \rightarrow t\bar{t}$ Cross-section Limits

Although we cannot present evidence for physics beyond the standard model, a shape-fitting analysis is employed to establish production cross-section limits for a generic object which decays to $t\bar{t}$. These limits are determined as a function of the mass of the parent object.

4.2.1 Establishing Upper Limits

Assuming that the only sources present in the data (Figure 4.2) are $X \rightarrow t\bar{t}$, standard model $t\bar{t}$, and QCD W +jets background, we can express the form of the $M_{t\bar{t}}$ distribution for the number of data events, N_d , simply as:

$$\frac{dN_d}{dM_{t\bar{t}}} = N_{signal} + \alpha N_{t\bar{t}} + \beta N_{W+jets}$$

where the background shapes, $N_{t\bar{t}}$ and N_{W+jets} , are normalized to unity such that α and β represent the number of $t\bar{t}$ and QCD W +jets background events, respectively. We normalize N_{signal} , the signal shape, to the product $A \cdot (\sigma_X \cdot \text{BR}\{X \rightarrow t\bar{t}\}) \cdot \int \mathcal{L} dt$ where A is the signal acceptance (Table 3.7), $\int \mathcal{L} dt$ is the total integrated Run 1 luminosity, and $\sigma_X \cdot \text{BR}\{X \rightarrow t\bar{t}\}$ is production cross-section times $t\bar{t}$ branching ratio for a generic object X . For this shape fitting analysis, we define the likelihood function, L , as

$$L = \prod_i \mathcal{P}_i \tag{4.1}$$

where \mathcal{P}_i , the poisson probability of observing n_i data events in the i^{th} mass bin,

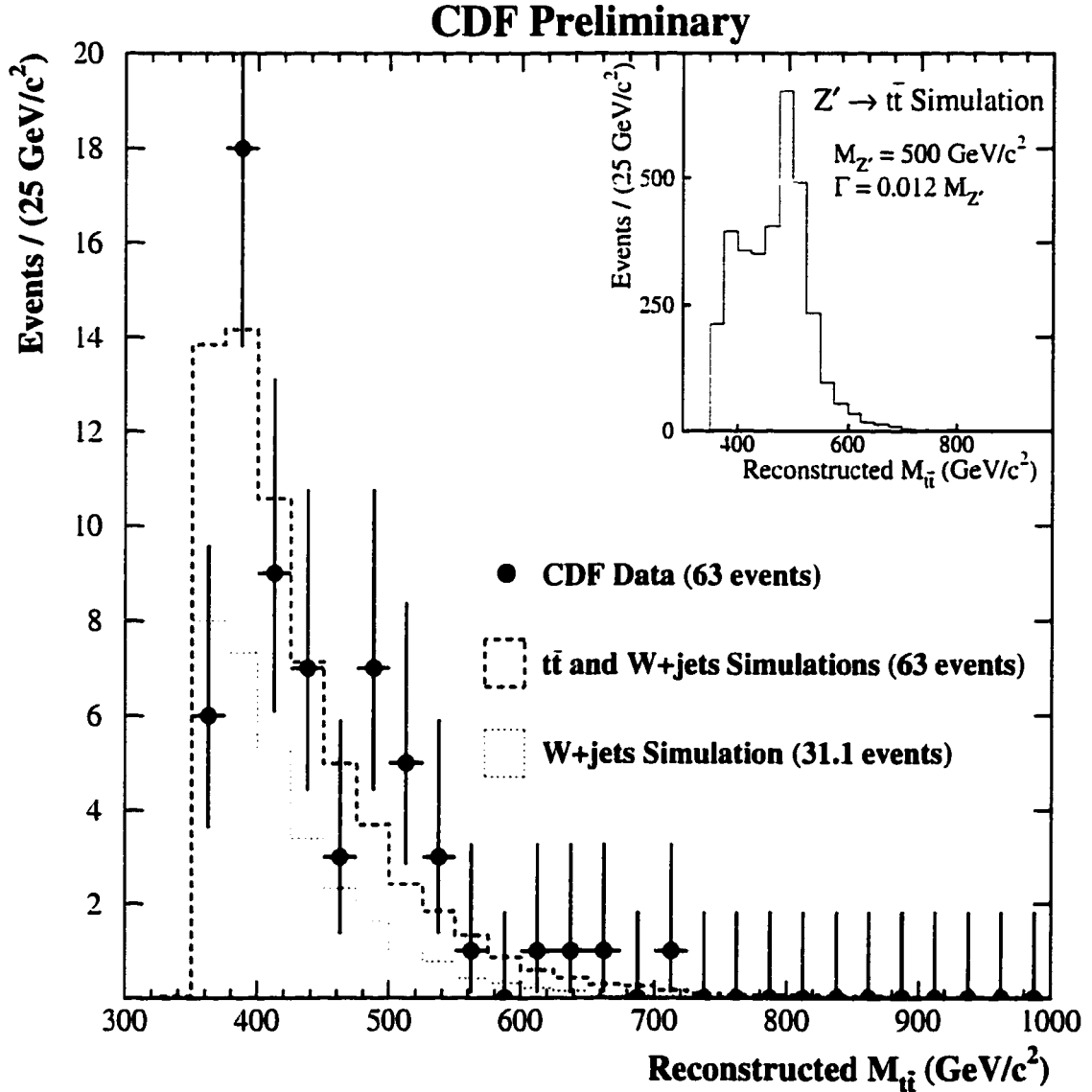


Figure 4.2: The observed $M_{t\bar{t}}$ spectrum (points) compared to the QCD W +jets background (fine dashed) and the total standard model prediction including both QCD W +jets and $t\bar{t}$ production (thick dashed). The $t\bar{t}$ prediction has been normalized such that the number of events in the total standard model prediction is equal to the number of events in the data. The inset shows the expected $M_{t\bar{t}}$ shape resulting from the simulation of a narrow resonance ($M_{Z'} = 500 \text{ GeV/c}^2$, $\Gamma = 0.012 M_{Z'}$) in the CDF detector.

is given by

$$\mathcal{P}_i = \frac{\mu_i^{n_i} e^{-\mu_i}}{n_i!}.$$

Here, μ_i is the expected number of events in this bin given by

$$\mu_i = N_{signal}(i) + \alpha N_{t\bar{t}}(i) + \beta N_{W+jets}(i)$$

where $N_{signal}(i)$, $N_{t\bar{t}}(i)$, and $N_{W+jets}(i)$ is the value of the i^{th} bin in the respective template. The MINUIT package is then used to determine α and β such that $-\log(L)$ is minimized, thereby maximizing L .

Figure 4.3 shows the maximal likelihood as a function of $\sigma_X \cdot \text{BR}\{X \rightarrow t\bar{t}\}$ for several X masses, where $X \rightarrow t\bar{t}$ is modelled by topcolor $Z' \rightarrow t\bar{t}$ with a natural width $\Gamma = 0.012M_{Z'}$. Also listed in Figure 4.3 are the resulting 95% confidence level (C.L.) upper limits on production cross-section for $X \rightarrow t\bar{t}$. These limits are obtained by integrating the likelihood over $\sigma_X \cdot \text{BR}\{X \rightarrow t\bar{t}\}$ and determining the value which corresponds to 95% of the area. Neglecting the effect of systematic uncertainties, Figure 4.4 displays the 95% C.L. upper limits as a function of M_X . These Run 1 limits *without the inclusion of systematic uncertainties* are given in Table 4.3, while Table 4.2 lists the most probable $\sigma_X \cdot \text{BR}\{X \rightarrow t\bar{t}\}$ whose errors are given by a 1/2 unit change in $-\log(L)$. (See Appendix A for more details on errors resulting from a background-constrained likelihood technique.)

4.2.2 Verifying the 95% Level of Confidence

In an attempt to verify the accuracy of the confidence level associated to limits that are determined by integrating the likelihood function, we first carefully establish an operational definition of a “95% C.L. upper limit” as follows:

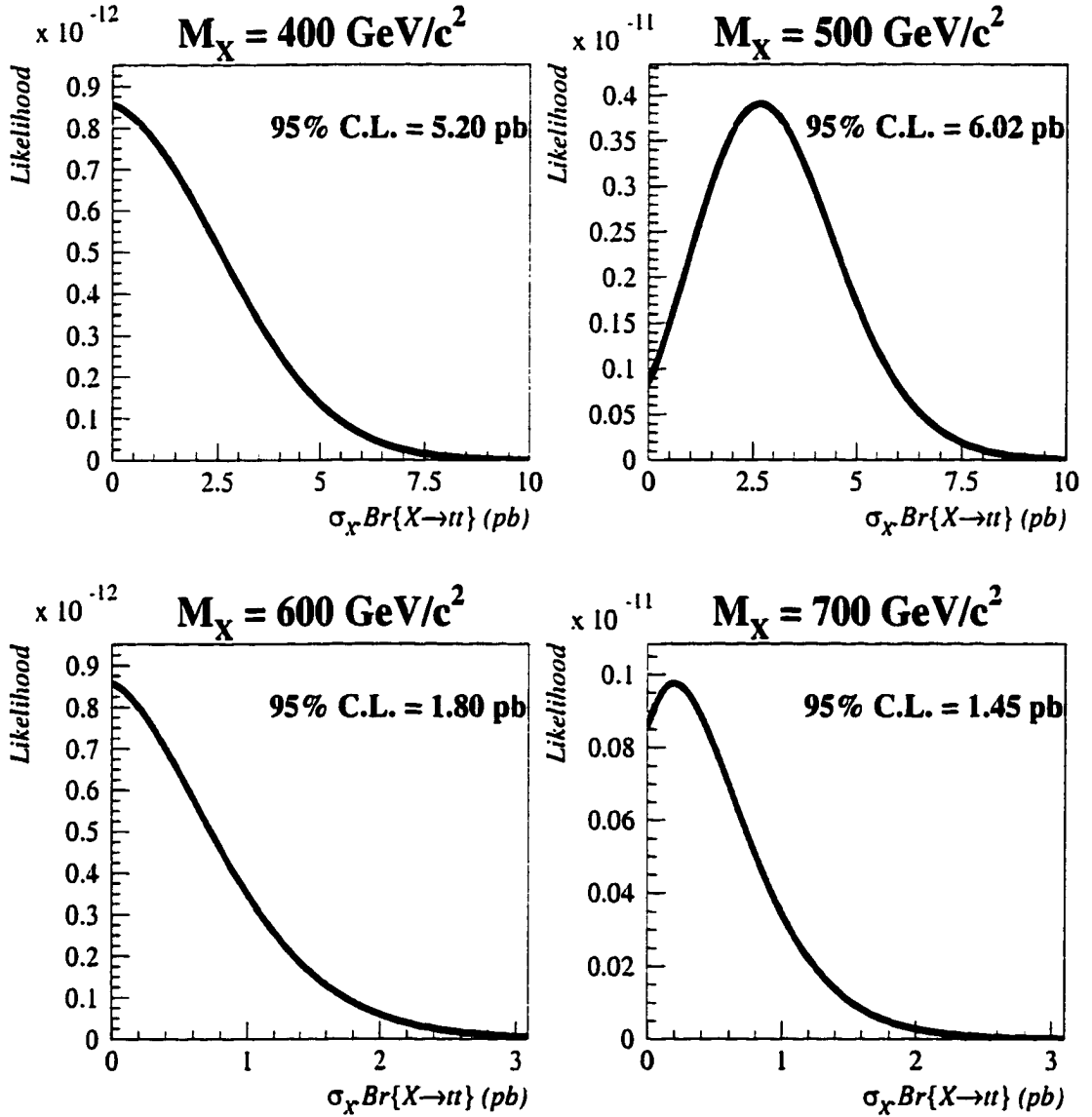


Figure 4.3: Likelihood as a function of $X \rightarrow t\bar{t}$ production cross-section times branching ratio for $M_X = 400, 500, 600$, and $700 \text{ GeV}/c^2$ and natural width $\Gamma = 0.012M_X$. The effects of systematic uncertainties are not included.

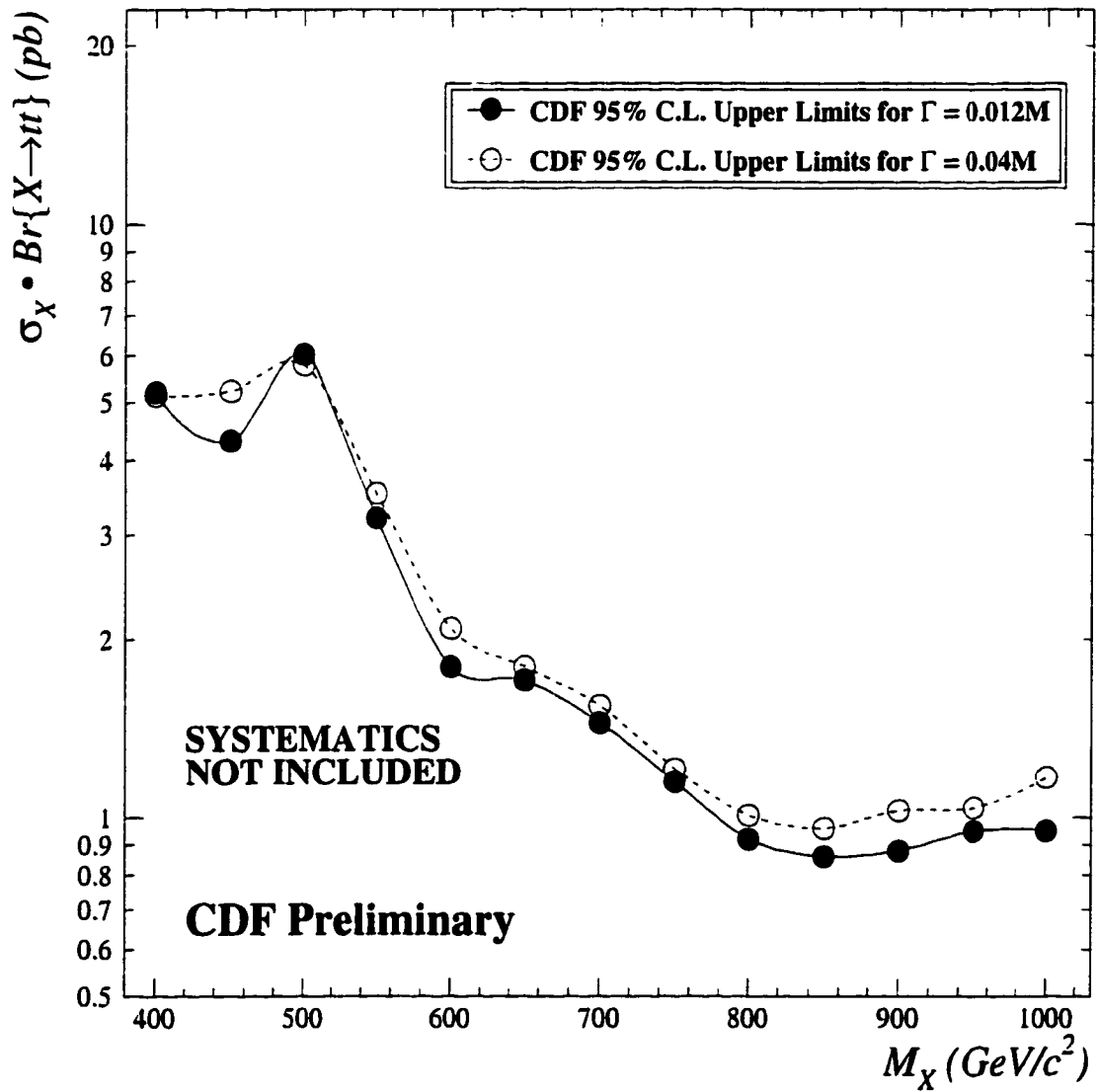


Figure 4.4: The 95% C.L. upper limits on $\sigma_X \cdot BR\{X \rightarrow t\bar{t}\}$ as a function of M_X . The effects of systematic uncertainties are not included.

M_x (GeV/c ²)	Most Probable $\sigma_x \text{BR}\{X \rightarrow t\bar{t}\}$ (pb) for $\Gamma = 0.012M_x$	Most Probable $\sigma_x \text{BR}\{X \rightarrow t\bar{t}\}$ (pb) for $\Gamma = 0.04M_x$
400	$0.00^{+2.5}_{-0.00}$	$0.00^{+2.3}_{-0.00}$
450	$0.00^{+1.4}_{-0.00}$	$0.00^{+2.0}_{-0.00}$
500	$2.65^{+1.8}_{-1.6}$	$2.29^{+1.9}_{-1.7}$
550	$0.61^{+1.2}_{-0.61}$	$0.76^{+1.3}_{-0.76}$
600	$0.00^{+0.70}_{-0.00}$	$0.08^{+0.86}_{-0.08}$
650	$0.33^{+0.61}_{-0.33}$	$0.29^{+0.67}_{-0.29}$
700	$0.19^{+0.52}_{-0.19}$	$0.21^{+0.57}_{-0.21}$
750	$0.00^{+0.41}_{-0.00}$	$0.00^{+0.45}_{-0.00}$
800	$0.00^{+0.21}_{-0.00}$	$0.00^{+0.24}_{-0.00}$
850	$0.00^{+0.17}_{-0.00}$	$0.00^{+0.20}_{-0.00}$
900	$0.00^{+0.16}_{-0.00}$	$0.00^{+0.20}_{-0.00}$
950	$0.00^{+0.18}_{-0.00}$	$0.00^{+0.20}_{-0.00}$
1000	$0.00^{+0.17}_{-0.00}$	$0.00^{+0.23}_{-0.00}$

Table 4.2: The most probable values of cross-section times branching ratio for narrow resonances (with natural width $\Gamma = 0.012M_x$ and $\Gamma = 0.04M_x$) decaying to $t\bar{t}$. These values do not include the effects of systematic uncertainties.

M_x (GeV/c ²)	95% C.L. Limits on $\sigma_x \text{BR}\{X \rightarrow t\bar{t}\}$ (pb) for $\Gamma = 0.012M_x$	95% C.L. Limits on $\sigma_x \text{BR}\{X \rightarrow t\bar{t}\}$ (pb) for $\Gamma = 0.04M_x$
400	5.20	5.14
450	4.32	5.23
500	6.02	5.78
550	3.20	3.52
600	1.80	2.09
650	1.71	1.80
700	1.45	1.55
750	1.15	1.21
800	0.92	1.01
850	0.86	0.96
900	0.88	1.03
950	0.95	1.04
1000	0.95	1.17

Table 4.3: The 95% C.L. upper limits cross-section times branching ratio for narrow resonances (with natural width $\Gamma = 0.012M_x$ and $\Gamma = 0.04M_x$) decaying to $t\bar{t}$. These values do not include the effects of systematic uncertainties.

Suppose that the measurement of some observable O yields the value X and that one wishes to establish the 95% C.L. upper limit, Y , on O . Y is that value such that if the true mean of O were Y and the measurement were repeated a large number of times, then values of less than or equal to X will be observed 5% of the time[26].

To analytically verify that our method of determining the 95% C.L. upper limit on σ_X satisfies this definition, we employ a toy Monte Carlo. For this study, a “pseudo-experiment” is generated by first poisson fluctuating the expected numbers of signal and background events (\bar{N}_s and \bar{N}_b , respectively) and then choosing these events according to the corresponding template shapes. By performing a likelihood fit to the template shapes, we extract the fitted number of signal and background events (N_s and N_b , respectively) for this pseudo-experiment, as well as the number of signal events corresponding to the 95% C.L. upper limit (called N_s^{95}) determined through integration as described in Section 4.2.1. An additional 100 pseudo-experiments are then generated by poisson fluctuating N_s^{95} and N_b . We then determine the value of F_{\leq} , defined to be the fraction of these 100 pseudo-experiments which fit to a number of signal events which is less than or equal to N_s . This entire process is repeated 200 times for each study.

We perform these studies using a variety of gaussian signal and background templates for the general case, as well as with template shapes which are specific to this $M_{t\bar{t}}$ analysis. In the latter case, we generate pseudo-experiments which include events from the *two* $X \rightarrow t\bar{t}$ background sources, but the method described above is unchanged. As we expect, in both the general and $M_{t\bar{t}}$ -specific studies, we find that F_{\leq} is, on average, equal to 5%, independent of \bar{N}_s and \bar{N}_b , supporting the validity of our method for setting 95% C.L. upper limits on $\sigma_X \cdot \text{BR}\{X \rightarrow t\bar{t}\}$.

Chapter 5

Systematic Uncertainties

While the effects of statistical uncertainties are, by definition, included in our likelihood expression (Equation 4.1), various sources of systematic uncertainty influence the shape of the resulting likelihood functions and, therefore, affect the fitted values and the 95% C.L. upper limits on $\sigma_X \cdot \text{BR}\{X \rightarrow t\bar{t}\}$ (listed in Tables 4.2 and 4.3). The effects of systematic uncertainties can result in uncertainty in the $M_{t\bar{t}}$ template shapes and/or the signal acceptance rate. Systematic effects which change the shape of expected signal and background $M_{t\bar{t}}$ distributions will clearly have an effect on the likelihood functions established in this shape-fitting analysis. It is also clear that any change in the expected acceptance for the signal process will change $\sigma_X \cdot \text{BR}\{X \rightarrow t\bar{t}\}$.

By considering a variety of sources of systematic uncertainty, the aim of this chapter is to first estimate the total 1σ (one standard deviation) systematic uncertainty for a given value of likelihood. Because likelihood is a direct function of $\sigma_X \cdot \text{BR}\{X \rightarrow t\bar{t}\}$, the primary goal becomes determining the likelihood uncertainty, Δ , as a function of $\sigma_X \cdot \text{BR}\{X \rightarrow t\bar{t}\}$. After obtaining the functional form of Δ , it is a straightforward matter to appropriately convolute this uncertainty with the

likelihood function, L , which is established using the method described in Section 4.2.1. Assuming that each likelihood value varies according to gaussian errors about its central value, the smeared likelihood function, L' , which incorporates the effects due to systematic uncertainty, is given by:

$$L'(\sigma) \equiv \int_0^\infty L(x) \times \frac{1}{\sqrt{2\pi}\Delta(x)} e^{-\frac{(\sigma-x)^2}{2\Delta(x)^2}} dx$$

where σ represents $\sigma_x \cdot \text{BR}\{X \rightarrow t\bar{t}\}$ and Δ is written as an explicit function of the variable of integration [27].

5.1 Determining the Likelihood Uncertainty

While several sources may result in both shape and acceptance contributions to the total systematic uncertainty, we investigate these types of systematic effect separately.

5.1.1 Shape Effects

To estimate the effects of a particular source of systematic uncertainty which alters the expected signal and/or background $M_{t\bar{t}}$ shapes, we employ pseudo-experiments generated from Monte Carlo. For a selected amount of input signal, $\sigma_x \cdot \text{BR}\{X \rightarrow t\bar{t}\}$, we generate pseudo-experiments by first poisson fluctuating the expected number of signal events, as well as the gaussian-smeared predicted number of background events. In addition to the predicted non- $t\bar{t}$ contribution of 31.1 ± 8.5 events (see Section 4.1), this study assumes that the standard model $t\bar{t}$ production cross-section is given by its Run 1 measured value of 5.1 ± 1.6 pb, which corresponds to 29.4 ± 9.2 events in this analysis. Then for each pseudo-experiment, events are selected according to the corresponding *nominal* templates

(such as those in Figure 4.1). Each pseudo-experiment is then fit to these same templates to determine the most probable (or “fitted”) value of $\sigma_x \cdot \text{BR}\{X \rightarrow t\bar{t}\}$, called σ_{fit} . A new fitted value of $\sigma_x \cdot \text{BR}\{X \rightarrow t\bar{t}\}$, called σ'_{fit} , is determined by re-fitting each pseudo-experiment to the set of signal and background templates whose shapes reflect a 1σ (one standard deviation) shift in a given systematic effect. After generating 1000 pseudo-experiments, we determine mean values of σ_{fit} and $(\sigma'_{\text{fit}} - \sigma_{\text{fit}})$, called $\overline{\sigma_{\text{fit}}}$ and $\overline{\Delta}$, respectively. This entire process is repeated as $\sigma_x \cdot \text{BR}\{X \rightarrow t\bar{t}\}$ is incremented from 0.0 to 50.0 pb. It is the functional dependence of $\overline{\Delta}$ on $\overline{\sigma_{\text{fit}}}$ which provides an estimate for the likelihood uncertainty, Δ , as a function of $\sigma_x \cdot \text{BR}\{X \rightarrow t\bar{t}\}$ for this particular source systematic of uncertainty. Note that $\Delta \equiv (\sigma' - \sigma)$ is a signed quantity, where a negative value indicates that for the given systematic effect, the value of $\sigma_x \cdot \text{BR}\{X \rightarrow t\bar{t}\}$ is decreased.

5.1.2 Acceptance Effects

To estimate the effect of systematic sources which affect the expected signal acceptance rate, A (see Table 3.7, we simply apply a 1σ shift to the source of systematic uncertainty and determine the new signal acceptance, A' . The difference between A' and A is taken to be ΔA , the one standard deviation change in A due to a given source of systematic uncertainty. Unlike shape effects, the σ_{fit} dependence of Δ ($= \sigma'_{\text{fit}} - \sigma_{\text{fit}}$) which results from changing the signal acceptance by ΔA can be determined analytically. Because $\sigma_{\text{fit}} = \frac{n}{A\mathcal{L}}$ where n = the number of fitted signal events, σ'_{fit} is given by $\sigma'_{\text{fit}} = \frac{n}{(A+\Delta A)\mathcal{L}} = (\frac{A}{A+\Delta A})\sigma_{\text{fit}}$. Accordingly,

$$\frac{\sigma'_{\text{fit}} - \sigma_{\text{fit}}}{\sigma_{\text{fit}}} = \frac{A}{A + \Delta A} - 1,$$

or equivalently,

$$\Delta = \left(\frac{A}{A + \Delta A} - 1 \right) \sigma_{fit}. \quad (5.1)$$

For each source at a given mass M_X , the shape+acceptance systematic uncertainty for a $+1\sigma$ (-1σ) shift is given by adding the $+1\sigma$ (-1σ) shape and acceptance Δ curves in quadrature — unless the two are clearly correlated, in which case the contributions from shape and acceptance are added linearly. Obviously, when shape and acceptance effects are added in quadrature, the resulting total value of Δ will be positive definite. Yet, when shape and acceptance effects are added linearly, the value of the total Δ can be positive or negative. It is the *magnitude* of the total systematic uncertainty curve which is used to estimate the 1σ systematic uncertainty on likelihood.

5.2 Sources of Systematic Uncertainty

5.2.1 Jet E_T Systematic

As described in Section 3.4.1, an event's reconstructed $t\bar{t}$ invariant mass is determined by varying the measured lepton and jet transverse energies, as well as the measured transverse components of the unclustered energy in the event. While negligible effects on mass reconstruction result from both the small uncertainties on measured lepton energy and the somewhat more substantial uncertainty on the unclustered energy measurement[14], the determination of $M_{t\bar{t}}$ can be affected considerably by the uncertainty in the measured jet energies.

The systematic uncertainty in the measured jet E_T stems from the uncertainty in the generic energy corrections which are applied to all jets in an event. As in the top quark mass analysis[14], the total uncertainty in jet E_T is given by the quadrature sum of the individual uncertainties discussed in Section 3.3.1 and

shown in Figure 3.10.

Signal $M_{t\bar{t}}$ templates (for $M_{Z'} = 400, 500, 600, 700,$ and $800 \text{ GeV}/c^2$ with $\Gamma = 0.012M_{Z'}$) and background $M_{t\bar{t}}$ templates are generated from Monte Carlo in which the measured E_T of each jet is shifted by one standard deviation. The dependence of $\bar{\Delta}$ on $\sigma_X \cdot \text{BR}\{X \rightarrow t\bar{t}\}$ is given in Figure 5.1.

The change in signal acceptance, ΔA , due to shifting jet E_T by $\pm 1\sigma$ is listed in Table 5.1. The resulting likelihood uncertainty as a function of $\sigma_X \cdot \text{BR}\{X \rightarrow t\bar{t}\}$ is also shown in Figure 5.1.

M_x	ΔA for -1σ jet E_T shift	ΔA for $+1\sigma$ jet E_T shift
400 GeV/c^2	-0.0012	0.0001
500 GeV/c^2	0.0008	0.0000
600 GeV/c^2	0.0003	0.0002
700 GeV/c^2	-0.0002	0.0005
800 GeV/c^2	-0.0007	0.0006

Table 5.1: The change in Monte Carlo signal acceptance rate, ΔA , due to shifting jet E_T by $\pm 1\sigma$.

For each mass, we fit each of the two “Jet E_T Total” curves (for $\pm 1\sigma$) in Figure 5.1 to a line passing through the origin. We take the larger of the two slopes (for $\pm 1\sigma$) as the jet E_T systematic uncertainty as a function of $\sigma_X \cdot \text{BR}\{X \rightarrow t\bar{t}\}$; i.e., the curves that fit to slopes of 6.1%, 12%, 6.2%, 4.4% and 4.4% for $M_X = 400, 500, 600, 700,$ and $800 \text{ GeV}/c^2$, respectively.

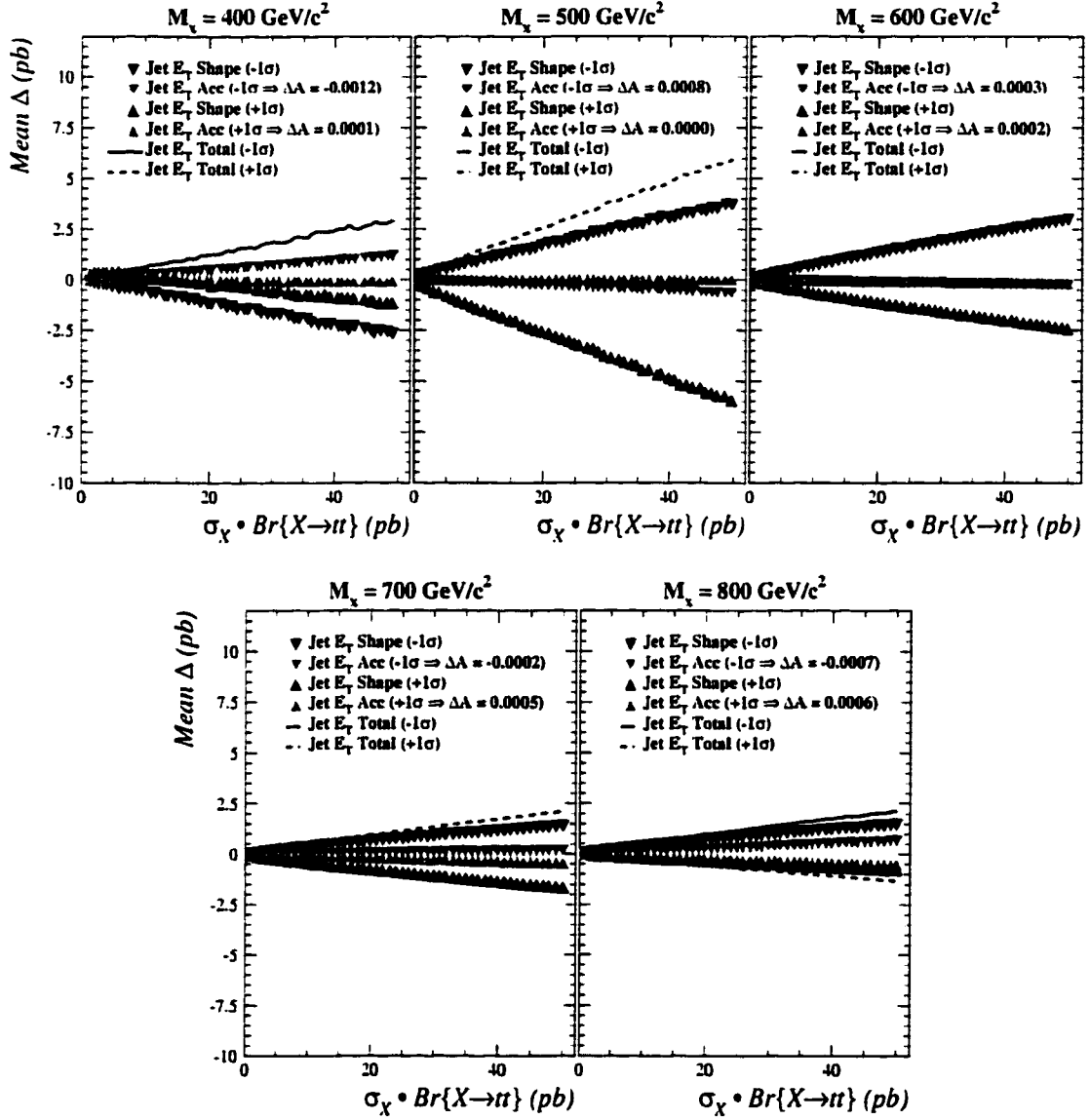


Figure 5.1: The shape and acceptance contributions to the likelihood systematic uncertainty, Δ , resulting from $\pm 1\sigma$ shifts in jet E_T .

M_X	ΔA for $M_{top} = 170 \text{ GeV}/c^2$	ΔA for $M_{top} = 180 \text{ GeV}/c^2$
400 GeV/c^2	0.0001	0.0017
500 GeV/c^2	-0.0029	-0.0021
600 GeV/c^2	-0.0013	0.0007
700 GeV/c^2	-0.0019	0.0029
800 GeV/c^2	-0.0040	0.0016

Table 5.2: The change in Monte Carlo signal acceptance rate, ΔA , due to shifting M_{top} by $\pm 1\sigma$.

5.2.2 M_{top} Systematic

The combined CDF and DØ top quark mass measurement has determined M_{top} to be $174.3 \pm 5.1 \text{ GeV}/c^2$ [28]. Our limits on $X \rightarrow t\bar{t}$ production assume $M_{top} = 175 \text{ GeV}/c^2$, as this is the top quark mass used in the generation of Z' and standard model $t\bar{t}$ Monte Carlo. Presently, we consider the systematic uncertainties resulting from this M_{top} assumption. For this study, we generate Z' and standard model $t\bar{t}$ Monte Carlo samples with $M_{top} = 170$ and $180 \text{ GeV}/c^2$. Processing these samples with the $M_{t\bar{t}}$ analysis cuts discussed earlier, we construct signal and background templates which reflect a $\pm 1\sigma$ error on M_{top} . For $M_X = 400, 500, 600, 700$, and $800 \text{ GeV}/c^2$ with $\Gamma = 0.012M_X$, these templates are used to establish an estimate of the M_{top} shape contribution to the dependence of Δ on $\sigma_X \cdot \text{BR}\{X \rightarrow t\bar{t}\}$. The resulting likelihood uncertainty is given in Figure 5.2.

The change in signal acceptance, ΔA , due to shifting M_{top} by $\pm 1\sigma$ is listed in Table 5.2. The resulting likelihood uncertainty as a function of $\sigma_X \cdot \text{BR}\{X \rightarrow t\bar{t}\}$ is also shown in Figure 5.2.

As before, we fit each of the two “ M_{top} Total” curves for each mass in Figure

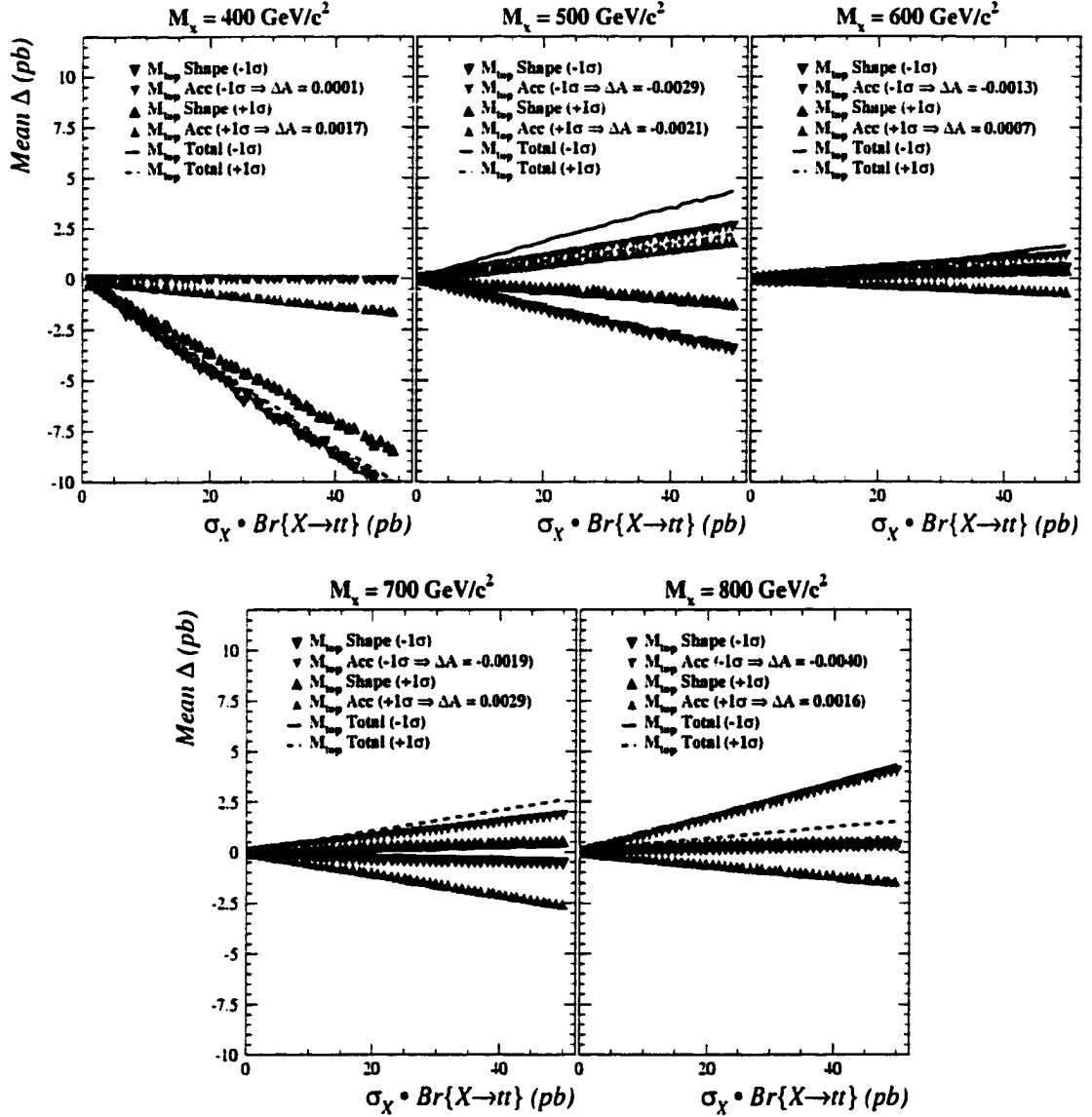


Figure 5.2: The shape and acceptance contributions to the likelihood systematic uncertainty, Δ , resulting from $\pm 1\sigma$ shifts in M_{top} .

5.2 to a line passing through the origin. We take the larger of the two slopes (for $\pm 1\sigma$) as the M_{top} systematic uncertainty as a function of $\sigma_X \cdot \text{BR}\{X \rightarrow t\bar{t}\}$ for that mass; i.e., for the M_{top} systematic, the curves that fit to slopes of 22%, 8.9%, 3.1%, 5.3% and 8.7% in magnitude are taken to be the 1σ uncertainty for $M_X = 400, 500, 600, 700$, and $800 \text{ GeV}/c^2$, respectively.

5.2.3 Initial State Radiation Systematic

Incorrect modelling of radiative jets originating from initial or final state partons will certainly affect an event's measured $M_{t\bar{t}}$ and, therefore, the signal and background templates used to establish likelihood functions which result from the fitting procedure used in this analysis.

To investigate the systematic effects of initial state radiation (ISR), we rely heavily upon the PYTHIA Monte Carlo generator because, unlike HERWIG, it allows the user to generate events with or without ISR. For this reason, the “nominal” standard model $t\bar{t}$ template in this study comes from PYTHIA $t\bar{t}$ Monte Carlo generated at a top mass of $175 \text{ GeV}/c^2$. The $M_{t\bar{t}}$ templates which reflect the elimination of ISR also come from Z' and standard model $t\bar{t}$ Monte Carlo generated with PYTHIA. As a very conservative estimate, we assume that one-half of the effect realized by the removal of ISR is an approximation of changing ISR by -1σ . We further assume that the magnitude of the shape systematic observed for this -1σ shift is unchanged for a $+1\sigma$ shift in ISR, but its sign is reversed. For $M_X = 400, 500, 600, 700$, and $800 \text{ GeV}/c^2$ and $\Gamma = 0.012M_X$, an estimate for the ISR shape contribution to Δ is given in Figure 5.3.

The elimination of ISR changes the signal acceptance as listed in Table 5.3. As with ISR shape effects, we assume that (a) one-half of this change is a conservative estimate of the effect due to a -1σ shift and (b) for a $+1\sigma$ shift in ISR, the

M_X	Change in A due to eliminating ISR
400 GeV/c ²	-0.0063
500 GeV/c ²	-0.0066
600 GeV/c ²	-0.0029
700 GeV/c ²	-0.0030
800 GeV/c ²	-0.0055

Table 5.3: The change in Monte Carlo signal acceptance rate due to eliminating ISR. One-half of this change is taken to be the -1σ uncertainty in signal acceptance due to ISR. The -1σ and $+1\sigma$ uncertainties are assumed to be symmetric.

magnitude of the change in A is unchanged, but the sign is reversed. The resulting likelihood uncertainty as a function of $\sigma_X \cdot \text{BR}\{X \rightarrow t\bar{t}\}$ is also shown in Figure 5.3.

By definition, the magnitude of the ISR shape effects for $+1\sigma$ and -1σ shifts are equal for a given mass. But from Equation 5.1 in Section 5.1.2, if ΔA is symmetric (as we assume), then the magnitude of the acceptance effect is asymmetric. Therefore, as the elimination of ISR reduces signal acceptance for all M_X (see Table 5.3), it is the -1σ “ISR Total” curve, in all cases, which fits to the largest slope and represents the ISR systematic uncertainty for each mass; *i.e.*, for the ISR systematic, the curves that fit to slopes of 14%, 10%, 4.2%, 3.7% and 5.6% are taken to be the 1σ uncertainty for $M_X = 400, 500, 600, 700$, and $800 \text{ GeV}/c^2$, respectively.

5.2.4 Final State Radiation Systematic

Ideally, to investigate the systematic effects of incorrectly modelling final state radiation (FSR), we would create signal and background $M_{t\bar{t}}$ templates from Monte

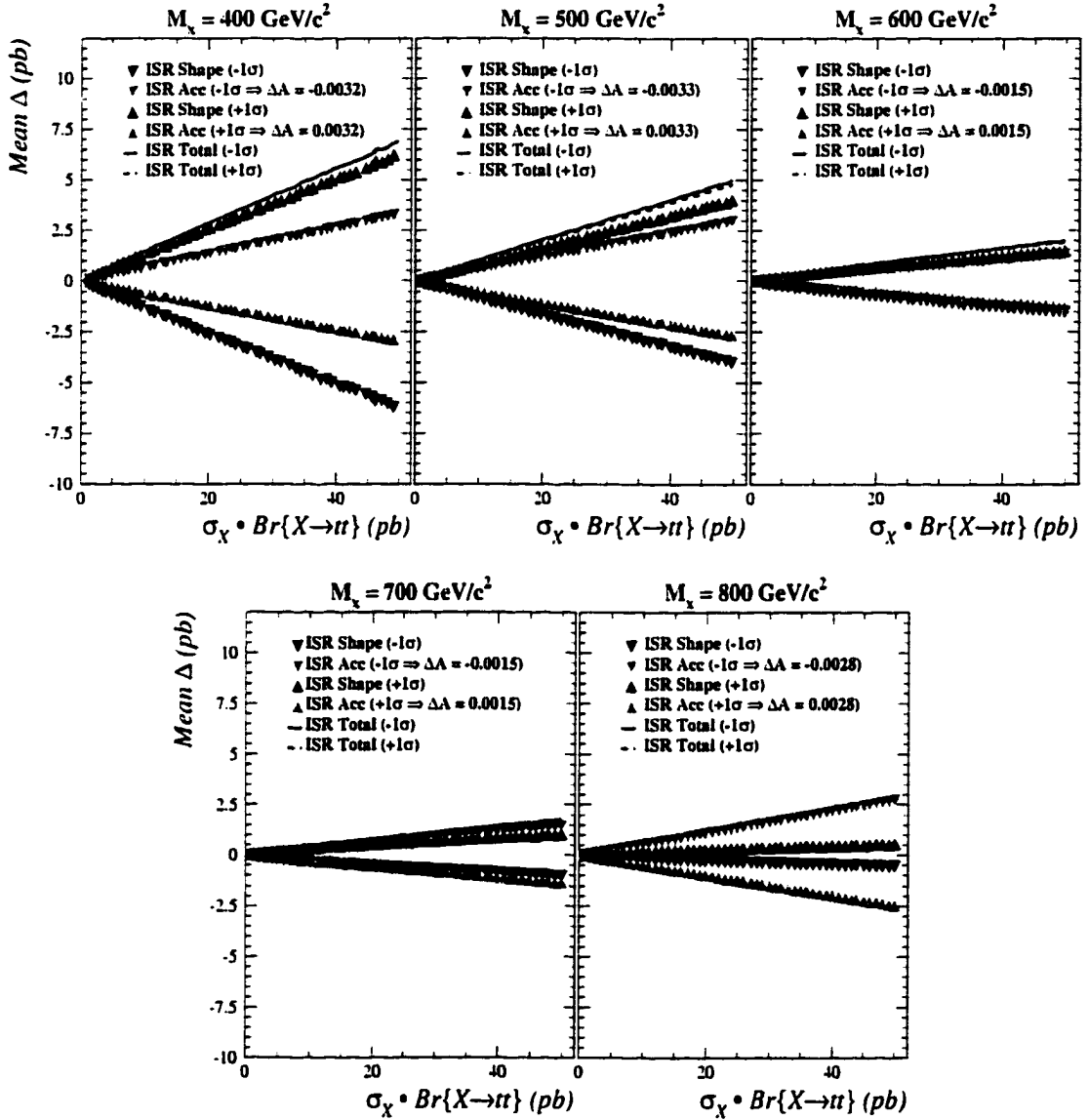


Figure 5.3: The shape and acceptance contributions to the likelihood systematic uncertainty, Δ , resulting from $\pm 1\sigma$ shifts in ISR.

Carlo samples which were generated with no FSR, as was done for the ISR systematic uncertainty. However, the resulting jets from such events would be excessively columnated and the applied jet energy corrections would no longer be appropriate. For this reason, we use Monte Carlo samples which include FSR, but we then adequately eliminate its effects by selecting only events which contain exactly four jets, each of which matches to a generator-level quark within a cone of $\Delta R = 0.4$. This procedure removes not only events affected by FSR, but can also eliminate those which are affected by ISR and any inefficiency in the matching prescription itself. We conservatively assume that the matching procedure is 100% efficient, and thus, any actual inefficiency is reflected in an overestimate of the FSR shape systematic. Additionally, we are able to isolate the systematic effects of only FSR by applying this four-jet matching method to the “no ISR” signal and background Monte Carlo samples employed in Section 5.2.3.

FSR Shape Systematic

Operationally, we establish the FSR systematic shape systematic effect by using the “no ISR” signal and background templates as “nominal FSR”; *i.e.*, pseudo-experiments are generated from PYTHIA Z' with no ISR, HERWIG $t\bar{t}$ with no ISR, and VECBOS QCD W +jets background. Then, as mentioned, M_{ii} templates which reflect no FSR are created from these “no ISR” Monte Carlo samples by selecting only those events which contain four (and only four) jets, each of which matches to a generator-level quark. As we assumed for ISR, we take one-half of the effect realized by the removal of FSR as an approximation of changing FSR by -1σ . And again, we assume that the magnitude of the shape systematic observed for this -1σ shift is equal to that resulting from a $+1\sigma$ shift in FSR, but that its sign is reversed. Shown in Figure 5.3 is the likelihood uncertainty due to shape effects

obtained from fitting pseudo-experiments to the previously described “nominal FSR” and “no FSR” templates.

FSR Acceptance Systematic

As mentioned above, the systematic effects of FSR would, ideally, be estimated by using “no FSR” Monte Carlo samples, but then the jet energy corrections would no longer be applicable due to the presence of highly columnated jets in each event.

In the shape analysis above, we isolate the systematic effect due to FSR by first starting with “no ISR” signal and background Monte Carlo samples. Yet, while some events will satisfy the analysis cuts whether FSR jets are considered or not, the presence of FSR itself in a particular event may affect the actual $M_{t\bar{t}}$ measurement for that event by:

- reducing one or more of the quark-jet energies resulting from top decay; or
- altogether replacing one or more of the quark-jets as the event’s the leading four jets.

Accordingly, in the preceeding section, we establish the effect of FSR on shape by investigating the change in the $M_{t\bar{t}}$ spectrum resulting from the elimination of events which appear to include radiative jets from the final state partons; *i.e.*, we eliminate events which:

- contain more than 4 jets; or
- contain one or more jets which do not match to the generator-level quarks resulting from top decay.

However, to establish the FSR systematic effects on signal acceptance, we investigate the change in “no ISR” Z' acceptance resulting from:

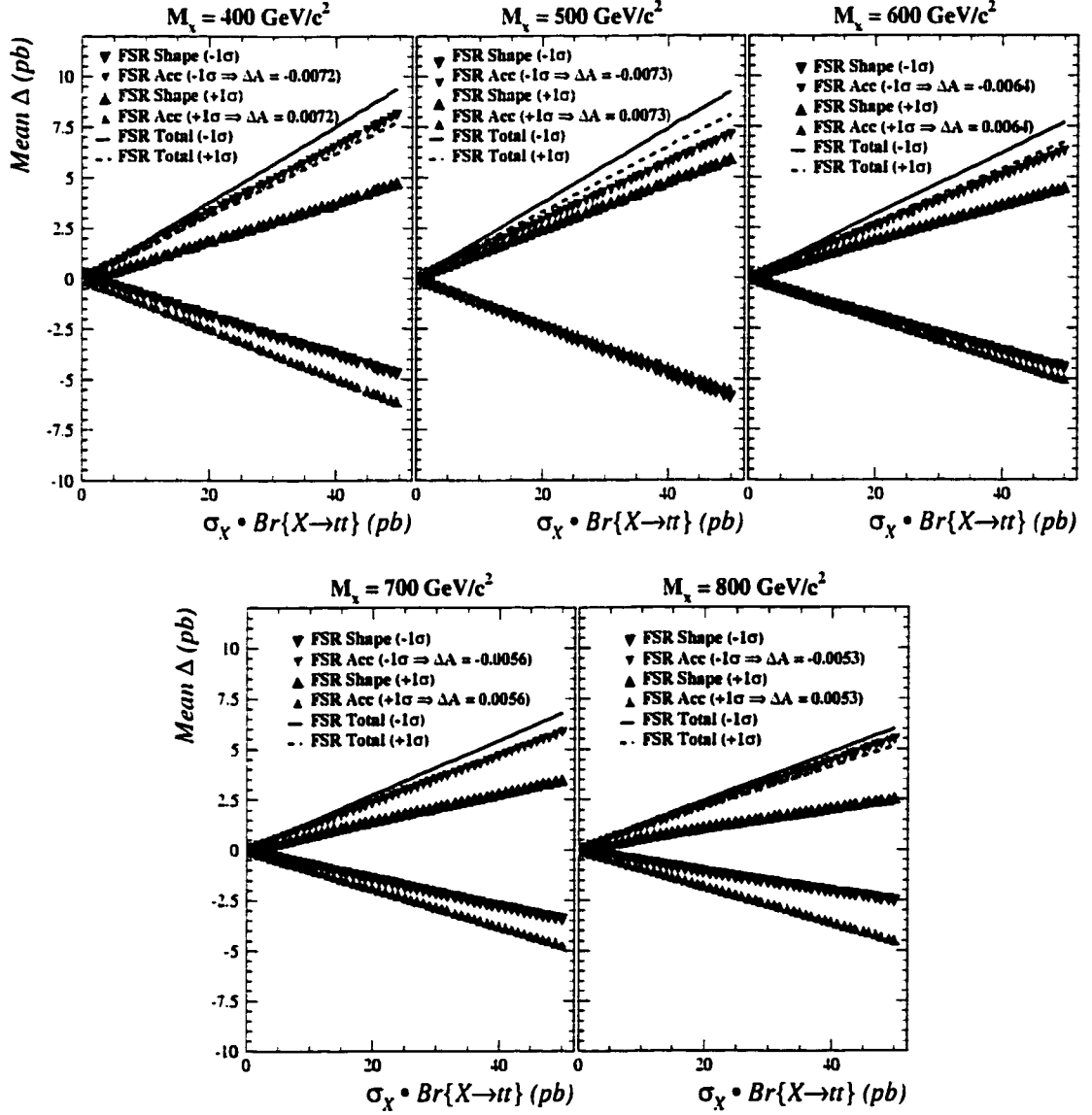


Figure 5.4: The shape and acceptance contributions to the likelihood systematic uncertainty, Δ , resulting from $\pm 1\sigma$ shifts in FSR.

- the elimination of events which pass *as a result of* FSR when they otherwise would not have passed without the presence of FSR (*e.g.*, an event in which one of the four actual $t\bar{t}$ jets failed the selection criteria, while an extra FSR jet in the event met these requirements); and
- the addition of events which pass when FSR jets are *ignored* even though they otherwise would not have passed (*e.g.*, an event in which three actual $t\bar{t}$ jets and an FSR jet constitute the leading four, but yield a $M_{jjj}^u = 100$ GeV/c², while if the fifth highest E_T jet in the event is used instead of the FSR jet, $M_{jjj}^u = 175$ GeV/c²).

Thus, we would like to establish the systematic effect of FSR on signal acceptance by first determining the “no ISR” signal acceptance, $A_{\text{no ISR}}$, from the “no ISR” Monte Carlo samples. We would then determine $A'_{\text{no ISR}}$, the acceptance for the “no ISR” events in which:

- each of the four generator-level quarks matches (1-to-1) to one of the four or more jets in the event; and
- the event survives the kinematic, $M_{3\text{-body}}$, and χ_c^2 requirements when only these four matched jets are used.

An estimate of the fractional change in total signal acceptance, A , due solely to the elimination of FSR would then be given by $\frac{\Delta A}{A_{\text{no ISR}}}$ where $\Delta A = A'_{\text{no ISR}} - A_{\text{no ISR}}$.

Unfortunately, it is somewhat difficult to determine $A'_{\text{no ISR}}$ because, in general, it requires an additional analysis of each event using a different set of four jets. For this reason, we determine an upper limit for $\frac{\Delta A}{A_{\text{no ISR}}}$ via a method that is both straightforward and operationally tenable.

To determine $A_{\text{no ISR}}$ and $A'_{\text{no ISR}}$, events can be separated into two classes: those with exactly four jets ($N_{jet} = 4$) and those with greater than four ($N_{jet} \geq 5$).

(We will subsequently designate these subsamples by superscripts of “4” and “5,” respectively.) $A_{\text{no ISR}}$ and $A'_{\text{no ISR}}$ would then be obtained simply from a sum of the acceptances determined in the two exclusive N_{jet} subsamples, *i.e.*, $A_{\text{no ISR}} = A^4_{\text{no ISR}} + A^5_{\text{no ISR}}$ and $A'_{\text{no ISR}} = A^{4'}_{\text{no ISR}} + A^{5'}_{\text{no ISR}}$, where $A^n_{\text{no ISR}}$ ($A^{n'}_{\text{no ISR}}$) is the “ n ”-subsample component of $A_{\text{no ISR}}$ ($A'_{\text{no ISR}}$).

In an effort to establish an upper limit on $\frac{\Delta A}{A_{\text{no ISR}}}$, we propose that

$$\frac{A^{5'}_{\text{no ISR}}}{A^5_{\text{no ISR}}} \geq \frac{A^{4'}_{\text{no ISR}}}{A^4_{\text{no ISR}}}. \quad (5.2)$$

Due to the kinematic jet cuts used in this analysis, events with $N_{jet} = 4$ which contribute to $A'_{\text{no ISR}}$ must necessarily also contribute to $A_{\text{no ISR}}$ (that is, $N_{jet} = 4$ events can only be eliminated by requiring that the four jets match to generator-level partons and the event still survive the $M_{t\bar{t}}$ cuts). Yet, it is possible that events with $N_{jet} \geq 5$ will contribute to $A'_{\text{no ISR}}$, but not to $A_{\text{no ISR}}$ (that is, in addition to eliminating some events, the requirement that four jets – but not necessarily the leading four – match to generator-level partons and that the event still satisfy the $M_{t\bar{t}}$ cuts allows *additional* events to survive). Therefore, we expect that $A^{5'}_{\text{no ISR}} \approx A^5_{\text{no ISR}}$ (or possibly, $A^{5'}_{\text{no ISR}} > A^5_{\text{no ISR}}$). Quantitatively, we have found that for “no ISR” Monte Carlo Z' samples of various masses, $\frac{A^{4'}_{\text{no ISR}}}{A^4_{\text{no ISR}}} \approx 0.78$ (see Table 5.4). Certainly then, it is reasonable to assume that for this analysis Inequality (5.2) holds absolutely.

From Inequality (5.2), it can be shown that

$$\frac{\Delta A^4}{A^4_{\text{no ISR}}} \geq \frac{\Delta A}{A_{\text{no ISR}}} \quad (5.3)$$

where $\Delta A^4 = A^4_{\text{no ISR}} - A^{4'}_{\text{no ISR}}$. And, therefore, we have established that $\frac{\Delta A^4}{A^4_{\text{no ISR}}}$, a quantity that we can calculate in a straightforward manner, is an upper limit on

	$M_{Z'} = 400 \text{ GeV}/c^2$	$M_{Z'} = 500 \text{ GeV}/c^2$	$M_{Z'} = 600 \text{ GeV}/c^2$	$M_{Z'} = 700 \text{ GeV}/c^2$	$M_{Z'} = 800 \text{ GeV}/c^2$
$N_{\text{no ISR}}^4$	1842	2131	2307	2136	2110
$N_{\text{no ISR}}^{4'}$	1357	1636	1824	1719	1720
$N_{\text{no ISR}}^5$	717	837	796	757	649
$\frac{A_{\text{no ISR}}^{4'}}{A_{\text{no ISR}}^4}$	0.72	0.75	0.78	0.79	0.80

Table 5.4: Number of events and acceptance ratio for N_{jet} subsamples described in the text. Note: $\frac{A_{\text{no ISR}}^{4'}}{A_{\text{no ISR}}^4} = \frac{N_{\text{no ISR}}^{4'}}{N_{\text{no ISR}}^4}$ only holds *approximately* due tagging, lepton identification, and “Level 3” efficiencies.

$$\frac{\Delta A}{A_{\text{no ISR}}}.$$

Table 5.5 lists $A_{\text{no ISR}}^4$, $A_{\text{no ISR}}^{4'}$, ΔA^4 , and the upper limit on the change in total signal acceptance, A , due eliminating FSR. As before, we assume that (a) one-half of this change is a conservative estimate of the effect due to a -1σ shift and (b) for a $+1\sigma$ shift in FSR, the magnitude of the change in A is unchanged, but the sign is reversed. The resulting likelihood uncertainty as a function of $\sigma_X \cdot \text{BR}\{X \rightarrow t\bar{t}\}$ is also shown in Figure 5.4.

Again, for each mass, we fit each of the two “FSR Total” curves in Figure 5.4 to a line passing through the origin. For the same reasons mentioned in Section 5.2.3, we find that it is the -1σ “FSR Total” curve, in all cases, which fits to the largest slope and represents the FSR systematic uncertainty as a function of $\sigma_X \cdot \text{BR}\{X \rightarrow t\bar{t}\}$; i.e., for the FSR systematic, the curves that fit to slopes of 19%, 19%, 16%, 14% and 12% are taken to be the 1σ uncertainty for $M_X = 400, 500, 600, 700$, and

M_X	$A_{\text{no ISR}}^4$	$A_{\text{no ISR}}^{4'}$	ΔA^4	$\frac{\Delta A^4}{A_{\text{no ISR}}^4} \cdot A$
400 GeV/c ²	0.0323	0.0232	0.0091	-0.0144
500 GeV/c ²	0.0374	0.0281	0.0093	-0.0146
600 GeV/c ²	0.0405	0.0314	0.0090	-0.0127
700 GeV/c ²	0.0374	0.0297	0.0077	-0.0111
800 GeV/c ²	0.0370	0.0297	0.0073	-0.0106

Table 5.5: Monte Carlo signal acceptance rates as described in the text. The upper limit on the change in acceptance due to no FSR is given by $\frac{\Delta A^4}{A_{\text{no ISR}}^4} \cdot A$.

800 GeV/c², respectively.

5.2.5 b -tagging Systematic

Next we consider the effects due to the uncertainty in the rate of identifying b -jets using the tagging algorithms described in Section 3.1.4.

b -tagging Shape Systematic

While an error in the b -tagging efficiency would have a negligible effect on the acceptance rate (see Section 5.8.1), it is possible that a change in the tagging information available in a particular event would change the measured $M_{t\bar{t}}$ [29]. We investigated the systematic shape effects of the b -tagging rate by comparing results from the nominal templates to those from $M_{t\bar{t}}$ signal and background templates which include only “tagged” events ($+1\sigma$) or only “untagged” events (-1σ). We understand this to be a very conservative estimate of an effect that is already expected to be small. The resulting likelihood uncertainty as a function of $\sigma_X \cdot \text{BR}\{X \rightarrow t\bar{t}\}$ is shown in Figure 5.5.

Because we assume that the uncertainty in b -tagging efficiency has a negligible effect on acceptance, we fit each of the two “ b -tagging Shape” curves to a line

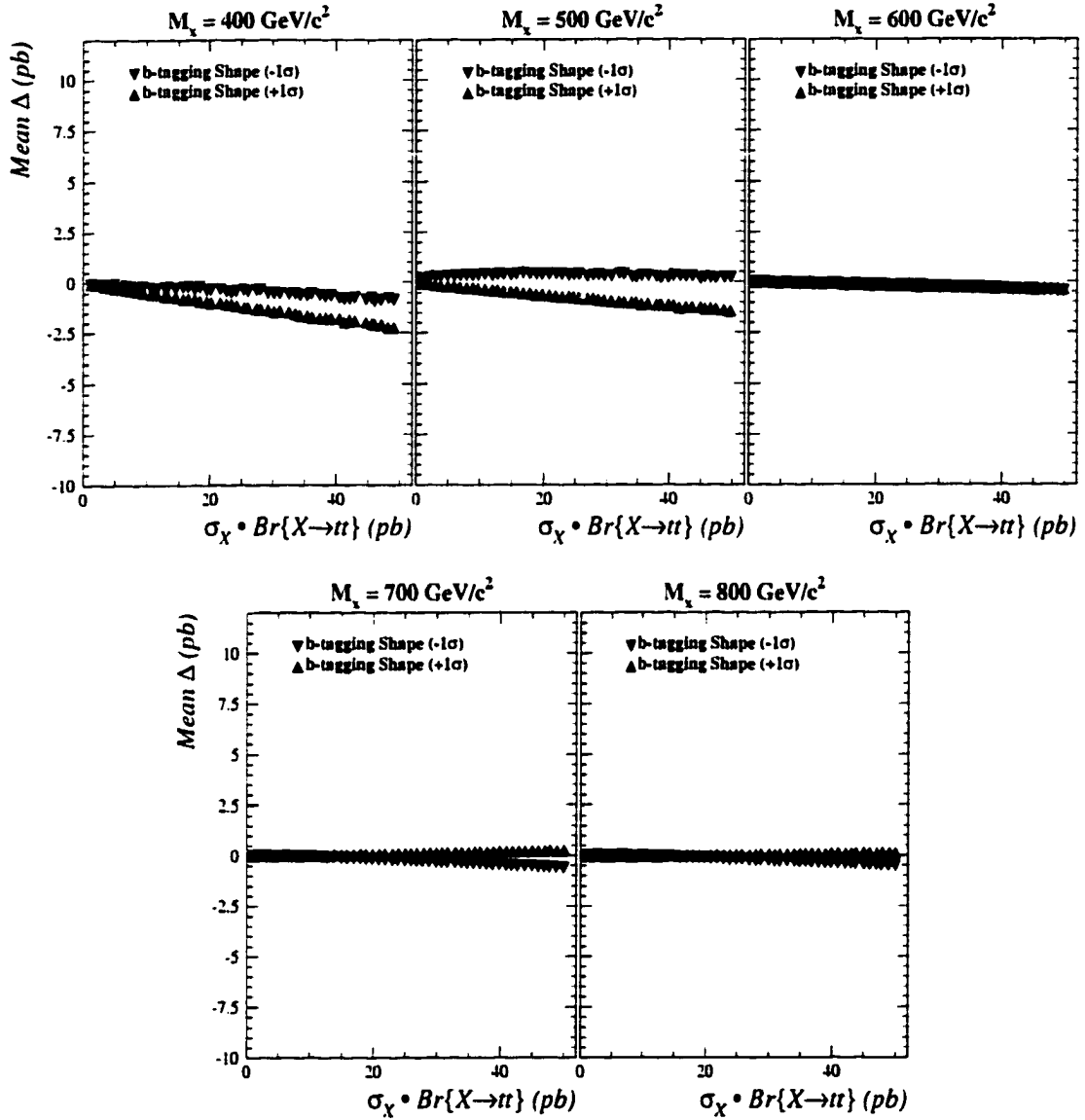


Figure 5.5: The shape and acceptance contributions to the likelihood systematic uncertainty, Δ , resulting from $\pm 1\sigma$ shifts in the b -tagging efficiency. The $+1\sigma$ curve is obtained by using a template comprised of only Monte Carlo events which contain a b -tag, while the -1σ curve results from using the distribution of untagged simulated events.

passing through the origin for each mass in Figure 5.5. We take the larger of the two slopes (for $\pm 1\sigma$) as the systematic uncertainty due to b -tagging efficiency as a function of $\sigma_X \cdot \text{BR}\{X \rightarrow t\bar{t}\}$; i.e., the curves that fit to slopes of 4.6%, 2.9%, 0.79%, 1.1% and 0.85% for $M_X = 400, 500, 600, 700$, and $800 \text{ GeV}/c^2$, respectively.

b -tagging Acceptance Systematic

Unlike many analyses which rely on b -tagging information, a reasonable error in our estimate of the data b -tagging rate would have essentially no effect on the background or signal acceptance rates. If the jet E_T and η requirements were identical for “tagged” and “untagged” events, then it is obvious that the signal and background acceptances would be independent of the b -tagging rate. In this $M_{t\bar{t}}$ analysis, the only additional kinematic requirement for an “untagged” event is that the fourth jet, like the first three, also satisfy the “tight” jet requirements. Yet, a change in the b -tagging rate would introduce a scale factor, F , which would affect the signal or background acceptance, A , in the following way:

$$A \sim \frac{F N_{tag} + (1 - F) R N_{tag} + N_{untag}}{N_{generated}} \quad (5.4)$$

where

- N_{tag} = number of surviving tagged events,
- N_{untag} = number of surviving untagged events,
- $R = \frac{\text{number of tagged events with a 4}^{th} \text{ tight jet}}{\text{number of tagged events}}.$

Re-written, the Equation 5.4 becomes

$$A \sim \frac{[F + (1 - F)R]N_{tag} + N_{untag}}{N_{generated}} \quad (5.5)$$

From this expression, it can be seen that A is independent of F (*i.e.*, the b -tagging rate) if $[F + (1 - F)R]$ is constant. For significant changes in F , we have found that $[F + (1 - F)R]$ differs from unity by less than 3% and we therefore conclude that the systematic uncertainty on b -tagging rate has a negligible effect on systematic acceptance effects in this analysis.

5.2.6 Structure Function Systematic

In addition to the VECBOS QCD W +jets background sample, the Monte Carlo we use in constructing the nominal $M_{t\bar{t}}$ templates comes from PYTHIA Z' using the CTEQ2L structure function and HERWIG standard model $t\bar{t}$ using MRSD0'. These were the favored choices of parton distribution function at the time of generation for both the Z' and $t\bar{t}$ Monte Carlo. To investigate the systematic effect of the structure function uncertainty, we compare the results from the nominal templates to those from PYTHIA Z' using MRSD0' and HERWIG $t\bar{t}$ using CTEQ2L. We assume that a -1σ shift in structure function is represented by changing the structure functions in this manner. And for the $+1\sigma$ shift, we assume that magnitude of the observed change in $\bar{\Delta}$ is unchanged, but that the sign is reversed (for both shape and acceptance). For $\Gamma = 0.012M_X$, these templates are used to establish an estimate of the structure function shape contribution to Δ . The resulting likelihood uncertainty is given in Figure 5.6.

The change in signal acceptance, ΔA , due to shifting the structure function by -1σ is listed in Table 5.6. The resulting likelihood uncertainty as a function of $\sigma_X \cdot \text{BR}\{X \rightarrow t\bar{t}\}$ is also shown in Figure 5.6.

After fitting the two "Total" curves for each mass in Figure 5.6 to a line passing through the origin, we select the curve which fits to the largest slope as an estimate of the structure function systematic uncertainty as a function of $\sigma_X \cdot \text{BR}\{X \rightarrow t\bar{t}\}$;

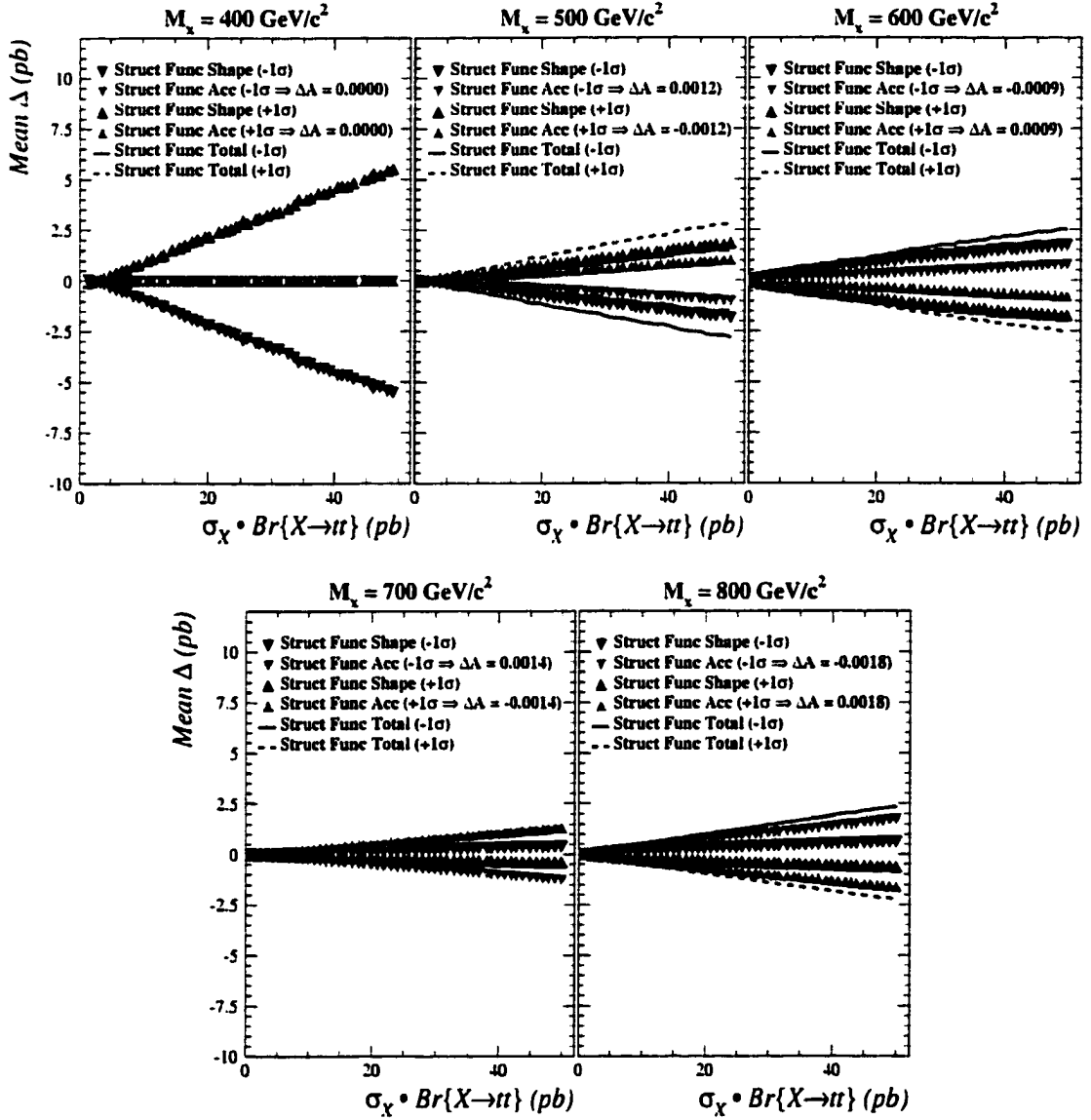


Figure 5.6: The shape and acceptance contributions to the likelihood systematic uncertainty, Δ , resulting from $\pm 1\sigma$ shifts in structure function.

M_x	Change in A for MRSD0'
400 GeV/c ²	0.0000
500 GeV/c ²	0.0012
600 GeV/c ²	-0.0009
700 GeV/c ²	0.0014
800 GeV/c ²	-0.0018

Table 5.6: The change in Monte Carlo signal acceptance rate, ΔA , due to using the MRSD0' structure function instead of CTEQ2L (assumed to be a -1σ shift in structure function uncertainty).

i.e., for the structure function systematic, the curves that fit to slopes of 11%, 5.8%, 5.5%, 2.8% and 4.8% in magnitude are taken to be the 1σ uncertainty for $M_x = 400, 500, 600, 700$, and 800 GeV/c², respectively.

5.2.7 QCD Background Shape Systematic

The nominal VECBOS QCD W+jets background shape is generated with Q^2 set equal to the average of the jet P_T^2 (*viz.*, $\langle P_T^2 \rangle$). Here, we investigate the effect of changing the QCD W+jets background shape by selecting $Q^2 = M_W^2$ and take this change to be representative of a 1σ uncertainty in the QCD W+jets background shape. For $M_x = 400, 500, 600, 700$, and 800 GeV/c² with $\Gamma = 0.012M_x$, the resulting likelihood uncertainty Δ is very small, as expected. This functional form of Δ , which represents the 1σ systematic uncertainty due to the QCD W+jets shape uncertainty, fits to a line passing through the origin with slopes of 1.3%, 0.52%, 0.17%, 0.11% and 0.045% in magnitude for $M_x = 400, 500, 600, 700$, and 800 GeV/c², respectively.

M_X	ΔA due to additional acceptance systematics
400 GeV/c ²	0.0026
500 GeV/c ²	0.0029
600 GeV/c ²	0.0029
700 GeV/c ²	0.0027
800 GeV/c ²	0.0027

Table 5.7: The 1σ uncertainty in Monte Carlo signal acceptance rate, ΔA , due to several additional acceptance sources such as trigger efficiency, lepton identification efficiency, tracking efficiency, z -vertex efficiency, and Monte Carlo statistics.

5.2.8 Additional Acceptance Systematics

We take $0.05A$ to be the 1σ systematic uncertainty in the signal acceptance due to uncertainty in trigger efficiency (1% [9]); lepton identification efficiency, tracking efficiency, z -vertex efficiency (4% [30]); and Monte Carlo statistics (2%, see Section 4.2.1). The systematic uncertainty in A due to these additional sources is shown in Table 5.7. Following our established convention, if we assume that ΔA is symmetric and is equal to $\pm 0.05A$, then the M_X -independent slope of the resulting likelihood uncertainty as a function of $\sigma_X \cdot \text{BR}\{X \rightarrow t\bar{t}\}$ is determined to be 5.3% for $\Delta A = -0.05A$ (*cf.*, Equation 5.1 in Section 5.1.2).

5.2.9 Luminosity Systematic

In a separate CDF analysis, the total integrated luminosity, $\int \mathcal{L} dt$, was measured to be $106.0 \pm 4.1 \text{ pb}^{-1}$ [11]. Because this uncertainty is effectively an acceptance effect, the functional form of the contribution to Δ is given by:

	Change in $X \rightarrow t\bar{t}$ Acceptance, A , Due to $\pm 1\sigma$ Systematic Shifts				
Source of Systematic Uncertainty	$M_X =$ 400 GeV/c ²	$M_X =$ 500 GeV/c ²	$M_X =$ 600 GeV/c ²	$M_X =$ 700 GeV/c ²	$M_X =$ 800 GeV/c ²
Jet E_T	+0.0001 -0.0012	+0.0000 +0.0008	+0.0002 +0.0003	+0.0005 -0.0002	+0.0006 -0.0007
M_{top}	+0.0017 +0.0001	-0.0021 -0.0029	+0.0007 -0.0013	+0.0029 -0.0019	+0.0016 -0.0040
ISR	+0.0032 -0.0032	+0.0033 -0.0033	+0.0015 -0.0015	+0.0015 -0.0015	+0.0028 -0.0028
FSR	+0.0072 -0.0072	+0.0073 -0.0073	+0.0064 -0.0064	+0.0055 -0.0055	+0.0053 -0.0053
Structure Function	-0.0000 +0.0000	-0.0012 +0.0012	-0.0009 +0.0009	-0.0014 +0.0014	-0.0018 +0.0018
Additional Sources	+0.0026 -0.0026	+0.0029 -0.0029	+0.0029 -0.0029	+0.0027 -0.0027	+0.0027 -0.0027

Table 5.8: The 1σ systematic uncertainty (ΔA) in the Monte Carlo signal acceptance, A . The top and bottom values for each entry represent changes due to shifting the given systematic by $+1\sigma$ and -1σ , respectively.

$$\Delta = \left(\frac{\int \mathcal{L} dt}{\int \mathcal{L} dt \pm 4.1 \text{pb}^{-1}} - 1 \right) \sigma_{\text{fit}}.$$

The slope of the resulting likelihood uncertainty as a function of $\sigma_X \cdot \text{BR}\{X \rightarrow t\bar{t}\}$ is then 4.0% and is independent of M_X .

5.2.10 Summary of Acceptance Systematics

In summary, the changes in signal acceptance, A , due to the various sources of systematic uncertainty are listed in Table 5.8.

5.2.11 Correlation Between Jet E_T and M_{top} Systematics

It has been suggested that perhaps the systematic effects of M_{top} and jet E_T are highly correlated and treating them as independent effects is overly optimistic. To

investigate this possibility, we create signal and background templates which reflect simultaneously the 1σ uncertainties in both M_{top} and jet E_T ; these shapes result from Monte Carlo generated with $M_{top} = 170$ or $180 \text{ GeV}/c^2$ and jet E_T shifted by $\pm 1\sigma$. Then, using these templates, we performed pseudo-experiment studies which indicate that the shape effects from M_{top} and jet E_T uncertainties are somewhat correlated. As a result, we conservatively assume that the two are 100% correlated and, therefore, obtain a combined jet E_T/M_{top} systematic by adding the totals for the two sources linearly.

5.2.12 Combining Systematics

Having determined the total (shape + acceptance) systematic uncertainty for each source, we now combine them to determine the overall uncertainty for each value of M_x . As discussed in Section 5.2.11, we assume that, for a given value of M_x , the effects due to jet E_T and M_{top} are 100% correlated and add linearly. The combined jet E_T/M_{top} systematic and all other sources are assumed to be uncorrelated with each other and, therefore, add in quadrature. A linear fit to this quadrature sum is constrained to pass through the origin and is shown for $M_x = 400, 500, 600, 700$, and $800 \text{ GeV}/c^2$ in Figures 5.7 through 5.11. Also shown in these figures are the contributions from the various individual sources of systematic uncertainty.

In an effort to remain conservative in our estimate of systematic uncertainties, the value of Δ is assumed to be constant for values of $\sigma_x \cdot \text{BR}\{X \rightarrow t\bar{t}\}$ which are less than the unsmeared 95% C.L. values listed in Table 4.3. While conservative at small values of $\sigma_x \cdot \text{BR}\{X \rightarrow t\bar{t}\}$, it is overly optimistic to assume for large values of $\sigma_x \cdot \text{BR}\{X \rightarrow t\bar{t}\}$ that Δ is given by the value corresponding to the unsmeared 95% C.L. limit. However, our method of assuming a constant value of Δ only for values of $\sigma_x \cdot \text{BR}\{X \rightarrow t\bar{t}\}$ which are less than the limits listed in Table 4.3 avoids any

underestimate of the systematic uncertainty above the value of unsmeared 95% C.L. limit.

For $M_X = 400, 500, 600, 700,$ and $800 \text{ GeV}/c^2$, we fit the combined systematic uncertainty curve to a line passing through the origin and take its slope as the overall systematic uncertainty Δ as a function of $\sigma_X \cdot \text{BR}\{X \rightarrow t\bar{t}\}$ for values of $\sigma_X \cdot \text{BR}\{X \rightarrow t\bar{t}\}$ greater than the 95% C.L. limits listed in Table 4.3. These values of slope and their individual contributions are listed in Table 5.9. For $M_X = 450, 550, 650,$ and $750 \text{ GeV}/c^2$, we interpolate between the values in Table 5.9 to determine the portion of Δ with non-zero slope. Furthermore, we assume that the systematic uncertainty for $M_X = 800 \text{ GeV}/c^2$ applies to all $M_X \geq 800 \text{ GeV}/c^2$. The non-zero slope of the total systematic uncertainty for $M_X = 400 \text{ GeV}/c^2$ to $1 \text{ TeV}/c^2$ is listed in Table 5.10.

5.2.13 Systematics for $\Gamma = 0.04M_X$

For resonances with a natural width Γ that is significantly less than $0.06M_X$, the CDF detector resolution is dominant and the $M_{t\bar{t}}$ templates for a given resonance mass are all expected to have very similar shapes. For this reason, the above systematics, established for $M_X = 400 \text{ GeV}/c^2$ to $1 \text{ TeV}/c^2$ with natural width $\Gamma = 0.012M_X$, are also expected to be valid uncertainties for convoluting the $\Gamma = 0.04M_X$ likelihood shapes. To be certain, we use the methods described above to determine the FSR and ISR contributions to the likelihood systematic uncertainty at $M_X = 500 \text{ GeV}/c^2$ for $\Gamma = 0.04M_X$. We choose $M_X = 500 \text{ GeV}/c^2$ because of its direct relevance to the data in this region. Furthermore, we selected FSR and ISR as sources of interest due to their significant contribution to the systematic uncertainty at $M_X = 500 \text{ GeV}/c^2$ for $\Gamma = 0.012M_X$. We find that (a) the FSR total systematic uncertainty at $\Gamma = 0.04M_X$ is nearly *identical* to that at $\Gamma = 0.012M_X$

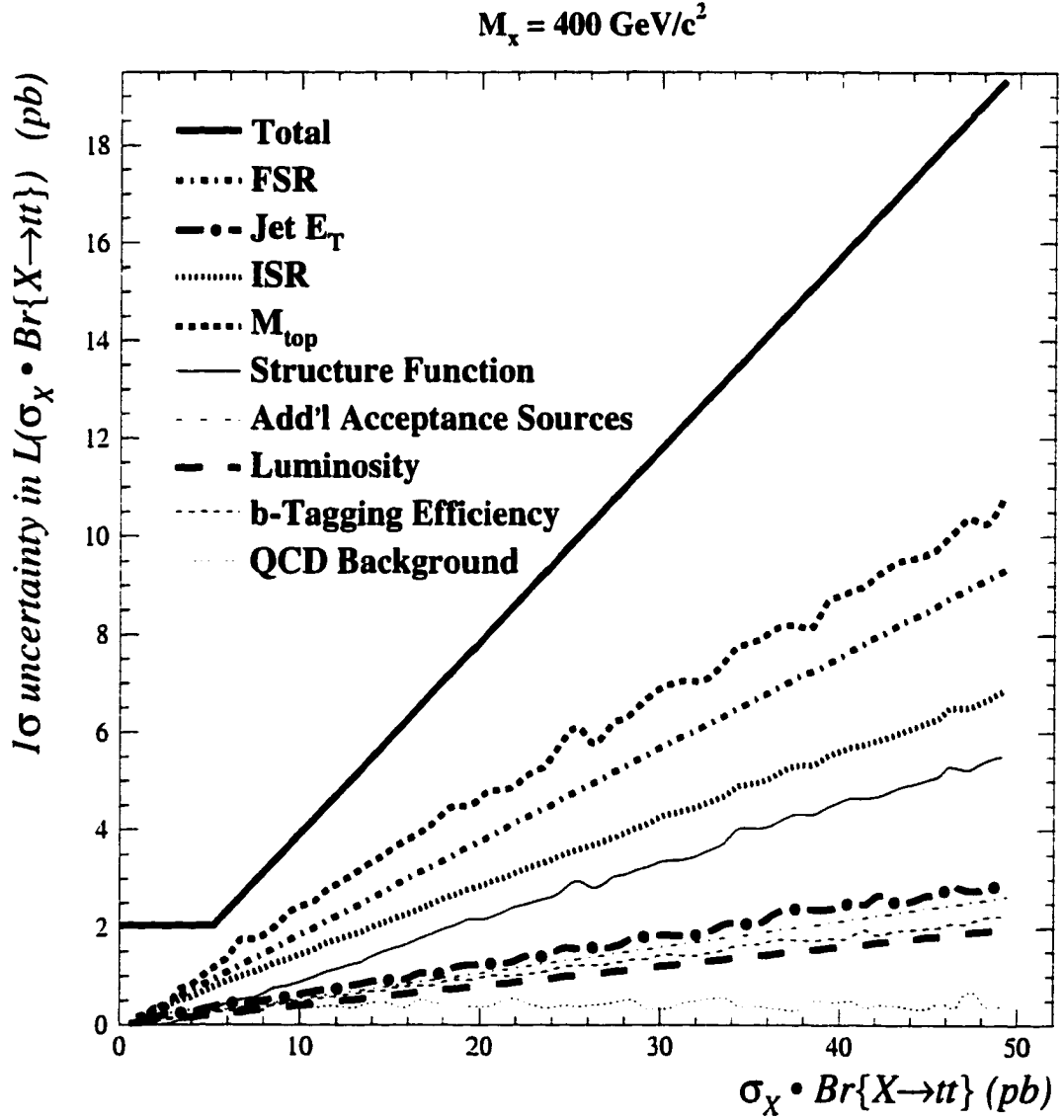


Figure 5.7: The total and individual contributions to the likelihood uncertainty, Δ , for $M_X = 400 \text{ GeV}/c^2$ resulting from $\pm 1\sigma$ shifts in each source of systematic uncertainty.

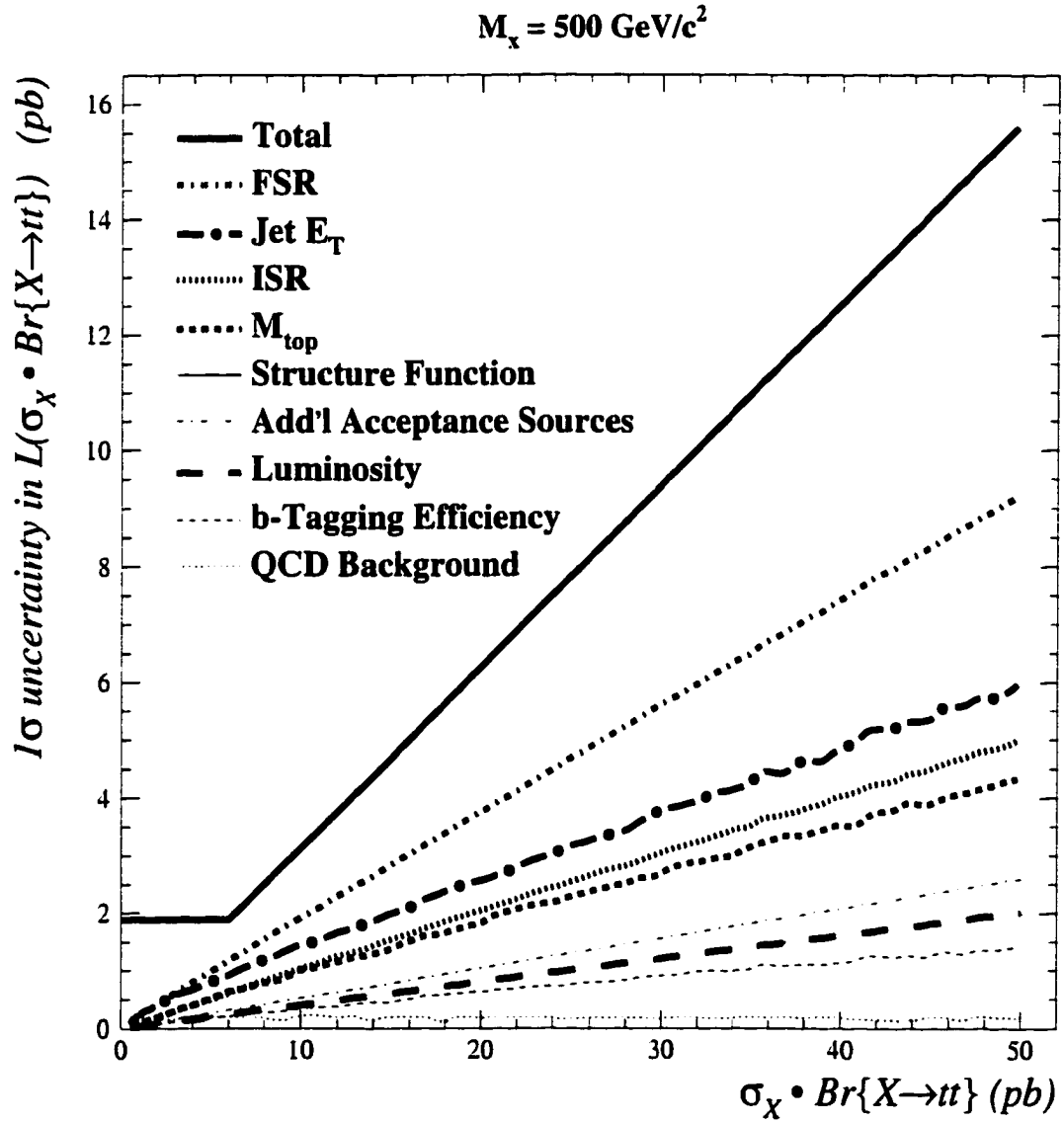


Figure 5.8: The total and individual contributions to the likelihood uncertainty, Δ , for $M_X = 500 \text{ GeV}/c^2$ resulting from $\pm 1\sigma$ shifts in each source of systematic uncertainty.

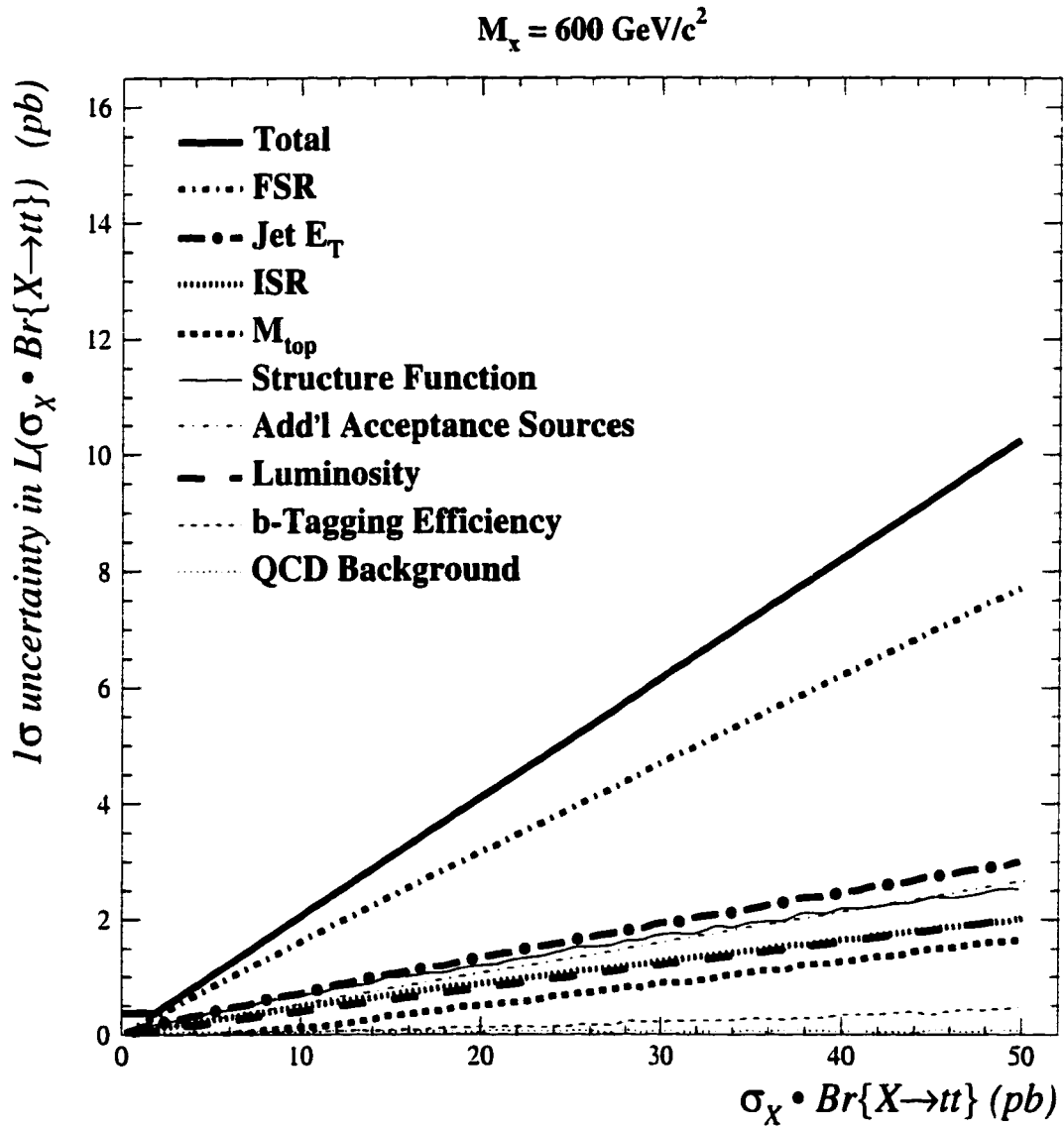


Figure 5.9: The total and individual contributions to the likelihood uncertainty, Δ , for $M_X = 600 \text{ GeV}/c^2$ resulting from $\pm 1\sigma$ shifts in each source of systematic uncertainty.

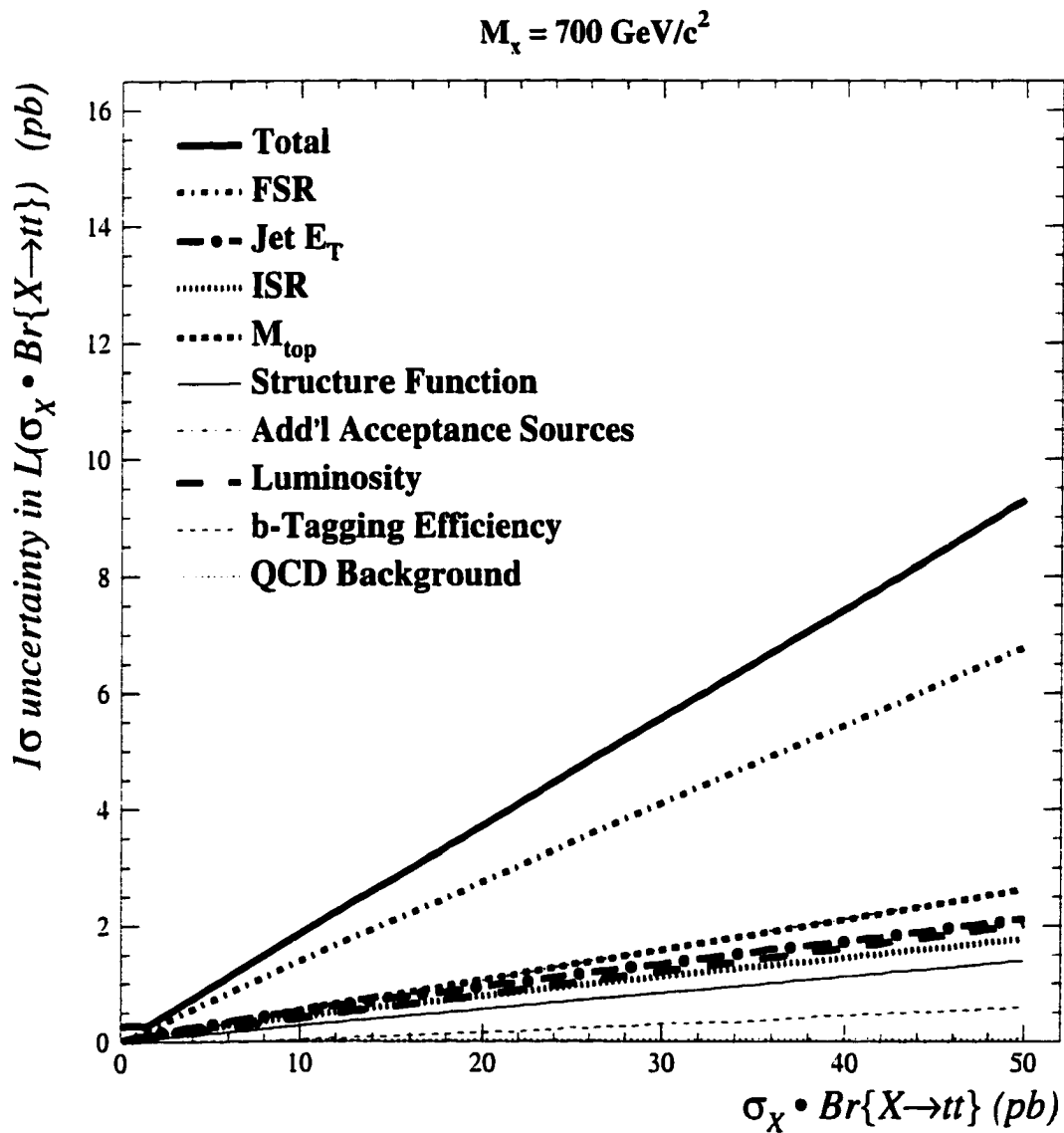


Figure 5.10: The total and individual contributions to the likelihood uncertainty, Δ , for $M_X = 700 \text{ GeV}/c^2$ resulting from $\pm 1\sigma$ shifts in each source of systematic uncertainty.

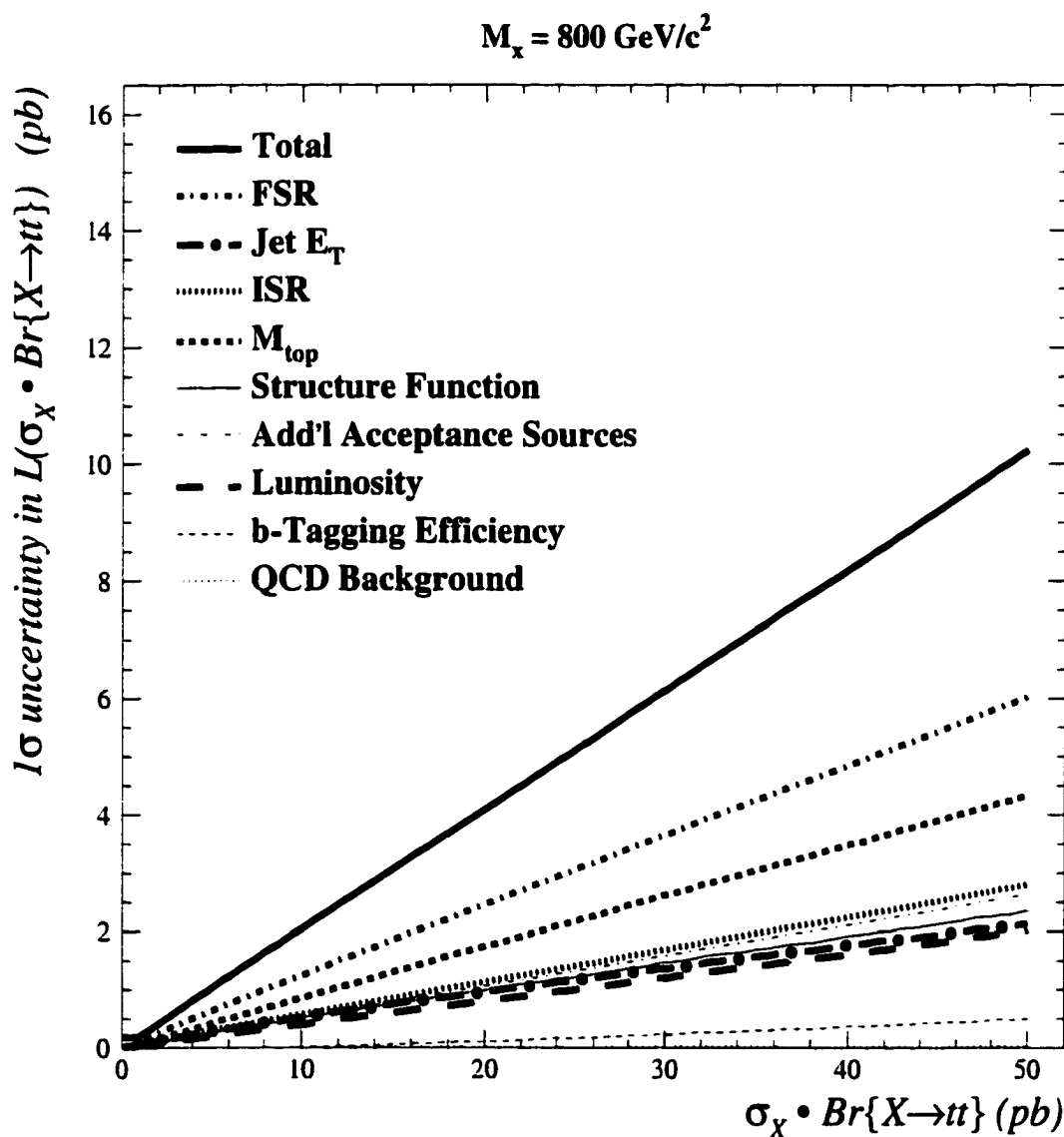


Figure 5.11: The total and individual contributions to the likelihood uncertainty, Δ , for $M_X = 800 \text{ GeV}/c^2$ resulting from $\pm 1\sigma$ shifts in each source of systematic uncertainty.

	Systematic Uncertainty in Likelihood (values in percent of $\sigma_X \cdot \text{BR}\{X \rightarrow t\bar{t}\}$)				
	$M_X =$ 400 GeV/c ²	$M_X =$ 500 GeV/c ²	$M_X =$ 600 GeV/c ²	$M_X =$ 700 GeV/c ²	$M_X =$ 800 GeV/c ²
Jet E_T	6.1	12	6.2	4.4	4.4
M_{top}	22	8.9	3.1	5.3	8.7
Jet E_T and M_{top}	28	21	9.3	9.7	13
Initial state radiation	14	10	4.2	3.7	5.6
Final state radiation	19	19	16	14	12
b -tagging	4.6	2.9	0.79	1.1	0.85
Structure function	11	5.8	5.5	2.8	4.8
QCD background shape	1.3	0.52	0.17	0.11	0.045
Additional acceptance effects	5.3	5.3	5.3	5.3	5.3
Luminosity	4.0	4.0	4.0	4.0	4.0
Total	39	26	21	19	20

Table 5.9: The systematic uncertainty in likelihood value as a percentage of $\sigma_X \cdot \text{BR}\{X \rightarrow t\bar{t}\}$. These values are determined directly using methods described in Section 5 with results depicted in Figures 5.7 through 5.11. We take these values to be valid only for $\sigma_X \cdot \text{BR}\{X \rightarrow t\bar{t}\}$ greater than the 95% C.L. limits which do *not* include systematic uncertainties (Table 4.3). Below the unsmeared 95% C.L. limit, the total systematic uncertainty is assumed to be constant.

M_x (GeV/c ²)	Total systematic uncertainty as a percentage of $\sigma_x \cdot \text{BR}\{X \rightarrow t\bar{t}\}$
400	39
450	35
500	31
550	26
600	21
650	20
700	19
750	20
800	20
850	20
900	20
950	20
1000	20

Table 5.10: For $M_x = 400$ GeV/c² to 1 TeV/c², the total systematic likelihood uncertainty, Δ , listed as percentage of $\sigma_x \cdot \text{BR}\{X \rightarrow t\bar{t}\}$. We take these values to be valid only for $\sigma_x \cdot \text{BR}\{X \rightarrow t\bar{t}\}$ greater than the 95% C.L. limits which do *not* include systematic uncertainties (Table 4.3). Below the unsmeared 95% C.L. limit, the total systematic uncertainty is assumed to be constant.

and (b) the ISR total systematic (as well as its shape and acceptance components) is *smaller* at $\Gamma = 0.04M_X$ than at $\Gamma = 0.012M_X$. Therefore, we believe that it is reasonable to assume that the conservative systematic uncertainties determined for $\Gamma = 0.012M_X$ also hold for $\Gamma = 0.04M_X$. However, the point at which Δ is taken to be constant depends on the 95% C.L. limit without systematics (as listed in Table 4.3).

5.3 Results Including Systematic Uncertainty

As mentioned, the effects of systematic uncertainty are included by convoluting the likelihood functions for each mass and natural width ($M_X = 400 \text{ GeV}/c^2$ to $1 \text{ TeV}/c^2$ and $\Gamma = 0.012M_X, 0.04M_X$) with the total systematic uncertainty, Δ . For a natural width $\Gamma = 0.012M_{Z'}$, Figure 5.12 shows both the original maximal likelihood shape and the smeared likelihood distribution as a function of $\sigma_X \cdot \text{BR}\{X \rightarrow t\bar{t}\}$ for several X masses, where $X \rightarrow t\bar{t}$ is modelled by PYTHIA $Z' \rightarrow t\bar{t}$ with a natural width $\Gamma = 0.012M_{Z'}$. Also shown in Figure 5.12 are the 95% C.L. upper limits on $\sigma_X \cdot \text{BR}\{X \rightarrow t\bar{t}\}$ with the effects of systematic uncertainties included. Table 5.11 lists the resulting fitted values and Table 5.12 lists the 95% C.L. upper limits for all masses with natural width $\Gamma = 0.012M_X, 0.04M_X$. Figure 5.13 displays these 95% C.L. upper limits on $\sigma_X \cdot \text{BR}\{X \rightarrow t\bar{t}\}$ as a function of M_X .

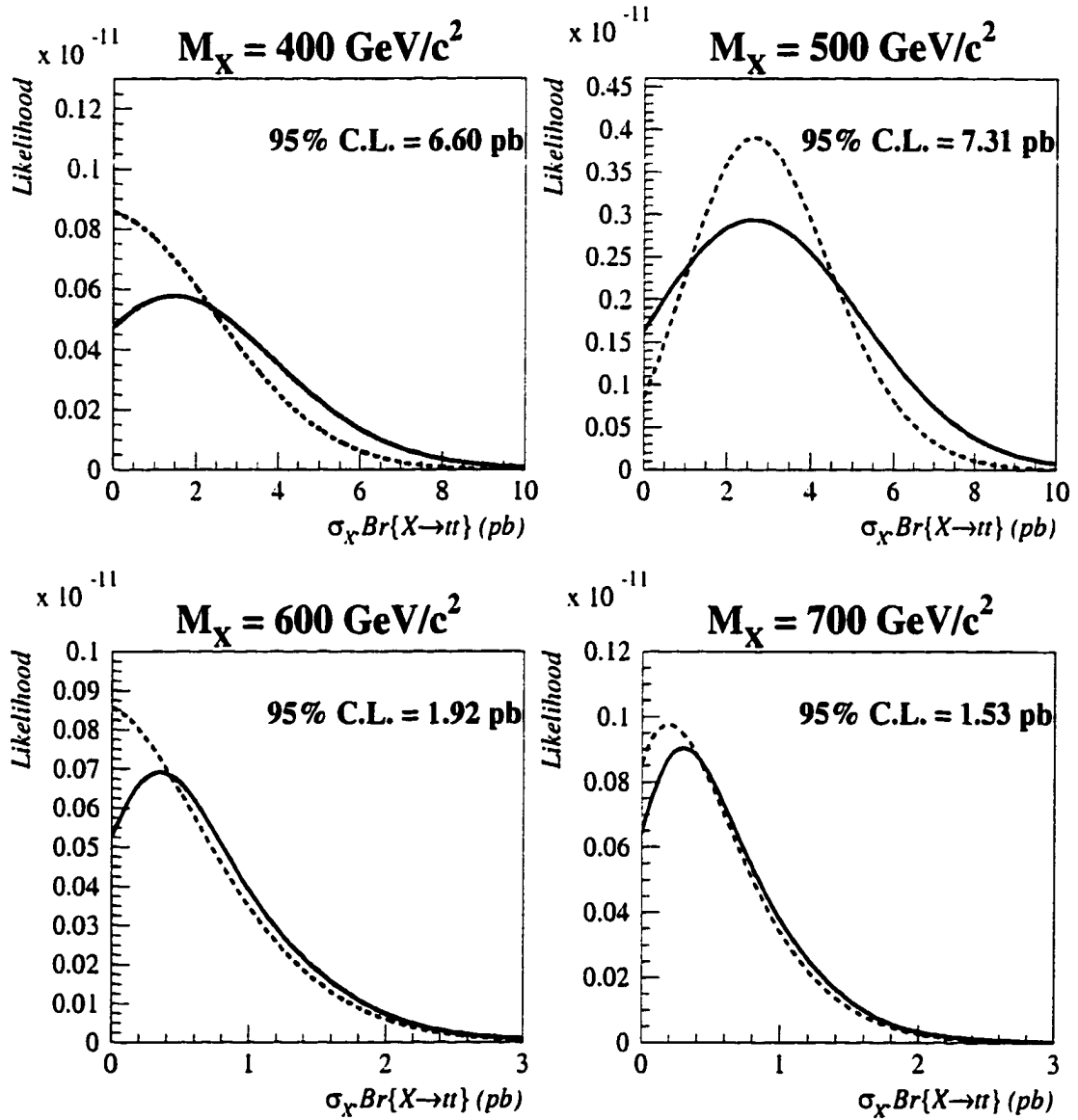


Figure 5.12: Likelihood as a function of $X \rightarrow t\bar{t}$ production cross-section times branching ratio for $M_X = 400, 500, 600$, and $700 \text{ GeV}/c^2$ and natural width $\Gamma = 0.012M_X$. Both the likelihood shape for statistical uncertainties only (dashed) and the likelihood with systematic uncertainties (solid) are shown.

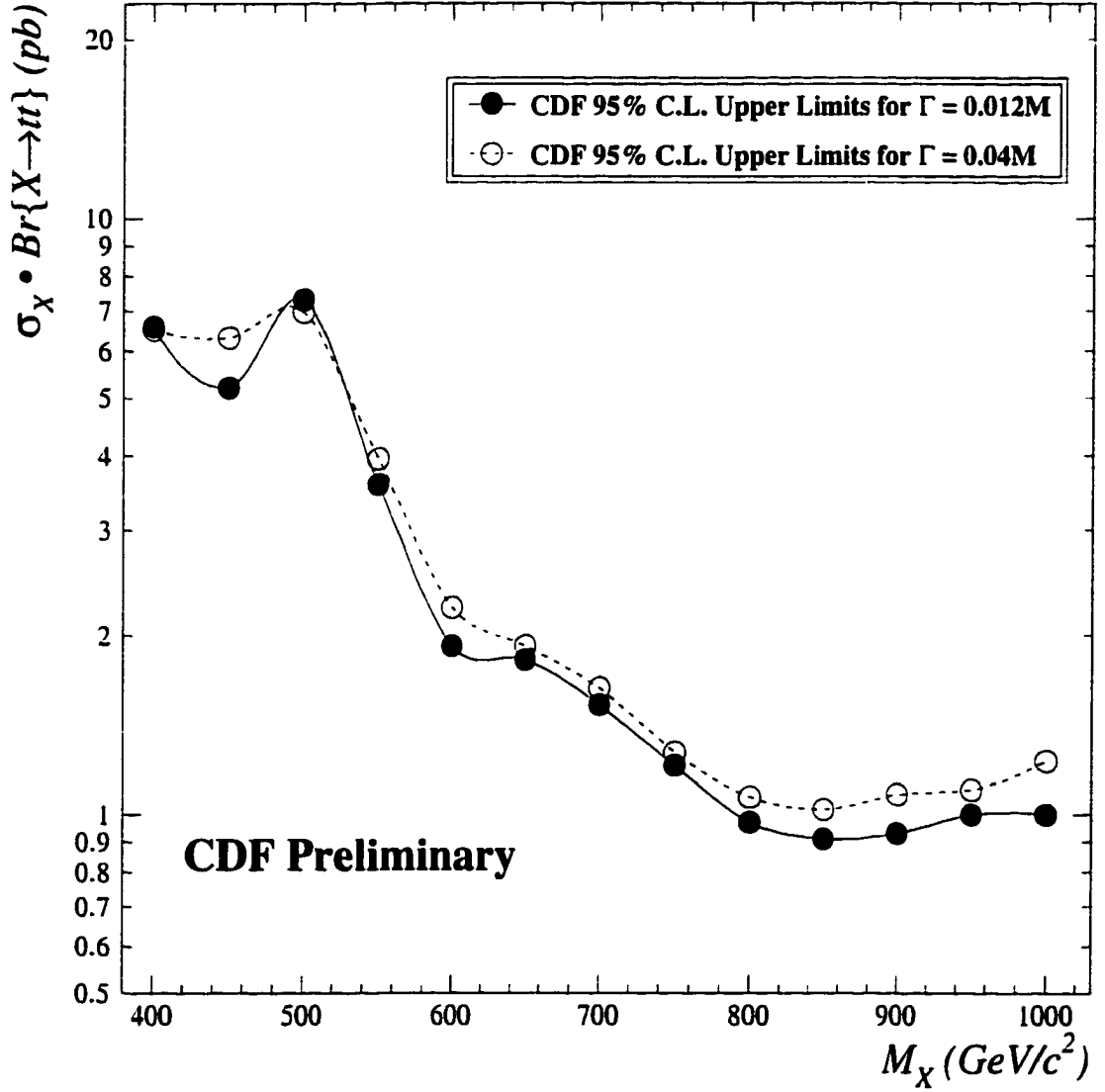


Figure 5.13: The CDF Run 1 95% confidence level $\sigma_X \cdot BR\{X \rightarrow tt\}$ limits as a function of M_X . The effects of systematic uncertainties are included.

M_x (GeV/c ²)	Most Probable $\sigma_x \text{BR}\{X \rightarrow t\bar{t}\}$ (pb) for $\Gamma = 0.012M_x$	Most Probable $\sigma_x \text{BR}\{X \rightarrow t\bar{t}\}$ (pb) for $\Gamma = 0.04M_x$
400	$1.47^{+2.6}_{-1.5}$	$1.42^{+2.5}_{-1.4}$
450	$1.05^{+1.9}_{-1.1}$	$1.32^{+2.4}_{-1.3}$
500	$2.63^{+2.6}_{-2.4}$	$2.28^{+2.5}_{-2.3}$
550	$0.86^{+1.3}_{-0.86}$	$0.97^{+1.4}_{-0.97}$
600	$0.35^{+0.60}_{-0.35}$	$0.42^{+0.73}_{-0.42}$
650	$0.40^{+0.62}_{-0.40}$	$0.40^{+0.65}_{-0.40}$
700	$0.30^{+0.49}_{-0.30}$	$0.32^{+0.53}_{-0.32}$
750	$0.21^{+0.36}_{-0.21}$	$0.22^{+0.38}_{-0.22}$
800	$0.15^{+0.27}_{-0.15}$	$0.16^{+0.31}_{-0.16}$
850	$0.13^{+0.25}_{-0.13}$	$0.15^{+0.29}_{-0.15}$
900	$0.13^{+0.26}_{-0.13}$	$0.16^{+0.30}_{-0.16}$
950	$0.14^{+0.28}_{-0.14}$	$0.16^{+0.30}_{-0.16}$
1000	$0.14^{+0.28}_{-0.14}$	$0.18^{+0.35}_{-0.18}$

Table 5.11: The most probable values of cross-section times branching ratio for narrow resonances (with natural width $\Gamma = 0.012M_x$ and $\Gamma = 0.04M_x$) decaying to $t\bar{t}$. These values include the effects of systematic uncertainties.

M_x (GeV/c ²)	95% C.L. Upper Limit on $\sigma_x \text{BR}\{X \rightarrow t\bar{t}\}$ (pb) for $\Gamma = 0.012M_x$	95% C.L. Upper Limit on $\sigma_x \text{BR}\{X \rightarrow t\bar{t}\}$ (pb) for $\Gamma = 0.04M_x$
400	6.60	6.51
450	5.21	6.32
500	7.31	6.97
550	3.58	3.95
600	1.92	2.23
650	1.82	1.92
700	1.53	1.63
750	1.21	1.27
800	0.97	1.07
850	0.91	1.02
900	0.93	1.08
950	1.00	1.10
1000	1.00	1.23

Table 5.12: The 95% C.L. upper limits cross-section times branching ratio for narrow resonances (with natural width $\Gamma = 0.012M_x$ and $\Gamma = 0.04M_x$) decaying to $t\bar{t}$. These values include the effects of systematic uncertainties.

Chapter 6

Conclusions

As no known particle decays to a $t\bar{t}$ pair within the framework of the standard model, this thesis presents the world's first search for a $t\bar{t}$ resonance. Accordingly, the discovery of such a resonance would provide the only direct evidence to date for physics beyond the standard model.

After establishing selection criteria to isolate events containing candidate $t\bar{t}$ pairs which decay to an electron or muon and four jets, this thesis describes additional event requirements which preferentially select $X \rightarrow t\bar{t}$ events if they exist. Applying these selection criteria to the Run 1 data sample collected from $p\bar{p}$ collisions at Fermilab's CDF detector, we measure the $t\bar{t}$ invariant mass spectrum using a method which improves resolution by incorporating our knowledge of the top quark mass.

Finding no evidence worthy of a $t\bar{t}$ resonance discovery, we investigate the effects of systematic uncertainties and establish model-independent limits on the production cross-section for narrow resonances as shown in Figure 6.1. Figure 6.1 also shows $\sigma_X \cdot \text{BR}\{X \rightarrow t\bar{t}\}$ for a model of topcolor assisted technicolor[25]. In this model, the Z' is leptophobic; that is to say that it does not decay to lepton pairs. In

addition, it does not couple strongly to $b\bar{b}$ pairs. Therefore, the most natural way to search for this object is through its decay to $t\bar{t}$. The limits derived in Chapter 5 exclude at the 95% confidence level the existence of a leptophobic Z' boson with mass $M_{Z'} < 480 \text{ GeV}/c^2$ for natural width $= 0.012 M_{Z'}$, and $M_{Z'} < 780 \text{ GeV}/c^2$ for natural width $= 0.04 M_{Z'}$. Because our resolution is approximately 6% of the resonance mass, our detector resolution will no longer be the dominant factor in determining the Z' signal shape for widths larger than 4%. Extensive simulation would be required in order to set limits at larger widths, including simulation of possible model-dependent interference effects with standard model $t\bar{t}$ production.

With a dramatic luminosity increase provided by the Main Injector and a center of mass energy $\sqrt{s} = 2 \text{ TeV}$, Fermilab's Tevatron is expected to remain on the frontier of experimental high energy particle physics for the duration of "Run 2" which is planned to start in the Spring of 2001. An extensive upgrade to the CDF detector coupled with a data set which is anticipated to be a factor 20 greater than that of Run 1 yields exciting prospects for continued physics at CDF. Using a high statistics data sample collected during Run 2, we can expect that the structure of the $M_{t\bar{t}}$ spectrum will be understood at a deeper level, likely providing answers to questions regarding any potential non-standard model excess and concerns about the behavior near the $t\bar{t}$ threshold. And while the analysis presented in this thesis is not sensitive to the additional topcolor models presented in Reference [25], the prospects for probing these and other non-standard model theories are promising for the Run 2 $X \rightarrow t\bar{t}$ search.

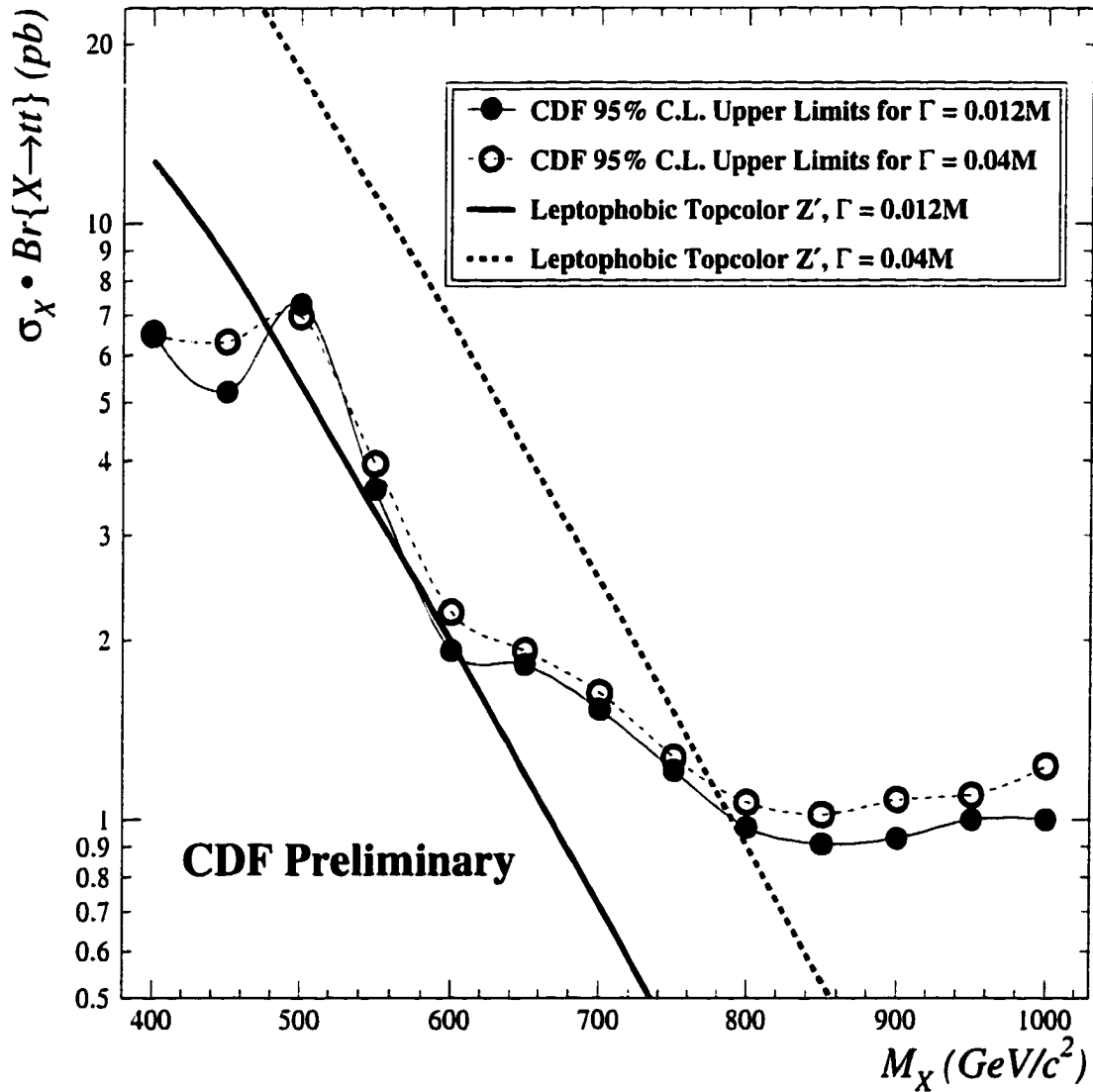


Figure 6.1: The CDF Run 1 95% confidence level $\sigma_X \cdot \text{Br}\{X \rightarrow t\bar{t}\}$ upper limits as a function of resonance mass M_X . The effects of systematic uncertainties are included. Included for reference are the predicted topcolor Z' cross-sections for a width = 1.2% and 4.0% of $M_{Z'}$.

Bibliography

- [1] Albert Einstein, "Physics and Reality," Franklin Institute Journal 221, number 3 (1936).
- [2] M. Gell-Mann, Phys. Rev. **92**, 883 (1953).
- [3] J.J. Aubert, *et al.*, Phys. Rev. Lett. **33**, 1404 (1974); J.-E. Augustin, *et al.*, Phys. Rev. Lett. **33**, 1406 (1974).
- [4] W. Bartel, *et al.*, "A Measurement of the Electroweak Induced Charge Asymmetry in $e^+e^- \rightarrow b\bar{b}$," Phys. Rev. B **146** 437 (1984).
- [5] D. Decamp, *et al.*, "Measurement of the Forward-Backward Asymmetry in $Z \rightarrow b\bar{b}$ and $Z \rightarrow c\bar{c}$," Phys. Rev. B **263** 325 (1991).
- [6] Particle Data Group, C. Caso, *et al.*, Eur. Phys. J. C, **3**, 1 (1998).
- [7] S.L. Glashow, J. Illiopoulos, and L. Maiani, Phys. Rev. D **2**, 1285 (1970).
- [8] L.H. Orr, "Decay Versus Hadronization for Top Quarks Produced in Hadron Colliders," Phys. Rev. D **44**, 88 (1991).
- [9] M. Kruse, Ph.D. Thesis, Purdue University (1996).
- [10] The Fermilab Beam Division's "Concepts Rookie Book," http://www-bd.fnal.gov/operations/rookie_books/concepts/conceptstoc.html.

- [11] A. Beretvas, D. Cronin-Hennessy, P.F. Derwent, Fermilab Preprint FERMILAB-PUB-99-162-E.
- [12] F. Bedeschi, *et al.*, "Design and Construction of the CDF Central Tracking Chamber," Nucl. Instr. and Meth., A268, 33 (1988).
- [13] G. Watts, Ph.D. Thesis, University of Rochester (1994).
- [14] T. Affolder, "Measurement of the Top Quark Mass using the Collider Detector at Fermilab," to be published in Phys. Rev. D.
- [15] P. Koehn, Ph.D. Thesis, University of Rochester (1996).
- [16] D. Kestenbaum, Ph.D. Thesis, Harvard University (1996).
- [17] J. Lewis and P. Avery, "CLEOMC: The CDF Interface to the CLEO Monte Carlo (QQ)," CDF/DOC/MONTECARLO/PUBLIC/2724 (1994).
- [18] A. Caner, "CDFSIM + QFL Simulation of the CDF Detector," CDF/ANAL/MONTECARLO/PUBLIC/2177, 1993.
- [19] T. Sjöstrand, Comput. Phys. Commun. **82**, 74 (1994). We use PYTHIA version 5.7.
- [20] G. Marchesini and B.R. Webber, Nucl. Phys. B **310**, 461 (1988); G. Marchesini *et. al.*, Comput. Phys. Commun. **67**, 465 (1992). We use HERWIG version 5.6.
- [21] J. Lys and A.B. Galtieri, CDF Internal Publication 4075.
- [22] F. Abe *et. al.*, Phys. Rev. Lett. **80**, 2767 (1998).
- [23] F. Abe *et. al.*, Phys. Rev. Lett. **76**, 3070 (1996). This luminosity measurement assumed a total $p\bar{p}$ cross-section of 80 mb.

- [24] E. Laenen, J. Smith, and W.L. Van Neerven, Phys. Lett. **321B**, 254 (1994).
- [25] R. M. Harris, C. T. Hill, and S. J. Parke, Fermilab-FN-687, hep-ph/9911288 (1999).
- [26] Private communication with E. Thorndike.
- [27] In “Top-quark search in the electron+jets channel in proton-antiproton collisions at $\sqrt{s} = 1.8$ TeV”, Phys. Lett. D, 43, 66 (1991), the effects of systematic uncertainties are incorporated into a shape-fitting likelihood function through the use of a Monte Carlo integration technique. Our expression for L' in Section 5 is simply the analytic representation of this technique.
- [28] L. Demortier, R. Hall, R. Hughes, B. Klima, R. Roser, M. Strovink, Fermilab Preprint Fermilab-TM-2084.
- [29] Recall that we select the “best” of the 24 combinatoric possibilities as the one with the lowest χ^2 value and which satisfies all available b -tagging information (Section 3.4.1).
- [30] “Measurement of the $t\bar{t}$ Production Cross Section in $p\bar{p}$ Collisions at $\sqrt{s} = 1.8$ TeV.” Phys. Rev. Lett. 80, 2773 (1998). FERMILAB-PUB-97/286-E.
- [31] Private communications with S. Blusk, L. Demortier, J. Lewis and G. Velez.
- [32] L. Lyons. “Statistics for Nuclear and Particle Physicists,” pp. 85-102.
- [33] W.T. Eadie, *et.al.*. “Statistical Methods in Experimental Physics,” pp. 155-162.

Appendix A

Errors from the

Background-Constrained Binned

Likelihood Fitting Method

In determining the likelihood as a function of $\sigma_x \cdot \text{BR}\{X \rightarrow t\bar{t}\}$ in Section 4.2.1, we employ a maximum likelihood method ([32],[33]) which does not constrain the amount of background employed in the fit. In our search for a narrow $t\bar{t}$ resonance, we purposefully choose an unconstrained fit so as to avoid tying our analysis to a particular standard model $t\bar{t}$ production cross-section assumption. Because we also find it less than appealing to treat separate background sources differently, we decided against the prospect of constraining only the non- $t\bar{t}$ background prediction within its errors.

However, before finally deciding on this method, we investigated the merits of a background-constrained likelihood fit. Specifically, we have studied the appropriateness of errors returned by a constrained fit. And while the results of this study are not directly related to the analysis presented in this thesis, background-

constraints are common to many other similar analyses and perhaps this information can be applicable at some other time.

A.1 Defining L and Errors

To avoid the complications of additional background sources (as we have in the $X \rightarrow t\bar{t}$ search), we simplify the situation by defining our likelihood function to fit for only one background shape,

$$L = \frac{1}{\sqrt{2\pi}\sigma_b} e^{-\frac{(n_b - n_b^{exp})^2}{2\sigma_b^2}} \prod_i^{bins} \frac{\mu_i^{n_i} e^{-\mu_i}}{n_i!} \quad (\text{A.1})$$

where

$$\mu_i = \mu_s + \mu_b = n_s f_s(i) + n_b f_b(i), \quad (\text{A.2})$$

n_s and n_b represent the fitted number of signal and background events, the i^{th} bin contains n_i observed events, f_s (f_b) is the signal (background) shape normalized to unity, and n_b is constrained to be n_b^{exp} within its error given by σ_b .

Clearly, if L is gaussian in n_s about its maximum at n_s^{max} , i.e., $L \sim e^{-(n_s - n_s^{max})^2}$, then $-\log(L)$ is parabolic in n_s about n_s^{max} . A commonly exploited property of the maximum likelihood method is that, for L gaussian in n_s , the error on n_s^{max} is given by the change in n_s which yields a $\frac{1}{2}$ unit increase in $-\log(L)$. However, we have found that in certain circumstances, L as defined above tends not to be gaussian about n_s^{max} and, thus, the statistical errors cannot be expected to correspond to a $\frac{1}{2}$ unit increase in $-\log(L)$. In an effort to determine appropriate errors on the fitted value of n_s , we calculate the errors using two different procedures: (1) the aforementioned $\frac{1}{2}\log(L)$ errors; (2) an L -integration method. Our L -integration method establishes the approximate ‘‘gaussian errors’’ for our generally non-gaussian L as

follows:

The positive error on the fitted value of n_s (*viz.*, $\sigma_{n_s}^+$) satisfies

$$\frac{1}{\mathcal{N}^+} \int_{n_s^{max}}^{n_s^{max} + \sigma_{n_s}^+} L \, dn_s = \frac{2}{3} \quad \text{where} \quad \mathcal{N}^+ = \int_{n_s^{max}}^{+\infty} L \, dn_s$$

while the negative error $\sigma_{n_s}^-$ is given by

$$\frac{1}{\mathcal{N}^-} \int_{n_s^{max}}^{n_s^{max} - \sigma_{n_s}^-} L \, dn_s = \frac{2}{3} \quad \text{where} \quad \mathcal{N}^- = \int_{n_s^{max}}^{-\infty} L \, dn_s.$$

Unfortunately, we find that the method of defining the errors in this manner is susceptible to the same L -shape pathology which make the $\frac{1}{2}\log(L)$ method untenable.

A.2 (In)appropriateness of Errors

To investigate the errors returned by the maximum likelihood method, we generate pseudo-experiments and examine the n_s “pull” distribution. The number of background events (N_b) for a particular pseudo-experiment is chosen by poisson fluctuating a value randomly selected from a gaussian distribution centered on the expected number of background events, n_b^{exp} , with a width equal σ_b . N_s , the number of signal events for a particular pseudo-experiment, is simply given by a poisson fluctuation of the expected number, n_s^{exp} . We then chose N_b (N_s) events according the background (signal) probability distribution, f_b (f_s).

We define the pull on the fitted number of signal events, n_s^{max} , as:

$$pull = \begin{cases} \frac{(n_s^{max} - n_s^{exp})}{\sigma_{n_s}^+} & \text{if } n_s^{max} < n_s^{exp} \\ \frac{(n_s^{max} - n_s^{exp})}{\sigma_{n_s}^-} & \text{if } n_s^{max} > n_s^{exp} \end{cases}$$

For properly determined errors, we expect the pull distribution to be gaussian distributed about 0.0 with a width of 1.0. We find this to be the case for pseudo-experiments in which n_s^{exp} is relatively large or if the background and signal shapes themselves are similar. However, if the background and signal shapes are relatively distinct and n_s^{exp} is small, we find that the pull distribution does not have the expected width or structure. Figure A.1 displays the pull distributions obtained from $\frac{1}{2}\log(L)$ errors for the four cases listed in Table A.1. The CPU-intensive calculations of the pull determined with L -integration errors follow similar trends.

A.3 Unphysical Regions of Parameter Space

It is the effects of the unphysical region of n_s - n_b space which have been found to be responsible for the inappropriate errors returned for the case of small n_s^{exp} and relatively distinct background and signal templates. We have found that by placing no direct constraints on the fitted parameters, MINUIT, which determines the maximum of L by minimizing the $-\log(L)$, will inevitably search in the region of n_s - n_b phase-space where one or more of the μ_i , defined in Equation A.2, are zero or negative. In this region, the poisson probability terms in L lose all meaning and the occurrence of non-positive μ_i prohibit the determination of

$$-\log(L) = \log(\sqrt{2\pi}\sigma_b) + \frac{(n_b - n_b^{exp})^2}{2\sigma_b^2} - \sum_i^{bins} n_i \log(\mu_i) - \mu_i - \log(n_i!).$$

	Small number of signal	Large number of signal
<p>Similar shapes ($R_{max} = 1.31$)</p>	<p>$n_s^{exp} = 5, n_b^{exp} = 50, \sigma_b = 7$</p> <p>signal shape: $\frac{1}{\sqrt{2\pi}(125)} e^{-\frac{(M_{\ell\bar{\ell}} - 572.5)^2}{2(125)^2}}$ </p> <p>background shape: $\frac{1}{\sqrt{2\pi}(125)} e^{-\frac{(M_{\ell\bar{\ell}} - 562.5)^2}{2(125)^2}}$ </p>	<p>$n_s^{exp} = 50, n_b^{exp} = 50, \sigma_b = 7$</p> <p>signal shape: $\frac{1}{\sqrt{2\pi}(125)} e^{-\frac{(M_{\ell\bar{\ell}} - 572.5)^2}{2(125)^2}}$ </p> <p>background shape: $\frac{1}{\sqrt{2\pi}(125)} e^{-\frac{(M_{\ell\bar{\ell}} - 562.5)^2}{2(125)^2}}$ </p>
<p>Dissimilar shapes ($R_{max} = 4.85E + 08$)</p>	<p>$n_s^{exp} = 5, n_b^{exp} = 50, \sigma_b = 7$</p> <p>signal shape: $\frac{1}{\sqrt{2\pi}(125)} e^{-\frac{(M_{\ell\bar{\ell}} - 762.5)^2}{2(125)^2}}$ </p> <p>background shape: $\frac{1}{\sqrt{2\pi}(125)} e^{-\frac{(M_{\ell\bar{\ell}} - 462.5)^2}{2(125)^2}}$ </p>	<p>$n_s^{exp} = 50, n_b^{exp} = 50, \sigma_b = 7$</p> <p>signal shape: $\frac{1}{\sqrt{2\pi}(125)} e^{-\frac{(M_{\ell\bar{\ell}} - 762.5)^2}{2(125)^2}}$ </p> <p>background shape: $\frac{1}{\sqrt{2\pi}(125)} e^{-\frac{(M_{\ell\bar{\ell}} - 462.5)^2}{2(125)^2}}$ </p>

Table A.1: The four situations for which pseudo-experiments were generated. The shapes are confined to the 32 bin, 200-1000 GeV/c² $M_{\ell\bar{\ell}}$ spectrum. The resulting pull distributions are shown in Figure A.1. The definition of R_{max} is described in Section A.3.

For these reasons, we necessarily require that MINUIT avoid searching for the minimum of $-\log(L)$ in the region of n_s - n_b space where one or more $\mu_i \leq 0$.

While we are unaware of a consensus concerning the method for limiting the MINUIT search, we have consulted with several collaborators familiar with this minimization package and the binned likelihood method[31]. In this analysis, we choose to effectively restrict MINUIT's search to the $\mu_i > 0$ region of n_s - n_b space by setting $-\log(L)$ equal to an exceedingly large value when n_s and n_b are chosen such that any $\mu_i \leq 0$.

While this method is common to similar analyses which also do not directly restrict n_s or n_b and it sufficiently forces MINUIT to search exclusively in the $\mu_i > 0$ region, we find that it can result in the distortion of the L shape and thereby adversely affect the returned errors on n_s^{max} . These effects, for a given value of n_b^{exp} , are observed only when n_s^{exp} is sufficiently small *and* the background and signal templates are sufficiently different. We quantify the later by defining R_{max} , the maximum of the ratio of $f_s(i)$ to $f_b(i)$:

$$R_{max} = \max \left(\frac{f_s(i)}{f_b(i)} \right) \quad \text{for } 1 \leq i \leq \text{number of bins}$$

As can be seen from Equation A.2, the requirement that $\mu_i > 0$ imposes a dramatic, yet continuous boundary in the negative n_s region. Consider, for example, the case of similar background and signal shapes as described in Table A.1 (see Figure A.2a). In the instance of $n_s^{exp} = 5$ and $n_b^{exp} = 50$, it is quite conceivable that a pseudo-experiment would contain no signal events ($N_s = 0$) and, say, $N_b = 48$ background events (see Figure A.2b). Due to the similarity of background and signal templates, coupled with the fact that n_b is gaussian constrained to n_b^{exp} within its error, it is not surprising that the maximum value of L should occur at $n_s \approx -2$ (shown in Figure A.2c) and $n_b \approx 50$. In mapping L as a function of n_s ,

however, there exists a certain range of negative values of n_s for which n_b will have to increase dramatically in order to satisfy the $\mu_i > 0$ condition. The location (call it n'_s) of this region of offending negative values of n_s approximately satisfies

$$n'_s f_s(i) + n_b^{exp} f_b(i) \leq 0$$

or re-written in terms of R_{max}

$$n'_s \leq \frac{-n_b^{exp}}{R_{max}} \quad (\text{A.3})$$

Yet in this particular case, $R_{max} = \frac{f_s(32)}{f_b(32)} = 1.31$ and consequently, we do not expect the shape of L to be distorted in the region of n_s^{max} . Now suppose (as shown in Figure A.3a) that in the example above, $f_b(32)$ were reduced by a factor of 50. (Note that in this particular pseudo-experiment, there are no events in bin 32, as shown in Figure A.3b.) This change results in a scaling of R_{max} by a factor of 50, ensuring that the maximum of L is no longer located at $n_s \approx -2$ because now, according to Equation A.3, n'_s falls in the region of interest and dramatically distorts the shape of L . This is clearly evident in Figure A.3c whose maximum now occurs at $n_s = -0.764$.

From this study it seems reasonable to require that

$$n_s^{exp} \gg \frac{-n_b^{exp}}{R_{max}}$$

in order to obtain appropriate errors from the background-constrained, binned likelihood described here.

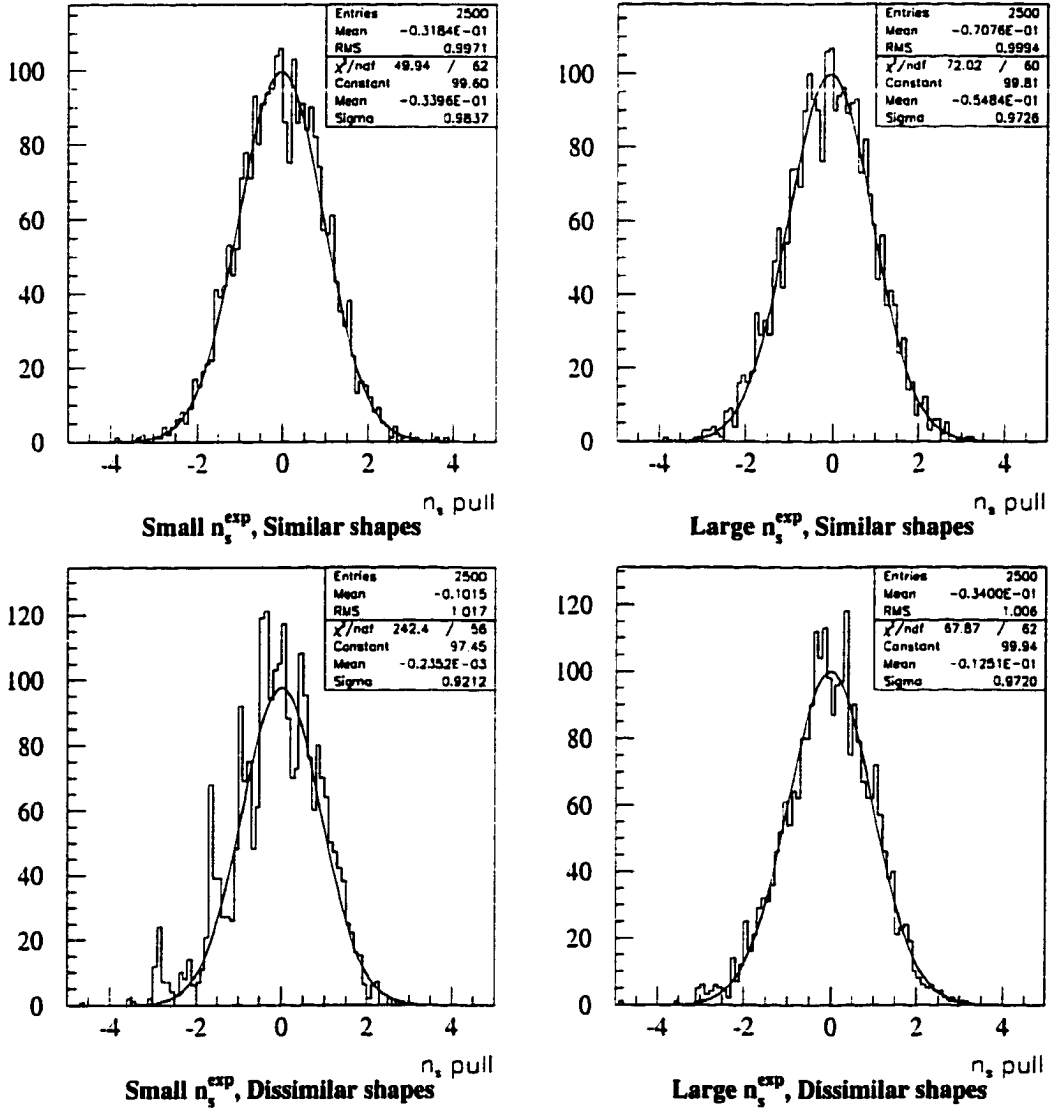


Figure A.1: n_s "pull" distributions (using $\frac{1}{2}\log(L)$ errors) for the four cases listed in Table A.1. Upper left: small signal, similar shapes; Upper right: large signal, similar shapes; Lower left: small signal, dissimilar shapes; Lower right: large signal, dissimilar shapes.

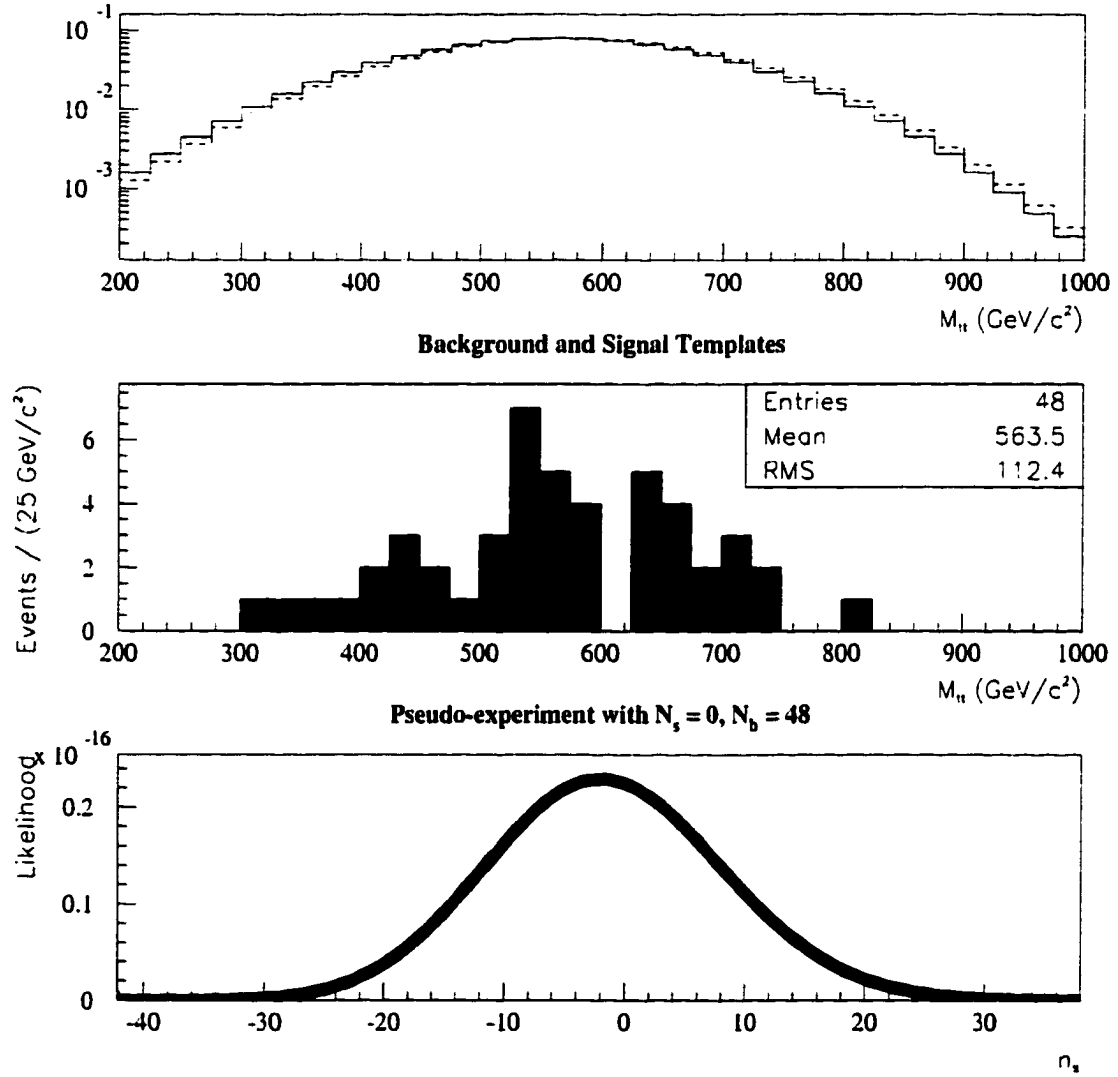


Figure A.2: Top: Background and signal templates as described in Section A.3. $R_{max} = 1.31$. Solid histogram = background template. Dashed histogram = signal template. Middle: Pseudo-experiment with $N_s = 0$ and $N_b = 48$, chosen from the above templates. Bottom: L as a function of n_s for this particular pseudo-experiment. The maximum occurs at $n_s = -2.01$.

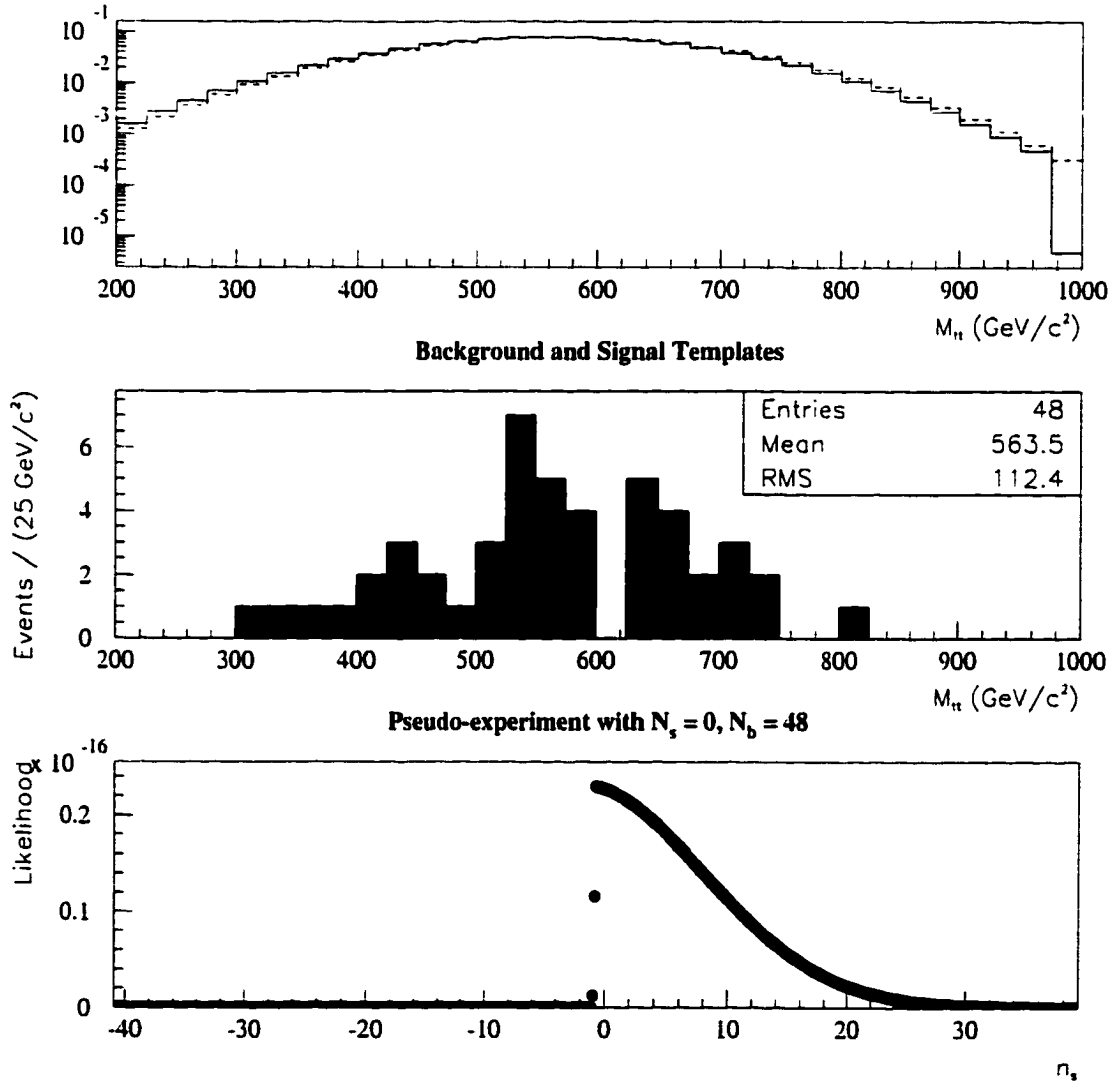


Figure A.3: Top: Same background and signal templates as figure 2a except $f_b(32) \rightarrow \frac{f_b(32)}{50}$. $R_{max} = 65.4$. Solid histogram = background template. Dashed histogram = signal template. Middle: Same pseudo-experiment (with $N_s = 0$ and $N_b = 48$) as figure 2b. Bottom: L as a function of n_s for this particular pseudo-experiment. The maximum occurs at $n_s = -0.746$.



2017 ProQuest Distribution Agreement

This Agreement is between the author (Author) and ProQuest LLC, through its ProQuest Dissertation Distribution business (formerly ProQuest/UMI). Under this Agreement, Author grants ProQuest certain rights to preserve, archive and distribute the dissertation or thesis (the Work), abstract, and index terms provided by Author to ProQuest.

Section I. License for Inclusion of the Work in ProQuest Publishing Program

Grant of Rights. Author hereby grants to ProQuest the **non-exclusive**, worldwide right to reproduce, distribute, display and transmit the Work (in whole or in part) in such tangible and electronic formats as may be in existence now or developed in the future. Author further grants to ProQuest the right to include the abstract, bibliography and other metadata in the ProQuest Dissertations & Theses database (PQDT) and in ProQuest Dissertation Abstracts International and any successor or related index and/or finding products or services.

ProQuest Publishing Program - Election and Elements. The rights granted above shall be exercised according to the publishing option selected by Author in Section III, Author Options, and subject to the following additional Publishing Program requirements:

- **Distribution of the Work.** Except as restricted by Author in the publishing option selected, the rights granted by Author automatically include (1) the right to allow sale and distribution of the Work, in whole or in part, by ProQuest and its sales agents and distributors and (2) the right to make the Abstract, bibliographic data and any meta data associated with the Work available to search engines and harvesters.
- **Restrictions.** ProQuest will use commercially reasonable efforts to restrict the distribution of the Work as provided under the publishing option selected by Author or *as later elected by Author* through direct contact with ProQuest. Such election is subject to Author's Degree Granting Institution Directives. With respect to restrictions requested after submission of the Work, Author acknowledges that ProQuest cannot recall or amend previously distributed versions of the Work.
- **Removal of Work from the Program.** ProQuest may elect not to distribute the Work if it believes that all necessary rights of third parties have not been secured. Refer to the website http://www.proquest.com/products_umi/dissertations/ for information about copyright and your dissertation or thesis. If Author's degree is rescinded, and/or the degree-granting institution so directs, ProQuest will expunge the Work from its publishing program in accordance with its then current publishing policies.
- **Degree Granting Institution Directives.** Author is solely responsible for any conflict between policies and directions of Author's degree-granting institution, Author's choice of publishing model, and/or any restriction Author places on the use of the Work. For the avoidance of doubt, ProQuest is not responsible for access to the Work that is provided by Author's degree-granting institution through its library or institutional repository. Author must work directly with Author's degree granting institution to ensure application of any restrictions to access relating to the Work by Author's degree granting institution.

Delivery of the Work. Author shall provide to ProQuest the Work and all necessary supporting documents during the online submission process, according to the Instructions accompanying this agreement.

Rights Verification. Author represents and warrants that Author is the copyright holder of the Work and has obtained all necessary rights to permit ProQuest to reproduce and distribute third party materials contained in any part of the Work, including all necessary licenses for any non-public, third party software necessary to access, display, and run or print the Work. Author is solely responsible and will indemnify ProQuest for any third party claims related to the Work as submitted for publication.

Open Access Publishing Plus

- ☒ I want the broadest possible dissemination of my work, and I want to provide free global access to the electronic copy of my work via the internet.
- ☒ I understand that I will not be eligible to receive royalties.

I want major search engines (e.g. Google, Yahoo) to discover my work. Learn more:

<http://www.proquest.com/en-US/products/dissertations/google.shtml>

☒ Yes
☐ No

Acknowledgment: I have read, understand and agree to this ProQuest Publishing Agreement, including all rights and restrictions included within the publishing option chosen by me as indicated above.

REQUIRED Author's signature  Date 12 AUG 17

(Print Name) JOSH A. CASSADA

Institution conferring degree UNIVERSITY OF ROCHESTER

This page must accompany your manuscript and the rest of the submission materials

Dissertation/Master's Thesis Submission Form

Please print clearly in block letters

Personal Information

Last Name

CASSADA

Middle Name or Initial

A

First Name

JOSH

Country (ies) of Citizenship

US

Institution conferring degree

UNIVERSITY of ROCHESTER

Degree awarded (abbreviate; e.g., Ph.D.)

Ph.D.

College, School, or Division

Year degree awarded

2000

Department or Program

DEPARTMENT of PHYSICS AND ASTRONOMY

Year manuscript completed

2000

Advisor/Committee Chair

DR. PAUL TIPTON

Please check type of manuscript:

☐ M (Master's Thesis)

☒ D (Dissertation)

Committee Member _____ Committee Member _____
Committee Member _____ Committee Member _____
Committee Member _____ Committee Member _____
Language of manuscript ENGLISH

Primary Subject Category: Enter the 4-digit code and category name from the Subject Category Guide that most closely describes the area of your research.

Code 0798 Category Particle Physics

You may suggest two additional subject categories that may aid in the discovery of your work in our digital database.

Code _____ Category _____ Code _____ Category _____

Provide up to 6 keywords or short phrases for citation indices, library cataloging, and database searching.

TOP QUARK
TOP ANTI-TOP

Current Contact Information

Current Email
Address

cassada.josh@gmail.com

Street Address

2316 DOUAN SPRINGS LANE

Please provide your postal address if you are interested in receiving royalties on sales of your

City

FRIENDSWOOD

Province

TX

Daytime Phone

207 522 6114

Country

US

Postal Code

77546

Evening Phone

Permanent Contact Information

Permanent
Email Address

Street Address
(line 1)

City

Country

SAME

Province

Postal Code

Future Phone

Alternate
Future Phone

THIS PAGE MUST ACCOMPANY YOUR MANUSCRIPT AND THE REST OF YOUR SUBMISSION MATERIALS

Subject Categories

The ProQuest Dissertations & Theses (PQDT) database and the ProQuest citation indices are arranged by subject categories. Please select the one category below that best describes your field of research or creative work. You may add one or two additional categories on your submission form that will also be associated with your work as secondary subjects.

Arts, Business, Education, Humanities, and Social Sciences

AREA, ETHNIC, AND GENDER STUDIES

African American studies 0296
African studies 0293
American studies 0323
Asian American studies 0343
Asian studies 0342
Baltic studies 0361
Black studies 0325
Canadian studies 0385
Caribbean studies 0432
Classical studies 0434

East European studies 0437
Ethnic studies 0631
European studies 0440
French Canadian culture 0482
Gender studies 0733
GLBT studies 0492
Hispanic American studies 0737
Holocaust studies 0507
Islamic culture 0512
Judaic studies 0751
Latin American studies 0550
Middle Eastern studies 0555
Native American studies 0740
Near Eastern studies 0559

North African studies 0560
Pacific Rim studies 0561
Regional studies 0604
Scandinavian studies 0613
Slavic studies 0614
South African studies 0654
South Asian studies 0638
Sub Saharan Africa studies 0639
Women's studies 0453

BUSINESS

Accounting	0272
Arts management	0424
Banking	0770
Business	0310
Entrepreneurship	0429
Finance	0508
Management	0454
Marketing	0338
Sports management	0430

COMMUNICATIONS AND INFORMATION SCIENCES

Communication	0459
Information science	0723
Journalism	0391
Library science	0399
Mass communication	0708
Technical communication	0643
Web studies	0646

FINE AND PERFORMING ARTS

Art criticism	0365
Art history	0377
Cinematography	0435
Dance	0378
Design	0389
Film studies	0900
Fine arts	0357
Music	0413
Performing arts	0641
Theater	0465
Theater history	0644

EDUCATION

Adult education	0516
Art education	0273
Bilingual education	0282
Business education	0688
Community college education	0275
Continuing education	0651
Curriculum development	0727
Early childhood education	0518
Education	0515
Education finance	0277
Education policy	0458
Educational administration	0514
Educational evaluation	0443
Educational leadership	0449
Educational psychology	0525
Educational technology	0710
Educational tests & measurements	0288
Elementary education	0524
English as a second language	0441
Foreign language instruction	0444
Gifted education	0445
Health education	0680
Higher education	0745
Higher education administration	0446
History of education	0520
Home economics education	0278
Industrial arts education	0521
Instructional design	0447
Language arts	0279
Mathematics education	0280
Middle school education	0450
Multicultural education	0455
Music education	0522
Pedagogy	0456
Performing arts education	0457
Philosophy of education	0998
Physical education	0523
Reading instruction	0535
Religious education	0527
School counseling	0519
Science education	0714
Secondary education	0533
Social sciences education	0534
Sociology of education	0340
Special education	0529
Teacher education	0530
Vocational education	0747

HUMANITIES

HISTORY

African history	0331
American history	0337
Ancient history	0579
Asian history	0332
Black history	0328
Canadian history	0334
European history	0335
History	0578
History of Oceania	0504
History of science	0585
Latin American history	0336
Medieval history	0581
Middle Eastern history	0333
Military history	0772
Modern history	0582
Russian history	0724
World history	0506

LANGUAGE & LITERATURE

African literature	0316
American literature	0591
Ancient languages	0289
Asian literature	0305
British and Irish literature	0593
Canadian literature	0352
Caribbean literature	0360
Classical literature	0294
Comparative literature	0295
English literature	0593
French Canadian literature	0355
Germanic literature	0311
Icelandic & Scandinavian literature	0362
Language	0679
Latin American literature	0312
Linguistics	0290
Literature	0401
Literature of Oceania	0356
Medieval literature	0297
Middle Eastern literature	0315
Modern language	0291
Modern literature	0298
Rhetoric	0681
Romance literature	0313
Slavic literature	0314

PHILOSOPHY AND RELIGION

Aesthetics	0650
Biblical studies	0321
Canon law	0375
Clerical studies	0319
Comparative religion	0618
Divinity	0376
Epistemology	0393
Ethics	0394
Logic	0395
Metaphysics	0396
Pastoral counseling	0397
Philosophy	0422
Philosophy of Religion	0322
Philosophy of science	0402
Religion	0318
Religious history	0320
Spirituality	0647
Theology	0469

LAW AND LEGAL STUDIES

Alternative dispute resolution	0649
Intellectual property	0513
International law	0616
Law	0398
Patent law	0562

SOCIAL SCIENCES

Archaeology	0324
Area planning and development	0341
Criminology	0627
Cultural anthropology	0326
Demography	0938
Economic history	0509
Economic theory	0511
Economics	0501
Economics, Commerce-Business	0505
Economics, Labor	0510
Folklore	0358
Forensic anthropology	0339
Geography	0366
Individual & family studies	0628
International relations	0601
Labor relations	0629
Military studies	0750
Organization theory	0635
Organizational behavior	0703
Peace studies	0563
Physical anthropology	0327
Political Science	0615
Public administration	0617
Public policy	0630
Recreation and tourism	0814
Social research	0344
Social structure	0700
Social work	0452
Sociolinguistics	0636
Sociology	0626
Transportation planning	0709
Urban planning	0999

INTERDISCIPLINARY

Alternative energy	0363
Biographies	0304
Climate change	0404
Cultural resources management	0436
Energy	0791
Food science	0359
Home economics	0386
Information technology	0489
Multimedia	0558
Museum studies	0730
Sustainability	0640
Textile research	0994
Wood sciences	0746

Behavioral, Natural, and Physical Sciences**AGRICULTURE**

Agriculture	0473
Agronomy	0285
Animal diseases	0476
Animal sciences	0475
Fisheries and aquatic sciences	0792
Forestry	0478
Horticulture	0471
Plant pathology	0480
Plant sciences	0479
Range management	0777
Soil sciences	0481
Urban forestry	0281
Wildlife management	0286

ARCHITECTURE

Architecture	0729
Architectural engineering	0462
andscape architecture	0390

BEHAVIORAL SCIENCES

Animal behavior	0602
Behavioral sciences	0384
Clinical psychology	0622
Cognitive psychology	0633
Counseling psychology	0603
Developmental psychology	0620
Experimental psychology	0623
Occupational psychology	0624
Personality psychology	0625
Physiological psychology	0989
Psychobiology	0349
Psychology	0621
Quantitative psychology and psychometrics	0632
Social psychology	0451

BIOLOGICAL SCIENCES

Biochemistry	0487
Bioinformatics	0715

Biology	0306
Biomechanics	0648
Biophysics	0786
Biostatistics	0308
Cellular biology	0379
Developmental biology	0758
Endocrinology	0409
Entomology	0353
Evolution & development	0412
Genetics	0369
Histology	0414
Limnology	0793
Microbiology	0410
Molecular biology	0307
Morphology	0287
Neurosciences	0317
Parasitology	0718
Physiology	0719
Plant biology	0309
Systematic biology	0423
Virology	0720

ECOSYSTEM SCIENCES

Ecology	0329
Macroecology	0420
Paleoecology	0426

ENGINEERING

Aerospace engineering	0538
Artificial intelligence	0800
Automotive engineering	0540
Biomedical engineering	0541
Chemical engineering	0542
Civil engineering	0543
Computer engineering	0464
Computer science	0984
Electrical engineering	0544
Engineering	0537
Geological engineering	0466
Geophysical engineering	0467
Geotechnology	0428
Industrial engineering	0546
Mechanical engineering	0548
Mining engineering	0551
Naval engineering	0468
Nanotechnology	0652
Nuclear engineering	0552
Ocean engineering	0547
Operations research	0796
Packaging	0549
Petroleum engineering	0765
Plastics	0795
Robotics	0771
System science	0790

ENVIRONMENTAL SCIENCES

Conservation biology	0408
Environmental economics	0438
Environmental education	0442
Environmental engineering	0775
Environmental geology	0407
Environmental health	0470
Environmental justice	0619
Environmental law	0439
Environmental management	0474
Environmental philosophy	0392
Environmental science	0768
Environmental studies	0477
Land use planning	0536
Natural resource management	0528
Water resources management	0595
Wildlife conservation	0284

GEOSCIENCES

Aeronomy	0367
Atmospheric chemistry	0371
Atmospheric sciences	0725
Biogeochemistry	0425
Biological oceanography	0416
Chemical oceanography	0403
Continental dynamics	0406
Geobiology	0483
Geochemistry	0996
Geographic information science and geodesy	0370
Geology	0372
Geomorphology	0484
Geophysics	0373
Hydrologic sciences	0388
Marine geology	0556
Meteorology	0557
Mineralogy	0411
Paleoclimate science	0653
Paleontology	0418
Petroleum geology	0583
Petrology	0584
Physical geography	0368
Physical oceanography	0415
Planetology	0590
Plate tectonics	0592
Remote sensing	0799
Sedimentary geology	0594

**HEALTH AND MEDICAL
SCIENCES**

Aging	0493
Alternative medicine	0496
Audiology	0300
Dentistry	0567
Epidemiology	0766
Gerontology	0351
Health care management	0769
Health sciences	0566
Immunology	0982
Kinesiology	0575
Medical ethics	0497
Medical imaging and radiology	0574
Medicine	0564
Mental health	0347
Nursing	0569
Nutrition	0570
Obstetrics and gynecology	0380
Occupational health	0354
Occupational therapy	0498
Oncology	0992
Ophthalmology	0381
Osteopathic medicine	0499
Pathology	0571
Pharmaceutical sciences	0572
Pharmacology	0419
Physical therapy	0382
Public health	0573
Public health occupations education	0500
Speech therapy	0460
Surgery	0576
Toxicology	0383
Veterinary medicine	0778

**MATHEMATICAL AND
PHYSICAL SCIENCES**

Analytical chemistry	0486
Applied mathematics	0364
Astronomy	0606
Astrophysics	0596
Atomic physics	0748
Chemistry	0485
Condensed matter physics	0611
Electromagnetics	0607
High temperature physics	0597
Inorganic chemistry	0488
Low temperature physics	0598
Materials science	0794
Mathematics	0405
Mechanics	0346
Molecular chemistry	0431
Molecular physics	0609
Nanoscience	0565
Nuclear chemistry	0738
Nuclear physics	0756
Optics	0752
Organic chemistry	0490
Particle physics	0798
Physical chemistry	0494
Physics	0605
Plasma physics	0759
Polymer chemistry	0495
Quantum physics	0599
Statistics	0463
Theoretical mathematics	0642
Theoretical physics	0753